Improvement of laser-wakefield accelerators: towards a compact free electron laser

Rémi Lehe

▶ **To cite this version:**

Rémi Lehe. Improvement of laser-wakefield accelerators: towards a compact free electron laser. Plasma Physics [physics.plasm-ph]. Ecole Polytechnique, 2014. English. NNT : . tel-01088398

HAL Id: tel-01088398
https://pastel.hal.science/tel-01088398

Submitted on 27 Nov 2014

HAL is a multi-disciplinary open access archive for the deposit and dissemination of scientific research documents, whether they are published or not. The documents may come from teaching and research institutions in France or abroad, or from public or private research centers.

L'archive ouverte pluridisciplinaire **HAL**, est destinée au dépôt et à la diffusion de documents scientifiques de niveau recherche, publiés ou non, émanant des établissements d'enseignement et de recherche français ou étrangers, des laboratoires publics ou privés.

Improvement of the quality of laser-wakefield accelerators: towards a compact free-electron laser

THÈSE

présentée et soutenue publiquement le 11 juillet 2014

pour l'obtention du

Doctorat de l'École Polytechnique

par

Rémi Lehe

Composition du jury

Rapporteurs :	Gilles Maynard	LPGP, Orsay
	Vladimir Tikhonchuk	CELIA, Talence
Examinateurs :	Marie-Emmanuelle Couprie	SOLEIL, Gif-sur-Yvette
	Patrick Mora	CPHT, Palaiseau
	Carl B. Schroeder	LBNL, Berkeley
	Luís O. Silva	IST, Lisbonne
Directeur de thèse :	Victor Malka	LOA, Palaiseau

Mis en page avec la classe thesul.

Acknowledgements

The three years that I spent working on this thesis were an edifying – and enjoyable – adventure, and I would like to thank those who contributed to it and made it possible.

First of all, I am extremely grateful to my PhD advisor Victor Malka. Among many other things, I thank him for the trust and freedom he granted me, for his experienced and yet open-minded guidance, and for the excellent conditions in which I had the priviledge to work. I also warmly thank my co-advisor Agustin Lifschitz for introducing me to PIC codes, as well as for the availability and deep expertise which he always displayed in our numerous discussions.

I wish to express my gratitude to Gilles Maynard and Vladimir Tikhonchuk for thoroughly reviewing this manuscript. I also thank them, as well as the jury members Marie-Emmanuelle Couprie, Patrick Mora, Carl Schroeder and Luís Silva, for taking the time to attend my defense, and for their very interesting questions and remarks.

I am also indebted to my close collaborators and co-authors for their help and contribution. I am thankful to Xavier Davoine for the several research projects that emerged from our conversations, and for our close collaboration throughout those three years. I am also grateful to Igor Andriyash for our daily (and lively) discussions, as well as for his remarkable coding skills – which allowed for an extremely fruitful collaboration. I wish to warmly thank Cedric Thaury, in particular for his creative suggestions, his shrewd feedback on several papers, and for his invaluable insight into the experimental realities. I am also thankful to Jean-Marcel Rax for his astute remarks and comments, and for sharing his extensive and impressive knowledge in physics throughout our various discussions.

I also wish to express my gratitude to Antoine Rousse for welcoming me in LOA, and for his commitment in making it a world-class laboratory, with an outstanding working environment. More generally, I wish to thank the current and past members of FLEX and SPL at LOA, for the excellent atmosphere that pervades these two collaborating teams. I am thus thankful to Sébastien Corde, Jérôme Faure, Alessandro Flacco, Julien Gautier, Stéphane Sebban, Guillaume Lambert, Kim Ta Phuoc, Fabien Tissandier, Benjamin Vauzour, Boris Vodungbo, as well as the students with whom I shared an office at different times, and with whom I had many stimulating conversations and debates: Adrien Depresseux, Andreas Doepp, Emilien Guillaume, Florian Mollica, Loann Pommarel, François Sylla, and Mina Veltcheva.

It was a priviledge to work also with other teams, both at the national and international level. I am thankful to Marie-Emmanuelle Couprie's team at Soleil for our collaboration on the LWFA-based FEL – and in particular to Alexandre Loulergue, for our numerous interactions regarding our respective simulations. I am also grateful to Luís Silva for hosting me in his very welcoming team in Lisbon for three weeks. In this regard, I am particularly thankful to Paulo Alves, Ricardo Fonseca, Thomas Griesmayer, Vishwa Bandhu Pathak, Anne Stockem and Marija Vranić for allowing me to make the most of this stay – both scientifically and culturally. During this stay, I also had the good fortune to meet Axel Hübl, with whom I then collaborated on several projects. I thank Axel for the agreeable interactions we had when working together, and I would like to extend my thanks to Michael Bussmann for encouraging this collaboration by welcoming me at the Helmholtz Zentrum Dresden Rossenforf (HZDR).

Teaching at Ecole Polytechnique during those years was a very enjoyable experience, and I thank the researchers and fellow graduate students with whom I worked on this occasion. My thanks thus go to Silke Biermann, Jonathan Biteau, Vincent Boudry, Pierre Chopin, Antoine Georges, Marie-Blandine Martin, Thomas Mueller, Arnd Specka and Daniel Suchet, for the pleasant working environment which they contributed to.

Finally, I wish to thank my parents and my sister, in particular for preparing the post-defense food and drinks, and more generally for their indefectible support during these three years, and throughout the path that lead to it. I express my warmest thanks to Anna for sharing three beautiful years of life together. Although she was busy with a thesis of her own, she also contributed in an infinite number of ways to the present work, from keeping my motivation up and patiently listening to my physics-related ramblings, to proofreading parts of this manuscript and helping me rehearse the defense. I affectionately thank her for this invaluable support.

Contents

Introduction

Context

Nowadays several important technologies rely on high-energy electron accelerators. This includes for instance nondestructive testing, in the industry, as well as high-energy colliders and intense x-ray sources, in fundamental research. In these examples, the electrons are accelerated to high energies by *radiofrequency* accelerators. However, because the accelerating field is intrinsically limited in a radiofrequency accelerator, these devices require a considerable acceleration distance – which can reach the kilometer scale for very high energies.

Laser-wakefield acceleration (LWFA), on the other hand, is a developing acceleration technique, which is considerably different from conventional radiofrequency acceleration. In a laser-wakefield accelerator, a high-power femtosecond laser pulse is focused into a gas jet, where it generates a powerful accelerating structure. Inside this structure, the accelerating field can exceed 100 GV.m^{-1} – which is three orders of magnitude higher than the maximum field of conventional radiofrequency accelerators. As a result, laser-wakefield acceleration is characterized by shorter acceleration distances, and opens up interesting prospects towards more compact accelerators[1].

Over the past ten years, the development of LWFA has reached several major landmarks. These landmarks include for example the observation of the first quasi-monoenergetic beam [Mangles et al., 2004; Faure et al., 2004; Geddes et al., 2004], the production of more tunable and more stable beams [Faure et al., 2006], and the production of the first beam beyond 1 GeV [Leemans et al., 2006]. This evolution was only made possible by the development of high-power femtosecond laser systems in the 90s, and has been closely tied to their continued improvement since then. Today LWFA is still undergoing a rapid evolution, as recently-available Petawatt laser systems provide ever increasing laser power and allow to reach unprecedented electron energies [Kim et al., 2013; Wang et al., 2013].

In parallel to these experimental achievements, the theoretical understanding of LWFA has also progressed considerably. The theory of laser-wakefield acceleration has indeed largely benefited from numerical simulation tools, and especially from *particle-in-cell* (PIC) algorithms. As computational capabilities steadily rised during the last decade, two-dimensional and three-dimensional PIC simulations have become increasingly wide-spread, and are now a key research tool in laser-wakefield acceleration.

Thanks to the above-mentioned developments, several practical applications of LWFA are now being considered. In addition to their compactness, laser-wakefield accelerators produce interesting beams with a short duration, a small transverse size, and a high peak intensity.

[1] One should not forget, however, that the overall size of a laser-wakefield accelerator is not only determined by the acceleration distance, but also by the size of the associated femtosecond laser system.

These specificities have inspired many prospective applications, ranging from electron diffraction in crystals [He et al., 2013] to biological phase-contrast imaging [Fourmaux et al., 2011] and high-resolution gamma radiography [Ben-Ismail et al., 2011]. In addition, laser-wakefield accelerators are also considered for the design of more compact linear colliders and x-ray sources (especially synchrotrons and free-electron lasers). While these technologies currently require expensive large-scale facilities, their compact LWFA-based counterparts could be more affordable, and would thus open new opportunities in many fields of research.

This is particularly true for free-electron-lasers (FELs). FELs are by far the brightest existing X-rays sources, and they are instrumental in many areas of research, including atomic physics, solid-state physics, fundamental chemistry and biochemistry. However, the existing X-ray FELs are kilometer-size facilities, and there are only a few of them world-wide. This has spurred a global effort in the LWFA community towards the development of more compact LWFA-based FELs. At the *Laboratoire d'Optique Appliquée* (LOA) for instance, this effort is particularly present and is currently supported by a European Research Council grant. In addition, LOA is part of the LUNEX5 collaboration, which aims to demonstrate the operation of a soft X-ray LWFA-based FEL.

However, there are still important challenges to overcome for the development of compact FELs – and more generally for the development of the above-mentioned applications. Many of these challenges are related to the imperfect quality of LWFA beams. In spite of their interesting specificities, LWFA beams are also characterized by a large energy spread, a large divergence and a certain lack of stability. Although much work has already been done in order to enhance the quality of LWFA beams (e.g. [Faure et al., 2006; Rechatin et al., 2009b; Gonsalves et al., 2011]), it is currently still necessary to improve the energy spread, divergence and stability of the beams.

Objective and outline of this thesis

In this context, the objective of this thesis is to propose different solutions in order to further improve the quality of LWFA beams. The main motivation behind this is the development of compact FELs, and thus the implications of the proposed solutions for this goal are emphasized. Moreover, this work is carried out mostly through particle-in-cell simulations and analytical models. Nevertheless, care has been taken to propose experimentally realistic solutions, and to briefly discuss their practical implementation. On the whole, the manuscript is organized as follows.

Chapter 1 introduces the main theoretical concepts that underpin laser-wakefield acceleration, and which I draw upon in the rest of the manuscript. In particular, the concept of emittance, which is key to the quality of the beam, is defined.

Chapter 2 describes the principle of PIC simulations. Moreover, it is shown in this chapter that PIC simulations can sometimes overestimate the emittance and divergence of LWFA beams. Since emittance and divergence are paramount properties in our case, I propose a modified PIC algorithm which limits this overestimation.

Using this modified algorithm, a first method towards higher beam quality is studied in chapter 3. This method focuses on *injection*, i.e. the process by which an electron bunch is generated before being accelerated. In this chapter, I show that a new regime of *colliding-pulse injection* could lead to high-quality beams having a low emittance.

Even with a low emittance, the divergence of the beam may still be too high. Therefore, chapter 4 proposes a second method, which further reduces the divergence of the beam *after it exits the accelerator*. This method uses a second well-calibrated gas jet, which acts like a lens and collimates the electrons.

Finally, chapter 5 puts the results of chapter 3 and chapter 4 into context by discussing the development of compact LWFA-based FELs. In this chapter, I consider the combination of a laser-wakefield accelerator with different types of undulator. In particular, an innovative millimeter-scale *nanowire undulator* is proposed, and it is shown that this undulator could be advantageously combined with the beams obtained in chapter 3.

In addition, the appendices A, B, C and D gather the somewhat more technical results and derivations that are used inside the chapters. Finally, appendix E is a list of my publications and conference contributions.

Chapter 1

Physics of laser-wakefield acceleration

This chapter sums up the main theoretical results behind laser-wakefield acceleration, which will then be used in the rest of this manuscript. It is first shown that an intense laser pulse can drive a strong wakefield, when it propagates through a gas. This wakefield is characterized by extremely strong electric fields, which can be used to accelerate electrons over very short distances. I describe the main steps involved when accelerating electrons in this way. Since much of this manuscript deals with the emittance of the accelerated beam, I also define emittance in this chapter, and detail its principal sources of degradation.

Contents

1.1 Generation of a plasma wakefield by a laser pulse

1.1.1 Qualitative picture

When a femtosecond high-power laser pulse ($\gtrsim$ 10 TW) is focused into a low-density gas ($\sim 10^{18}$ – 10^{19} atoms per cm^{-3}), it produces a wake characterized by strong electric and magnetic fields. This section explains qualitatively how this wake is generated.

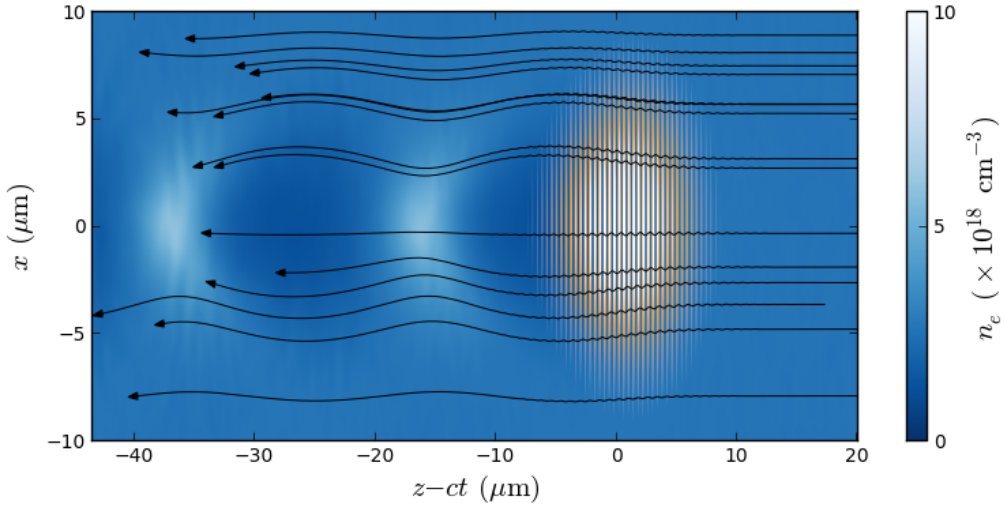

Figure 1.1: Representation of the laser pulse and wakefield in the copropagating coordinate system $(z - ct, x)$. The laser pulse, which propagates to the right, is displayed in red and yellow, while the electron density is represented in blue tones. The black lines correspond to the trajectories of a few typical electrons in the copropagating coordinates.

Figure 1.1 shows an image of such a laser pulse, propagating in a gas. For such a hig-intensity laser pulse, the peak electric field is usually well above the ionization threshold of the gas, and therefore ionization occurs well ahead of the maximum of the pulse. This separates the atoms into electrons and positively charged ions, and thereby generate a plasma. The ions are heavier than the electrons by several orders of magnitude, and hence they are essentially motionless on the timescales of interest. The wake is therefore mainly due to the motion of the electrons, and for this reason only the density of the electrons is displayed in fig. 1.1.

In order to understand this density pattern, the trajectory of typical electrons are shown in fig. 1.1. These trajectories are plotted as a function of the copropagating coordinate $z - ct$ (where z is the spatial coordinate along the axis of propagation), since the laser pulse remains essentially stationary in this coordinate system.[1]. Once the electrons are reached by the pulse, their motion can be decomposed on two timescales. On a short timescale, the electrons feel the oscillating electric and magnetic field of the laser pulse and respond by wiggling at the frequency of the laser. On a longer timescale, the average result of these oscillations is to push the electrons away from the pulse[2]. Since only the electrons are pushed away (the ions remain again mostly motionless), this creates a zone of rarefied electron density but unchanged ion density behind the laser pulse. This global charge separation generates strong electric fields, which pull the

[1] For a laser wavelength of the order of 1 μm and for the plasma densities considered here (10^{18} – 10^{19} electrons per cm^{-3}), the plasma is *underdense* and the laser pulse has a group velocity close to c (see e.g. Kruer [2003]).

[2] This average effect is explained in section 1.1.2 and appendix A.

electrons back. As can be seen in fig. 1.1, the electrons rush back but tend to overshoot, and thus generate quasi-periodic plasma oscillations behind the pulse.

The aim of the next sections is to describe this wakefield quantitatively, and in particular to show that it can be used to accelerate relativistic electrons.

1.1.2 Ponderomotive formalism

From the previous qualitative picture, the electromagnetic fields and the trajectories of the electrons are the superposition of a fast, oscillating component, which is driven by the laser pulse, and slowly-varying component, which is driven by the charge separation. The total electromagnetic fields (i.e. the superposition of these two components) can be determined from the dimensionless potentials $\boldsymbol{a}_{tot} = e\boldsymbol{A}_{tot}/mc$ and $\phi_{tot} = e\Phi_{tot}/mc^2$, which – in the Lorenz gauge – verify the following equations

$$\left(\boldsymbol{\nabla}^2 - \frac{1}{c^2}\frac{\partial^2}{\partial t^2}\right)\boldsymbol{a}_{tot} = -4\pi r_e(\boldsymbol{j}_{i,tot} - \boldsymbol{j}_{e,tot}) \tag{1.1}$$

$$\left(\boldsymbol{\nabla}^2 - \frac{1}{c^2}\frac{\partial^2}{\partial t^2}\right)\phi_{tot} = -4\pi r_e(n_{i,tot} - n_{e,tot}) \tag{1.2}$$

$$\frac{1}{c}\frac{\partial \phi_{tot}}{\partial t} + \boldsymbol{\nabla}\cdot\boldsymbol{a}_{tot} = 0 \tag{1.3}$$

where r_e is the classical radius of the electron[3]. $n_{i,tot} = \rho_{i,tot}/e$ and $\boldsymbol{j}_{i,tot} = \boldsymbol{J}_{i,tot}/ec$ are the normalized density and current associated with the ions and $n_{e,tot} = \rho_{e,tot}/(-e)$ and $\boldsymbol{j}_{e,tot} = \boldsymbol{J}_{e,tot}/(-ec)$ are those associated with the electrons of the plasma[4]. As mentioned previously, the ions can be considered motionless on the timescale of interest (thus $\boldsymbol{j}_{i,tot} \approx \boldsymbol{0}$), and have a uniform density $n_{i,tot} = n_0$. However the electrons do move, and each electron satisfies the equations of motion

$$\frac{1}{c}\frac{d\boldsymbol{x}_{tot}}{dt} = \frac{\boldsymbol{u}_{tot}}{\gamma_{tot}} \tag{1.4}$$

$$\frac{1}{c}\frac{d\boldsymbol{u}_{tot}}{dt} = \frac{1}{c}\frac{\partial \boldsymbol{a}_{tot}}{\partial t} + \boldsymbol{\nabla}\phi_{tot} - \frac{\boldsymbol{u}_{tot}}{\gamma_{tot}} \times (\boldsymbol{\nabla} \times \boldsymbol{a}_{tot}) \tag{1.5}$$

where γ_{tot} is its Lorentz factor, $\boldsymbol{u}_{tot} = \boldsymbol{p}_{tot}/mc$ its normalized momentum, and where the subscript *tot* again refers to the supersition of a fast oscillation and a slowly-varying motion.

The general system of eqs. (1.1) to (1.5) can be simplified by a few approximations. First, as suggested previously, it is assumed that the laser pulse and the corresponding wakefield propagate very close to the speed of light, and they are essentially stationary during the time it takes for a plasma electron to slip through the laser pulse (quasi-static approximation). Thus all quantities in the wakefield are assumed to depend on z and t only through $\xi = ct - z$. In this case, it turns out that it is convenient to distinguish the components of $\boldsymbol{a}$ along z and perpendicular to it, and to use the gauge-invariant pseudo-potential $\psi = \phi - a_z$ instead of a_z ($\boldsymbol{a}$ can thus be expressed as $\boldsymbol{a} = \boldsymbol{a}_\perp + (\phi - \psi)\boldsymbol{e}_z$, where $\boldsymbol{e}_z$ is the unit vector along z). The fields and velocities are furthermore decomposed into their rapidly oscillating part and slowly-varying part. For instance, for any electron, $\boldsymbol{u}_{tot} = \boldsymbol{u}_s + \boldsymbol{u}_f$ where the subscript s or f denote respectively the slow and fast component.

[3] Equations (1.1) to (1.3) are valid both in SI and Gaussian units, with $r_e = e^2/4\pi\epsilon_0 mc^2$ [SI] $= e^2/mc^2$ [Gaussian] $= 2.82 \times 10^{-15}$ m.

[4] In these notations, $n_i > 0$ and $n_e > 0$.

By linearity of the Maxwell equations, it possible to separate the equations for the slow and fast components. Hence, the slow components for instance satisfy

$$\begin{aligned}
&\boldsymbol{\nabla}_\perp^2 \boldsymbol{a}_{\perp,s} = 4\pi r_e \boldsymbol{j}_{e,\perp,s} \\
&\boldsymbol{\nabla}_\perp^2 \phi_s = 4\pi r_e (n_{e,s} - n_0) \\
&\boldsymbol{\nabla}_\perp^2 \psi_s = 4\pi r_e (n_{e,s} - n_0 - j_{e,z,s}) \\
&\frac{\partial \psi_s}{\partial \xi} + \boldsymbol{\nabla}_\perp \cdot \boldsymbol{a}_{\perp,s} = 0
\end{aligned}$$

However, due to nonlinearities in the equations of motion, it is less straightforward to derive the slow components of eqs. (1.4) and (1.5). Mora and Antonsen [1997] showed that they become (See appendix A for a short version of the derivation) [5]

$$\frac{1}{c}\frac{d\boldsymbol{x_s}}{dt} = \frac{\boldsymbol{u}_s}{\gamma_s} \tag{1.6}$$

$$\frac{1}{c}\frac{d\boldsymbol{u}_s}{dt} = \frac{1}{c}\frac{\partial \boldsymbol{a}_s}{\partial t} + \boldsymbol{\nabla}\phi_s - \frac{\boldsymbol{u}_s}{\gamma_s} \times (\boldsymbol{\nabla} \times \boldsymbol{a}_s) - \frac{1}{2\gamma_s}\boldsymbol{\nabla}\langle \boldsymbol{a}_{\perp,f}^2 \rangle \tag{1.7}$$

where the brackets denote an average over one laser period, and where

$$\gamma_s = \sqrt{1 + \boldsymbol{u}_s^2 + \langle \boldsymbol{a}_{\perp,f}^2 \rangle} \tag{1.8}$$

In addition, Noether's theorem provides an integral of motion (see appendix A), which reads :

$$\gamma_s - u_{z,s} = 1 + \psi_s \tag{1.9}$$

Importantly, the equations of motions for the slow components (eqs. (1.6) and (1.7)) are the same as that for the total components (eqs. (1.4) and (1.5)), except for the extra *inertial* term eq. (1.9), and the extra *ponderomotive* force term $-\boldsymbol{\nabla}\langle \boldsymbol{a}_{\perp,f}^2 \rangle/(2\gamma_s)$ in eq. (1.7). As evidenced by its expression, the ponderomotive force repells the electrons from the regions of strong oscillating electromagnetic field (typically, the area covered by the laser pulse).

In the rest of this section, we are mostly interested in the slowly-varying components of the motion and the fields, since they directly represent the shape and amplitude of the wake and of its accelerating fields. For this reason, we hereafter drop the subscript s – so that e.g. $\boldsymbol{u}$ implicitly refers to $\boldsymbol{u}_s$. We also relabel $\boldsymbol{a}_{\perp,f}$ as $\boldsymbol{a}_l$ since this quantity essentially represents the laser field. Furthermore, because the intensity of the laser pulse is usually cylindrically symmetric, it can be assumed that all the quantities of the corresponding wakefield are cylindrically symmetric. Finally, using the relation $d\xi/dt = 1 - \beta_z = (\gamma - u_z)/\gamma = (1 + \psi)/\gamma$, the equation of motion can be rewritten as a function of ξ instead of t. Taking these elements into account, the final set of wakefield equations is, after some algebra :

$$\frac{\partial}{\partial r}\left(\frac{1}{r}\frac{\partial (r\, a_r)}{\partial r}\right) = 4\pi r_e j_{e,r} \tag{1.10}$$

$$\frac{1}{r}\frac{\partial}{\partial r}\left(r\frac{\partial \phi}{\partial r}\right) = 4\pi r_e (n_e - n_0) \tag{1.11}$$

$$\frac{1}{r}\frac{\partial}{\partial r}\left(r\frac{\partial \psi}{\partial r}\right) = 4\pi r_e (n_e - n_0 - j_{e,z}) \tag{1.12}$$

[5] Notice that the motion of the electrons is studied here from a Lagrangian point of view. The alternative Eulerian point of view is also commonly used in plasma physics, but is better adapted to cases in which there is a well-defined value of the velocity at each point in space (e.g. for collisional plasmas, or for cold plasmas without trajectory crossing). This is not the case here, since the plasma is non-collisional (the mean free path is a few tens of microns long at typical densities) and since trajectory crossing does occur in certain regimes (see section 1.1.4).

$$\frac{\partial \psi}{\partial \xi} + \frac{1}{r}\frac{\partial (r a_r)}{\partial r} = 0 \tag{1.13}$$

$$\frac{dr}{d\xi} = \frac{u_r}{1+\psi} \tag{1.14}$$

$$\frac{du_r}{d\xi} = \frac{\partial a_r}{\partial \xi} + \frac{\partial \phi}{\partial r} + \left(\frac{\gamma}{1+\psi} - 1\right)\frac{\partial \psi}{\partial r} - \frac{1}{2(1+\psi)}\frac{\partial \langle \boldsymbol{a}_l^2 \rangle}{\partial r} \tag{1.15}$$

$$\gamma = \frac{1 + u_r^2 + \langle \boldsymbol{a}_l^2 \rangle + (1+\psi)^2}{2(1+\psi)} \tag{1.16}$$

$$u_z = \gamma - 1 - \psi \tag{1.17}$$

where eq. (1.16) results from the combination of eqs. (1.8) and (1.9). Notice that the longitudinal components of eqs. (1.6) and (1.7) are not included in the final set of equations, due to their redundancy with the integral of motion eq. (1.17).

Finally, the more meaningful fields $\boldsymbol{E}$ and $\boldsymbol{B}$ can be obtained from the potentials ψ, ϕ and a_r using the relations

$$\boldsymbol{E} = \frac{mc^2}{e}\left(\frac{\partial \psi}{\partial \xi}\right)\boldsymbol{e}_z - \frac{mc^2}{e}\left(\frac{\partial \phi}{\partial r} + \frac{\partial a_r}{\partial \xi}\right)\boldsymbol{e}_r \qquad \boldsymbol{B} = \frac{mc}{e}\left(\frac{\partial (\psi - \phi)}{\partial r} - \frac{\partial a_r}{\partial \xi}\right)\boldsymbol{e}_\theta \tag{1.18}$$

In particular, the force that the wakefield exerts on a relativistic electron with $\beta_z \approx 1$ and $\beta_x, \beta_y \ll 1$ is $\boldsymbol{F} \approx -e(\boldsymbol{E} + c\boldsymbol{e}_z \times \boldsymbol{B})$, and it can be expressed simply as

$$\boldsymbol{F} = -mc^2 \frac{\partial \psi}{\partial \xi}\boldsymbol{e}_z + mc^2 \frac{\partial \psi}{\partial r}\boldsymbol{e}_r \tag{1.19}$$

The aspect of the wakefield described by the above set of equations in fact strongly depends on the strength of the laser pulse $\langle \boldsymbol{a}_l^2 \rangle$. In pratice, two limiting cases are particularly insightful : the *linear regime* and the *blow-out regime*.

1.1.3 Linear regime

If $\langle \boldsymbol{a}_l^2 \rangle \ll 1$ even at the peak of the pulse, then the wake is weakly driven, and it can be treated as small perturbation of the quiescent background plasma. In particular, the electron density is weakly perturbed, and can be written as $n_e = n_0 + \delta n$, with $|\delta n| \ll n_0$. In this linear regime [Gorbunov and Kirsanov, 1987; Sprangle et al., 1988], $\langle \boldsymbol{a}_l^2 \rangle$, u_z, u_r,ψ, ϕ, δn and a_r are small and can be considered as first-order quantities. Moreover, with these assumptions, the Taylor development up to first order of γ yields $\gamma = 1 + \langle \boldsymbol{a}_l^2 \rangle / 2$.

Also, in this linear regime, the trajectories of the electrons are laminar (i.e. there are no trajectory crossing) and cold fluid theory can thus be used. Therefore, u_r, u_z and γ – which were previously seen as Lagrangian variables – can now also be seen as Eulerian variables. In this case, eq. (1.14) can be replaced by the equation of conservation $\partial_t n_e + \boldsymbol{\nabla} \cdot (n_e \boldsymbol{u}/\gamma) = 0$[6]. With our assumptions, this equation can be rewritten as

$$\frac{\partial}{\partial \xi}\frac{n_e(1+\psi)}{\gamma} + \frac{1}{r}\frac{\partial}{\partial r}\left(\frac{r n_e u_r}{\gamma}\right) = 0$$

[6]Stricly speaking, in order to use this equation, one should first show that it is indeed valid for the slow components of $n_{e,tot}$, $\boldsymbol{u}_{tot}$ and γ_{tot}. See Mora and Antonsen [1997] for a demonstration.

The linearized set of equation then becomes :

$$\frac{\partial}{\partial r}\left(\frac{1}{r}\frac{\partial\,(r\,a_r)}{\partial r}\right) = 4\pi r_e n_0 u_r \tag{1.20}$$

$$\frac{1}{r}\frac{\partial}{\partial r}\left(r\frac{\partial\,\phi}{\partial r}\right) = 4\pi r_e \delta n \tag{1.21}$$

$$\frac{1}{r}\frac{\partial}{\partial r}\left(r\frac{\partial\,\psi}{\partial r}\right) = 4\pi r_e \left(\delta n + n_0\psi - \frac{n_0\langle \boldsymbol{a}_l^2\rangle}{2}\right) \tag{1.22}$$

$$\frac{\partial\psi}{\partial\xi} + \frac{1}{r}\frac{\partial(r a_r)}{\partial r} = 0 \tag{1.23}$$

$$\frac{\partial\delta n}{\partial\xi} + \frac{n_0}{r}\frac{\partial(r u_r)}{\partial r} = -n_0\frac{\partial\psi}{\partial\xi} + \frac{n_0}{2}\frac{\partial\langle \boldsymbol{a}_l^2\rangle}{\partial\xi} \tag{1.24}$$

$$\frac{\partial u_r}{\partial\xi} = \frac{\partial a_r}{\partial\xi} + \frac{\partial\phi}{\partial r} - \frac{1}{2}\frac{\partial\langle \boldsymbol{a}_l^2\rangle}{\partial r} \tag{1.25}$$

These equations can be combined into an equation for the density perturbation.

$$\frac{\partial^2\delta n}{\partial\xi^2} + k_p^2\delta n = \frac{n_0}{2}\boldsymbol{\nabla}^2\langle \boldsymbol{a}_l^2\rangle \qquad \left(\equiv \frac{n_0}{2}\frac{\partial^2\langle \boldsymbol{a}_l^2\rangle}{\partial\xi^2} + \frac{n_0}{2}\frac{1}{r}\frac{\partial}{\partial r}\left(r\frac{\partial\,\langle \boldsymbol{a}_l^2\rangle}{\partial r}\right) \right) \tag{1.26}$$

where $k_p^2 = 4\pi r_e n_0$ is the plasma wavevector (and $\omega_p \equiv ck_p$ is the corresponding plasma frequency). This equation is that of a driven harmonic oscillator. In this case, the driver is the ponderomotive force of the laser pulse, which according to eq. (1.26) generates a periodic oscillation of the electron density, with a wavelength $\lambda_p = 2\pi/k_p$.

Combining eq. (1.26) with eq. (1.22), one finds a corresponding equation for ψ.[7]

$$\frac{\partial^2\psi}{\partial\xi^2} + k_p^2\psi = \frac{k_p^2\langle \boldsymbol{a}_l^2\rangle}{2} \tag{1.27}$$

which can be solved by using Green functions.

$$\psi = \frac{k_p}{2}\int_{-\infty}^{\xi} \langle \boldsymbol{a}_l^2(\xi')\rangle\, \sin[\,k_p(\xi-\xi')\,]\,d\xi' \tag{1.28}$$

The above expression of ψ entirely determines the wakefield, since $E_z = mc^2(\partial_\xi\psi)/e$, $u_z = \gamma - 1 - \psi = \langle \boldsymbol{a}_l^2\rangle/2 - \psi$ and since it can be shown from eqs. (1.20), (1.23), (1.25) and (1.27) that $E_r = -mc^2(\partial_r\psi)/e$, $B_\theta = 0$, and $u_r = -(\partial_\xi\partial_r\psi)/k_p^2$.

Let us express these fields explicitly in the case where the driver is a femtosecond laser pulse. In this case, $\boldsymbol{a}_l$ can be modeled by the following expression.

$$|\boldsymbol{a}_l| = a_0\cos[\,k_0(z-ct+\xi_l)\,]\exp\left(-\frac{r^2}{w^2}\right)h(z-ct+\xi_l)$$

where w and a_0 are the waist and the peak amplitude of the pulse, and where ξ_l characterizes the position of its centroid. In the above expression, h is a bell-shaped function that accounts

[7] More precisely, eqs. (1.22) and (1.26) lead to $\frac{1}{r}\partial_r(r\partial_r f) - k_p^2 f = 0$, with $f = \partial_\xi^2\psi + k_p^2\psi - k_p^2\langle \boldsymbol{a}_l^2\rangle/2$. The solution to the differential equation for f is $f = C_1K_0(k_pr) + C_2I_0(k_pr)$, where I_0 and K_0 are the modified Bessel functions. However, due to the respective divergence of K_0 and I_0 at $r = 0$ and $r = \infty$, the only physical solution is $f = 0$.

for the longitudinal profile of the pulse. It is common to take either a Gaussian function or a sine-like function for h:

$$h(x) = \exp\left(-2\log(2)\frac{x^2}{c^2\tau^2}\right) \qquad \text{(Gaussian)}$$

$$h(x) = \begin{cases} \cos\left(\frac{\pi}{2}\frac{x}{c\tau}\right) & \text{if } |x| < c\tau \\ 0 & \text{otherwise} \end{cases} \qquad \text{(Sine-like)}$$

where τ is the FWHM[8] duration of the intensity profile of the pulse. (These profiles are represented in the left panel of fig. 1.2.) With these expressions, the wakefield variables behind the pulse ($\xi > \xi_l + c\tau$) are

$$\begin{aligned}
\psi &= \frac{\eta\, a_0^2}{4}\, \sin[\, k_p(\xi-\xi_l)\,]\exp\left(-\frac{2r^2}{w^2}\right) \\
E_z &= \frac{\eta\, a_0^2}{4}\frac{mc\omega_p}{e}\, \cos[\, k_p(\xi-\xi_l)\,]\exp\left(-\frac{2r^2}{w^2}\right) \\
E_r &= \eta\, a_0^2\frac{mc^2 r}{ew^2}\, \sin[\, k_p(\xi-\xi_l)\,]\exp\left(-\frac{2r^2}{w^2}\right) \\
\frac{\delta n}{n_0} &= -\eta\, a_0^2\left(\frac{1}{4}+\frac{2}{k_p^2w^2}-\frac{4r^2}{k_p^2w^4}\right)\sin[\, k_p(\xi-\xi_l)\,]\exp\left(-\frac{2r^2}{w^2}\right) \\
u_z &= -\frac{\eta\, a_0^2}{4}\, \sin[\, k_p(\xi-\xi_l)\,]\exp\left(-\frac{2r^2}{w^2}\right) \\
u_r &= \eta\, a_0^2\frac{r}{k_pw^2}\, \cos[\, k_p(\xi-\xi_l)\,]\exp\left(-\frac{2r^2}{w^2}\right)
\end{aligned}$$

where η is a dimensionless coefficient that depends on the longitudinal profile of the laser pulse.

$$\begin{aligned}
\eta &= \frac{1}{1-(\omega_p\tau/\pi)^2}\sin(\omega_p\tau) && \text{for a sine-like pulse} \\
\eta &= \sqrt{\frac{\pi}{4\log(2)}}(\omega_p\tau)\exp\left(-\frac{(\omega_p\tau)^2}{16\log(2)}\right) && \text{for a Gaussian pulse}
\end{aligned} \qquad (1.29)$$

The coefficient η quantifies how efficiently the laser pulse excites the wakefield, and it essentially depends on the pulse duration τ. As shown in fig. 1.2, there is in fact a resonance which makes the wakefield maximal for $\tau \approx 2.5\omega_p^{-1}$. For a density $n_0 \sim 10^{18}\,\mathrm{cm}^{-3}$, this imposes to use a laser pulse having a duration $\tau \sim 40\,\mathrm{fs}$ in order to optimally drive the wakefield.

Let us now focus on the force experienced by a relativistic electron, if it traveled along with the wakefield. The transverse component of this force is $\boldsymbol{F}_\perp = -e(E_r - \beta_z cB_\theta)\boldsymbol{e}_r = -eE_r\boldsymbol{e}_r$. According to the expression of E_r and as represented in fig. 1.3, this force is focusing in the first half-wavelength of the wakefield ($0 < k_p(\xi-\xi_l) < \pi$) and defocusing in the second half-wavelength ($\pi < k_p(\xi-\xi_l) < 2\pi$). Similarly, the longitudinal force is $F_z = -eE_z$, and it is decelerating in the first quarter-wavelength ($0 < k_p(\xi-\xi_l) < \pi/2$) and accelerating in the second quarter-wavelength ($\pi/2 < k_p(\xi-\xi_l) < \pi$). On the whole, the second quarter-wavelength is both accelerating and focusing, and thus, if relativistic electrons traveled along in this region, they would be accelerated while being maintained transversely inside the wakefield. Incidentally, the accelerating electric field E_z can be evaluated by using the above wakefield formulas. Considering

[8] FWHM is the abbreviation of *full width at half maximum*.

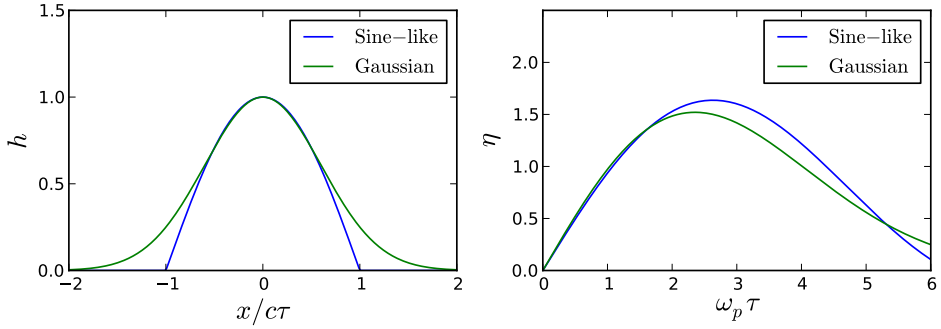

Figure 1.2: Left panel: Plots of the longitudinal profile of a Gaussian and a sine-like pulse. Right panel: Plot of the quantity η as a function of $\omega_p\tau$ (as given by eq. (1.29)). Both curves exhibits a distinct resonance for $\omega_p\tau \approx 2.5$.

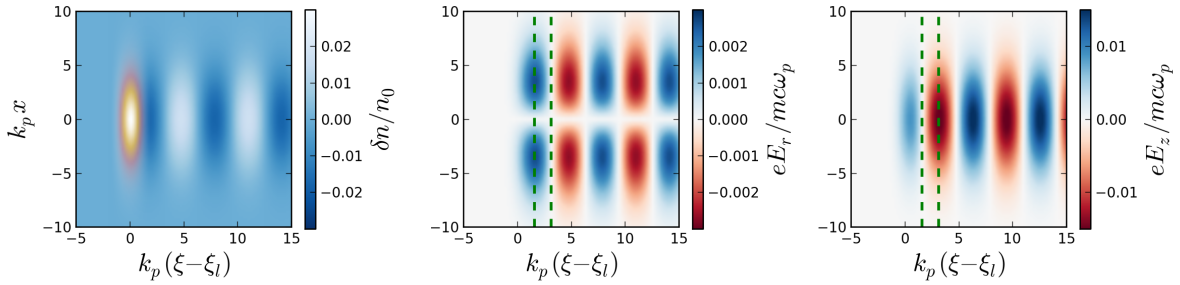

Figure 1.3: Colormaps of the density perturbation δn, the radial electic field E_r and the longitudinal electric field E_z in the linear wakefield, as infered from eq. (1.28). The red and yellow spot on the first plot represents the laser pulse. The dashed green lines delimit the second quarter-wavelength, which is both focusing and accelerating. Because the wakefield is plotted here as a function of $\xi = ct - z$, the respective positions of the laser pulse and of its wakefield are inverted compared to fig. 1.1, which was plotted as a function of $z - ct$.

a density $n_0 = 10^{18}$ cm^{-3} and a resonant laser pulse ($\eta \approx 1.5$), the maximum accelerating field in the wake is

$$|E_{z,\max}| = 36 \times a_0^2 \quad \text{GV.m}^{-1}$$

Thus the accelerating field rapidly increases when a_0 increases. However, when a_0 approaches unity, the linear approximation is not valid anymore and the nature of the wakefield changes.

1.1.4 Blow-out regime

In the linear regime ($a_0^2 \ll 1$), the electron density in the wakefield is only weakly perturbed. However, this is no longer true when $a_0^2 > 1$. In fact, when $a_0^2 \gg 1$ and moreover $k_p w \simeq 2\sqrt{a_0}$ [Lu et al., 2006b], the transverse ponderomotive force is so strong that it can expell *all* the electrons from the first bucket of the wakefield. This regime is known as the blow-out (or bubble) regime [Pukhov and Meyer-ter Vehn, 2002; Lu et al., 2006b,a] and is represented in fig. 1.4. In this case, the laser pulse effectively acts as a *snowplow* for the electron density, and creates a bare ion cavity. As can be seen in fig. 1.4, the expelled electrons tend to gather in a thin sheath, that surrounds the ion cavity. These electrons are then pulled towards the axis by the electric field

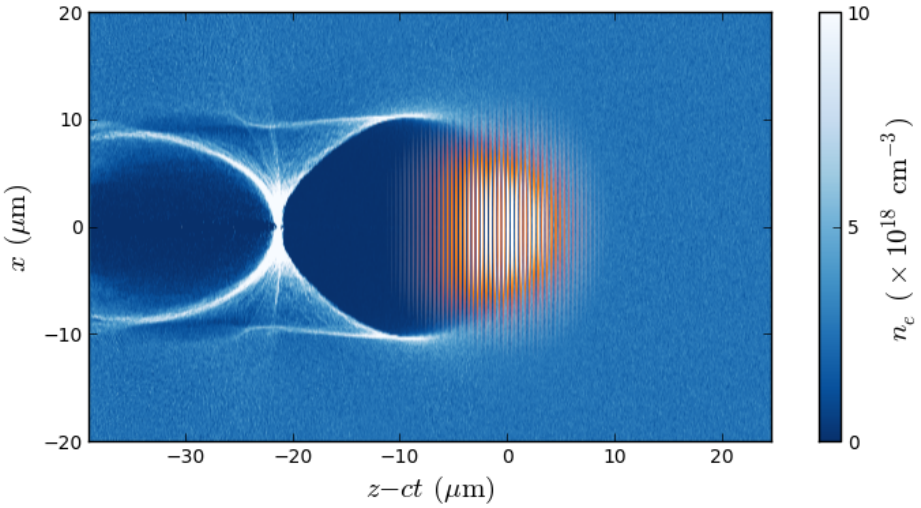

Figure 1.4: Representation of the wakefield in the blow-out regime. The laser pulse is displayed in red and yellow, while the electron density is represented in blue tones.

of the ion cavity, and eventually close the cavity.

This regime is highly non-linear, and in particular it exhibits considerable trajectory crossing for the electrons. As a result, cold fluid theory cannot be used, and instead strong assumptions have to be made regarding n_e and $j_{e,z}$. Yet these assumptions have to be consistent with the equation of conservation $\partial_t \rho + \boldsymbol{\nabla} \cdot \boldsymbol{J} = 0$, at least on a global level. In our case, this equation can be integrated to yield[9] :

$$\int_0^\infty r(n_e - n_0 - j_{e,z})\, dr = 0 \tag{1.30}$$

which holds for any ξ. In agreement with this condition and the qualitative picture of the bubble, the density and currents at a given ξ are modeled by the following expression

$n_e = 0$	$\boldsymbol{j_e} = \boldsymbol{0}$	for $r < r_b(\xi)$	(bare ion cavity)
$n_e = n_0$	$\boldsymbol{j_e} = \boldsymbol{0}$	for $r > r_b(\xi) + \Delta$	(unperturbed plasma)
$n_e - j_{e,z} = \frac{n_0 r_b(\xi)}{2\Delta}$		for $r_b(\xi) < r < r_b(\xi) + \Delta$	(electron sheath)

where $r_b(\xi)$ is the radius of the ion cavity (or *bubble*) at the position ξ, and Δ is the width of the sheath, and where it has been furthermore assumed that $\Delta \ll r_b(\xi)$ (thin sheath). With these assumptions, the electromagnetic potentials can be deduced from eqs. (1.11) to (1.13), and the resulting expressions inside the bubble (i.e. for $r < r_b(\xi)$) are

$$\psi = -\frac{k_p^2 r^2}{4} + \frac{k_p^2}{4} r_b(r_b + \Delta) \tag{1.31}$$

$$\phi = -\frac{k_p^2 r^2}{4} + \phi_0(\xi) \tag{1.32}$$

$$a_r = -\frac{k_p^2 r}{8} \frac{d}{d\xi} r_b(r_b + \Delta) \tag{1.33}$$

[9] More specifically, in our case the equation of conservation can be rewritten as $\partial_\xi(n_e - n_0 - j_{e,z}) + \frac{1}{r}\partial_r(r\partial_r j_{e,r}) = 0$, and then integrated radially : $d_\xi \int_0^\infty r(n_e - n_0 - j_{e,z})\, dr = 0$. Since $n_e - n_0 - j_{e,z}$ is zero ahead of the pulse (unperturbed neutral plasma), eq. (1.30) holds for any ξ.

where $\phi_0(\xi)$ is a constant of integration. According to eq. (1.18), the resulting fields inside the bubble are :

$$E_z = \frac{m\omega_p^2}{2e}\left(r_b + \frac{\Delta}{2}\right)\frac{d\,r_b}{d\xi} \tag{1.34}$$

$$E_r = \frac{m\omega_p^2 r}{2e} + \frac{m\omega_p^2 r}{8e}\left(\frac{d^2}{d\xi^2}r_b(r_b+\Delta)\right) \tag{1.35}$$

$$B_\theta = \frac{m\omega_p^2 r}{8ec}\left(\frac{d^2}{d\xi^2}r_b(r_b+\Delta)\right) \tag{1.36}$$

According to eq. (1.19), for a relativistic electron that travels inside the cavity with $\beta_z \approx 1$ and $\beta_x, \beta_y \ll 1$, the transverse force associated with these fields is $\boldsymbol{F}_\perp = mc^2\partial_r\psi = -m\omega_p^2 r/2$. Contrary to the force of the linear wakefield, this force is always focusing, always linear in r, and is independent of ξ. Similarly, the longitudinal force is $F_z = -mc^2\partial_\xi\psi \approx -m\omega_p^2 r_b d_\xi r_b/2$ and it does not depend[10] on r. This force is zero near the maximum of the cavity ($d_\xi r_b = 0$), decelerating in the first half of the cavity ($d_\xi r_b > 0$) and accelerating in the second half of the cavity ($d_\xi r_b < 0$).

A more detailed calculation of the longitudinal electric field requires the knowledge of r_b, which is determined by the equation of motion for the electrons of the sheath. Combining eqs. (1.14) to (1.16), this equation reads :

$$\frac{d}{d\xi}(1+\psi)\frac{d\,r_b}{d\xi} = \frac{\partial a_r}{\partial\xi} + \frac{\partial\phi}{\partial r} + \frac{1}{2(1+\psi)^2}\left(1 + \langle \boldsymbol{a}_l^2\rangle + (1+\psi)^2\left[\left(\frac{dr_b}{d\xi}\right)^2 - 1\right]\right)\frac{\partial\psi}{\partial r} - \frac{1}{2(1+\psi)}\frac{\partial\langle \boldsymbol{a}_l^2\rangle}{\partial r} \tag{1.37}$$

If we are only interested in the evolution of r_b *behind* the laser pulse, then $\langle \boldsymbol{a}_l^2\rangle \approx 0$. Moreover, according to eqs. (1.31) to (1.33), $\psi(r = r_b) = k_p^2 r_b\Delta/4$, and thus the equation of motion simplifies to :

$$\left(1 + \frac{3}{8}k_p^2 r_b\Delta + \frac{1}{4}k_p^2 r_b^2\right)\frac{d^2 r_b}{d\xi^2} = -\frac{k_p^2 r_b}{4}\left[1 + \frac{1}{(1+k_p^2 r_b\Delta/4)^2} + \left(\frac{dr_b}{d\xi}\right)^2\left(2 + \frac{\Delta}{r_b}\right)\right]$$

For strong blowouts, one has $k_p^2 r_b\Delta \gg 1$ [Lu et al., 2006b]. Using this and the relation $\Delta \ll r_b$, the equation of motion can be rewritten as :

$$\frac{d}{d\xi}r_b\frac{dr_b}{d\xi} = -1 - \left(\frac{dr_b}{d\xi}\right)^2 \tag{1.38}$$

Let us denote by ξ_m the position where r_b is maximal. Then in the neighborhood of ξ_m, $d_\xi r_b \ll 1$, and the above equation yields $r_b d_\xi r_b = -(\xi - \xi_m)$. Since $E_z \approx m\omega_p^2 r_b d_\xi r_b/2e$, one has, in the neighborhood of ξ_m :

$$E_z = -\frac{m\omega_p^2}{2e}(\xi - \xi_m)$$

Using this last relation, one can evaluate the order of magnitude of the accelerating field inside the cavity. The typical length of the cavity is $4\sqrt{a_0}\times c/\omega_p$ [Lu et al., 2007], and thus the accelerating field at the back of the cavity evaluates as

$$|E_z| \sim \frac{mc\omega_p}{e}\sqrt{a_0} \quad \sim 96\times\sqrt{a_0} \quad \mathrm{GV.m^{-1}} \quad (\text{for } n_0 \sim 10^{18}\,\mathrm{cm^{-3}})$$

[10] This can be seen as a consequence of the Panofsky-Wenzel theorem, which states that $\partial_r E_z = -\partial_\xi(E_r - cB_\theta)$, for an electromagnetic structure propagating at c.

1.2 Principle of the laser-wakefield accelerator

The last section demonstrated that a laser-wakefield constitutes a suitable accelerating structure (with fields that are both accelerating and focusing), and that its accelerating electric field can be as high as several tens of GV.m^{-1}. This is three orders of magnitude higher than the maximal accelerating field that can be reached in a conventional accelerators (i.e. accelerators that use radio-frequency cavities). It implies that a laser-wakefield accelerator requires a much shorter acceleration distance than a conventional one, for the same final electron energy. Considering the size (and cost) of current high-energy accelerators, a corresponding laser-wakefield accelerator would thus be an interesting alternative. The idea of the laser-wakefield accelerator (LWFA) was first proposed by Tajima and Dawson [1979], and evolved considerably since then. The next sections describe the successive stages that are involved when using a laser-wakefield to accelerate electrons.

1.2.1 Injection and beamloading

In a laser-wakefield accelerator, the electrons that are to be accelerated must have a relativistic velocity along z once they are in the accelerating and focusing part of the wakefield. A resting electron would indeed slip back with respect to the propagating wakefield, and would therefore experience a succession of accelerating and decelerating fields, with no net energy gain. The acceleration scheme thus starts with an *injection* process, i.e. a process by which a fraction of the electrons of the plasma are placed inside the accelerating and focusing region, with enough initial speed that they can then remain in it.

Injection does not happen in the stationary wakefield described in the previous section. In the linear regime for example, all the electrons slip through the wakefield, while in the blow-out regime, the electrons simply go around the cavity without entering it. Triggering injection thus requires an extra physical phenomenon. One way through which injection commonly occurs is by a sudden expansion of the plasma wavelength (in the linear regime) or of the ion cavity (in the blow-out regime) [Kalmykov et al., 2009; Kostyukov et al., 2010; Yi et al., 2011]. In this case, the electrons that are inside the accelerating region at the time of this expansion can stay longer inside it than they would normally do. They can thereby be accelerated longer and reach a sufficient velocity to remain in this region. In this case, the electrons are typically injected at the back of the cavity.

In practice, this sudden expansion can spontaneously occur in standard experimental conditions. This is because, when a high-power laser propagates in a gas of density $\sim 10^{19}\,\mathrm{cm}^{-3}$, its transverse size (or waist) does not remain stationary. In fact, the leading edge of the generated wakefield exerts a feedback on the laser pulse and effectively acts as a focusing lens [Sprangle et al., 1991, 1987]. As a consequence, the laser pulse *self-focuses* to a waist w_0 of a few microns, its strength $\langle \boldsymbol{a}_l^2 \rangle$ correspondingly increases, and the strength of the ponderomotive force term $-\partial_r \langle \boldsymbol{a}_l^2 \rangle \propto \langle \boldsymbol{a}_l^2 \rangle / w_0$ in eq. (1.37) also increases. This pushes the electrons further away from the axis and results in a larger ion cavity. This mecanism is known as *self-injection*. However, self-injection lacks stability, and it is sometimes preferable to controllably trigger the injection. There are several methods for doing so (e.g. by using a density downramp, or a colliding laser pulse), and these methods will be described in more details in section 3.1.

When the injected charge is very high, the bunch can even alter the accelerating and focusing fields of the wake – a phenomenon known as *beamloading*. This happens because a highly-charged electron bunch radially repells the plasma electrons (due to its space-charge forces) and can thus drive a wakefield of its own, within the laser wakefield. The altered accelerating and focusing

fields can be calculated by using the ponderomotive formalism of section 1.1.2, and by separating the electron population into a low-energy population (the plasma electrons) and a localized, quasistatic population of relativistic electrons (the bunch). For instance, when $\langle \boldsymbol{a}_l^2 \rangle \ll 1$ and when the density of the bunch is relatively low ($n_b \ll n_0$), the counterpart of the linear wakefield equation eq. (1.26) is

$$\frac{\partial^2 \delta n}{\partial \xi^2} + k_p^2 \delta n = \frac{n_0}{2} \boldsymbol{\nabla}^2 \langle \boldsymbol{a}_l^2 \rangle - k_p^2 n_b$$

where n_b is the density of the bunch, and where, as before, δn is the perturbation in the density of the plasma electrons. Thus the presence of an accelerated beam leads to an additional driving term $-k_p^2 n_b$ in the wakefield equation. The total wakefield is the linear superposition of the laser-driven wakefield and the beam-driven wakefield. This also implies that the *tail* of the bunch effectively feels the wakefield that the *head* drives, and hence experiences different fields than in the absence of beamloading. In the presence of beamloading, the accelerating force experienced by the tail is typically lower [Katsouleas et al., 1987], while the focusing force is higher.

The consequences of beamloading are significantly different in the blow-out regime ($\langle \boldsymbol{a}_l^2 \rangle > 1$). Beamloading in the blow-out regime can be analyzed by rederiving the equations of section 1.1.4 with an additional relativistic electron population [Tzoufras et al., 2008, 2009]. When doing so, it appears that the expression of ψ as a function of r_b (eq. (1.31)) is unchanged[11]. Since the force on a relativistic electron is $\boldsymbol{F} = -mc^2 \partial_\xi \psi \boldsymbol{e}_z + mc^2 \partial_r \psi \boldsymbol{e}_r$ (eq. (1.19)), the expression of the accelerating and focusing forces are also unchanged : $F_z = -m\omega_p^2 r_b (d_\xi r_b)/2$ and $F_r = -m\omega_p^2 r/2$. However, the trajectory of the electrons of the sheath r_b does change, and eq. (1.38) is replaced by

$$\frac{d}{d\xi} r_b \frac{dr_b}{d\xi} = -1 - \left(\frac{dr_b}{d\xi} \right)^2 + \frac{4}{k_p^2 r_b^2} \frac{I(\xi)}{I_A}$$

where $I_A = ec/r_e = 17\,\mathrm{kA}$ and where $I(\xi)$ is the instantaneous current of the accelerated bunch at the position ξ.[12] The effect of the additional term $4I/(k_p^2 r_b^2 I_A)$ is to push the electron sheath further away from the axis. This is represented in the upper panel of figure fig. 1.5.

The above equation also implies that, if the electron bunch is in the accelerating part of the laser-driven cavity ($d_\xi r_b < 0$), then it can flatten (or even invert) the evolution of $r_b d_\xi r_b$ with ξ, and thereby reduce the variations of $F_z = -m\omega_p^2 r_b (d_\xi r_b)/2$ with ξ. (See the lower panel of figure fig. 1.5.) However, contrary to the linear regime, the focusing force in the blow-out regime $\boldsymbol{F}_\perp = -m\omega_p^2 r/2\, \boldsymbol{e}_r$ is not modified by beamloading.

1.2.2 Acceleration and betatron oscillations

Once the electrons are injected, they start being accelerated. Moreover, since these electrons can be injected off-axis, or with an initial non-zero transverse velocity, they will oscillate transversely in the focusing wakefield [Esarey et al., 2002]. These oscillations are known as *betatron oscillations*.

Let us study these oscillations in case of the blow-out regime. The motion of the injected electrons satisfies

$$\frac{d\, p^\mu}{d\tau} = \frac{q}{m} p_\nu F^{\mu\nu} \tag{1.39}$$

[11] This is because $n - j_z \approx 0$ for a relativistic bunch. As a consequence, the source terms associated with the relativistic bunch cancel out in the equation $\frac{1}{r}\partial_r (r \partial_r \psi) = -4\pi r_e (n - j_z)$ (eq. (1.12)).

[12] Here we adopt the convention $I > 0$ for an electron bunch.

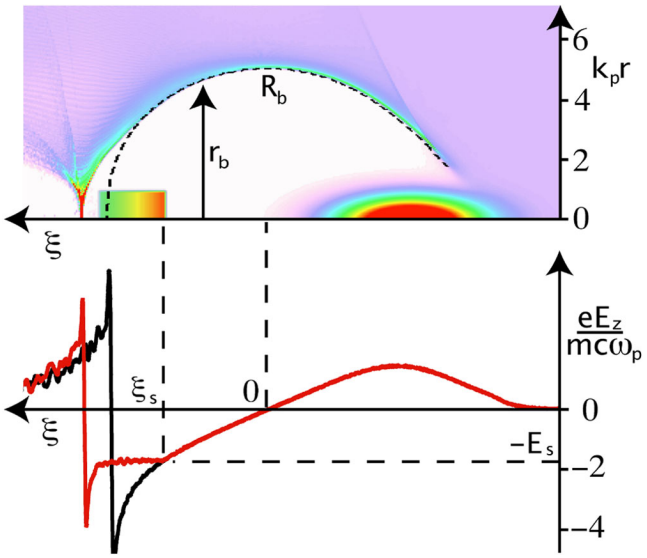

Figure 1.5: Upper panel: Representation of the wakefield in the blow-out regime, when a high-charge accelerated bunch is present (represented as a rectangle near the back of the cavity). The dashed black lines represents the shape of the sheath $r_b(\xi)$ in the absence of this bunch. Lower panel: Plot of the corresponding accelerating field. The red and black curves correspond respectively to the case with and without an electron bunch. The deformation of the sheath by the bunch in the upper panel leads to a modification in the evolution of E_z with ξ. *From Tzoufras et al. [2008]*

The transverse components of this equation yield

$$\frac{d\,\boldsymbol{p}_\perp}{dt} = -e(\boldsymbol{E}_\perp + c(\boldsymbol{\beta}\times\boldsymbol{B})_\perp) \approx -e(\boldsymbol{E}_\perp + c\boldsymbol{e}_z\times\boldsymbol{B}_\perp)$$

where the approximation comes from the fact that the injected electrons have $\beta_z \approx 1$ and $\beta_x, \beta_y \ll 1$. In the blow-out regime, $-e(\boldsymbol{E}_\perp + c\boldsymbol{e}_z\times\boldsymbol{B}_\perp) \approx -m\omega_p^2\boldsymbol{x}_\perp/2$, and the equation of the transverse motion becomes

$$\frac{d^2\,\boldsymbol{x}_\perp}{dt^2} + \left(\frac{1}{\gamma}\frac{d\,\gamma}{dt}\right)\frac{d\,\boldsymbol{x}_\perp}{dt} + \frac{\omega_p^2}{2\gamma}\boldsymbol{x}_\perp = 0 \tag{1.40}$$

where $d_t\gamma$ is given by the 0^{th} component of eq. (1.39) :

$$\frac{d\,\gamma}{dt} = -\frac{e}{mc}\boldsymbol{\beta}\cdot\boldsymbol{E} \approx -\frac{eE_z}{mc}$$

When the electrons are accelerated ($d_t\gamma > 0$), eq. (1.40) is the equation of a damped harmonic oscillator, whose characteristic frequency $\omega_\beta = \omega_p/\sqrt{2\gamma}$ progressively decreases. For 50 MeV electrons and a density $n_0 \sim 10^{18}\,\mathrm{cm}^{-3}$, the adiabaticity parameter $\omega_\beta^2/d_t\omega_\beta$ is of the order of 10^2, meaning that this change of frequency is slow compared to the oscillations themselves. In this case, the WKB approximation can be used, and the solutions of eq. (1.40) are of the form :

$$x = x_0\left(\frac{\gamma_0}{\gamma(t)}\right)^{1/4}\cos\left(\int_{t_0}^{t}\omega_\beta(t')dt' + \varphi_x\right) \qquad y = y_0\left(\frac{\gamma_0}{\gamma(t)}\right)^{1/4}\cos\left(\int_{t_0}^{t}\omega_\beta(t')dt' + \varphi_y\right)$$

This implies that, on average, the transverse size of a bunch decreases as $\gamma^{-1/4}$ during acceleration. The above expressions can also be used to find the angle of the electron trajectory with respect to the propagation axis : $\theta_x \approx d_t x/c$, $\theta_y \approx d_t y/c$.

$$\theta_x = -\frac{k_p x_0}{\sqrt{2\gamma_0}}\left(\frac{\gamma_0}{\gamma}\right)^{3/4}\sin\left(\int_{t_0}^{t}\omega_\beta(t')dt' + \varphi_x\right) \qquad \theta_y = -\frac{k_p y_0}{\sqrt{2\gamma_0}}\left(\frac{\gamma_0}{\gamma}\right)^{3/4}\sin\left(\int_{t_0}^{t}\omega_\beta(t')dt' + \varphi_y\right)$$

This in turn implies that the divergence of the beam evolves on average as $\gamma^{-3/4}$.

Since the electrons oscillate transversally, they emit a corresponding electromagnetic radiation [Esarey et al., 2002; Kostyukov et al., 2003]. As a consequence of their relativistic speed, the radiation is collimated along the trajectory and Doppler-shifted [Jackson, 1998], its characteristic frequency ω_r being of the order of $\omega_\beta/(1-\beta) \approx 2\gamma^2\omega_\beta$. In this regard, *betatron radiation* can be viewed as a millimeter-scale counterpart of the large-scale synchrotron sources, which use relativistic electrons and magnetic wigglers to produce intense X-rays. An estimation of the characteristic photon energy (for 200 MeV electrons and $n_0 \sim 10^{19}\,\mathrm{cm}^{-3}$) yields $\hbar\omega_r \sim 1\,\mathrm{keV}$, which is indeed also in the X-ray range. A more detailed description of the spectral and angular distribution of this radiation requires a rigorous analysis of the radiated Lienard and Wiechert fields. This analysis leads to the following expression for the radiated energy per unit frequency and solid angle, in the direction $\boldsymbol{n}$ [Jackson, 1998]

$$\frac{d^2I}{d\omega d\Omega} = \frac{mcr_e}{4\pi^2}\left|\int_{-\infty}^{\infty} e^{i\omega(t-\boldsymbol{n}\cdot\boldsymbol{r}(t)/c)}\frac{\boldsymbol{n}\times[(\boldsymbol{n}-\boldsymbol{\beta})\times\dot{\boldsymbol{\beta}}]}{(1-\boldsymbol{n}\cdot\boldsymbol{\beta})^2}dt\right|^2 \tag{1.41}$$

In practice, because of the complexity of the motion (evolution of γ and of the amplitude of oscillation), this expression is integrated numerically [Thomas, 2010; Chen et al., 2013].

1.2.3 Termination of the acceleration

The acceleration process can be terminated by several phenomena, which therefore limit the maximal energy that can be reached.

One of these limiting phenomena is *electron dephasing*, which is due to the fact that the group velocity of the laser pulse is in fact slightly lower than c. For instance, in the linear regime, the group velocity of the pulse satisfies $v_g/c \approx 1 - \omega_p^2/2\omega_0^2$ where ω_0 is the frequency of the laser and ω_p the plasma frequency. For a plasma density $n_0 = 10^{19}\,\mathrm{cm}^{-3}$ and a laser having a central wavelength $\lambda_0 = 0.8\,\mu\mathrm{m}$, one has $1 - v_g/c \approx 3\times10^{-3}$. On the contrary, the accelerated electrons typically have a velocity that is much closer to c. For 50 MeV electrons for instance, $1-\beta_z \approx 5\times10^{-5}$. Therefore the electrons progressively catch up with the laser pulse during the acceleration process. Once they are at a quarter-wavelength distance from the laser pulse (in the linear regime) or once they reach the maximum of the cavity (in the blow-out regime), they enter the decelerating zone and therefore do not gain energy anymore. Although electron dephasing cannot be avoided, the moment at which the electrons stop gaining energy can at least be delayed, for instance by using a low density gas. $1 - v_g/c$ is indeed proportional to n_0 and thus the pulse propagates faster at lower density.

Another common cause why acceleration may cease is that the laser simply becomes too weak to drive a substantial accelerating wakefield. This can happen either through *pulse diffraction* or *pulse depletion*. In pulse diffraction, the laser pulse that was focused into the gas progressively defocuses. Because its waist then increases, $\langle \boldsymbol{a}_l^2 \rangle$ decreases and the driven wakefield becomes weak. This phenomenon can happen quickly, as the typical Rayleigh length in the experiments

is of the order of a few hundreds of microns. Diffraction can however be prevented, for example by performing laser-wakefield acceleration inside a preformed plasma channel [Steinhauer and Ahlstrom, 1971; Johnson and Chu, 1974; Esarey et al., 1994], which then guides the laser pulse like an optical fiber. In this case, pulse depletion becomes the dominant phenomenon. Depletion occurs because the laser constantly loses energy to generate the wakefield. This constant loss progressively damps the amplitude of the laser and hence that of the wakefield. Like electron dephasing, pulse depletion cannot be avoided, but its consequences can be delayed, for example by using a laser pulse with higher initial energy.

1.2.4 Experimental demonstration

The generation of a wakefield described in the previous sections requires both an extremely intense (∼100 TW) and extremely short (∼ 30 fs) laser pulse. These specifications are very demanding, and were only made possible by the invention of chirped-pulse amplification (CPA) [Strickland and Mourou, 1985]. Using this technology, an initial low-intensity femtosecond pulse can be amplified by several successive passes in laser-pumped cristals. Titanium:Sapphir cristals are commonly used, because of their ability to amplify light over the wide range of wavelengths that necessarily composes a femtosecond pulse. In this case, the central wavelength of the amplified pulse is $\lambda_0 \approx 0.8\,\mu$m.

By using CPA lasers, laser-wakefield acceleration was first observed with externally injected electrons [Clayton et al., 1993; Nakajima et al., 1995; Amiranoff et al., 1998] (i.e. electrons that were pre-accelerated by a conventional device and synchonized with the laser pulse). In these experiments, the length of the injected bunch was longer than a plasma wavelength, and the wakefield induced a large energy spread on the accelerated bunch. Similarly, in the first experiments relying on self-injection [Modena et al., 1995; Umstadter et al., 1996a; Leemans et al., 2002; Malka et al., 2002], the accelerated bunch typically had a thermal energy distribution, with most electrons at low energy (<10 MeV). Yet in 2004, three groups first demonstrated the possibility to accelerate a quasimonoenergetic bunch of electrons up to ∼100 MeV [Mangles et al., 2004; Faure et al., 2004; Geddes et al., 2004]. They used a laser energy $E_{laser} \sim 1\,$J and a gas density $n_0 \sim 10^{19}\,\mathrm{cm}^{-3}$, and reached better beam quality through a better control of self-injection and of the dephasing length. However, the produced bunches typically lacked stability, and controlled injection methods were later shown to improve the stability and tunability of the beams [Faure et al., 2006; Geddes et al., 2008; Gonsalves et al., 2011]. In parallel, betatron radiation from an LWFA was first measured by Rousse et al. [2004] and successfully compared with numerical predictions [Phuoc et al., 2005; Albert et al., 2008]. The existence of beamloading was also experimentally demonstrated [Rechatin et al., 2009a], through the associated alteration of the accelerating field.

The first GeV beam (1.0 GeV) was produced in 2006 [Leemans et al., 2006] by using a plasma channel to guide the laser pulse over a 3 cm acceleration distance. A low density $n_0 \sim 10^{18}\,\mathrm{cm}^{-3}$ was also used in order to avoid electron dephasing. Recently, two groups demonstrated multi-GeV energies [Kim et al., 2013; Wang et al., 2013] (with respectively 2 GeV and 3 GeV). This was made possible by using state-of-the-art PetaWatt-class lasers, which produce femtosecond pulses with considerably higher laser energy ($E_{laser} = 30\,$J in the experiments of Wang et al. [2013], $E_{laser} = 150\,$J in those of Kim et al. [2013]).

The research effort is now mainly focused on two objectives: increasing the maximal energy of the electrons and improving the quality and stability of the beams. By a good beam quality, one usually means a high charge per bunch, a low energy dispersion and short bunch duration (longitudinal quality), as well as a low divergence and low transverse beam size (transverse

quality). Since this manuscript deals with several concepts that aim at improving the transverse quality, this notion is detailed further in the next section.

1.3 Transverse quality of an electron bunch

Transverse quality (low divergence, low transverse size) is crucial for a number of potential applications of laser-wakefield accelerators. For instance, it is hoped that LWFA can be used to build compact high-energy colliders [Schroeder et al., 2010]. One of the key requirements here is to have a high luminosity, which in turn requires a small transverse size [Humphries, 1990]. LWFA are also considered as a potential source of X-rays (for instance using betatron radiation) for single-shot phase-contrast imaging [Fourmaux et al., 2011]. In this case, the resolution of the image is directly related to the size of the source i.e. the transverse size of the bunch. Finally, transverse quality is even more critical for a prospective LWFA-based free-electron laser (FEL) [Nakajima, 2008]. The FEL mechanism indeed requires both a small transverse size (so as to preserve the high intensity of the bunch) and a low divergence (for coherence purposes).

Yet transverse size and divergence are no intrinsic properties of the bunch. As shown in section 1.2.2, the transverse size and divergence of a bunch are clearly modified during the acceleration. Moreover, these quantities can further be manipulated after the acceleration, by the use of drift spaces and focusing devices (e.g. quadrupole lenses). There is however a more intrinsic measurement of transverse quality, which is known as *emittance*.

1.3.1 Emittance and transverse quality

Emittance along the transverse x and y axes is defined as

$$\epsilon_x \equiv \frac{1}{mc}\sqrt{\langle x^2\rangle\langle p_x^2\rangle - \langle xp_x\rangle^2} \qquad \epsilon_y \equiv \frac{1}{mc}\sqrt{\langle y^2\rangle\langle p_y^2\rangle - \langle yp_y\rangle^2} \tag{1.42}$$

where the brackets denote an average over the electron bunch. The relevance of emittance lies in the fact that, under certain conditions, it remains constant throughout acceleration and further beam manipulation [Reiser, 2008]. The conditions for this to hold true are the monoenergicity of the bunch (i.e. all electrons have the same γ) and the linearity of the transverse forces (i.e. the transverse forces must be of the form $F_x = -Kx$, $F_y = -K'y$). This latter assumption is indeed quite natural, since it is verified by the forces of the ion cavity ($K = K' = m\omega_p^2/2$), by those of quadrupole lenses (with $K = -K'$) and even by drift spaces ($K = K' = 0$).

The fact that emittance is constant has important implications for the transverse properties of the bunch. This is most easily seen by noticing that eq. (1.42) implies

$$\langle x^2\rangle\langle p_x^2\rangle \geq \epsilon_x^2 m^2 c^2 \tag{1.43}$$

For a monoenergetic bunch, this becomes $\langle x^2\rangle\langle \theta_x^2\rangle \geq \epsilon_x^2/\gamma^2$. Thus emittance imposes a fundamental limit on the beam size and divergence that can be reached by beam manipulation. For instance, a drift space followed by a quadrupole lens can be used to reduce the divergence of a bunch. However, equation eq. (1.43) shows that this necessarily comes at the cost of larger beam size, and that for a given value of this beam size, there is a lower bound for the minimal divergence that can be achieved.

More insight can be gained into the meaning of emittance (e. g. along x) by interpreting it in relation with the x-p_x phase space. Emittance is sometimes interpreted as the area covered by the electron bunch in this 2D space. Yet, it is more rigorous to see emittance as the product

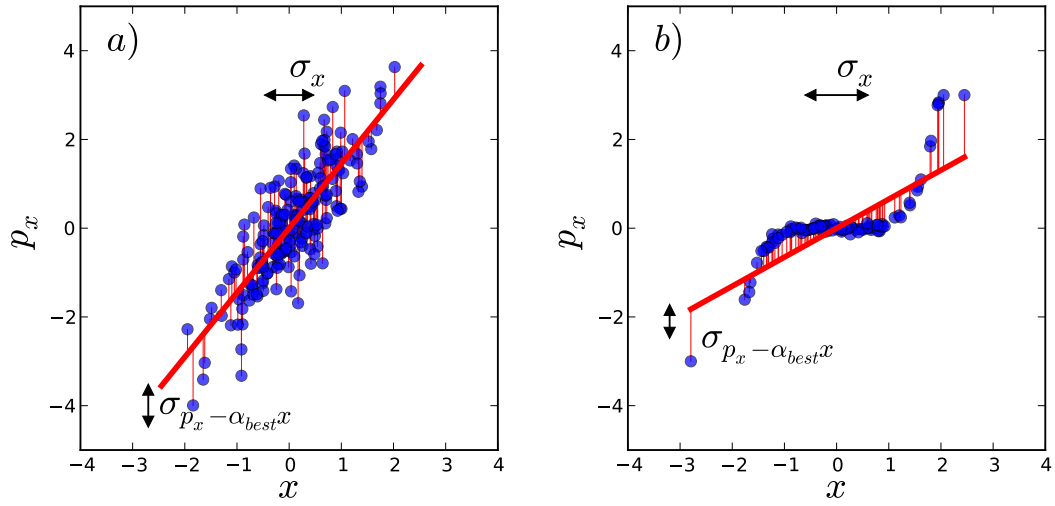

Figure 1.6: Illustration of equation (1.44). The plots represent the x-p_x phase space for two given electron bunches. (Each blue dot represents an individual electron.) In each case, the thick red line corresponds to the best linear fit ($p_x = \alpha_{best} x$) of the phase space. The thin red lines correspond to the distances of the electrons from this best fit. The RMS of these (algebraic) distances is also depicted ($\sigma_{p_x-\alpha_{best}x}$). In case *a*, the area occupied by the bunch in phase space is relatively large. In case *b*, the area in phase space is low, but because of the non-linearities in the particle distribution, the RMS distance to the best linear fit is still large, and the emittance is comparable to that of case *a*.

of the RMS size of the bunch (along x) by *the RMS distance (along p_x) of the electrons from the best linear fit of the phase space* :

$$\epsilon_x = \sigma_x \times \sigma_{p_x-\alpha_{best}x} \qquad \text{where} \quad \sigma_x \equiv \sqrt{\langle x^2 \rangle} \quad \sigma_{p_x-\alpha_{best}x} \equiv \sqrt{\langle\, (p_x - \alpha_{best}\, x)^2 \,\rangle} \tag{1.44}$$

where α_{best} is the coefficient of the best linear fit to the phase space[13]. This is represented[14] in fig. 1.6. Equation (1.44) shows that emittance depends on the extent of the bunch in phase space (see fig. 1.6a), which is indeed related to the area. However, it also takes into account the nonlinear distortions of phase space (see fig. 1.6b).

1.3.2 Sources of emittance degradation

As explained in the last section, under a certain number of assumptions, emittance is constant and is thus determined at injection. However, when these assumptions break down, emittance can evolve. Although emittance can in principle decrease, in practice this evolution usually corresponds to an increase (i.e. a degradation of transverse quality). This degradation can have several origins [Reiser, 2008]. The most common ones for LWFA are the following.

[13] Here the *best* linear fit is defined as that which minimizes $\chi^2(\alpha) = \langle\, (p_x - \alpha x)^2 \,\rangle$. From this definition, it is easy to show that the α which corresponds this best fit is $\alpha_{best} = \langle x p_x \rangle / \langle x^2 \rangle$. Injecting this expression into the definition of $\sigma_{p_x-\alpha_{best}x}$ demonstrates equation eq. (1.44).

[14] For the clarity of fig. 1.6, the number of represented electrons was chosen irrealistically low ; typical bunches contain $\sim 10^8 - 10^9$ elelectrons.

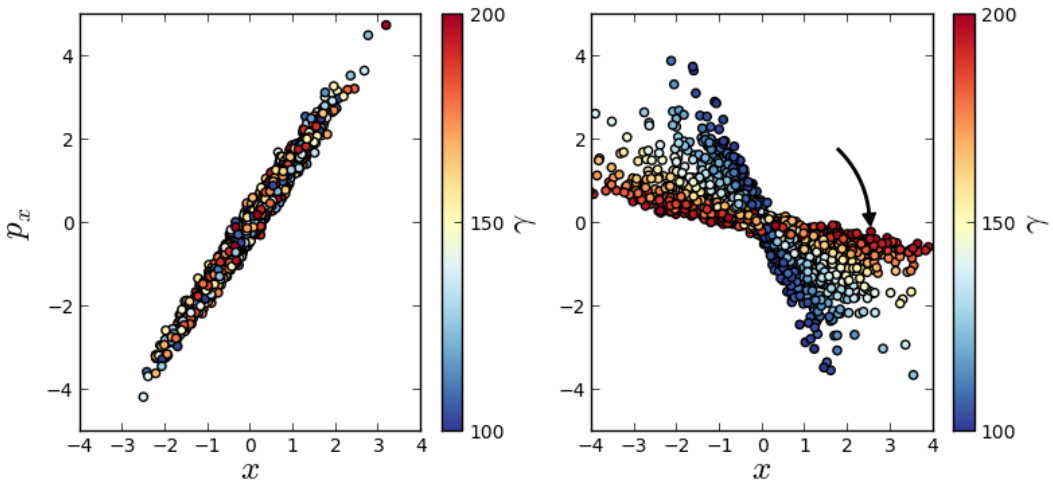

Figure 1.7: Schematic representation of the decoherence phenomenon, for a bunch containing electrons with energies from $\gamma = 100$ to $\gamma = 200$. *Left-hand panel:* initial distribution of the electrons in phase space. *Right-hand panel:* distribution in phase space at a later time, after a fraction of a betatron oscillation. The low-energy electrons rotate faster than the high-energy electrons in phase space, and this increases the emittance of the bunch.

Degradation by a finite energy spread : When a bunch is not strictly monoenergetic, its emittance varies according to $d_t\epsilon_x^2 = 2(\langle p_x^2\rangle\langle xp_x/\gamma\rangle - \langle p_x^2/\gamma\rangle\langle xp_x\rangle)/m^3c^2$. In the case of betatron motion, this evolution of emittance can be intuitively interpreted in phase-space. When performing betatron oscillations, the individual electrons rotate around the origin of the $x - p_x$ phase space, with a frequency $\omega_\beta = \omega_p/\sqrt{2\gamma}$. However, since ω_β depends on γ, this frequency varies across the bunch (low-energy electrons rotate faster). As represented in fig. 1.7, if the electrons are initially all distributed along the same straight line (low emittance bunch), then this spread in frequencies results in an increased emittance at a later time. This phenomenon is known as *decoherence* [Michel et al., 2006].

Degradation by a ξ-dependent focusing force : It can happen that, in addition to being linear in the transverse variable x and y, the focusing forces also depend on the longitudinal variable ξ. (i.e. $F_x = -K(\xi)x$, $F_y = -K'(\xi)y$). This is the case of the focusing forces of the laser-wakefield in the linear regime, close to the axis. In this case, the electrons at different ξ rotate with different frequencies in phase space. This can again lead to decoherence, which is due here to the finite length of the beam along ξ instead of the finite spread in γ, and can degrade the emittance of the bunch [Mehrling et al., 2012]. However, in the case of a ξ-dependent focusing force, the *slice emittance* is said to be preserved, meaning that the emittance of a thin slice of the bunch located at a given ξ is still constant in time.

Degradation by nonlinear forces : Focusing forces that are not linear in the transverse variables x and y can also degrade emittance. In this case, the rotating frequency of individual electrons in phase space depend on their transverse coordinate. As a result, if the electrons of a bunch are initially distributed along a straight line, their distribution in phase space later becomes distorted, and will look similar to that of fig. 1.6b.

Nonlinear forces can appear in various focusing systems, especially when electrons travel very far from the axis. Common examples include the aberrations of quadrupole lenses, but also the focusing fields of a linear laser-wakefield at high radius (due to the term $\exp(-2r^2/w_0^2)$). This does not happen however in the blow-out regime, for which the focusing forces are always linear in r (and independent of ξ) as long as the electrons remain inside the ion cavity.

Another important source of nonlinearities are the space charge forces that the beam exerts on itself. Unless the beam is transversely uniform, these space charge forces are indeed always nonlinear in r. For a monoenergetic, axisymmetric beam, the associated growth in emittance was calculated by Wangler et al. [1985] and yields

$$\frac{d\epsilon_x^2}{dt} = -\frac{\langle x^2 \rangle}{4\gamma} \frac{I}{I_A} \frac{dU}{dt} \tag{1.45}$$

where $I_A \equiv ec/r_e = 17\,\mathrm{kA}$ is the Alfvén current, I is the instantaneous current of the beam, and where U is an dimensionless parameter which depends on the transverse distribution of the bunch :

$$U \equiv 4 \int_0^\infty \left(\frac{I_{int}(r)^2}{I^2} - \frac{I_{unif}(r)^2}{I^2} \right) \frac{dr}{r}$$

Here $I_{int}(r)$ denotes the current of the beam through a disk of radius r (thus $I_{int}(0) = 0$ and $I_{int}(\infty) = I$) and $I_{unif}(r)$ denotes the current (through a disk of radius r) of a *transversely uniform* beam having the same total current I and the same RMS radius $\langle r^2 \rangle$ as the actual beam.[15] U is zero when the actual beam is transversely uniform, and strictly positive for any other distribution. (In the case of a transversely Gaussian beam for instance, $U = 0.154$.) Thus eq. (1.45) implies that the emittance of a beam grows as its distribution evolves towards a uniform distribution, under the action of space charge forces.

It should however be noticed that, according to eq. (1.45), this increase in emittance is significant only for low-energy, wide bunches. In the case of LWFA bunches, which are very narrow ($\sqrt{\langle x^2 \rangle} \sim 1\,\mu\mathrm{m}$), the degradation of emittance due to space-charge forces is usually negligible. For instance, if we consider an LWFA bunch with $\gamma = 400$ and $I = 30\,\mathrm{kA}$ that evolves from a Gaussian profile to a uniform profile while keeping $\sqrt{\langle x^2 \rangle} \approx 1\,\mu m$, the corresponding increase in emittance is $\Delta\epsilon_x^2 = 1.6 \times 10^{-4}\,\mathrm{mm^2.mrad^2}$. If the initial emittance of the bunch is 0.100 mm.mrad, then the final emittance is close to 0.101, and thus the degradation in emittance is indeed barely noticeable.

[15] Since $I_{int}(r)$ and $I_{unif}(r)$ approach I as r approaches infinity, the integral definition of U does converges.

Chapter 2

A Cherenkov-free PIC algorithm

Although some aspects of laser-wakefield acceleration were modeled analytically in chapter 1, many phenomena – such as self-focusing and self-injection – are still too intricate to be captured by simple analytical formulas. Therefore, numerical simulations are often needed when studying laser-wakefield acceleration. This chapter focuses on the Particle-In-Cell (PIC) algorithm, which is a common simulation tool in this context. After explaining the working principle of the PIC algorithm, I show that PIC simulations of laser-wakefield acceleration are subject to an important numerical artifact, known as the *numerical Cherenkov effect*. This artifact should be avoided, since it indirectly leads to a spurious growth of emittance during the simulations. In order to reduce this unphysical growth of emittance, I propose a modified PIC algorithm which is not subject to the numerical Cherenkov effect. This algorithm is validated in typical LWFA simulations, and it indeed reduces – and in some cases suppresses – the unphysical growth of emittance. Because an accurate evaluation of emittance is crucial in chapter 3 and chapter 4, this Cherenkov-free algorithm will be largely used in these chapters.

Contents

2.1 The Particle-In-Cell algorithm

2.1.1 Overview of the algorithm

As mentioned in the previous chapter, the governing equations of laser-wakefield acceleration are the Maxwell equations and the equations of dynamics. The Maxwell equations capture how charged particles generate electromagnetic fields, while the equations of motion describe how these fields act back on the particles (and possibly accelerate some of them). In chapter 1, these equations were written in terms of the potentials ϕ and $\boldsymbol{a}$. However, when solving them numerically, it is more common to use the fields $\boldsymbol{E}$ and $\boldsymbol{B}$. The system of equation to solve is thus:

$$\boldsymbol{\nabla}\cdot\boldsymbol{E} = \frac{\rho}{\epsilon_0} \qquad \boldsymbol{\nabla}\cdot\boldsymbol{B} = 0 \qquad \boldsymbol{\nabla}\times\boldsymbol{E} = -\frac{\partial \boldsymbol{B}}{\partial t} \qquad \boldsymbol{\nabla}\times\boldsymbol{B} = \mu_0\boldsymbol{J} + \frac{1}{c^2}\frac{\partial \boldsymbol{E}}{\partial t} \tag{2.1}$$

$$\frac{d\boldsymbol{x}_l}{dt} = \boldsymbol{v}_l \qquad \frac{d\boldsymbol{p}_l}{dt} = q_l\left(\boldsymbol{E} + \boldsymbol{v}_l \times \boldsymbol{B}\right) \tag{2.2}$$

where the equations of dynamics eq. (2.2) apply to each particle of the plasma (these particles are indexed by l), with $\boldsymbol{v}_l = \boldsymbol{p}_l/\sqrt{m_l^2 + \boldsymbol{p}_l^2/c^2}$. Moreover, in the Maxwell equations, ρ and $\boldsymbol{J}$ are defined by $\rho = \sum_l q_l \delta(\boldsymbol{x} - \boldsymbol{x}_l)$, $\boldsymbol{J} = \sum_l q_l \boldsymbol{v}_l \delta(\boldsymbol{x} - \boldsymbol{x}_l)$. The next paragraphs describes how these equations are implemented in the Particle-In-Cell (PIC) algorithm [Hockney and Eastwood, 1988; Birdsall and Langdon, 2004].

Numerical implementation of the equations of dynamics. In theory, eq. (2.2) should be integrated for every single particle of the plasma. However, in practice this would be very computationally demanding, even for current supercomputers. For instance, when simulating a 3D volume $100\,\mu\text{m} \times 100\,\mu\text{m} \times 100\,\mu\text{m}$ with a plasma of density $n_0 = 10^{19}\,\text{cm}^{-3}$, one would need to track about 10^{13} particles. In order to avoid this unnecessary computational load, particles that are close to each other in phase space are grouped into a *macroparticle*. Each macroparticle is then treated as a solid body having a definite momentum $\boldsymbol{p}_m$ but having a certain spatial extent about its average position $\boldsymbol{x}_m$:

$$\frac{d\boldsymbol{x}_m}{dt} = \boldsymbol{v}_m = \frac{\boldsymbol{p}_m}{\sqrt{m_m^2 + \boldsymbol{p}_m^2/c^2}} \qquad \frac{d\boldsymbol{p}_m}{dt} = q_m\left[\,\bar{\boldsymbol{E}}(\boldsymbol{x}_m) + \boldsymbol{v}_m \times \bar{\boldsymbol{B}}(\boldsymbol{x}_m)\,\right] \tag{2.3}$$

$$\text{where} \qquad \bar{\boldsymbol{E}} = \int d\boldsymbol{x'}\, g(\boldsymbol{x}' - \boldsymbol{x}_m)\boldsymbol{E}(\boldsymbol{x}') \qquad \bar{\boldsymbol{B}} = \int d\boldsymbol{x'}\, g(\boldsymbol{x}' - \boldsymbol{x}_m)\boldsymbol{B}(\boldsymbol{x}') \tag{2.4}$$

$$\rho(\boldsymbol{x}) = \sum_m N_m q_m\, g(\boldsymbol{x} - \boldsymbol{x}_m) \qquad \boldsymbol{J}(\boldsymbol{x}) = \sum_m N_m\, q_m \boldsymbol{v}_m g(\boldsymbol{x} - \boldsymbol{x}_m) \tag{2.5}$$

where m indexes the macroparticles, and where g is a bounded-support, normalized function ($\int g(\boldsymbol{x})d\boldsymbol{x} = 1$) which represents the spatial extent of one macroparticle. (Thus according to eq. (2.4), $\bar{\boldsymbol{E}}$ and $\bar{\boldsymbol{B}}$ are the averages of the fields over the extent of a macroparticle.) N_m is the number of *real* particles that are represented by a macroparticle, while q_m and m_m are the charge and mass of a single *real* particle. (All the real particles represented by a given macroparticle have the same mass and charge.) Notice that although $\boldsymbol{x}_m$ and $\boldsymbol{p}_m$ evolve in time, the spatial extent of the macroparticle g remains constant, and it always keeps a well-defined momentum. This is an approximation, since both the spatial extent and the momentum spread

of the corresponding set of real particles can certainly evolve[1]. However, if the real particles represented by one macroparticle are close enough in phase space, this approximation has little impact.

The motion of the macroparticles is integrated in time, by discretizing eq. (2.3) over successive timesteps $t_n = n\Delta t$. A leap-frog method is generally used, and thus the positions are defined at integer timesteps $n\Delta t$ while the momenta are defined at half-timesteps $(n+1/2)\Delta t$. Section 2.1.2 explains how the equation of motion is discretized and integrated in practice.

Discretization of the Maxwell equations. The Maxwell equations are also discretized in time according to a leap-frog scheme. Here, $\boldsymbol{E}$ is defined at integer timesteps $n\Delta t$ and $\boldsymbol{B}$ is defined at half-integer timesteps $(n+1/2)\Delta t$. Yet the Maxwell equations also have to be discretized in space, and hence the fields $\boldsymbol{E}$, $\boldsymbol{B}$, $\boldsymbol{J}$ and ρ are defined at specific points across a Cartesian grid. For reasons that will be clear in the next section, the different components of these fields are in fact defined at different points in space. The configuration of these fields is known as the Yee lattice [Yee, 1966], and it is detailed in fig. 2.1, along with the field notations which will be used in section 2.1.2.

The evolution of the fields on the grid is tightly coupled with the motion of the charged macroparticles through this grid. This coupling requires some values to be communicated between the macroparticles and the grid. In particular, the charge and current of the macroparticles have to be *projected* onto the grid (through the discretized version of eq. (2.5)), and conversely the fields of the grid have to be *interpolated* to the macroparticles (through the discretized version of eq. (2.4)). The discretization of these equations will be described in the next section.

2.1.2 The PIC cycle

After this general overview, let us examine in more details how the fields and the positions and momenta of the macroparticles are advanced in time. This is done by recursively updating the macroparticles quantities ($\boldsymbol{x}_m$, $\boldsymbol{p}_m$) and the fields ($\boldsymbol{E}$, $\boldsymbol{B}$), over successive timesteps. One single update of $\boldsymbol{x}_m$, $\boldsymbol{p}_m$, $\boldsymbol{E}$, $\boldsymbol{B}$ (over one timestep) is know as a *PIC cycle*. This section describes the operations involved in a PIC cycle.

Let us thus assume, as a starting configuration for the PIC cycle, that the fields $\boldsymbol{B}^{n-1/2}$, $\boldsymbol{E}^n$ and $\boldsymbol{B}^{n+1/2}$ are known on the whole grid, as well as the positions of the macroparticles at time $n\Delta t$ (denoted as $\boldsymbol{x}_m^n$) and their momenta at time $(n-1/2)\Delta t$ (denoted as $\boldsymbol{p}_m^{n-1/2}$). This configuration is represented in the following sketch. (Integer times are represented as white dots, while half-integer times are represented in black ; the quantities that are unknown yet are represented in gray.)

[1] It is sometimes said that the macroparticle method solves the Vlasov equation $\partial_t f + \boldsymbol{v}\cdot\boldsymbol{\nabla}_{\boldsymbol{x}} f + q(\boldsymbol{E}+\boldsymbol{v}\times\boldsymbol{B})\cdot\boldsymbol{\nabla}_{\boldsymbol{p}} f = 0$. Here the expression of f corresponding to e.g. one macroparticle is $f = N_m g(\boldsymbol{x}-\boldsymbol{x}_m)\delta(\boldsymbol{p}-\boldsymbol{p}_m)$, where the evolution of $\boldsymbol{p}_m$ and $\boldsymbol{x}_m$ are given by eq. (2.3). Strictly speaking, this is not an exact solution of the Vlasov equation, precisely because of the approximation that g does not change in time and that the distribution in $\boldsymbol{p}$ remains a delta-function. It is nonetheless a solution of the reduced equation $\int_{U(g)} d\boldsymbol{x}\,[\,\partial_t f + \boldsymbol{v}\cdot\boldsymbol{\nabla}_{\boldsymbol{x}} f + q(\boldsymbol{E}+\boldsymbol{v}\times\boldsymbol{B})\cdot\boldsymbol{\nabla}_{\boldsymbol{p}} f\,] = 0$, where $U(g)$ represents the bounded support of g.

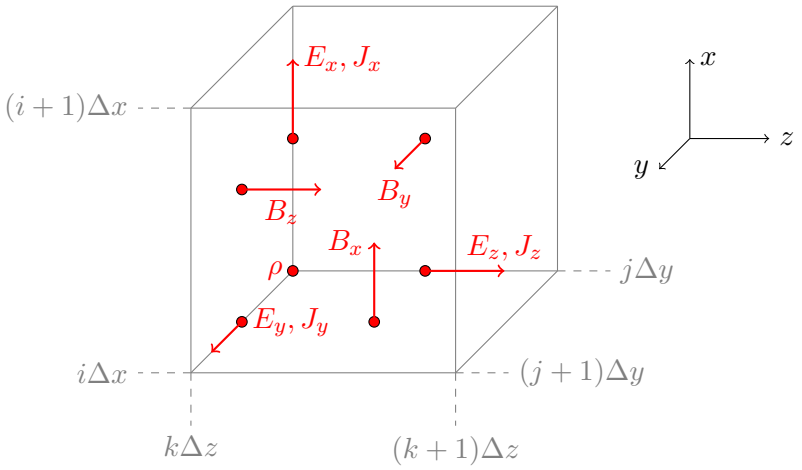

Field	Position in space and time				Notation
	x	y	z	t	
E_x	$(i+\frac{1}{2})\Delta x$	$j\Delta y$	$k\Delta z$	$n\Delta t$	$E_{x}{}^{n}_{i+\frac{1}{2},j,k}$
E_y	$i\Delta x$	$(j+\frac{1}{2})\Delta y$	$k\Delta z$	$n\Delta t$	$E_{y}{}^{n}_{i,j+\frac{1}{2},k}$
E_z	$i\Delta x$	$j\Delta y$	$(k+\frac{1}{2})\Delta z$	$n\Delta t$	$E_{z}{}^{n}_{i,j,k+\frac{1}{2}}$
B_x	$i\Delta x$	$(j+\frac{1}{2})\Delta y$	$(k+\frac{1}{2})\Delta z$	$(n+\frac{1}{2})\Delta t$	$B_{x}{}^{n+\frac{1}{2}}_{i,j+\frac{1}{2},k+\frac{1}{2}}$
B_y	$(i+\frac{1}{2})\Delta x$	$j\Delta y$	$(k+\frac{1}{2})\Delta z$	$(n+\frac{1}{2})\Delta t$	$B_{y}{}^{n+\frac{1}{2}}_{i+\frac{1}{2},j,k+\frac{1}{2}}$
B_z	$(i+\frac{1}{2})\Delta x$	$(j+\frac{1}{2})\Delta y$	$k\Delta z$	$(n+\frac{1}{2})\Delta t$	$B_{z}{}^{n+\frac{1}{2}}_{i+\frac{1}{2},j+\frac{1}{2},k}$
ρ	$i\Delta x$	$j\Delta y$	$k\Delta z$	$n\Delta t$	$\rho^{n}_{i,j,k}$
J_x	$(i+\frac{1}{2})\Delta x$	$j\Delta y$	$k\Delta z$	$(n+\frac{1}{2})\Delta t$	$J_{x}{}^{n+\frac{1}{2}}_{i+\frac{1}{2},j,k}$
J_y	$i\Delta x$	$(j+\frac{1}{2})\Delta y$	$k\Delta z$	$(n+\frac{1}{2})\Delta t$	$J_{y}{}^{n+\frac{1}{2}}_{i,j+\frac{1}{2},k}$
J_z	$i\Delta x$	$j\Delta y$	$(k+\frac{1}{2})\Delta z$	$(n+\frac{1}{2})\Delta t$	$J_{z}{}^{n+\frac{1}{2}}_{i,j,k+\frac{1}{2}}$

Figure 2.1: Representation of the Yee lattice. The table shows at which position each component of the fields is defined (i,j,k and n are integers ; Δx, Δy, Δz are the spatial steps of the grid). The above sketch represents one grid cell, and the positions of the fields within it.

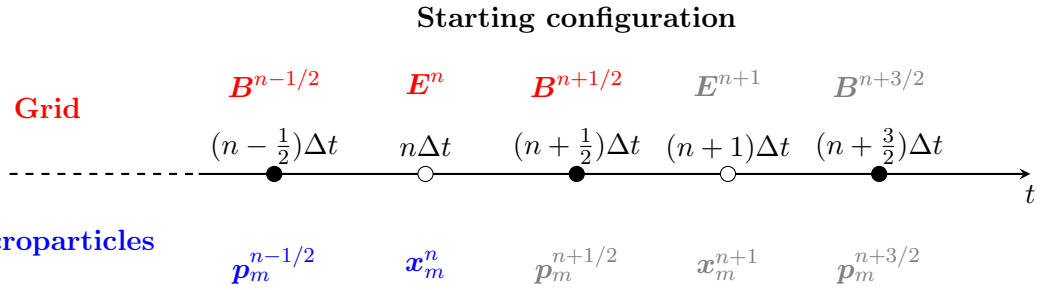

Let us see how the same configuration can be obtained at the next iteration ($n \to n+1$). In other words, we will examine how the unknown quantities $\boldsymbol{p}_m^{n+1/2}$, $\boldsymbol{x}_m^{n+1}$, $\boldsymbol{E}^{n+1}$ and $\boldsymbol{B}^{n+3/2}$ can be obtained from the known quantities $\boldsymbol{p}_m^{n-1/2}$, $\boldsymbol{x}_m^{n}$, $\boldsymbol{B}^{n-1/2}$, $\boldsymbol{E}^{n}$ and $\boldsymbol{B}^{n+1/2}$. The successive steps that are involved in this process are represented in fig. 2.2.

a) Interpolation (see fig. 2.2a). As explained in the previous section, the equations of motion for the macroparticles require the knowledge of $\bar{\boldsymbol{E}}(\boldsymbol{x}_m)$ and $\bar{\boldsymbol{B}}(\boldsymbol{x}_m)$, which are defined by eq. (2.4). These fields have to be interpolated from the grid, and therefore eq. (2.4) is replaced by its discretized version

$$\begin{aligned}\bar{\boldsymbol{E}}^n(\boldsymbol{x}_m^n) = \sum_{i,j,k} \Big[& S_{i+\frac{1}{2},j,k}(\boldsymbol{x}_m^n) E_{x\,i+\frac{1}{2},j,k}^{\,n} \boldsymbol{e}_x \\ & + S_{i,j+\frac{1}{2},k}(\boldsymbol{x}_m^n) E_{y\,i,j+\frac{1}{2},k}^{\,n} \boldsymbol{e}_y \\ & + S_{i,j,k+\frac{1}{2}}(\boldsymbol{x}_m^n) E_{z\,i,j,k+\frac{1}{2}}^{\,n} \boldsymbol{e}_z \Big]\end{aligned} \tag{2.6}$$

$$\begin{aligned}\bar{\boldsymbol{B}}^n(\boldsymbol{x}_m^n) = \sum_{i,j,k} \Big[& S_{i,j+\frac{1}{2},k+\frac{1}{2}}(\boldsymbol{x}_m^n) \frac{1}{2} \left(B_{x\,i,j+\frac{1}{2},k+\frac{1}{2}}^{\,n+\frac{1}{2}} + B_{x\,i,j+\frac{1}{2},k+\frac{1}{2}}^{\,n-\frac{1}{2}} \right) \boldsymbol{e}_x \\ & + S_{i+\frac{1}{2},j,k+\frac{1}{2}}(\boldsymbol{x}_m^n) \frac{1}{2} \left(B_{y\,i+\frac{1}{2},j,k+\frac{1}{2}}^{\,n+\frac{1}{2}} + B_{y\,i+\frac{1}{2},j,k+\frac{1}{2}}^{\,n-\frac{1}{2}} \right) \boldsymbol{e}_y \\ & + S_{i+\frac{1}{2},j+\frac{1}{2},k}(\boldsymbol{x}_m^n) \frac{1}{2} \left(B_{z\,i+\frac{1}{2},j+\frac{1}{2},k}^{\,n+\frac{1}{2}} + B_{z\,i+\frac{1}{2},j+\frac{1}{2},k}^{\,n-\frac{1}{2}} \right) \boldsymbol{e}_z \Big]\end{aligned} \tag{2.7}$$

The interpolation factors $S_{i',j',k'}$ (which are also known as *shape factors*) are defined by

$$S_{i',j',k'}(\boldsymbol{x}_m^n) \equiv \int_{(i'-\frac{1}{2})\Delta x}^{(i'+\frac{1}{2})\Delta x} dx \int_{(j'-\frac{1}{2})\Delta y}^{(j'+\frac{1}{2})\Delta y} dy \int_{(k'-\frac{1}{2})\Delta z}^{(k'+\frac{1}{2})\Delta z} dz \; g(\boldsymbol{x} - \boldsymbol{x}_m^n) \tag{2.8}$$

where i',j',k' can be integers or half-integers.[2] In eqs. (2.6) and (2.7), the sums over i,j,k correspond to sums over all grid cells. However, because g has a bounded support, the shape factors are zero for most of the cells. In fact, the support of g typically spans a few grid cells, and thus only the grid cells that are in the immediate neighborhood of the macroparticles contribute to the interpolation. There are canonical expressions for g and S (e.g. [Hockney and Eastwood, 1988]), for which these non-zero contributions involve one neighbor (*nearest-grid-point* method, or NGP), two neighbors (*cloud-in-cell*, or CIC) or three neighbors (*triangular-shaped-cloud*, or

[2] Equations (2.6) and (2.7) can be derived from eq. (2.4) by considering that the fields $\boldsymbol{E}$ and $\boldsymbol{B}$ are piecewise constant in between the grid points.

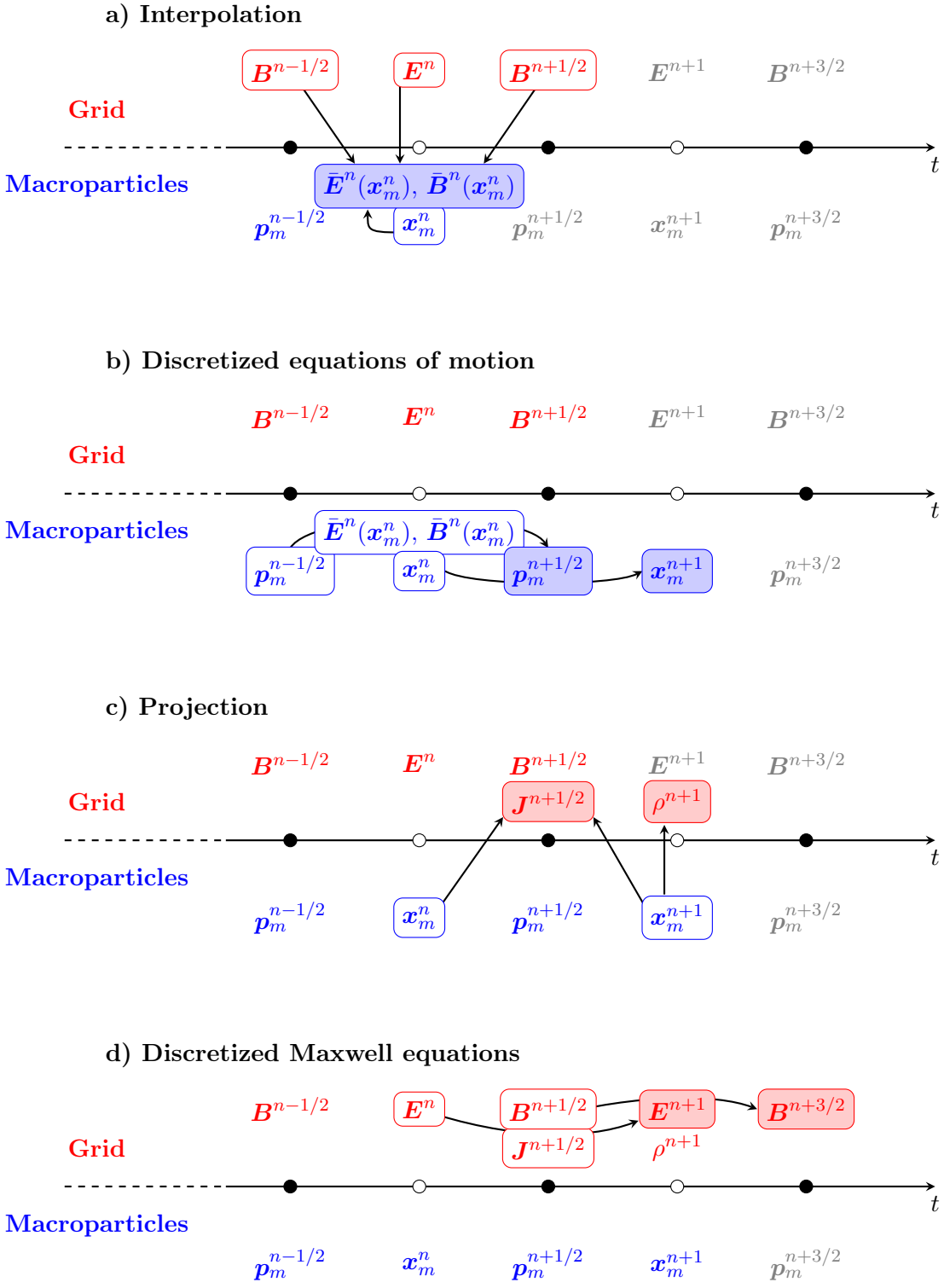

Figure 2.2: Schematic representation of the different steps within a PIC cycle. See paragraphs a), b), c) and d) in the text for an explanation.

TSC) along *each* dimension[3]. The choice of the interpolation method is a trade-off between numerical noise and computational cost. An interpolation involving many neighbors (such as TSC) typically reduces the noise, but requires of course more operations.

Note that the leap-frog algorithm for the equations of motion requires the knowledge of $\bar{\boldsymbol{B}}$ at the integer time $n\Delta t$, whereas $\boldsymbol{B}$ is known at half-integer times on the grid. For this reason, $\boldsymbol{B}$ also needs to be interpolated in time. This is done by simply averaging $\boldsymbol{B}^{n+1/2}$ and $\boldsymbol{B}^{n-1/2}$ in eq. (2.7).

b) Advancing the macroparticles in time (see fig. 2.2b). Once the fields $\bar{\boldsymbol{E}}^n$ and $\bar{\boldsymbol{B}}^n$ are known, the equations of motion can be used to obtain $\boldsymbol{p}^{n+1/2}$ from $\boldsymbol{p}^{n-1/2}$. Several choices can be made regarding the discretization of the equation of motion eq. (2.2). The most common[4] choice is known as the Boris pusher [Boris, 1970; Hockney and Eastwood, 1988] and reads:

$$\frac{\boldsymbol{p}_m^{n+1/2} - \boldsymbol{p}_m^{n-1/2}}{\Delta t} = q_m \left[\bar{\boldsymbol{E}}^n + \left(\frac{\boldsymbol{p}_m^{n+1/2} + \boldsymbol{p}_m^{n-1/2}}{2\gamma^n} \right) \times \bar{\boldsymbol{B}}^n \right] \qquad \gamma^n \equiv \sqrt{1 + \left(\frac{\boldsymbol{p}_m^{n-1/2} + \boldsymbol{p}_m^{n+1/2}}{2 m_m c} \right)^2} \tag{2.9}$$

Notice that this equation is implicit ($\boldsymbol{p}_m^{n+1/2}$ appears on both sides of the equation). Therefore, in practice, a specific algorithm is needed in order to extract $\boldsymbol{p}_m^{n+1/2}$ (see [Boris, 1970; Hockney and Eastwood, 1988]). Once $\boldsymbol{p}_m^{n+1/2}$ is known, $\boldsymbol{x}_m^{n+1}$ can be directly obtained from $\boldsymbol{x}_m^n$, through the discretized equation

$$\frac{\boldsymbol{x}_m^{n+1} - \boldsymbol{x}_m^n}{\Delta t} = \frac{\boldsymbol{p}^{n+1/2}}{\sqrt{m_m^2 + (\boldsymbol{p}_m^{n+1/2})^2/c^2}} \tag{2.10}$$

c) Projection (see fig. 2.2c). The Maxwell equations require the current and charge density to be known on the grid, at time $(n+1/2)\Delta t$ and $(n+1)\Delta t$ respectively. This is done by projecting the charge and currents of the macroparticles onto the grid, through eq. (2.5). In the case of the charge density, ρ^{n+1} is obtained by calculating the average of ρ (from eq. (2.5)) over each grid cell:

$$\rho_{i,j,k}^{n+1} = \frac{1}{\Delta x \Delta y \Delta z} \int_{(i-\frac{1}{2})\Delta x}^{(i+\frac{1}{2})\Delta x} dx \int_{(j-\frac{1}{2})\Delta y}^{(j+\frac{1}{2})\Delta y} dy \int_{(k-\frac{1}{2})\Delta z}^{(k+\frac{1}{2})\Delta z} dz \; \rho(\boldsymbol{x}) = \frac{1}{\Delta x \Delta y \Delta z} \sum_m N_m q_m S_{i,j,k}(\boldsymbol{x}_m^{n+1})$$

[3] More precisely, $S_{i',j',k'}(\boldsymbol{x})$ is typically of the form $S_{i',j',k'}(\boldsymbol{x}) = s(\frac{x-i'\Delta x}{\Delta x})\, s(\frac{y-j'\Delta y}{\Delta y})\, s(\frac{z-k'\Delta z}{\Delta z})$ where:

$$s(u) = \begin{cases} 1 & \text{if } |u| < 1/2 \\ 0 & \text{otherwise} \end{cases} \quad \text{for NGP} \qquad s(u) = \begin{cases} 1-|u| & \text{if } |u| < 1 \\ 0 & \text{otherwise} \end{cases} \quad \text{for CIC}$$

$$s(u) = \begin{cases} \frac{3}{4} - u^2 & \text{if } |u| < 1/2 \\ \frac{1}{2}\left(\frac{3}{2} - |u|\right)^2 & \text{if } 1/2 < |u| < 3/2 \\ 0 & \text{otherwise} \end{cases} \quad \text{for TSC}$$

[4] Another popular choice is the Vay pusher [Vay, 2008], which reads:

$$\frac{\boldsymbol{p}_m^{n+1/2} - \boldsymbol{p}_m^{n-1/2}}{\Delta t} = q_m \left[\bar{\boldsymbol{E}}^n + \frac{1}{2}\left(\frac{\boldsymbol{p}_m^{n+1/2}}{\gamma^{n+1/2}} + \frac{\boldsymbol{p}_m^{n-1/2}}{\gamma^{n-1/2}} \right) \times \bar{\boldsymbol{B}}^n \right] \qquad \gamma^{n\pm1/2} \equiv \sqrt{1 + \left(\frac{\boldsymbol{p}_m^{n\pm1/2}}{m_m c} \right)^2}$$

The Boris pusher intrinsically ensures that the kinetic energy of the particle remains constant when no electric field is present (i.e. when $\boldsymbol{E} = \boldsymbol{0}$ and $\boldsymbol{B} \neq \boldsymbol{0}$), while the Vay pusher ensures that there is no spurious force on the particle when the electric and magnetic fields compensate (i.e. when $\boldsymbol{E} + \boldsymbol{v} \times \boldsymbol{B} = \boldsymbol{0}$).

where the shape factor $S_{i,j,k}$ is again given by eq. (2.8). In principle, a similar averaged expression could be used to obtain $\boldsymbol{J}^{n+1/2}$ on the grid. However, such an expression would not automatically satisfy the discretized equation of continuity (i.e. the discretized version of $\partial_t \rho + \boldsymbol{\nabla} \cdot \boldsymbol{J} = 0$):

$$\frac{\rho^{n+1}_{i,j,k} - \rho^{n}_{i,j,k}}{\Delta t} + \frac{J_x{}^{n+\frac{1}{2}}_{i+\frac{1}{2},j,k} - J_x{}^{n+\frac{1}{2}}_{i-\frac{1}{2},j,k}}{\Delta x} + \frac{J_y{}^{n+\frac{1}{2}}_{i,j+\frac{1}{2},k} - J_y{}^{n+\frac{1}{2}}_{i,j-\frac{1}{2},k}}{\Delta y} + \frac{J_z{}^{n+\frac{1}{2}}_{i,j,k+\frac{1}{2}} - J_z{}^{n+\frac{1}{2}}_{i,j,k-\frac{1}{2}}}{\Delta z} = 0 \quad (2.11)$$

For this reason, $\boldsymbol{J}^{n+\frac{1}{2}}$ is instead commonly obtained by the Esirkepov algorithm [Esirkepov, 2001], which intrinsically satisfies eq. (2.11).

d) Updating the fields Knowing $\boldsymbol{J}^{n+1/2}$ allows $\boldsymbol{E}^{n+1}$ to be determined from $\boldsymbol{E}^{n}$. This is done through the discretized Maxwell-Ampère equation.

$$\frac{E_x{}^{n+1}_{i+\frac{1}{2},j,k} - E_x{}^{n}_{i+\frac{1}{2},j,k}}{c^2 \Delta t} = (D_y B_z^{n+\frac{1}{2}})_{i+\frac{1}{2},j,k} - (D_z B_y^{n+\frac{1}{2}})_{i+\frac{1}{2},j,k} - \mu_0 J_x{}^{n+\frac{1}{2}}_{i+\frac{1}{2},j,k} \quad (2.12)$$

$$\frac{E_y{}^{n+1}_{i,j+\frac{1}{2},k} - E_y{}^{n}_{i,j+\frac{1}{2},k}}{c^2 \Delta t} = (D_z B_x^{n+\frac{1}{2}})_{i,j+\frac{1}{2},k} - (D_x B_z^{n+\frac{1}{2}})_{i,j+\frac{1}{2},k} - \mu_0 J_y{}^{n+\frac{1}{2}}_{i,j+\frac{1}{2},k} \quad (2.13)$$

$$\frac{E_z{}^{n+1}_{i,j,k+\frac{1}{2}} - E_z{}^{n}_{i,j,k+\frac{1}{2}}}{c^2 \Delta t} = (D_x B_y^{n+\frac{1}{2}})_{i,j,k+\frac{1}{2}} - (D_y B_x^{n+\frac{1}{2}})_{i,j,k+\frac{1}{2}} - \mu_0 J_z{}^{n+\frac{1}{2}}_{i,j,k+\frac{1}{2}} \quad (2.14)$$

The numerical operators D_x, D_y, D_z are defined (for any field F) by

$$(D_x F)_{i',j',k'} = \frac{F_{i'+\frac{1}{2},j',k'} - F_{i'-\frac{1}{2},j',k'}}{\Delta x} \quad (2.15)$$

$$(D_y F)_{i',j',k'} = \frac{F_{i',j'+\frac{1}{2},k'} - F_{i',j'-\frac{1}{2},k'}}{\Delta y} \quad (2.16)$$

$$(D_z F)_{i',j',k'} = \frac{F_{i',j',k'+\frac{1}{2}} - F_{i',j',k'-\frac{1}{2}}}{\Delta z} \quad (2.17)$$

where i', j' and k' can be integers or half-integers. Using the same notations, the discretized version of the Maxwell-Faraday equation is

$$\frac{B_x{}^{n+\frac{1}{2}}_{i,j+\frac{1}{2},k+\frac{1}{2}} - B_x{}^{n-\frac{1}{2}}_{i,j+\frac{1}{2},k+\frac{1}{2}}}{\Delta t} = -(D_y E_z^n)_{i,j+\frac{1}{2},k+\frac{1}{2}} + (D_z E_y^n)_{i,j+\frac{1}{2},k+\frac{1}{2}} \quad (2.18)$$

$$\frac{B_y{}^{n+\frac{1}{2}}_{i+\frac{1}{2},j,k+\frac{1}{2}} - B_y{}^{n-\frac{1}{2}}_{i+\frac{1}{2},j,k+\frac{1}{2}}}{\Delta t} = -(D_z E_x^n)_{i+\frac{1}{2},j,k+\frac{1}{2}} + (D_x E_z^n)_{i+\frac{1}{2},j,k+\frac{1}{2}} \quad (2.19)$$

$$\frac{B_z{}^{n+\frac{1}{2}}_{i+\frac{1}{2},j+\frac{1}{2},k} - B_z{}^{n-\frac{1}{2}}_{i+\frac{1}{2},j+\frac{1}{2},k}}{\Delta t} = -(D_x E_y^n)_{i+\frac{1}{2},j+\frac{1}{2},k} + (D_y E_x^n)_{i+\frac{1}{2},j+\frac{1}{2},k} \quad (2.20)$$

When replacing n by $n+1$, eqs. (2.18) to (2.20) can be used to obtain $\boldsymbol{B}^{n+3/2}$ from $\boldsymbol{B}^{n+1/2}$ and $\boldsymbol{E}^{n+1}$. In the above discretized equations, all the numerical derivatives are time-centered and space-centered, and therefore they are second-order accurate. This is indeed the reason why the fields were defined at staggered positions in space and time, in the Yee lattice (fig. 2.1). Notice also that, when calculating $\boldsymbol{E}^{n+1}$ and $\boldsymbol{B}^{n+3/2}$, only two of the four Maxwell equations

are used. However, when $\boldsymbol{B}$ is updated with eqs. (2.12) to (2.14), its numerical divergence is automatically conserved. Therefore, if this divergence is initially zero, it remains zero throughout the simulation:

$$(D_x B_x^{n+\frac{1}{2}})_{i+\frac{1}{2},j+\frac{1}{2},k+\frac{1}{2}} + (D_y B_y^{n+\frac{1}{2}})_{i+\frac{1}{2},j+\frac{1}{2},k+\frac{1}{2}} + (D_z B_z^{n+\frac{1}{2}})_{i+\frac{1}{2},j+\frac{1}{2},k+\frac{1}{2}} = 0$$

Thus the discretized Maxwell equation corresponding to $\boldsymbol{\nabla} \cdot \boldsymbol{B} = 0$ is automatically satisfied. The remaining discretized Maxwell equation reads

$$(D_x E_x^n)_{i,j,k} + (D_y E_y^n)_{i,j,k} + (D_z E_z^n)_{i,j,k} - \frac{\rho_{i,j,k}^n}{\epsilon_0} = 0 \tag{2.21}$$

Under the condition that the discretized equation eq. (2.11) is satisfied, it can be shown that updating $\boldsymbol{E}$ preserves the left-hand side of the above equation. Thus, if the numerical divergence of $\boldsymbol{E}$ is initially equal to ρ, then eq. (2.21) is automatically satisfied throughout the simulation. Again, this occurs only under the condition that eq. (2.11) is satisfied, which motivates the use of the Esirkepov algorithm. When other algorithms are used to calculate $\boldsymbol{J}^{n+1/2}$, then additional corrections have to be applied to $\boldsymbol{E}$ so as to explicitly impose eq. (2.21). (The corresponding correcting algorithms are known as *Poisson correctors*.)

2.1.3 Calder Circ, a quasi-cylindrical PIC code

Although full PIC codes are powerful tools, which capture a wide range of physical phenomena, they also require large computational ressources. This is partly due to the use of a 3D Cartesian grid, which leads to a very large number of grid cells. (Typical 3D simulations of laser-wakefield acceleration require $\sim 10^6$–10^8 grid cells.) For this reason, these algorithms need to be highly parallelized, and high-resolution simulations can only be run on costly large-scale computer facilities. However, when the laser pulse is cylindrically-symmetric, it is possible to take advantage of the symmetry of the problem to reduce the computational cost of the algorithm. This idea was implemented by Lifschitz et al. [2009] at LOA, and resulted in the PIC code Calder Circ. This section explains the principle of this *reduced* PIC code.

Azimuthal decomposition In order to explain the principle of Calder Circ, let us consider the fields $\boldsymbol{E}$, $\boldsymbol{B}$, $\boldsymbol{J}$ and ρ in cylindral coordinates (r, θ, z). By definition these fields are 2π-periodic in θ and therefore they can be expressed as a Fourier series:

$$F(r,\theta,z) = \mathrm{Re}\left[\sum_{\ell=0}^{\infty} \tilde{F}_\ell(r,z) e^{-i\ell\theta}\right] \tag{2.22}$$

$$\text{with} \qquad \tilde{F}_\ell = C_\ell \int_0^{2\pi} d\theta\, F(r,\theta,z) e^{i\ell\theta} \qquad \text{and} \quad \begin{cases} C_0 = 1/2\pi \\ C_\ell = 1/\pi \quad \text{for } \ell > 0 \end{cases} \tag{2.23}$$

where F represents any of the quantities E_r, E_θ, E_z, B_r, B_θ, B_z, J_r, J_θ, J_z are ρ, and where the $\tilde{F}_\ell$ are the associated Fourier components (ℓ is the index of the corresponding azimuthal mode). In the general case, this azimuthal decomposition does not simplify the problem, since an infinity of modes have to be considered in eq. (2.22). However, in the case of a cylindrically-symmetric laser pulse, only the very first modes have non-zero components. For instance, the wakefield is represented exclusively by the mode $\ell = 0$. (This is because the quantities E_r, E_θ, E_z, B_r, B_θ, B_z, J_r, J_θ, J_z and ρ associated with the wakefield are independent of θ.) On the other

hand, the field of the laser pulse *does* depend on θ, in cylindrical coordinates. For example, for a cylindrically-symmetric pulse propagating along z and polarized along $\boldsymbol{e}_\alpha = \cos(\alpha)\boldsymbol{e}_x + \sin(\alpha)\boldsymbol{e}_y$:

$$\begin{aligned}\boldsymbol{E} &= E_0(r,z)\boldsymbol{e}_\alpha \\ &= E_0(r,z)[\ \cos(\alpha)(\cos(\theta)\boldsymbol{e}_r - \sin(\theta)\boldsymbol{e}_\theta)\ +\ \sin(\alpha)(\sin(\theta)\boldsymbol{e}_r + \cos(\theta)\boldsymbol{e}_\theta)\ ] \\ &= \mathrm{Re}[\ E_0(r,z)e^{i\alpha}e^{-i\theta}\ ]\boldsymbol{e}_r\ +\ \mathrm{Re}[\ -iE_0(r,z)e^{i\alpha}e^{-i\theta}\ ]\boldsymbol{e}_\theta\end{aligned}$$

Here the amplitude E_0 does not depend on θ because the pulse was assumed to be cylindrically symmetric. In this case, the above relation shows that the fields E_r and E_θ of the laser are represented exclusively by the mode $\ell = 1$. A similar calculation shows that the same holds for B_r and B_θ. On the whole, only the modes $\ell = 0$ and $\ell = 1$ are a priori necessary to model laser-wakefield acceleration. This is the basic idea of Calder Circ. In this algorithm, the infinite sum in eq. (2.22) is truncated at a chosen ℓ_{max}. In principle, $\ell_{max} = 1$ is sufficient for laser-wakefield acceleration. However, ℓ_{max} is kept as a free parameter in the algorithm, in order to verify that higher modes are negligible, as well as to allow for less-symmetric configurations. Because Calder Circ is able to take into account the modes with $\ell > 0$, it is said to be quasi-cylindrical (in contrast to cylindrical codes, which assume that all fields are independent of θ, and thus only consider the mode $\ell = 0$).

Discretized Maxwell equations When the Fourier expressions of the fields are injected into the Maxwell equations (written in cylindrical coordinates), the different azimuthal modes decouple. In this case, the Maxwell-Ampère and Maxwell-Faraday equations – which are needed to update the fields in the PIC cycle – can be written separately for each azimuthal mode ℓ:

$$\begin{aligned}\frac{\partial \tilde{B}_{r,\ell}}{\partial t} &= \frac{i\ell}{r}\tilde{E}_{z,\ell} + \frac{\partial \tilde{E}_{\theta,\ell}}{\partial z} \\ \frac{\partial \tilde{B}_{\theta,\ell}}{\partial t} &= -\frac{\partial \tilde{E}_{r,\ell}}{\partial z} + \frac{\partial \tilde{E}_{z,\ell}}{\partial r} \\ \frac{\partial \tilde{B}_{z,\ell}}{\partial t} &= -\frac{1}{r}\frac{\partial (r\tilde{E}_{\theta,\ell})}{\partial r} - \frac{i\ell}{r}\tilde{E}_{r,\ell} \\ \frac{1}{c^2}\frac{\partial \tilde{E}_{r,\ell}}{\partial t} &= -\frac{i\ell}{r}\tilde{B}_{z,\ell} - \frac{\partial \tilde{B}_{\theta,\ell}}{\partial z} - \mu_0 \tilde{J}_{r,\ell} \\ \frac{1}{c^2}\frac{\partial \tilde{E}_{\theta,\ell}}{\partial t} &= \frac{\partial \tilde{B}_{r,\ell}}{\partial z} - \frac{\partial \tilde{B}_{z,\ell}}{\partial r} - \mu_0 \tilde{J}_{\theta,\ell} \\ \frac{1}{c^2}\frac{\partial \tilde{E}_{z,\ell}}{\partial t} &= \frac{1}{r}\frac{\partial (r\tilde{B}_{\theta,\ell})}{\partial r} + \frac{i\ell}{r}\tilde{B}_{r,\ell} - \mu_0 \tilde{J}_{z,\ell}\end{aligned}$$

In order to discretize these equations, each azimuthal mode is represented on a two-dimensional grid. (The two dimensions correspond to r and z.) Figure 2.3 summarizes the positions of the different fields within one grid cell, as well as the corresponding notations for these fields. Using

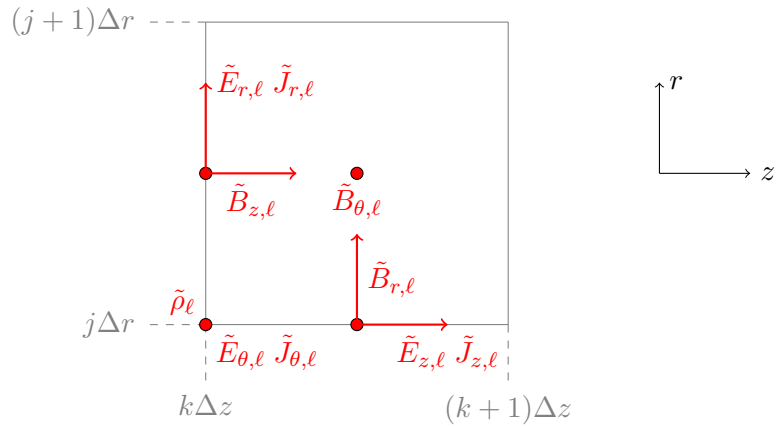

Field	Position in space and time			Notation
	r	z	t	
$\tilde{E}_{r,\ell}$	$(j+\frac{1}{2})\Delta r$	$k\Delta z$	$n\Delta t$	$\tilde{E}_{r\,j+\frac{1}{2},\ell,k}^{\,n}$
$\tilde{E}_{\theta,\ell}$	$j\Delta r$	$k\Delta z$	$n\Delta t$	$\tilde{E}_{\theta\,j,\ell,k}^{\,n}$
$\tilde{E}_{z,\ell}$	$j\Delta r$	$(k+\frac{1}{2})\Delta z$	$n\Delta t$	$\tilde{E}_{z\,j,\ell,k+\frac{1}{2}}^{\,n}$
$\tilde{B}_{r,\ell}$	$j\Delta r$	$(k+\frac{1}{2})\Delta z$	$(n+\frac{1}{2})\Delta t$	$\tilde{B}_{r\,j,\ell,k+\frac{1}{2}}^{\,n+\frac{1}{2}}$
$\tilde{B}_{\theta,\ell}$	$(j+\frac{1}{2})\Delta r$	$(k+\frac{1}{2})\Delta z$	$(n+\frac{1}{2})\Delta t$	$\tilde{B}_{\theta\,j+\frac{1}{2},\ell,k+\frac{1}{2}}^{\,n+\frac{1}{2}}$
$\tilde{B}_{z,\ell}$	$(j+\frac{1}{2})\Delta r$	$k\Delta z$	$(n+\frac{1}{2})\Delta t$	$\tilde{B}_{\theta\,j+\frac{1}{2},\ell,k}^{\,n+\frac{1}{2}}$
$\tilde{\rho}_\ell$	$j\Delta r$	$k\Delta z$	$n\Delta t$	$\tilde{\rho}_{j,l,k}^{n}$
$\tilde{J}_{r,\ell}$	$(j+\frac{1}{2})\Delta r$	$k\Delta z$	$(n+\frac{1}{2})\Delta t$	$\tilde{J}_{r\,j+\frac{1}{2},\ell,k}^{\,n+\frac{1}{2}}$
$\tilde{J}_{\theta,\ell}$	$j\Delta r$	$k\Delta z$	$(n+\frac{1}{2})\Delta t$	$\tilde{J}_{\theta\,j,\ell,k}^{\,n+\frac{1}{2}}$
$\tilde{J}_{z,\ell}$	$j\Delta r$	$(k+\frac{1}{2})\Delta z$	$(n+\frac{1}{2})\Delta t$	$\tilde{J}_{z\,j,\ell,k+\frac{1}{2}}^{\,n+\frac{1}{2}}$

Figure 2.3: Representation of the lattice in Calder Circ. The table shows at which position each component of the fields is defined (j,k and n are integers ; Δr and Δz are the spatial steps of the grid). The above sketch represents one grid cell, and the positions of the fields within it.

these notations, the discretized Maxwell-Ampère and Maxwell-Faraday equations are

$$
\begin{aligned}
\frac{\tilde{B_r}^{n+\frac{1}{2}}_{j,\ell,k+\frac{1}{2}} - \tilde{B_r}^{n-\frac{1}{2}}_{j,\ell,k+\frac{1}{2}}}{\Delta t} &= \frac{i\,\ell}{j\Delta r}\tilde{E_z}^{n}_{j,\ell,k+\frac{1}{2}} + (D_z\tilde{E}^n_\theta)_{j,\ell,k+\frac{1}{2}} \\
\frac{\tilde{B_\theta}^{n+\frac{1}{2}}_{j+\frac{1}{2},\ell,k+\frac{1}{2}} - \tilde{B_\theta}^{n-\frac{1}{2}}_{j+\frac{1}{2},\ell,k+\frac{1}{2}}}{\Delta t} &= -(D_z\tilde{E}^n_r)_{j+\frac{1}{2},\ell,k+\frac{1}{2}} + (D_r\tilde{E}^n_z)_{j+\frac{1}{2},\ell,k+\frac{1}{2}} \\
\frac{\tilde{B_z}^{n+\frac{1}{2}}_{j+\frac{1}{2},\ell,k} - \tilde{B_z}^{n-\frac{1}{2}}_{j+\frac{1}{2},\ell,k}}{\Delta t} &= -\frac{(j+1)\tilde{E_\theta}^{n}_{j+1,\ell,k} - j\tilde{E_\theta}^{n}_{j,\ell,k}}{(j+\frac{1}{2})\Delta r} - \frac{i\,\ell}{(j+\frac{1}{2})\Delta r}\tilde{E_r}^{n}_{j+\frac{1}{2},\ell,k} \\
\frac{\tilde{E_r}^{n+1}_{j+\frac{1}{2},\ell,k} - \tilde{E_r}^{n}_{j+\frac{1}{2},\ell,k}}{c^2\Delta t} &= -\frac{i\,\ell}{(j+\frac{1}{2})\Delta r}\tilde{B_z}^{n+\frac{1}{2}}_{j+\frac{1}{2},\ell,k} - (D_z\tilde{B}^{n+\frac{1}{2}}_\theta)_{j+\frac{1}{2},\ell,k} - \mu_0\tilde{J_r}^{n+\frac{1}{2}}_{j+\frac{1}{2},\ell,k} \\
\frac{\tilde{E_\theta}^{n+1}_{j,\ell,k} - \tilde{E_\theta}^{n}_{j,\ell,k}}{c^2\Delta t} &= (D_z\tilde{B}^{n+\frac{1}{2}}_r)_{j,\ell,k} - (D_r\tilde{B}^{n+\frac{1}{2}}_z)_{j,\ell,k} - \mu_0\tilde{J_\theta}^{n+\frac{1}{2}}_{j,\ell,k} \\
\frac{\tilde{E_z}^{n+1}_{j,\ell,k+\frac{1}{2}} - \tilde{E_z}^{n}_{j,\ell,k+\frac{1}{2}}}{c^2\Delta t} &= \frac{\left(j+\frac{1}{2}\right)\tilde{B_\theta}^{n+\frac{1}{2}}_{j+\frac{1}{2},\ell,k+\frac{1}{2}} - \left(j-\frac{1}{2}\right)\tilde{B_\theta}^{n+\frac{1}{2}}_{j-\frac{1}{2},\ell,k+\frac{1}{2}}}{j\Delta r} \\
&\quad + \frac{i\,\ell}{j\Delta r}\tilde{B_r}^{n+\frac{1}{2}}_{j,\ell,k+\frac{1}{2}} - \mu_0\tilde{J_z}^{n+\frac{1}{2}}_{j,\ell,k+\frac{1}{2}}
\end{aligned}
$$

The numerical operator D_r and D_z are defined by

$$
\begin{aligned}
(D_rF)_{j',\ell,k'} &= \frac{F_{j'+\frac{1}{2},\ell,k'} - F_{j'-\frac{1}{2},\ell,k'}}{\Delta r} \\
(D_zF)_{j',\ell,k'} &= \frac{F_{j',\ell,k'+\frac{1}{2}} - F_{j',\ell,k'-\frac{1}{2}}}{\Delta z}
\end{aligned}
$$

where j' and k' can be integers or half-integer. Notice that these discretized Maxwell equations are not valid on-axis (i.e. for $j = 0$), due to singulatities in some of the terms. Therefore, on the axis, these equations are replaced by specific boundary conditions, which are based on the symmetry properties of the fields (see Lifschitz et al. [2009]).

In a 3D Cartesian PIC code, there is typically ∼100 grid points along *each* tranverse dimension (x and y). In the case of Calder Circ, this is replaced by ∼100 grid points along the r direction, for each of the azimuthal modes (usually only the two modes $\ell = 0$ and $\ell = 1$). The total number of field variables is therefore ∼50 times lower in Calder Circ than in a 3D PIC code. This also implies that the computational ressources needed for a Calder Circ simulation are typically one order of magnitude below those needed by a 3D PIC code.

Interaction with the macroparticles Although the Maxwell equations are integrated in cylindrical coordinates, the motion of the particles is still integrated in Cartesian coordinates. Thus the discretized equations of motion eqs. (2.9) and (2.10) are unchanged. On the other hand, the projection and interpolation operations have to be modified, so as to take into account the specific representation of the fields in Calder Circ. In order to facilitate these operations, the shape function of the macroparticles $g(\boldsymbol{x})$ is assumed to be of the form $g(\boldsymbol{x}) = \tilde{g}(r,z)\delta(\theta)$.

In this case, the interpolation operations read

$$\bar{\boldsymbol{E}}^n(\boldsymbol{x}_m^n) = \mathrm{Re}\left(\sum_{\ell=0}^{\ell_{max}} \sum_{j,k} e^{-i\ell\theta_m} \left[\tilde{S}_{j+\frac{1}{2},k}(r_m, z_m) \tilde{E}_{r\,j+\frac{1}{2},\ell,k}^{\;n}\, \boldsymbol{e}_r \right.\right.$$
$$+ \tilde{S}_{j,k}(r_m, z_m) \tilde{E}_{\theta\,j,\ell,k}^{\;n}\, \boldsymbol{e}_\theta$$
$$\left.\left. + \tilde{S}_{j,k+\frac{1}{2}}(r_m, z_m) \tilde{E}_{z\,j,\ell,k+\frac{1}{2}}^{\;n} \boldsymbol{e}_z \right] \right)$$

$$\bar{\boldsymbol{B}}^n(\boldsymbol{x}_m^n) = \mathrm{Re}\left(\sum_{\ell=0}^{\ell_{max}} \sum_{j,k} e^{-i\ell\theta_m} \left[\tilde{S}_{j,k+\frac{1}{2}}(r_m, z_m) \frac{1}{2} \left(\tilde{B}_{r\,j+\frac{1}{2},\ell,k}^{\;n+\frac{1}{2}} + \tilde{B}_{r\,j+\frac{1}{2},\ell,k}^{\;n-\frac{1}{2}} \right) \boldsymbol{e}_r \right.\right.$$
$$+ \tilde{S}_{j+\frac{1}{2},k+\frac{1}{2}}(r_m, z_m) \frac{1}{2} \left(\tilde{B}_{\theta\,j,\ell,k}^{\;n+\frac{1}{2}} + \tilde{B}_{\theta\,j,\ell,k}^{\;n-\frac{1}{2}} \right) \boldsymbol{e}_\theta$$
$$\left.\left. + \tilde{S}_{j+\frac{1}{2},k}(r_m, z_m) \frac{1}{2} \left(\tilde{B}_{z\,j,\ell,k+\frac{1}{2}}^{\;n+\frac{1}{2}} + \tilde{B}_{z\,j,\ell,k+\frac{1}{2}}^{\;n-\frac{1}{2}} \right) \boldsymbol{e}_z \right] \right)$$

where the sums run over the grid points *and* over the azimuthal modes. Here the interpolation factors $\tilde{S}_{j',k'}$ are defined by

$$\tilde{S}_{j',k'}(r_m, z_m) \equiv \int_{(j'-\frac{1}{2})\Delta r}^{(j'+\frac{1}{2})\Delta r} r\, dr \int_{(k'-\frac{1}{2})\Delta z}^{(k'+\frac{1}{2})\Delta z} dz\; \tilde{g}(r - r_m, z - z_m).$$

Similarly, the charge density of the macroparticles has to be projected onto the grid points *and* the azimuthal modes (using eq. (2.23)):

$$\tilde{\rho}_{j,\ell,k} = \frac{1}{2\pi j \Delta r^2 \Delta z} \sum_m q_m N_m C_\ell e^{i\ell\theta_m} \tilde{S}_{j,k}(r_m, z_m)$$

where C_ℓ is defined in eq. (2.23). As in the case of 3D PIC codes, a similar formula can be used to calculate $\tilde{J}$ on the grid, but then it necessarily entails the use of a Poisson corrector. Alternatively, the Esirkepov algorithm (when adapted to a quasi-cylindrical grid [Davidson et al., 2014]) can be used to project the currents. The Poisson corrector of Calder Circ was developed by Agustin Lifschitz at LOA, while the Esirkepov algorithm was recently adapted to Calder Circ by Xavier Davoine at CEA.

The assumption that motivates Calder Circ (i.e. that only the modes $\ell = 0$ and $\ell = 1$ are non-zero) was tested by varying ℓ_{max} for the same simulation [Lifschitz et al., 2009]. As expected, modifying ℓ_{max} barely changes the results as long as $\ell_{max} \geq 1$, and the fields of the modes $\ell > 1$ are almost zero. These simulation results were also compared with those of a full 3D Cartesian code, and an excellent agreement was found. Thus Calder Circ appears to be a good solution for cylindrically-symmetric situation, since it requires only limited computational ressources but provides excellent physical accuracy. In particular, contrary to 2D Cartesian codes, Calder Circ correctly captures 3D effects like diffraction and self-focusing.[5]

[5] In 2D, the intensity of a laser pulse evolves as $I \propto 1/w$ instead of $I \propto 1/w^2$, where w is the waist of the laser. Thus any phenomenon that involves a large change in w (like diffraction or self-focusing) will lead to unphysical intensity values, in 2D simulations.

2.1.4 Numerical dispersion relation in vacuum

Although both the Cartesian and quasi-cylindrical PIC algorithms are second-order accurate in Δt, Δx, Δy, Δz, the discretization inevitably introduces numerical artifacts. One of these artifacts is *numerical dispersion*. In order to illustrate this concept, let us consider the discretized Maxwell equations in vacuum ($\boldsymbol{J} = \boldsymbol{0}$, $\rho = 0$). In the case of 3D Cartesian PIC codes, the discretized equations eqs. (2.12) to (2.14) and (2.18) to (2.21) can be combined into propagation equations.

$$\frac{{E_x}_{i+\frac{1}{2},j,k}^{n+1} - 2{E_x}_{i+\frac{1}{2},j,k}^{n} + {E_x}_{i+\frac{1}{2},j,k}^{n-1}}{c^2\Delta t^2} = (D_x(D_x E_x^n))_{i+\frac{1}{2},j,k} + (D_y(D_y E_x^n))_{i+\frac{1}{2},j,k} + (D_z(D_z E_x^n))_{i+\frac{1}{2},j,k}$$

$$\frac{{E_y}_{i,j+\frac{1}{2},k}^{n+1} - 2{E_y}_{i,j+\frac{1}{2},k}^{n} + {E_y}_{i,j+\frac{1}{2},k}^{n-1}}{c^2\Delta t^2} = (D_x(D_x E_y^n))_{i,j+\frac{1}{2},k} + (D_y(D_y E_y^n))_{i,j+\frac{1}{2},k} + (D_z(D_z E_y^n))_{i,j+\frac{1}{2},k}$$

$$\frac{{E_z}_{i,j,k+\frac{1}{2}}^{n+1} - 2{E_z}_{i,j,k+\frac{1}{2}}^{n} + {E_z}_{i,j,k+\frac{1}{2}}^{n-1}}{c^2\Delta t^2} = (D_x(D_x E_z^n))_{i,j,k+\frac{1}{2}} + (D_y(D_y E_z^n))_{i,j,k+\frac{1}{2}} + (D_z(D_z E_z^n))_{i,j,k+\frac{1}{2}}$$

The solutions of these equations are plane waves of the form $E_x, E_y, E_z \propto e^{i(k_x x + k_y y + k_z z - i\omega t)}$ with $(k_x, k_y, k_z) \in [-\frac{\pi}{\Delta x}, \frac{\pi}{\Delta x}] \times [-\frac{\pi}{\Delta y}, \frac{\pi}{\Delta y}] \times [-\frac{\pi}{\Delta z}, \frac{\pi}{\Delta z}]$ [6]. However, instead of satisfying the physical dispersion relation $\omega^2 = c^2(k_x^2 + k_y^2 + k_z^2)$, these waves satisfy the *numerical* dispersion relation

$$\frac{1}{c^2\Delta t^2}\sin^2\left(\frac{\omega\Delta t}{2}\right) = \frac{1}{\Delta x^2}\sin^2\left(\frac{k_x\Delta x}{2}\right) + \frac{1}{\Delta y^2}\sin^2\left(\frac{k_y\Delta y}{2}\right) + \frac{1}{\Delta z^2}\sin^2\left(\frac{k_z\Delta z}{2}\right) \qquad (2.24)$$

(This relation can be readily obtained by injecting the form $e^{i(k_x x + k_y y + k_z z - i\omega t)}$ into the discretized equations of propagation.) This dispersion relation reduces to the physical one for $\omega\Delta t \ll 1$ and $k_x\Delta x, k_y\Delta y, k_z\Delta z \ll 1$, but can considerably depart from it otherwise.

One consequence of the numerical dispersion relation eq. (2.24) is that Δt cannot be chosen arbitrarily high. If Δt is so high that $1/(c^2\Delta t^2) < 1/\Delta x^2 + 1/\Delta y^2 + 1/\Delta z^2$, then eq. (2.24) implies that ω is a purely imaginary number for $\boldsymbol{k} = \frac{\pi}{\Delta x}\boldsymbol{e}_x + \frac{\pi}{\Delta y}\boldsymbol{e}_y + \frac{\pi}{\Delta z}\boldsymbol{e}_z$. This in turn entails that the corresponding solution of the form $e^{i\boldsymbol{k}\cdot\boldsymbol{x} - i\omega t}$ can grow exponentionally in time. In practice, this leads to a numerical instability in the simulations. In order to avoid this instability, Δt must be small enough that $1/(c^2\Delta t^2) \geq 1/\Delta x^2 + 1/\Delta y^2 + 1/\Delta z^2$, a condition known as the *Courant-Friedrichs-Lewy (CFL) condition.*

Another consequence of the numerical dispersion relation is that the vacuum phase velocity v_ϕ of the electromagnetic waves differs from c in the simulations. According to eq. (2.24),

$$v_\phi = \frac{2}{k\Delta t}\arcsin\left(\sqrt{\frac{c^2\Delta t^2}{\Delta x^2}\sin^2\left(\frac{k_x\Delta x}{2}\right) + \frac{c^2\Delta t^2}{\Delta y^2}\sin^2\left(\frac{k_y\Delta y}{2}\right) + \frac{c^2\Delta t^2}{\Delta z^2}\sin^2\left(\frac{k_z\Delta z}{2}\right)}\right)$$

where $k = \sqrt{k_x^2 + k_y^2 + k_z^2}$. It can be shown[7] that this expression implies $v_\phi \leq c$. Thus in the simulations, the electromagnetic waves propagate with a phase velocity lower than c in vacuum.

[6] The highest wavectors that the simulation grid can support are $k_x = \pi/\Delta x$, $k_y = \pi/\Delta y$, $k_z = \pi/\Delta z$. For this reason, the wavenumbers $\boldsymbol{k}$ that are considered are always in the domain $[-\frac{\pi}{\Delta x}, \frac{\pi}{\Delta x}] \times [-\frac{\pi}{\Delta y}, \frac{\pi}{\Delta y}] \times [-\frac{\pi}{\Delta z}, \frac{\pi}{\Delta z}]$.

[7] This can be shown by remarking that the function $x \to \sin^2(\sqrt{x}/2)$ is concave on $[0, \pi^2]$. Because of this property, $\frac{\bar{\Delta}^2}{\Delta x^2}\sin^2\left(\sqrt{k_x^2\Delta x^2}/2\right) + \frac{\bar{\Delta}^2}{\Delta y^2}\sin^2\left(\sqrt{k_y^2\Delta y^2}/2\right) + \frac{\bar{\Delta}^2}{\Delta z^2}\sin^2\left(\sqrt{k_z^2\Delta z^2}/2\right) \leq \sin^2\left(\sqrt{(k_x^2 + k_y^2 + k_z^2)\bar{\Delta}^2}/2\right) = \sin^2(k\bar{\Delta}/2)$, where $\bar{\Delta}$ is defined by $\frac{1}{\bar{\Delta}^2} = \frac{1}{\Delta x^2} + \frac{1}{\Delta y^2} + \frac{1}{\Delta z^2}$. Thus $v_\phi \leq \frac{2}{k\Delta t}\arcsin\left(\frac{c\Delta t}{\bar{\Delta}}\sin\left(\frac{k\bar{\Delta}}{2}\right)\right)$. Since arcsin is convex on [0,1], $v_\phi \leq \frac{2c}{k\bar{\Delta}}\arcsin\left(\sin\left(\frac{k\bar{\Delta}}{2}\right)\right) = c$.

As will be shown in the next section, this numerical artifact can have a serious impact on the results of the simulations.

In the case of Calder Circ, the discretized equations of propagation are more complicated than in the Cartesian case, and the complete set of solutions (or *eigenmodes*) of these equations could not be found analytically. In particular, plane waves of the form $e^{i(k_x x+k_y y+k_z z-i\omega t)}$ are *not* solutions of the discretized Maxwell equations (essentially because their expression does not correspond to one single azimuthal mode). The only exceptions are the plane waves that propagate purely along the z axis ($k_x = k_y = 0$). These waves can be written as $E_r = \mathrm{Re}[\ E_0 e^{ik_z z-i\omega t-i\theta}\ ]$, $E_\theta = \mathrm{Re}[\ -iE_0 e^{ik_z z-i\omega t-i\theta}\ ]$, $B_r = \mathrm{Re}[\ iE_0/c \times e^{ik_z z-i\omega t-i\theta}\ ]$, $B_\theta = \mathrm{Re}[\ E_0/c \times e^{ik_z z-i\omega t-i\theta}\ ]$, $E_z = B_z = 0$, and therefore they are entirely contained in the mode $\ell = 1$. These expressions are indeed solutions of the discretized Maxwell equation, provided that ω and k_z satisfy

$$\frac{1}{c\Delta t}\sin\left(\frac{\omega\Delta t}{2}\right) = \frac{1}{\Delta z}\sin\left(\frac{k_z\Delta z}{2}\right).$$

Thus the quasi-cylindrical algorithm of Calder Circ is also subject to numerical dispersion. In fact, the above equation shows that the waves that propagate purely along the z axis ($k_x = 0$, $k_y = 0$) have the same dispersion relation in Calder Circ and in 3D Cartesian codes.

2.2 Numerical Cherenkov radiation in LWFA simulations

The fact that the phase velocity is spuriously lower than c in the simulations can sometimes have a substantial impact. In particular, it can lead to *numerical Cherenkov radiation*. In this section, we will see that numerical Cherenkov radiation can have important consequences for LWFA simulations.

2.2.1 Physical and numerical Cherenkov radiation

Numerical Cherenkov radiation is related to the well-known Cherenkov effect [Jackson, 1998]. The Cherenkov effect can occur whenever a relativistic charged particle travels through a medium in which the phase velocity of light v_ϕ is lower than c. In this case, if the particle travels faster than this phase velocity ($v > v_\phi$), it will emit a characteristic radiation. The exact expression of this radiation can be calculated analytically [Jackson, 1998], but its main angular and spectral features can by obtained simply from the resonance condition

$$\omega = \boldsymbol{v}\cdot\boldsymbol{k} \tag{2.25}$$

where $\boldsymbol{v}$ is the velocity of the particle. More specifically, when decomposing the emitted radiation into waves of the form $e^{i\boldsymbol{k}\cdot\boldsymbol{x}-i\omega t}$, the waves with the highest amplitude will be those which satisfy eq. (2.25). Qualitatively, this resonance condition corresponds to the particle remaining constantly in phase with the emitted wave ($\boldsymbol{k}\cdot\boldsymbol{x} - \omega t = \text{const.}$).

The condition eq. (2.25) can only be met if $\omega < |\boldsymbol{v}||\boldsymbol{k}|$, and thus we find again the necessary condition $v > v_\phi$. Notice that this necessary condition can be met in dielectric media (such as air or water), but not in vacuum ($v_\phi = c$) and not in plasmas ($v_\phi > c$). In the case of laser-wakefield acceleration, the accelerated bunch is relativistic, but it is surrounded either by a plasma (in the linear regime) or by an effective vacuum (in the blow-out regime, as the ions of the cavity have a negligible impact on the propagation of light). Thus the Cherenkov effect *cannot* occur in situations of laser-wakefield acceleration. However, it can occur in *numerical simulations* of laser-wakefield acceleration, due to numerical dispersion ($v_\phi \leq c$). In this case, the Cherenkov

effect is an unphysical numerical artifact, and it is therefore known as the *numerical Cherenkov effect*.

The above considerations are illustrated in fig. 2.4, in the case of a relativistic particle propagating along the z axis in vacuum. In this figure, the yellow and red surfaces represent the physical dispersion relation ($\omega^2 = c^2k^2$; left panel) and numerical dispersion relation (eq. (2.24) ; right panel). (In principle, ω should be plotted as a function of k_x, k_y and k_z but this would require 4D visualization. For this reason, we restricted ourselves to $k_y = 0$ in fig. 2.4 and plotted ω as a function of k_x and k_z only.) The resonance condition eq. (2.25) is represented as a translucid plane in fig. 2.4. According to the above analysis, resonant Cherenkov radiation appears wherever the plane and the surfaces intersect. In the case of the physical dispersion relation (left panel), they do not intersect and thus we find again that, physically, there is no Cherenkov radiation in vacuum. On the other hand, these surfaces do intersect in the case of the numerical dispersion relation, thereby leading to numerical Cherenkov radiation. Importantly, this figure shows that the intersection occurs only for certain wavevectors $\boldsymbol{k}$. The exact equation that these wavevectors satisfy can be found by combining eqs. (2.24) and (2.25).

$$\frac{1}{c^2\Delta t^2}\sin^2\left(\frac{vk_z\Delta t}{2}\right) = \frac{1}{\Delta x^2}\sin^2\left(\frac{k_z\Delta x}{2}\right) + \frac{1}{\Delta y^2}\sin^2\left(\frac{k_y\Delta y}{2}\right) + \frac{1}{\Delta z^2}\sin^2\left(\frac{k_z\Delta z}{2}\right)$$

The corresponding pattern in $\boldsymbol{k}$ space can be considered as a *signature* of numerical Cherenkov radiation. This fact will be used in the next section to identify Cherenkov radiation in the simulations.

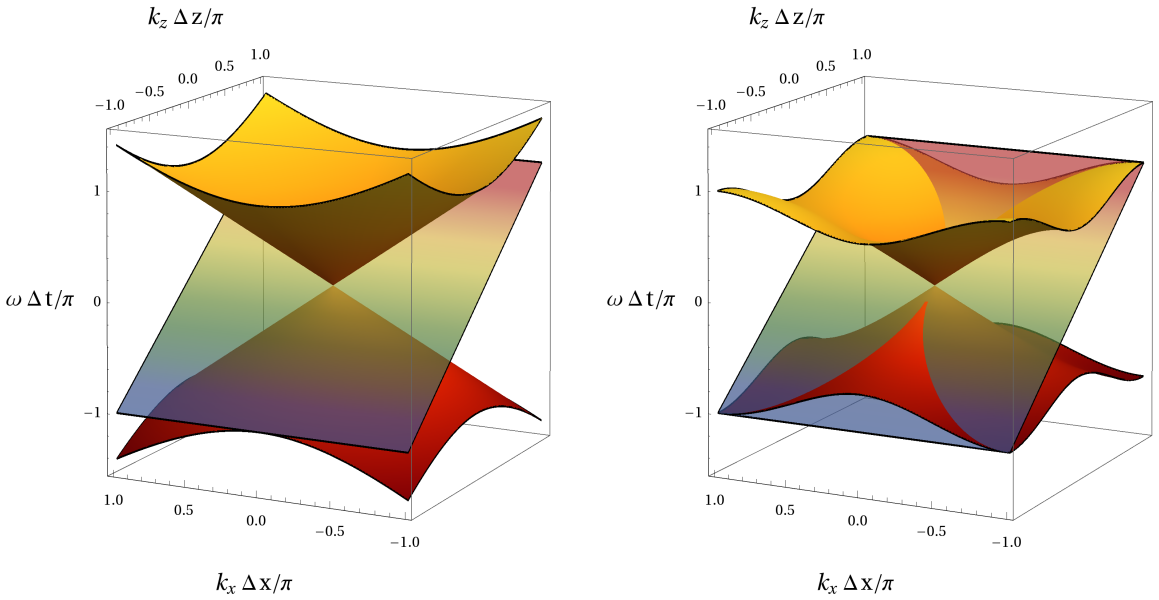

Figure 2.4: Representation of the numerical Cherenkov effect. Left panel: physical dispersion relation as a function of k_x and k_z, for $k_y = 0$. Right panel: Numerical dispersion relation as a function of k_x and k_z, for $k_y = 0$, $\Delta x = \Delta z$ and $\Delta t = 0.5\Delta z$. The translucid plane represents the resonance condition eq. (2.25). *(Adapted from Xu et al. [2013].)*

Numerical Cherenkov radiation is a known artifact in the PIC community [Godfrey, 1974]. In particular, it leads to a dramatic numerical instability in flowing-plasma simulations (i.e. simulations in which the whole plasma is moving at a relativistic speed) [Xu et al., 2013]. These simulations include for instance simulations of astrophysical shocks (e.g. Spitkovsky [2008];

Keshet et al. [2009]), as well as boosted-frame simulations [Vay, 2007; Martins et al., 2010]. However, numerical Cherenkov radiation is less conspicuous in standard simulations of LWFA, in which only a small part of the plasma (the injected bunch) has an ultra-relativistic speed. For this reason, the numerical Cherenkov effect was not suspected to have a significant impact for LWFA up to now.

2.2.2 Impact in LWFA simulations

In order to illustrate the impact of this artifact in standard LWFA simulation, let us consider a typical simulation of self-injection. In this simulation, a 1.5 J laser pulse with 35 fs FWHM duration is focused in a plasma of density $1.0 \times 10^{19}\,\mathrm{cm}^{-3}$. The laser self-focuses and leads to the self-injection and acceleration of a 250 pC bunch. I ran the simulation with the 3D Cartesian code Calder 3D [Lefebvre et al., 2003], using a resolution $\Delta z = 0.032\,\mu\mathrm{m}$, $\Delta x = \Delta y = 0.25\,\mu\mathrm{m}$ and $c\Delta t = 0.96\Delta z$[8].

Figure 2.5 is a snapshot of the simulation box after 250 μm of acceleration. The overall picture of the bubble (left panel) exhibits nothing unusual. However, zooming on the bunch and rescaling the fields (right panel) reveals that the bunch is surrounded by a high-frequency radiation. The typical field of this radiation ($\sim 1\,\mathrm{TV.m}^{-1}$) is much lower than that of the laser ($\sim 15\,\mathrm{TV.m}^{-1}$), which explains that it could not be seen on the left panel of fig. 2.5. Notice also that the right panel shows $E_x - cB_y$ instead of E_x. This is done in order to cancel the strong space-charge field that would otherwise dominate the figure[9]. The quantity $E_x - cB_y$ is interesting also because it corresponds approximatively to the force felt by an ultrarelativistic electron propagating along the z axis ($F_x = -e(E_x - vB_y) \approx -e(E_x - cB_y)$).

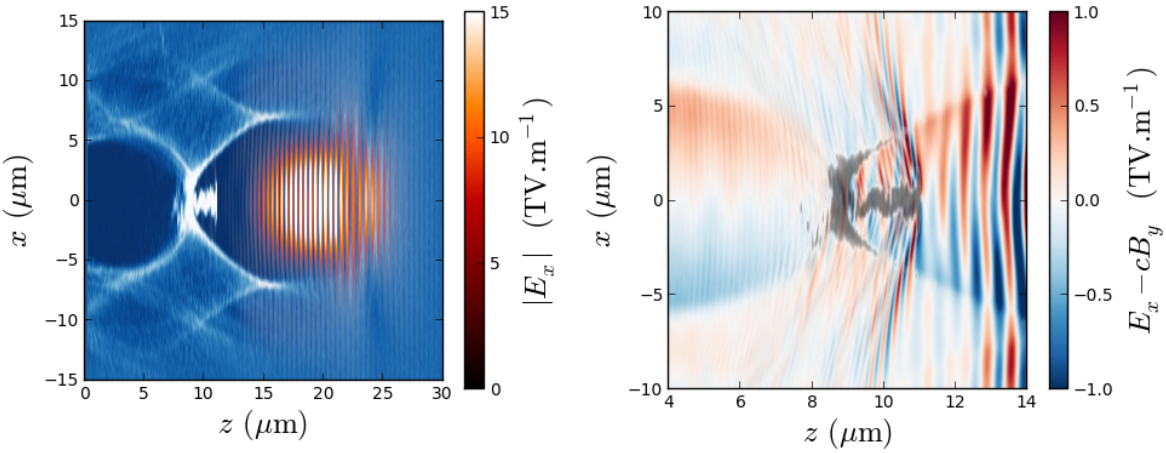

Figure 2.5: Snapshot of the Calder 3D simulation, after 250 μm of acceleration. Left panel: Representation of the electron density (blue) and the electric field (orange, superimposed with partial transparency). Right panel: Representation of the fields in the vicinity of bunch. The shaded areas correspond to zones of high electron density (here mainly the electron bunch and the back of the sheath).

[8] Δz is typically chosen to be small so as to resolve the wavelength of the laser ($\lambda = 0.8\,\mu\mathrm{m}$). Δx and Δy can be larger, since the characteristic lengths that need to be resolved transversely are much larger than λ.

[9] For a relativistic beam, the space charge electric field $\boldsymbol{E}_{sp}$ and the self-generated magnetic field $\boldsymbol{B}_{sp}$ cancel each other almost entirely – in the sense that $|\boldsymbol{E}_{sp} + \boldsymbol{v} \times \boldsymbol{B}_{sp}| \ll |\boldsymbol{E}_{sp}|$. [Jackson, 1998].

Although the observed radiation is less intense than the laser, it has nonetheless a significant amplitude. The fact that it directly surrounds the bunch suggests that it may be due to the numerical Cherenkov effect. In order to confirm this hypothesis, the 2D spatial Fourier transform of $E_x - cB_y$ is represented in fig. 2.6 (orange and dark tones). The dashed blue line represent the wavenumbers $\boldsymbol{k}$ that satisfy the equation

$$\frac{1}{c^2\Delta t^2}\sin^2\left(\frac{vk_z\Delta t}{2}\right) = \frac{1}{\Delta x^2}\sin^2\left(\frac{k_z\Delta x}{2}\right) + \frac{1}{\Delta z^2}\sin^2\left(\frac{k_z\Delta z}{2}\right) \tag{2.26}$$

with $v = 0.9999c$, i.e. the resonant wavenumbers $\boldsymbol{k}$ of the numerical Cherenkov effect. (The double-parabola shape of the dashed curves is directly related to the shape of the intersection in the right panel of fig. 2.4.) As can be seen, the wavevectors predicted by the above equation correspond exactly to those which have a substantial amplitude in the simulation. This confirms that the high-frequency fields of the simulation are due to the numerical Cherenkov effect, and thus that they are unphysical.

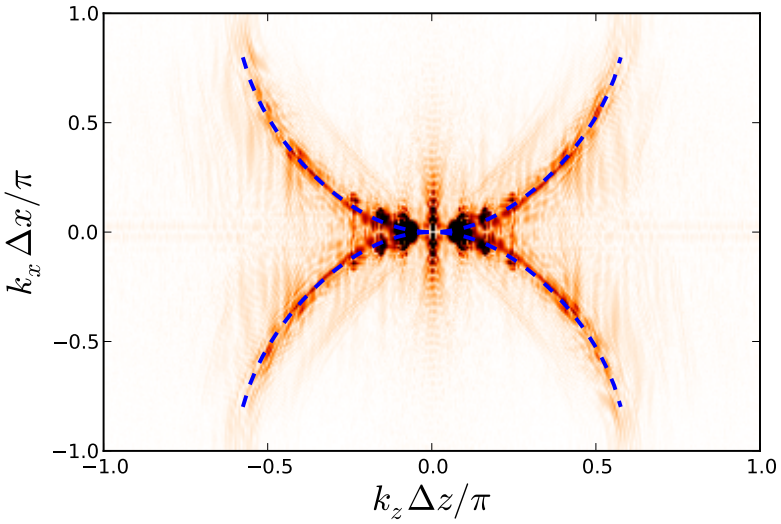

Figure 2.6: Amplitude of the Fourier transform of the fields $E_x - cB_y$ corresponding to fig. 2.5. The blue dashed curves materialize the solutions of eq. (2.26). The two black spots at $k_z = \pm 0.1\pi/\Delta z$ correspond to the laser pulse.

Simultaneously with the emission of this radiation, the emittance of the bunch is observed to grow considerably during the acceleration. This is represented in fig. 2.7. In this figure, only the electrons in the quasimonoenergetic peak of the spectrum are selected (left panel), and their emittance is plotted as a function of the acceleration distance (right panel). The growth of emittance is considerable, and reaches an average slope of 6 mm.mrad per mm of acceleration. Here the accelerated electrons are in a fully-evacuated cavity, characterized by linear focusing fields, and thus this growth of emittance could only be explained either by the energy-spread or by the space-charge effects (see section 1.3). However, when evaluating[10] these effects,

[10]The impact of the finite energy-spread on the emittance was evaluated by calculating $\Delta\epsilon_x^2 = \int dt\ 2(\langle p_x^2\rangle\langle xp_x/\gamma\rangle - \langle p_x^2/\gamma\rangle\langle xp_x\rangle)/m^3c^2$ for the macroparticles of the bunch, throughout the simulation (see section 1.3 ; the brackets denote an average over the macroparticles). The impact of space-charge was evaluated by using eq. (1.45), with the bunch parameters obtained in the PIC simulation: $I = 130\,\mathrm{kA}$, $\gamma \sim 200$, $\sqrt{\langle x^2\rangle} = 0.5\,\mu\mathrm{m}$.

the predicted increase in emittance is $\Delta\epsilon \approx 0.08\,\text{mm.mrad}$ for the energy-spread effects and $\Delta\epsilon \sim 10^{-3}\,\text{mm.mrad}$ for space-charge effects – which is much lower than the increase observed in fig. 2.7 ($\Delta\epsilon \approx 2\,\text{mm.mrad}$). Also, the observed growth of emittance could potentially be explained by the interaction of the electrons with the back of the laser pulse [Németh et al., 2008]. However, the laser is linearly polarized along the x direction in this simulation, and the fact that ϵ_x and ϵ_y grow at the same rate is in contradiction with this potential explanation. Thus the observed spectacular growth of emittance appears to be unphysical.

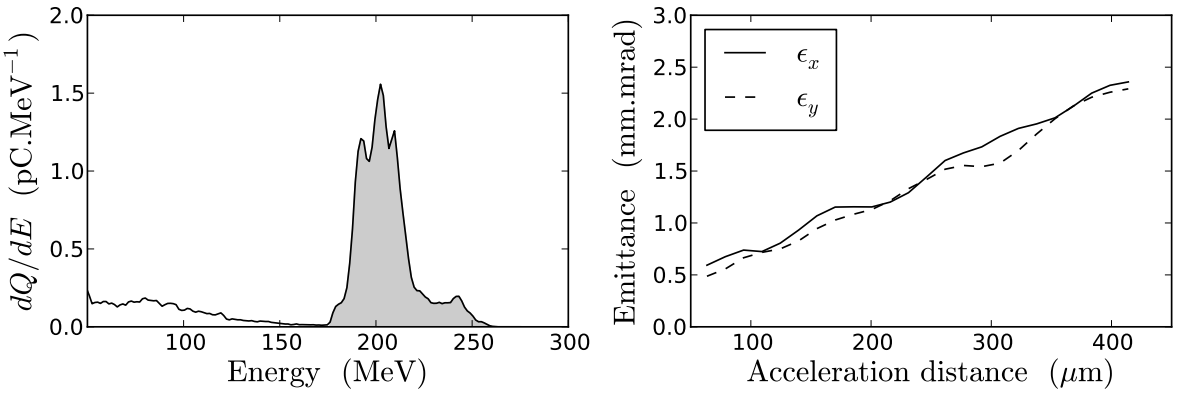

Figure 2.7: Left panel: Energy spectrum in the Calder 3D simulation, after 400 μm of acceleration. The shaded area corresponds to the selected part of the bunch. Right panel: Emittance of the selected electrons in the x and y directions, as a function of the acceleration distance.

The same phenomena – emission of numerical Cherenkov radiation and unphysical growth of emittance – are observed in simulations run with the quasi-cylindrical code Calder Circ. Here this is illustrated by a simulation of a somewhat different situation than in the case of Calder 3D. A 1 J laser pulse with 30 fs FWHM duration is focused into a gas jet having a density of $2.6 \times 10^{18}\,\text{cm}^{-3}$. The injection is triggered by a colliding counterpropagative laser pulse, and leads to the acceleration of a 25 pC bunch. The simulation was run in Calder Circ with two azimuthal modes ($\ell = 0$ and $\ell = 1$) and with $\Delta z = 0.008\,\mu\text{m}$, $\Delta r = 0.16\,\mu\text{m}$ and $c\Delta t = 0.96\Delta z$. (Because Calder Circ considerably reduces the computional cost of a simulation compared to Calder 3D, it was possible to use a much smaller Δz.)

Figure 2.8 displays a snapshot of the simulation. Again a strong high-frequency radiation is seen to surround the bunch. In parallel, fig. 2.9 shows the evolution of the emittance, for a selected fraction of the bunch. The emittance is also observed to grow, although with a lower slope than in the 3D simulation.

Importantly, both the emission of numerical Cherenkov radiation and the unphysical growth of emittance depend largely on the charge density of the bunch. (These effects are virtually absent for bunches with less than 20 pC of charge.) I thus hypothesized that both phenomena are related, i.e. that the relatively strong field of the numerical Cherenkov radiation ($\sim 1\,\text{TV.m}^{-1}$) scatters the electrons transversely and leads to a spurious growth of emittance. In order to confirm this hypothesis, I modified the PIC codes Calder 3D and Calder Circ so as to prevent the numerical Cherenkov effect.

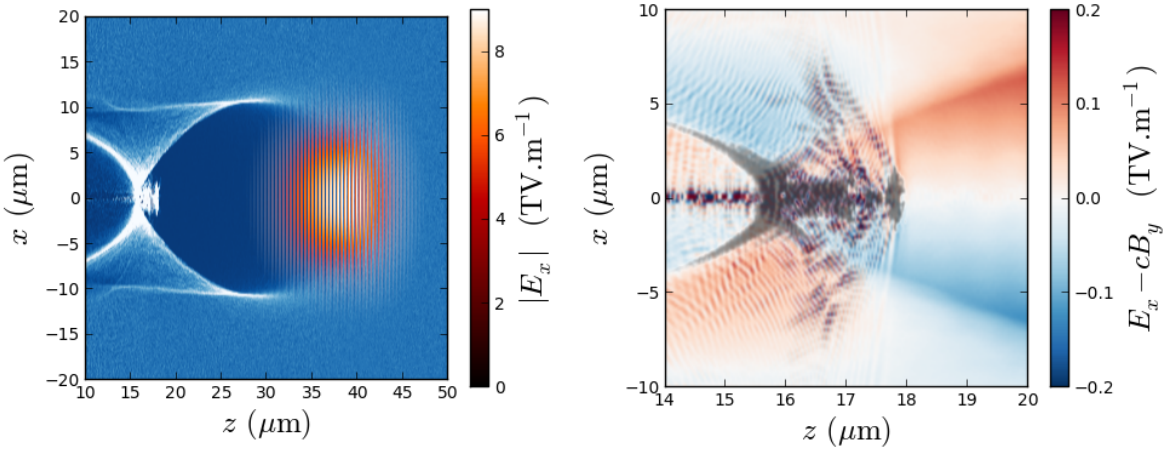

Figure 2.8: Snapshot of the Calder Circ simulation, after 300 μm of acceleration. Left panel: Representation of the electron density (blue) and the electric field (orange, superimposed with partial transparency). Right panel: Representation of the fields in the vicinity of bunch. The shaded areas correspond to zones of high electron density.

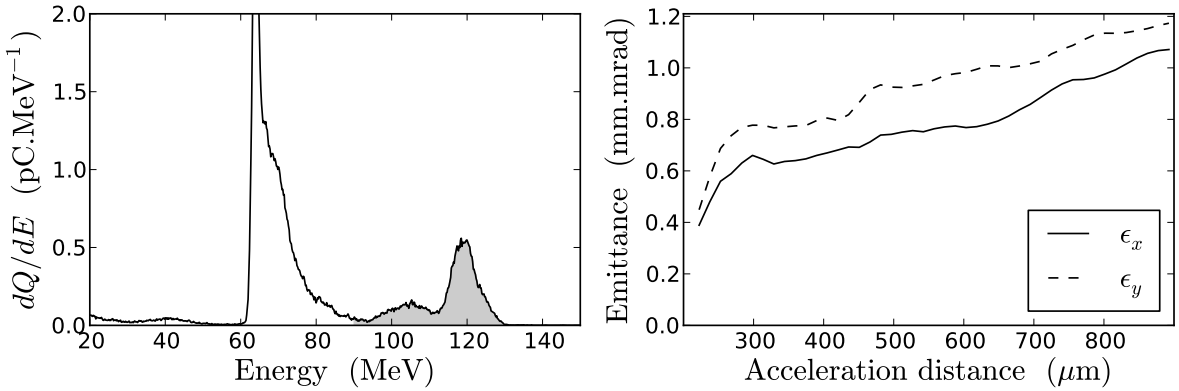

Figure 2.9: Left panel: Energy spectrum in the Calder Circ simulation, after 450 μm of acceleration. The shaded area corresponds to the selected part of the bunch. Right panel: Emittance of the selected electrons in the x and y directions, as a function of the acceleration distance.

2.3 A proposed Cherenkov-free algorithm

As mentioned in section 2.2.1, numerical Cherenkov is a known artifact in the case of flowing-plasma simulations, and a number of solutions have already been developed in this context. However, these solutions are not well adapted in the case of standard LWFA simulations.

For instance, one solution is to use digital filtering [Birdsall and Langdon, 2004] in order to heavily damp the spurious high-frequency fields [Greenwood et al., 2002, 2004; Vay et al., 2011]. However, any high-frequency digital filter inevitably damps the lower-frequency fields as well – albeit by a lesser amount. In simulations of laser-wakefield acceleration, these lower-frequency fields include for instance the laser pulse, and thus digital filtering can result in an unphysical progressive damping of the laser – with dramatic consequences for the physics of the simulation.

Another solution consists in modifying the discretization of the Maxwell equation, so as to alter the corresponding numerical dispersion relation. For instance, Pukhov [1999]; Karkkainen et al. [2006] adapted the discretization in such a way that the CFL condition is modified and allows to choose $c\Delta t = \Delta z$. In this case, the waves propagating along the z axis verify $v_\phi = c$ in vacuum and as a result the numerical Cherenkov effect can potentially be eliminated. However, Vay et al. [2011] showed that chosing $c\Delta t = \Delta z$ leads to the accumulation of numerical noise at the Nyquist frequency $k_z = \pi/\Delta z$. This numerical noise can rapidly grow to intolerable levels, and again requires digital filtering. Finally, Greenwood et al. [2004] developed a set of numerical schemes which can eliminate the numerical Cherenkov effect without requiring $c\Delta t = \Delta z$. In principle, these schemes are not subject to Nyquist noise and they could be a good solution for LWFA simulations. Yet these schemes were developed only for an isotropic Cartesian grid ($\Delta x = \Delta y = \Delta z$), whereas LWFA simulations are typically run on anisotropic grids ($\Delta z < \Delta x, \Delta y$).

Thus in sections 2.3.1 and 2.3.2, I propose two numerical schemes that are similar to that of Greenwood et al. [2004], but are adapted to an anisotropic Cartesian grid (section 2.3.1) and to a quasi-cylindrical grid (section 2.3.2). These numerical schemes efficiently suppress the numerical Cherenkov effect and lead to less Nyquist noise than the algorithms of Pukhov [1999]; Karkkainen et al. [2006].

2.3.1 Presentation of the algorithm for a 3D Cartesian grid

In the proposed scheme, the discretization of the Maxwell equations is altered. The fields are still defined at the same position as in the Yee lattice, but the discretization of the space derivatives in the Maxwell-Faraday equation is modified. (The discretization of the Maxwell-Ampère remains however unchanged[11].) The corresponding discretized equations thus read

$$\frac{{E_x}_{i+\frac{1}{2},j,k}^{n+1} - {E_x}_{i+\frac{1}{2},j,k}^{n}}{c^2\Delta t} = (D_y B_z^{n+\frac{1}{2}})_{i+\frac{1}{2},j,k} - (D_z B_y^{n+\frac{1}{2}})_{i+\frac{1}{2},j,k} - \mu_0 {J_x}_{i+\frac{1}{2},j,k}^{n+\frac{1}{2}} \tag{2.27}$$

$$\frac{{E_y}_{i,j+\frac{1}{2},k}^{n+1} - {E_y}_{i,j+\frac{1}{2},k}^{n}}{c^2\Delta t} = (D_z B_x^{n+\frac{1}{2}})_{i,j+\frac{1}{2},k} - (D_x B_z^{n+\frac{1}{2}})_{i,j+\frac{1}{2},k} - \mu_0 {J_y}_{i,j+\frac{1}{2},k}^{n+\frac{1}{2}} \tag{2.28}$$

$$\frac{{E_z}_{i,j,k+\frac{1}{2}}^{n+1} - {E_z}_{i,j,k+\frac{1}{2}}^{n}}{c^2\Delta t} = (D_x B_y^{n+\frac{1}{2}})_{i,j,k+\frac{1}{2}} - (D_y B_x^{n+\frac{1}{2}})_{i,j,k+\frac{1}{2}} - \mu_0 {J_z}_{i,j,k+\frac{1}{2}}^{n+\frac{1}{2}} \tag{2.29}$$

[11] Modifying the Maxwell-Ampère equation would impose to also modify the Esirkepov algorithm, which indeed relies on this Maxwell equation in order to ensure $\boldsymbol{\nabla} \cdot \boldsymbol{E} = \rho/\epsilon_0$. However, modifying the Esirkepov algorithm can be quite intricate, and for this reason the Maxwell-Ampère equation is left unchanged. Notice also that, because the Maxwell-Faraday equation is modified in the proposed scheme, the condition $(D_x B_x^{n+\frac{1}{2}})_{i+\frac{1}{2},j+\frac{1}{2},k+\frac{1}{2}} + (D_y B_y^{n+\frac{1}{2}})_{i+\frac{1}{2},j+\frac{1}{2},k+\frac{1}{2}} + (D_z B_z^{n+\frac{1}{2}})_{i+\frac{1}{2},j+\frac{1}{2},k+\frac{1}{2}} = 0$ is no longer ensured. It is however possible to show that the proposed scheme does ensure the modified condition $(D_x^* B_x^{n+\frac{1}{2}})_{i+\frac{1}{2},j+\frac{1}{2},k+\frac{1}{2}} + (D_y^* B_y^{n+\frac{1}{2}})_{i+\frac{1}{2},j+\frac{1}{2},k+\frac{1}{2}} + (D_z^* B_z^{n+\frac{1}{2}})_{i+\frac{1}{2},j+\frac{1}{2},k+\frac{1}{2}} = 0$, where the operators D^* are defined below.

$$\frac{B_{x\,i,j+\frac{1}{2},k+\frac{1}{2}}^{n+\frac{1}{2}} - B_{x\,i,j+\frac{1}{2},k+\frac{1}{2}}^{n-\frac{1}{2}}}{\Delta t} = -(D_y^* E_z^n)_{i,j+\frac{1}{2},k+\frac{1}{2}} + (D_z^* E_y^n)_{i,j+\frac{1}{2},k+\frac{1}{2}} \tag{2.30}$$

$$\frac{B_{y\,i+\frac{1}{2},j,k+\frac{1}{2}}^{n+\frac{1}{2}} - B_{y\,i+\frac{1}{2},j,k+\frac{1}{2}}^{n-\frac{1}{2}}}{\Delta t} = -(D_z^* E_x^n)_{i+\frac{1}{2},j,k+\frac{1}{2}} + (D_x^* E_z^n)_{i+\frac{1}{2},j,k+\frac{1}{2}} \tag{2.31}$$

$$\frac{B_{z\,i+\frac{1}{2},j+\frac{1}{2},k}^{n+\frac{1}{2}} - B_{z\,i+\frac{1}{2},j+\frac{1}{2},k}^{n-\frac{1}{2}}}{\Delta t} = -(D_x^* E_y^n)_{i+\frac{1}{2},j+\frac{1}{2},k} + (D_y^* E_x^n)_{i+\frac{1}{2},j+\frac{1}{2},k} \tag{2.32}$$

where D_x, D_y and D_z represent the standard space-centered operators defined in eqs. (2.15) to (2.17), but where D_x^*, D_y^* and D_z^* represent modified operators which are defined by

$$\begin{aligned}(D_z^* F)_{i',j',k'} = \alpha_z &\left(\frac{F_{i',j',k'+\frac{1}{2}} - F_{i',j',k'-\frac{1}{2}}}{\Delta z}\right) + \delta_z \left(\frac{F_{i',j',k'+\frac{3}{2}} - F_{i',j',k'-\frac{3}{2}}}{\Delta z}\right) \\ &+ \beta_{z,x} \left(\frac{F_{i'+1,j',k'+\frac{1}{2}} - F_{i'+1,j',k'-\frac{1}{2}}}{\Delta z} + \frac{F_{i'-1,j',k'+\frac{1}{2}} - F_{i'-1,j',k'-\frac{1}{2}}}{\Delta z}\right) \\ &+ \beta_{z,y} \left(\frac{F_{i',j'+1,k'+\frac{1}{2}} - F_{i',j'+1,k'-\frac{1}{2}}}{\Delta z} + \frac{F_{i',j'-1,k'+\frac{1}{2}} - F_{i',j'-1,k'-\frac{1}{2}}}{\Delta z}\right)\end{aligned}$$

and by similar relations for D_x^* and D_y^*. Thus these modified operators correspond to a weighted sum over the neighboring grid points, with weights given by the α, β and δ coefficients. These neighboring fields and their weights are represented graphically in fig. 2.10. With these definitions, the numerical operators are second-order accurate in Δx, Δy and Δz, provided that the coefficients satisfy the condition

$$\begin{cases} \alpha_x + 2\beta_{x,y} + 2\beta_{x,z} + 3\delta_x = 1 \\ \alpha_y + 2\beta_{y,x} + 2\beta_{y,z} + 3\delta_y = 1 \\ \alpha_z + 2\beta_{z,x} + 2\beta_{z,y} + 3\delta_z = 1 \end{cases}$$

Thus, once the β and δ coefficients are chosen, the α coefficients are fixed by the above condition.

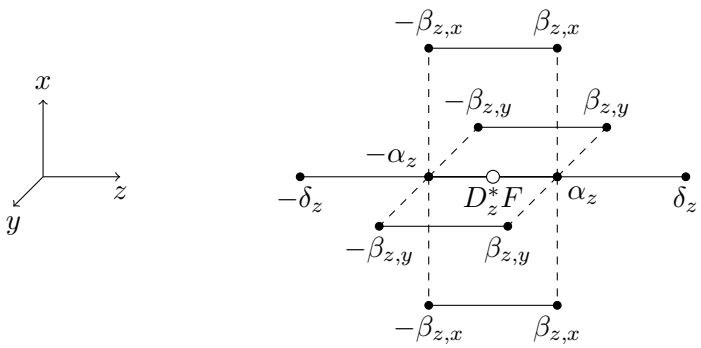

Figure 2.10: Schematic representation of the grid points that are used when calculating $D_x^* F$, along with their respective weights.

The numerical dispersion relation of this scheme can be found by injecting waves of form $e^{i\boldsymbol{k}\cdot\boldsymbol{x}-i\omega t}$ in the discretized Maxwell equations. This yields

$$\begin{aligned}\frac{s_t^2}{c^2\Delta t^2} =& \frac{s_x^2}{\Delta x^2}+\frac{s_y^2}{\Delta y^2}+\frac{s_z^2}{\Delta z^2}-4\left(\delta_x\frac{s_x^4}{\Delta x^2}+\delta_y\frac{s_y^4}{\Delta y^2}+\delta_z\frac{s_z^4}{\Delta z^2}\right)\\ &-4\left(\frac{1}{\Delta x^2}\beta_{x,y}+\frac{1}{\Delta y^2}\beta_{y,x}\right)s_x^2s_y^2\\ &-4\left(\frac{1}{\Delta y^2}\beta_{y,z}+\frac{1}{\Delta z^2}\beta_{z,y}\right)s_y^2s_z^2\\ &-4\left(\frac{1}{\Delta z^2}\beta_{z,x}+\frac{1}{\Delta x^2}\beta_{x,z}\right)s_z^2s_x^2\end{aligned} \tag{2.33}$$

where $s_t = \sin(\omega\Delta t/2)$ and $s_u = \sin(k_u\Delta u/2)$ for $u = x, y, z$. When the β and δ coefficients are zero, the operators D_x^*, D_y^*, D_z^* reduce to D_x, D_y, D_z (as defined by eqs. (2.15) to (2.17)). In this case, the above dispersion relation reduces to that of the standard scheme (eq. (2.24)), which was shown to lead to numerical Cherenkov radiation in the last section. Conversely, for well-chosen non-zero coefficients, the numerical dispersion relation can be tailored so as to avoid the numerical Cherenkov effect. Notice that, since the accelerated beam travels mainly along the z axis, the numerical Cherenkov effect needs only to be avoided for $\boldsymbol{v} = v\boldsymbol{e_z}$. In other words, the β and δ coefficients should be chosen in such a way that the numerical dispersion relation (eq. (2.33)) and the resonance condition $\omega = vk_z$ cannot be simultaneously satisfied. I found that this condition is satisfied for the following coefficients (see appendix B for a derivation of these coefficients):

$$\begin{cases} \delta_x = 0 \qquad \delta_y = 0 \qquad \delta_z = -\dfrac{1}{4}\left[\dfrac{\Delta z^2}{c^2\Delta t^2}\sin^2\left(\dfrac{\pi c\Delta t}{2\Delta z}\right)-1\right] \\ \beta_{z,x} = \dfrac{\Delta z^2}{8\Delta x^2} \qquad \beta_{z,y} = \dfrac{\Delta z^2}{8\Delta y^2} \qquad \beta_{x,z} = \dfrac{1}{8} \qquad \beta_{y,z} = \dfrac{1}{8} \qquad \beta_{x,y} = 0 \qquad \beta_{y,x} = 0 \end{cases}$$

and the corresponding dispersion relation is:

$$\frac{s_t^2}{c^2\Delta t^2} = \frac{s_x^2}{\Delta x^2}(1-s_z^2)+\frac{s_y^2}{\Delta y^2}(1-s_z^2)+\frac{s_z^2}{\Delta z^2}+\frac{s_z^4}{\Delta z^2}\left[\frac{\Delta z^2}{c^2\Delta t^2}\sin^2\left(\frac{\pi c\Delta t}{2\Delta z}\right)-1\right] \tag{2.34}$$

This numerical dispersion relation is represented in the left panel of fig. 2.11 (in the particular case $k_y = 0$). For comparison the numerical dispersion relation of the standard scheme (i.e. with zero β and δ coefficients) is represented in the right panel of fig. 2.11 (again for $k_y = 0$). As desired, the surface representing the resonant condition $\omega = vk_z$ and that representing the numerical dispersion relation do not intersect in the case of the proposed scheme. Importantly, the same occurs for any other value of k_y, and thus this scheme is in principle Cherenkov-free (for particles traveling parallel to the z axis[12]). This will be confirmed by the simulations of section 2.4.

[12] It is important to notice that, for particles traveling with an angle relative to the z axis (e.g. $\boldsymbol{v} = v\cos(\theta)\boldsymbol{e_z} + v\sin(\theta)\boldsymbol{e_x}$), the scheme is not Cherenkov-free anymore (as can be seen by plotting the intersection between the curve of $\omega(\boldsymbol{k})$ and $\boldsymbol{k}\cdot\boldsymbol{v} = vk_z\cos(\theta)+vk_x\sin(\theta)$ for $v \simeq c$). This is not a problem for simulations of laser-wakefield acceleration, since the relativistic particles travel with a very small angle relative to the z axis, and thus the scheme is very close from being Cherenkov-free for these particles. (As a consequence, the emitted Cherenkov radiation is negligible, as will be shown in section 2.4.) However, in other physical situations (such as fully-developped relativistic shocks for instance), relativistic particles may travel with a large angle relative to the z axis, and thus this scheme may not be very well suited.

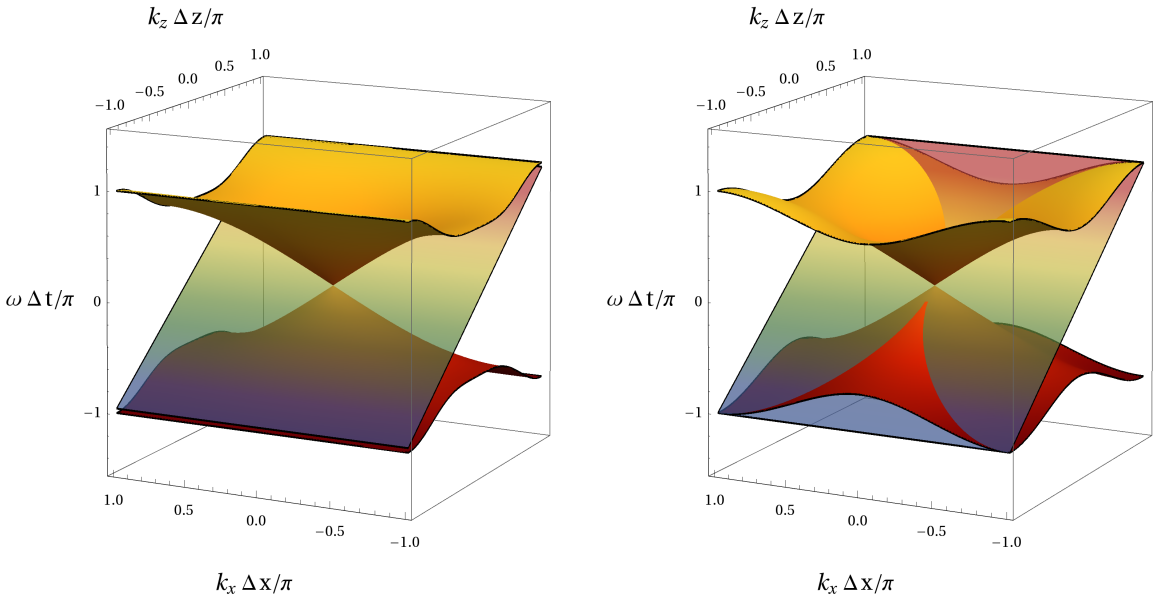

Figure 2.11: Left panel: representation of the dispersion relation given by eq. (2.34) (for $k_y = 0$). Right panel: representation of the dispersion relation for the standard scheme (eq. (2.24)). The translucid plane represents the resonant condition $\omega = vk_z$ (with $v = 0.9999c$).

Finally, an analysis of the modified dispersion relation (eq. (2.34)) reveals that the standard CFL condition should be replaced by the condition

$$\frac{1}{c^2\Delta t^2} \geq \max\left(\frac{1}{\Delta x^2} + \frac{1}{\Delta y^2} \;,\; \frac{1}{\Delta z^2} \right)$$

2.3.2 Presentation of the algorithm for a quasi-cylindrical grid

The quasi-cylindrical numerical scheme of Calder Circ is modified in a similar way as for the Cartesian scheme of Calder 3D. Again the discretization of the Maxwell-Faraday equation is modified, while the Maxwell-Ampère equation is left unchanged. The modified Maxwell-Faraday equation reads

$$\begin{aligned}
\frac{\tilde{B_r}^{n+\frac{1}{2}}_{j,\ell,k+\frac{1}{2}} - \tilde{B_r}^{n-\frac{1}{2}}_{j,\ell,k+\frac{1}{2}}}{\Delta t} &= -\frac{(D^*_\theta \tilde{E}^n_z)_{j,\ell,k+\frac{1}{2}}}{j\Delta r} + (D^*_z \tilde{E}^n_\theta)_{j,\ell,k+\frac{1}{2}} \\
\frac{\tilde{B_\theta}^{n+\frac{1}{2}}_{j+\frac{1}{2},\ell,k+\frac{1}{2}} - \tilde{B_\theta}^{n-\frac{1}{2}}_{j+\frac{1}{2},\ell,k+\frac{1}{2}}}{\Delta t} &= -(D^*_z \tilde{E}^n_r)_{j+\frac{1}{2},\ell,k+\frac{1}{2}} + (D^*_r \tilde{E}^n_z)_{j+\frac{1}{2},\ell,k+\frac{1}{2}} \\
\frac{\tilde{B_z}^{n+\frac{1}{2}}_{j+\frac{1}{2},\ell,k} - \tilde{B_z}^{n-\frac{1}{2}}_{j+\frac{1}{2},\ell,k}}{\Delta t} &= -\frac{(D^*_r r \tilde{E}^n_\theta)_{j+\frac{1}{2},\ell,k}}{(j+\frac{1}{2})\Delta r} + \frac{(D^*_\theta \tilde{E}^n_r)_{j+\frac{1}{2},\ell,k}}{(j+\frac{1}{2})\Delta r}
\end{aligned}$$

where the numerical operator D_z^*, D_θ^* and D_r^* are defined[13] by:

$$
\begin{aligned}
(D_z^* F)_{j',\ell,k'} =& \alpha_z \left(\frac{F_{j',\ell,k'+\frac{1}{2}} - F_{j',\ell,k'-\frac{1}{2}}}{\Delta z} \right) + \delta_z \left(\frac{F_{j',\ell,k'+\frac{3}{2}} - F_{j',\ell,k'-\frac{3}{2}}}{\Delta z} \right) \\
(D_\theta^* F)_{j',\ell,k'} =& \alpha_\theta \left(-i\ell F_{j',\ell,k'} \right) + \beta_{\theta,z} \left(-i\ell F_{j',\ell,k'+1} - i\ell F_{j',\ell,k'-1} \right) \\
(D_r^* F)_{j',\ell,k'} =& \alpha_r \left(\frac{F_{j'+\frac{1}{2},\ell,k'} - F_{j'-\frac{1}{2},\ell,k'}}{\Delta r} \right) \\
& + \beta_{r,z} \left(\frac{F_{j'+\frac{1}{2},\ell,k'+1} - F_{j'-\frac{1}{2},\ell,k'+1}}{\Delta r} + \frac{F_{j'+\frac{1}{2},\ell,k'+1} - F_{j'-\frac{1}{2},\ell,k'+1}}{\Delta r} \right)
\end{aligned}
$$

with the condition

$$
\begin{cases}
\alpha_z + 3\delta_z = 1 \\
\alpha_\theta + 2\beta_{\theta,z} = 1 \\
\alpha_r + 2\beta_{r,z} = 1
\end{cases}
$$

for these operators to be second-order accurate. These operators are represented in figure fig. 2.12. Again, when the β and δ coefficients are zero, this scheme reduces to the standard scheme of Calder Circ.

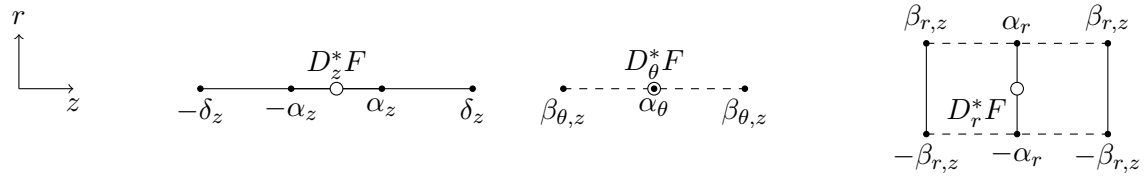

Figure 2.12: Schematic representation of the grid points that are used when calculating $D_z^* F$, $D_\theta^* F$ and $D_r^* F$, along with their respective weights.

As mentioned earlier, the numerical dispersion relation can only be found for waves that propagate along the z axis, and therefore the obtention of the β and δ coefficients is less rigorous than in the Cartesian case. Yet by using a heuristic approach and drawing upon an analogy with the Cartesian case (see appendix B), I proposed the following coefficients

$$
\delta_z = -\frac{1}{4}\left[\frac{\Delta z^2}{c^2 \Delta t^2} \sin^2\left(\frac{\pi c \Delta t}{2 \Delta z} \right) - 1 \right] \qquad \beta_{\theta,z} = \frac{1}{4} \qquad \beta_{r,z} = \frac{1}{4}
$$

which were then found to efficiently suppress the numerical Cherenkov effect in practice (see section 2.4).

2.3.3 Nyquist noise and velocity of the laser pulse

Notice that in both the proposed Cartesian Cherenkov-free algorithm and the proposed quasi-cylindrical algorithm, $c\Delta t/\Delta z$ is a free parameter – insofar as Δt satisfies the modified Courant-Friedrichs-Lewy (CFL) condition. In test simulations, it was found that choosing $c\Delta t/\Delta z = 1$

[13] With these definitions, $(D_r^* r \tilde{E}_\theta^n)_{j+\frac{1}{2},\ell,k}$ can be expressed as $(D_r^* r \tilde{E}_\theta^n)_{j+\frac{1}{2},\ell,k} = \alpha_r \left[(j+1)\, \tilde{E}_{\theta\, j+1,\ell,k}^{\ n} - j \tilde{E}_{\theta\, j,\ell,k}^{\ n} \right] + \beta_{r,z} \left[(j+1)\, \tilde{E}_{\theta\, j+1,\ell,k+1}^{\ n} - j \tilde{E}_{\theta\, j,\ell,k+1}^{\ n} \right] + \beta_{r,z} \left[(j+1)\, \tilde{E}_{\theta\, j+1,\ell,k-1}^{\ n} - j \tilde{E}_{\theta\, j,\ell,k-1}^{\ n} \right]$

leads to a high level of numerical noise at the Nyquist frequency $k_z = \pi/\Delta z$. This is similar to what was observed by Vay et al. [2011], also for $c\Delta t/\Delta z = 1$. Unless it is strongly filtered, this noise rapidly grows to unacceptable levels. Fortunately, reducing $c\Delta t/\Delta z$ was observed to lead to substantial reduction of this noise. In practice, choosing $c\Delta t = 0.96$ is usually sufficient for this noise to remain at a limited level, and in that case filtering is not needed.

On the other hand, the ratio $c\Delta t/\Delta z$ should not be reduced much below the above fiducial value. This is because a low $c\Delta t/\Delta z$ can spuriously modify the velocity of the laser pulse. In fact this holds for both the standard numerical scheme and the Cherenkov-free scheme. Using the numerical dispersion relations of these scheme, it is possible to show that the phase and group velocities of the laser pulse in vacuum are

$$\begin{cases} \dfrac{v_\phi}{c} = 1 - \dfrac{1}{12}\left(1 - \dfrac{c\Delta t}{\Delta z}\right)(k_{\text{laser}}\Delta z)^2 \\ \\ \dfrac{v_g}{c} = 1 - \dfrac{1}{4}\left(1 - \dfrac{c\Delta t}{\Delta z}\right)(k_{\text{laser}}\Delta z)^2 \end{cases} \quad \text{for the standard scheme}$$

$$\begin{cases} \dfrac{v_\phi}{c} = 1 + \dfrac{1}{6}\left(1 - \dfrac{c\Delta t}{\Delta z}\right)(k_{\text{laser}}\Delta z)^2 \\ \\ \dfrac{v_g}{c} = 1 + \dfrac{1}{2}\left(1 - \dfrac{c\Delta t}{\Delta z}\right)(k_{\text{laser}}\Delta z)^2 \end{cases} \quad \text{for the Cherenkov}-\text{free scheme}$$

In the above equations, $\boldsymbol{k} = k_{\text{laser}}\boldsymbol{e}_z$ is the mean wavevector of the laser pulse, and the approximation $k_{\text{laser}}\Delta z \ll 1$ was used (meaning that the wavelength of the laser pulse is well resolved). Importantly, these expressions are valid for both the quasi-cylindrical and Cartesian algorithms.

According to the above relation, the numerical group velocity v_g is lower than c in the standard scheme, and higher than c in the Cherenkov-free scheme. (Physically, the group velocity should be exactly c, and thus both scheme introduce unphysical dispersion.) When simulating laser-wakefield acceleration, it is important to ensure that the numerical alteration of the group velocity ($|v_g - c| \sim (1 - c\Delta t/\Delta z)(k_{\text{laser}}\Delta z)^2$) is negligible compared to the physical alteration caused by the plasma ($|v_g - c| \sim k_p^2/k_{\text{laser}}^2$). In other words, the criterion

$$1 - \frac{c\Delta t}{\Delta z} \ll \frac{k_p^2}{k_{\text{laser}}^4 \Delta z^2}$$

should be satisfied, and this prevents $c\Delta t/\Delta z$ from being too far from 1.

In conclusion of this section, the choice of $c\Delta t/\Delta z$ is a tradeoff between reducing the Nyquist noise and limiting the alteration of the laser velocity. Once this parameter is well chosen, the proposed algorithm appears to be a good solution to the numerical Cherenkov effect, and one which does not require additional numerical filtering. This is confirmed in the next section.

2.4 Validation of the algorithm and implications for LWFA simulations

2.4.1 Validation of the Cherenkov-free algorithm

In order to validate the proposed algorithm, the simulations of section 2.2.2 were re-run with the Cherenkov-free algorithm. The same physical and numerical parameters were used for these simulations, and in particular the value of the ratio $c\Delta t/\Delta z$ was also 0.96.

Figure 2.13 compares the standard and Cherenkov-free algorithms in the case of the Calder 3D simulation. On a global level, the aspect of the laser pulse and of the accelerating cavity is very similar (see the left panels), but the laser pulse has a slight advance ($\sim 1\,\mu$m) in the case of the Cherenkov-free algorithm. This advance is due to the numerical dispersion relation, which was shown to increase the laser speed in the Cherenkov-free scheme and decrease it in the standard scheme. Apart from this slight difference in velocity, the physics of the simulation is the same with both algorithm, and in particular the self-injected charge differs by less than 5 %.

Important differences are however observed when zooming on the accelerated bunch (right panels). First, a trailing high-frequency noise is observed in the case of the Cherenkov-free scheme. This is the Nyquist noise which was observed also by Vay et al. [2011]. Here I did not attempt to filter this noise, but it nonetheless remains at a relatively low level. (Again, this is a consequence of $c\Delta t/\Delta z < 1$.) The main result however is that the numerical Cherenkov radiation is entirely eliminated in the case of the proposed algorithm. Since no numerical filtering was used here, this is entirely due to the modified numerical dispersion relation. On the whole, the fact that the numerical Cherenkov radiation was suppressed without affecting the rest of the physics validates the proposed Cherenkov-free algorithm.

Figure 2.14 shows the evolution of the transverse emittance in both schemes. The spurious growth of emittance is substantially reduced with the Cherenkov-free algorithm. This confirms that the observed growth of emittance was partly caused by the unphysical Cherenkov radiation, which randomly scattered the electrons of the bunch. However it is unclear what causes the remaining growth of emittance (that which subsists with the Cherenkov-free algorithm). The corresponding variation of emittance ($\Delta\epsilon \approx 1\,$mm.mrad) is still above the theoretical estimates introduced in section 2.2.2, and thus we suspect that it is unphysical.

Similar results are obtained in the case of the Calder Circ simulation. Figure 2.15 represents a snapshot of the simulation with both schemes. Again the laser pulse and the cavity are nearly identical in both schemes, and the injected charge was observed to differ by less than 10 %. The right panels show that the Cherenkov radiation is entirely suppressed by the proposed algorithm. This comes at the cost of some additional noise on-axis. This noise might be due to the fact that the on-axis boundary conditions of Calder Circ may not be well adapted to the modified numerical scheme. At any rate, this noise seems to have little impact on the physics at stake here. This is confirmed by the plots of the emittance in fig. 2.16. This figure shows that the emittance is almost constant in the case of the Cherenkov-free scheme, which is what is expected physically. (The fact that the emittance is constant in the Cherenkov-free Calder Circ simulation but still grows in the Cherenkov-free Calder 3D simulation may be due to the higher resolution of the Calder Circ simulation.) The results of fig. 2.16 imply that the growth of emittance in the standard scheme was entirely due to the numerical Cherenkov radiation.

Since the proposed Cherenkov-free algorithms have proved to have an overall beneficial impact on the simulations, they have been permanently added as an option in the codes Calder 3D and Calder Circ. In addition, the Cartesian Cherenkov-free algorithm was implemented in the PIC codes Osiris and PIConGPU, through collaborations with research teams at the Instituto Superior Técnico (Lisbon) and at the Helmholtz-Zentrum Dresden-Rossendorf (Dresden) respectively. This algorithm and its impact on emittance also lead to a recent publication [Lehe et al., 2013].

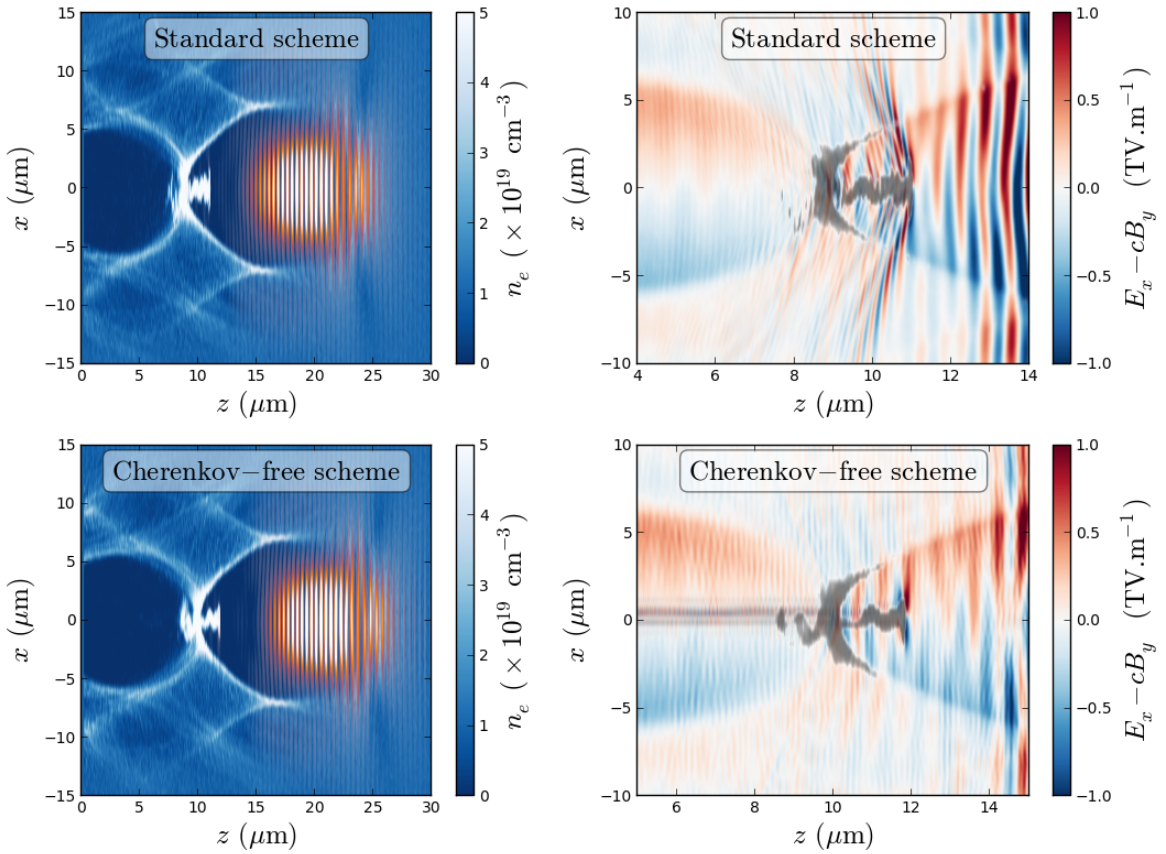

Figure 2.13: Snapshot of the Calder 3D simulation after 250 μm of acceleration, in the case of the standard algorithm and of the Cherenkov-free algorithm.

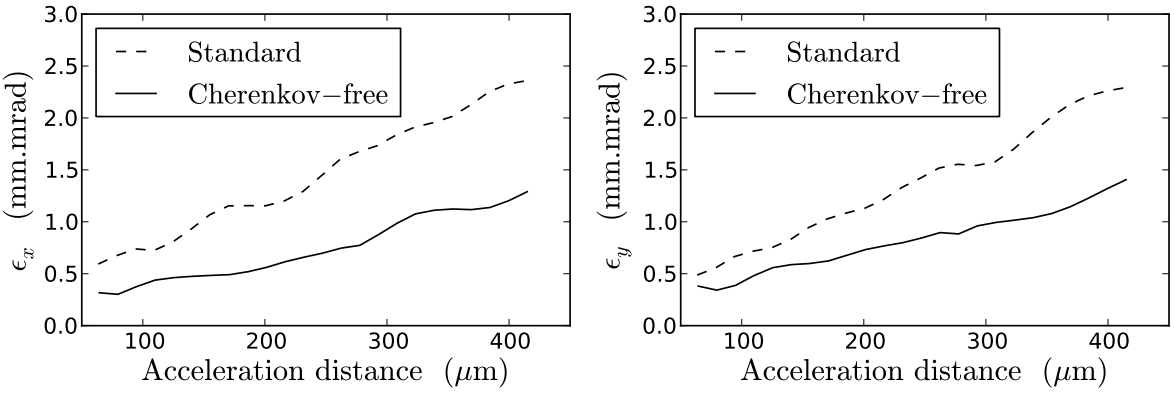

Figure 2.14: Evolution of the emittance in the Calder 3D simulation, for the bunch defined in fig. 2.7. The emittance along the x (left panel) and y (right panel) direction are represented, and the standard algorithm (dashed line) and Cherenkov-free algorithm (solid line) are compared.

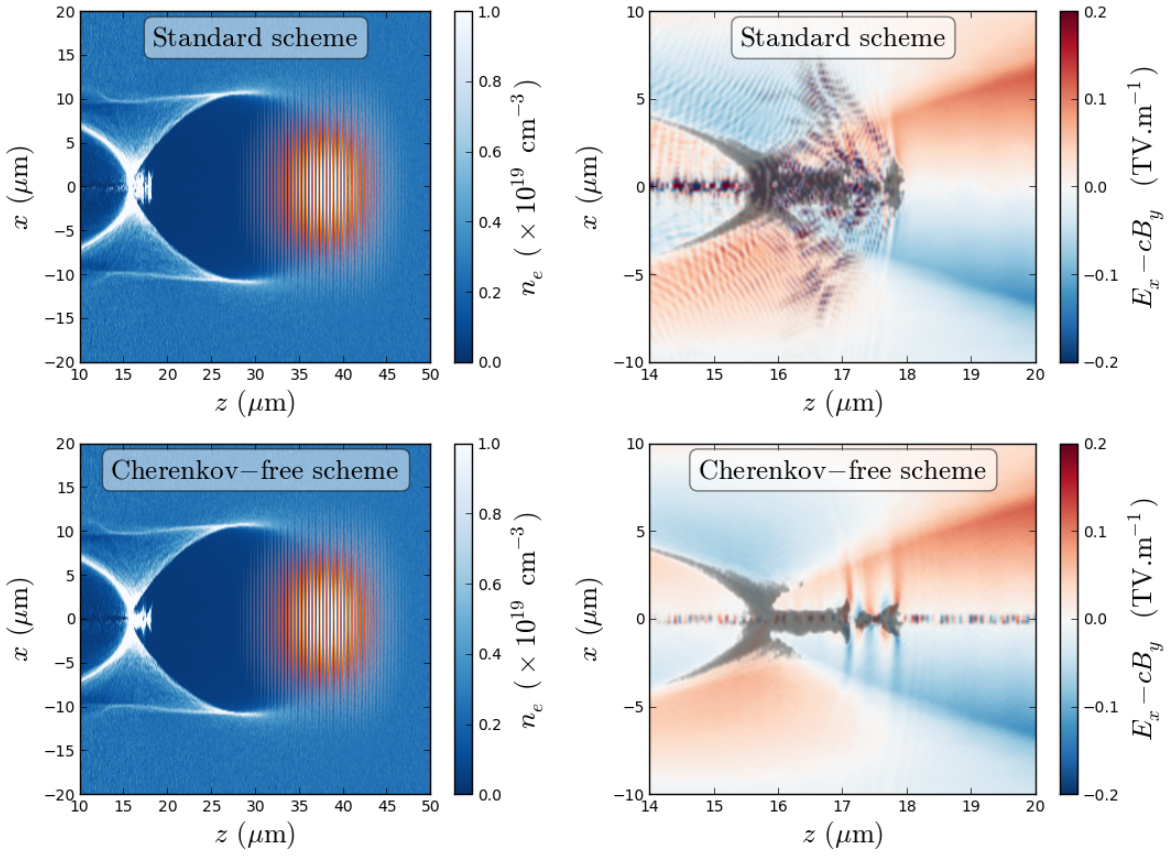

Figure 2.15: Snapshot of the Calder Circ simulation after 300 μm of acceleration, in the case of the standard algorithm and of the Cherenkov-free algorithm.

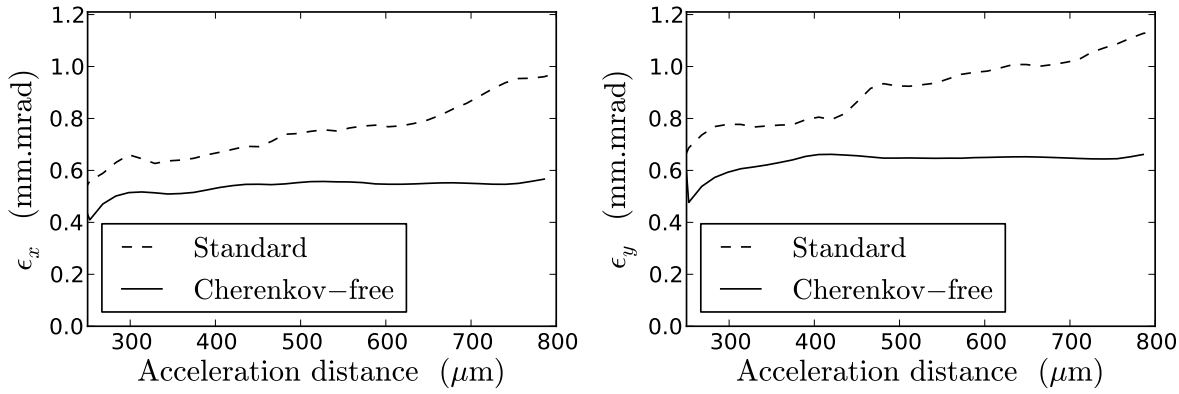

Figure 2.16: Evolution of the emittance in the Calder Circ simulation, for the bunch defined in fig. 2.9. The emittance along the x (left panel) and y (right panel) direction are represented, and the standard algorithm (dashed line) and Cherenkov-free algorithm (solid line) are compared.

2.4.2 Implications of the spurious growth of emittance

The results of the previous section prove that the growth of emittance in standard PIC simulations is largely unphysical (since it is partly due to unphysical Cherenkov radiation). This implies that standard PIC codes tend to spuriously overestimate the final emittance of the bunch. This artifact has important implications, that must be kept in mind when analyzing the results of the simulations.

For instance, as a direct consequence of this artifact, the transverse size and divergence of the beam also tend to be overestimated by the simulations. This is a serious issue, since the size and divergence of the beam are crucial parameters for many applications of LWFA (including for instance prospective linear colliders, phase-contrast imagers and free electron lasers). The divergence of the beam is also paramount when designing a Compton source (e.g. [Ta Phuoc et al., 2012]), i.e. a source in which a counterpropagating laser pulse collides with the relativistic electrons in order to produce X-ray radiation. In these sources, the wavelengths emitted by each individual electron are directly related to the angle of propagation of the electron considered. Therefore, in PIC simulations of Compton sources, the unphysically high divergence may result in an spuriously broad spectrum.

Finally, the divergence and size of the beam are even more crucial when estimating the emitted betatron radiation (see section 1.2.2). This is because, in the case of betatron radiation, the size and divergence also determine the wiggling parameter of the trajectory (e.g. [Corde et al., 2013a]). In order to illustrate this point, the emitted betatron radiation was calculated for the Calder Circ simulations of the previous section. This is done for both the simulation with the standard scheme and that with the Cherenkov-free scheme. In both cases, the energy emitted per unit frequency and solid angle $\frac{d^2I}{d\omega d\Omega}$ is calculated by using a post-processing code developed by Igor Andriyash (which numerically evaluates eq. (1.41)).

The results are shown in fig. 2.17 and fig. 2.18. In the case of the standard scheme (spuriously growing emittance), the radiation appears to have a wider angular spread than with the Cherenkov-free scheme (constant emittance). This is a direct consequence of the larger divergence in the standard scheme. In addition, the radiation extends to higher photon energies in fig. 2.17, which is a consequence of the higher wiggling parameter. On the whole, the total emitted energy seems to be higher in the case of the standard scheme, and the numerical calculation indeed reveals that it is about *twice* larger than in the Cherenkov-free scheme. These results show that the spurious growth of emittance in PIC codes can directly lead to a gross overestimation of the betatron radiation.

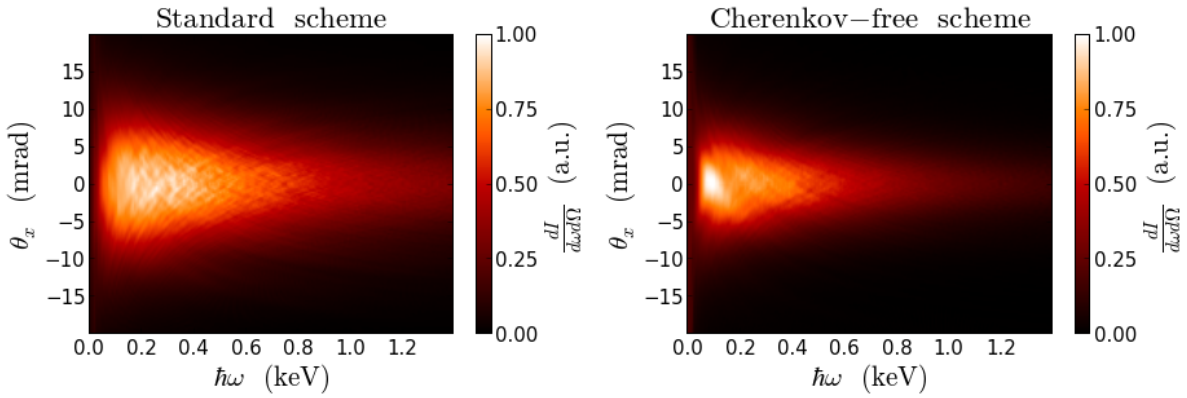

Figure 2.17: Representation of the emitted betatron energy per unit frequency and solid angle $\frac{d^2I}{d\omega d\Omega}$ in the $x-z$ plane. θ_x represents the angle between the z axis and the line of sight. The colorscale is the same on the left and right panel.

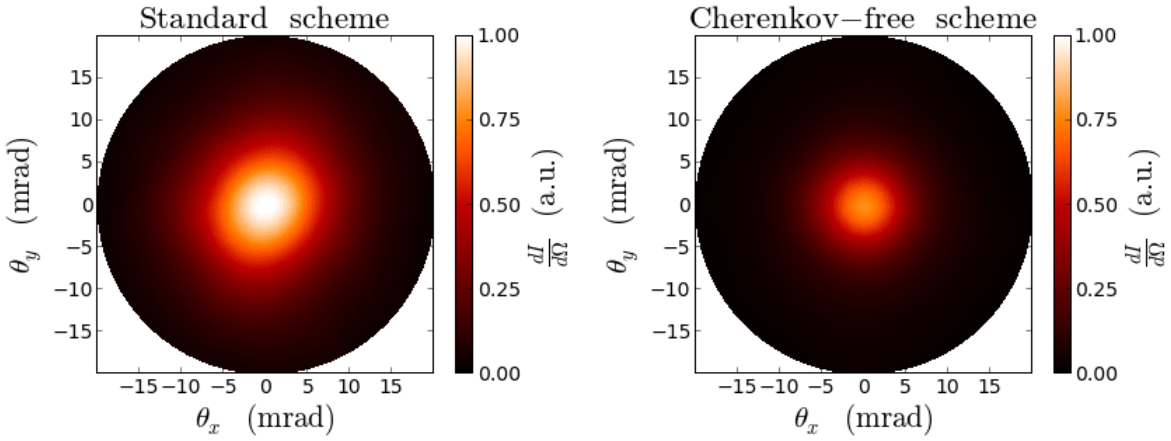

Figure 2.18: Representation of the betatron profile $\frac{dI}{d\Omega}$ $\left(\equiv \int \frac{d^2I}{d\omega d\Omega} d\omega\right)$. θ_x and θ_y are the angle between the z axis and the line of sight. The colorscale is identical on the left and right panel.

Chapter 3

Optical transverse injection

This chapter focuses on an interesting new mechanism of injection. Injection is a decisive step in a laser-wakefield accelerator as it largely determines the quality of the accelerated bunch. After briefly reviewing the different existing methods of injection, I show numerical evidence for a new mechanism of colliding-pulse injection – which is referred to here as *optical transverse injection*. In fact, previously known mechanisms of colliding-pulse injection were essentially longitudinal and conceptually relied on a small, local perturbation of the wakefield. On contrary, optical transverse injection is transverse in nature and relies on a global expansion of the whole accelerating cavity. Moreover, by using the Cherenkov-free algorithm of chapter 2, it is shown that this injection mechanism can lead to high-quality bunches, which are characterized in particular by a very low emittance.

Contents

3.1 Injection in the laser-wakefield

Injection was introduced in section 1.2.1, and consists in modifying the trajectory of some electrons so that they can remain inside the accelerating part of the wakefield instead of slipping through it. The injection process is in fact a crucial step in a laser-wakefield accelerator, since it determines several important properties of the accelerated bunch. For instance, the charge of the bunch is determined at the time of injection and, insofar as emittance is conserved during the acceleration, so is the transverse quality of the bunch. Moreover, injection determines the initial energy spread and duration of bunch, which then largely determines the final energy spread at the exit of the accelerator.

Thus all these properties crucially depend on the particular method of injection that is used, in a given experiment. From the conceptual point of view, the different methods of injection can be divided into two categories: those that rely on a *local perturbation* of an otherwise stationary wakefield, and those that rely on a *global deformation* of the wakefield. The next sections give a brief overview of these two categories.

3.1.1 Injection by a local perturbation in a stationary wakefield

In this type of injection, a local perturbation is applied to the wakefield and thus only a small fraction of the electrons have their trajectories modified, while the other electrons are unaffected. In particular, the wakefield as a whole is considered to remain stationary throughout the perturbation, and in particular its fields $\phi, \psi, \boldsymbol{a}$ depend on z and t only through $z - c\beta_p t$ where β_p is the group velocity of the driving pulse[1]. Moreover, the perturbation is usually maximal on axis, and as a consequence, the injected electrons originate mostly from on-axis positions. Therefore their motion in the wakefield is essentially longitudinal, i.e. their transverse momentum and transverse position can be neglected ($u_x, u_y \simeq 0$, $x, y \simeq 0$).

In these conditions, the trajectory of each electron is determined only by two variables: its longitudinal momentum u_z and its longitudinal position in the stationary wakefield $z - c\beta_p t$. These trajectories can thus be plotted in a two-dimensional phase space $(z - c\beta_p t\,,\, u_z)$, and, as explained in the next paragraphs, injection is determined by a two-dimensional separatrix within this phase space.

Injection and the separatrix. In fact, with the above hypotheses, the trajectories of the electrons in the phase space $(z - c\beta_p t\,,\, u_z)$ can be calculated analytically. In the absence of any perturbation, it is indeed possible to show[2] that each trajectory is characterized by a constant of motion $\mathcal{H}$, which reads

$$\mathcal{H} = \gamma - \beta_p u_z - (\phi - \beta_p a_z) \quad \simeq \gamma - \beta_p u_z - \psi \tag{3.1}$$

where γ and u_z are the slow components (i.e. averaged over one laser period) of the Lorentz factor and of the longitudinal momentum, and are related by $\gamma = \sqrt{1 + \langle \boldsymbol{a}_l^2 \rangle + u_z^2}$. Similarly, ϕ and $\boldsymbol{a}$ are the slow components of the dimensionless scalar and vector potential in the wakefield, and $\psi = \phi - a_z$. Notice that, in the right-hand side of eq. (3.1), β_p was approximated to 1 in the term $(\phi - \beta_p a_z)$. It is however possible to use the same approximation for $\gamma - \beta_p u_z$, since u_z

[1] Notice here that, although the pulse was considered to propagate at the speed of light ($\beta_p = 1$) in section 1.1.2, here we take into account the fact that its group velocity inside the plasma is actually lower ($\beta_p \lesssim 1$). Even though this slight difference between 1 and β_p has little impact on the calculation of the fields $\phi, \psi, \boldsymbol{a}$ of section 1.1.2, it is however paramount when calculating the trajectories of the injected electrons.

[2] This is a consequence of the Noether theorem, for a stationary wakefield propagating at the velocity β_p.

can be very to close to γ for a high-energy electron, and thus the difference between β_p and 1 is important in this particular expression.

Once ψ is known in the wakefield, the trajectories of the electrons in phase space can be obtained[3] from eq. (3.1). These trajectories are shown in fig. 3.1 for different values of $\mathcal{H}$. The blue trajectory corresponds to $\mathcal{H} = 1$, while the gray trajectories correspond to $\mathcal{H} < 1$. In some of these trajectories (those enclosed within the black curve), the electron can go from a low energy ($u_z \sim 1$) to a high energy ($u_z \sim 200$). These trajectories are those in which the electron is trapped in the wakefield and accelerated. However, because the electrons of the plasma are all at rest before the laser reaches them, they all have $\mathcal{H} = 1$ initially, and thus they all follow the blue trajectory. In this trajectory, the electrons simply slip through the wakefield, and the variations of their momentum u_z corresponds to the longitudinal plasma oscillations of the wakefield.

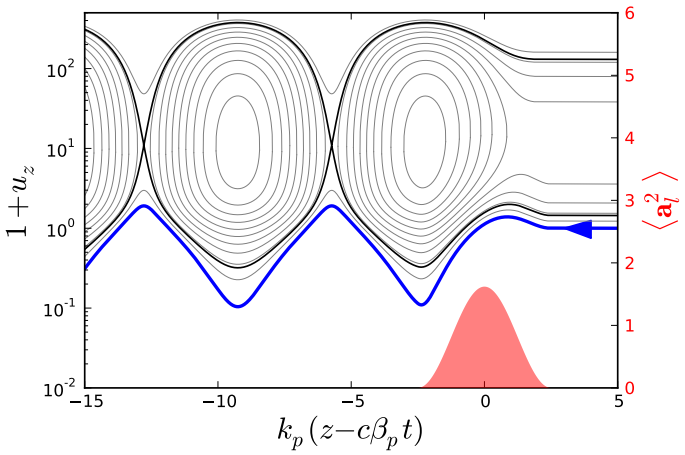

Figure 3.1: Representation of the possible trajectories for the electrons inside the wakefield, in the phase space $(z - c\beta_p t\,,\, u_z)$. (In order to be able to display both the low negative values and high positive values of u_z, the left axis represents $1 + u_z$ in logarithmic scale.) The red curve represents the amplitude $\langle \boldsymbol{a}_l^2 \rangle$ of the laser pulse (see the right axis). The black line corresponds to the separatrix, while the blue line represents the trajectory followed by the electrons that are initially at rest ($\mathcal{H} = 1$).

The black curve – which is known as the *separatrix* – separates the trajectories for which the electrons are accelerated from the trajectories for which they slip through the wakefield. Thus the injection process consists in modifying the motion of some of the plasma electrons, in such a way that they cross the separatrix. This is what happens for instance in ionization injection, and in warm and cold optical injection.

Ionization injection. In ionization injection [Pak et al., 2010; McGuffey et al., 2010], this modified motion is due to the fact that some electrons can be separated from their atoms much later than the others. In order to provoke this effect, a small amount of high-Z gas (such as N_2)

[3] More precisely, eq. (3.1) can be combined with the relation $\gamma = \sqrt{1 + \langle \boldsymbol{a}_l^2 \rangle + u_z^2}$ to yield

$$u_z = \gamma_p^2 \left[\beta_p(\mathcal{H} + \psi) \;\pm\; |\mathcal{H} + \psi| \sqrt{1 - \frac{1 + \langle \boldsymbol{a}_l^2 \rangle}{\gamma_p^2 (\mathcal{H} + \psi)^2}} \right]$$

where $\gamma_p = 1/\sqrt{1 - \beta_p^2}$. It is this expression which is plotted in fig. 3.1.

is mixed with the usual low-Z gas of the gas jet (H_2 or He). The low-Z atoms, as well as the L-shell of the high-Z atoms, are ionized well ahead of the peak of the pulse. However the K-shell of the high-Z atoms has a higher ionization potential, and it is ionized only later, near the peak of the pulse.

The trajectory of the electrons that originate from this shell is represented in fig. 3.2. In this figure, the dashed blue line represents the trajectory of an electron while it is still attached to an only partially-ionized ion. Since this ion is very heavy, its momentum is not significantly modified by the ponderomotive force of the laser ($u_z \simeq 0$). At some point, the K-shell of this ion is finally ionized (red dot in fig. 3.2). When this happens, the electron can be released inside the separatrix, and it can then be accelerated by the wakefield.

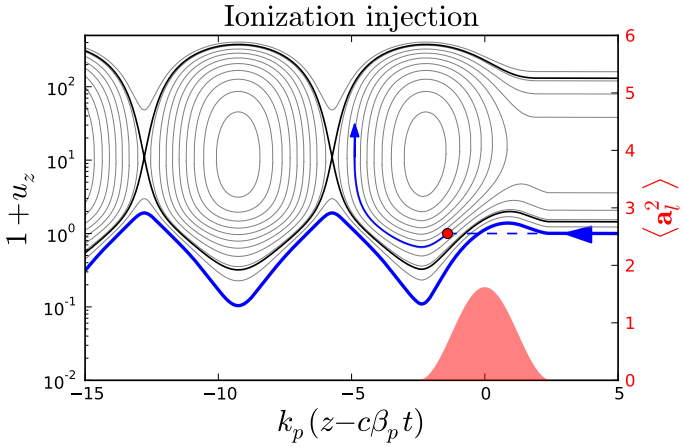

Figure 3.2: Schematic representation of ionization injection. The blue dashed curve corresponds to the trajectory of a partially-ionized ion, and the red dot marks the position were it becomes fully ionized. The subsequent trajectory of the released electron is represented by a thin blue line.

Although ionization injection is relatively easy to implement experimentally, it suffers from the fact that new electrons are continuously being injected by this process, as the driving laser propagates through the gas jet. This continuous injection typically results in a large energy spread for the final electron bunch. This is because the electrons that are injected at the beginning of the jet are accelerated for a longer time than those that are injected at the end of the jet. Thus, although some solutions have been suggested in order to avoid this problem [Pollock et al., 2011; Bourgeois et al., 2013], ionization injection is not naturally well-adapted for low energy spreads.

Warm and cold optical injection. In optical injection, a second laser pulse is used in order to locally perturb the wakefield. In this case, the time of interaction between this *injection pulse* and the wakefield is usually very short. As a consequence, the injection is localized in time and can thus result in a low energy spread.

The first theoretical works on optical injection proposed to use two othogonally crossing pulses [Umstadter et al., 1996b] or two copropagating pulses and an additional counter-propagating pulse [Esarey et al., 1997; Schroeder et al., 1999]. However, the geometry that is now perhaps most commonly considered – and the first one which was successfully implemented in experiments [Faure et al., 2006] – is that of two colliding pulses [Fubiani et al., 2004; Kotaki et al., 2004]. In this colliding-pulse geometry, the first pulse is a high-intensity pulse which drives the wakefield,

while the second pulse is a relatively low-intensity counter-propagating pulse. The polarizations of the pulses are chosen to be either both linear and parallel or both circular and opposite, so that they can produce a standing interference pattern as they overlap. When neglecting the envelopes of the pulses, the total laser field can indeed be written as

$$\begin{aligned}\boldsymbol{a}_l =& a_0[\,\sqrt{1-\epsilon}\cos(k_0 z-\omega_0 t)\boldsymbol{e}_x+\sqrt{\epsilon}\sin(k_0 z-\omega_0 t)\boldsymbol{e}_y\,]\\ &+a_1[\,\sqrt{1-\epsilon}\cos(k_0 z+\omega_0 t)\boldsymbol{e}_x-\sqrt{\epsilon}\sin(k_0 z+\omega_0 t)\boldsymbol{e}_y\,]\end{aligned} \tag{3.2}$$

where a_0 and a_1 are the amplitude of the driving pulse and the injection pulse respectively, and where $\epsilon \in [0,1]$ determines their polarizations (linear and parallel for $\epsilon = 0$ or $\epsilon = 1$; circular and opposite for $\epsilon = 0.5$). In this case, the intensity pattern is

$$\langle \boldsymbol{a}_l^2 \rangle = \frac{a_0^2+a_1^2}{2} + a_0 a_1 \cos(2k_0 z)$$

and corresponds to a standing modulated intensity as a function of z. This modulated pattern induces a longitudinal ponderomotive force, which pushes the electrons away from the local maxima of intensity. This force which can have two effects on the motion of the plasma electrons.

The first effect is to trap the electrons in the minima of the intensity pattern. As a consequence, instead of being pushed forward by the ponderomotive force of the envelope (see the increase of u_z at the position of the laser, for the blue curve of fig. 3.3), they remain on averge at a fixed z position ($\langle u_z \rangle \simeq 0$). Note that, when the electrons are trapped by the intensity pattern, they typically oscillate around this average fixed z, and thus their momentum u_z oscillates on a short timescale. However – for circularly polarized pulses – once the collision of the pulses is over, the electrons leave the driving pulse with no net gain in momentum [Davoine et al., 2010]. Thus the first possible effect of the pulse collision is to *dephase* the electrons with respect to the wakefield, with no net momentum gain. (This is represented by a red arrow in the left panel of fig. 3.3.) As a result, the electrons can cross the separatrix, and they can be accelerated by the wakefield. This mechanism is known as *cold optical injection* [Davoine et al., 2009].

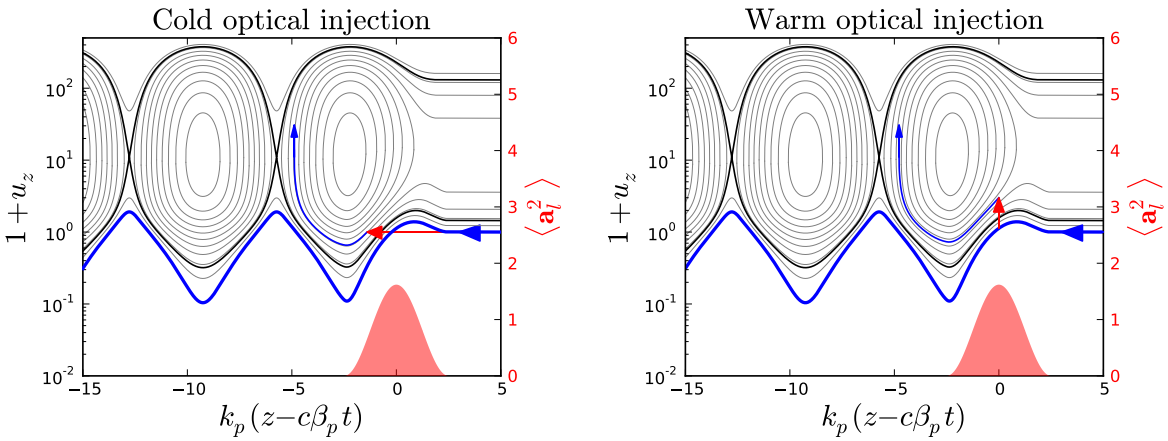

Figure 3.3: Schematic representation of cold optical injection (left panel) and warm optical injection (right panel). The red arrows represents the pertubation of the motion of some electrons, during the collision of the two laser pulses. *(Adapted from [Davoine et al., 2010]).*

In the case of a linearly-polarized pulse however, the ponderomotive force can have second effect. Due to the complex motion of the electrons in a linearly-polarized pulse (e.g. [Rax, 1992]),

the electrons can experience *stochastic heating* in the modulated intensity pattern [Sheng et al., 2002; Fubiani et al., 2004]. As a result, the electrons can gain a net momentum, as they are being dephased. Thus, depending on the intensity of this heating and depending on the vertical position of the separatrix, the electrons can also cross the separatrix vertically – in which case the mechanism is known as *warm optical injection* (see the right panel of fig. 3.3). Notice that, if on the other hand this heating is too weak or if the separatix is too high vertically (which is the case at low density), the cold injection mechanism can still happen with linearly polarized pulses [Davoine et al., 2010].

3.1.2 Injection through a global deformation of the wakefield

In the mechanisms of the previous section, it was assumed that only a small fraction of the electrons was perturbed and that their motion was essentially longitudinal. As a consequence, it was possible to interpret the injection by using a separatrix in a two-dimensional phase space. However, this is no longer valid for the injection methods in which the wakefield *as a whole* is considerably affected. In this case, it is not possible to use the separatrix for two reasons. Firstly, some of the injected electrons can have a substantial transverse motion, and as a consequence, their trajectory is not determined only by $z-c\beta_p t$ and u_z, but rather by the full three components of $\boldsymbol{r}$ and the full three components of $\boldsymbol{u}$. As a consequence, the separatrix is a five-dimensional hypersurface within a six-dimensional space, and cannot be represented anymore in the two-dimensional phase space $(z - c\beta_p t\,,\, u_z)$. Secondly, the wakefield is not stationary anymore, and thus the stucture of the phase-space trajectories evolves in time. In particular, the shape of the separatrix evolves in time and it cannot be represented on a stationary plot.

For these methods of injection, the mechanism is thus interpreted differently. In fact in these methods, the global deformation of the wakefield usually corresponds to a *transient expansion* of the plasma period (in the linear regime) or of the ion cavity (in the blow-out regime). As mentioned in section 1.2.1, the electrons that travel through the wakefield at the time of this expansion can then remain slightly longer inside the accelerating region. They can thereby acquire a high enough velocity for them to permanently remain in this region, instead of slipping through it. Note that this qualitative explanation can be cast into a more quantitative formalism, so as to derive the minimal rate of expansion that allows injection (see [Kalmykov et al., 2009; Kostyukov et al., 2010; Yi et al., 2011]). On the whole, this formalism confirms that an expanding cavity can trigger injection. Experimentally, the expansion of the cavity can be caused by different effects, which thus correspond to different methods of injection.

Longitudinal and transverse self-injection. As mentioned in section 1.2.1, the expansion of the cavity can occur *spontaneously* under certain experimental conditions. If the plasma density is high enough ($n_0 \sim 10^{19}\,\mathrm{cm}^{-3}$), then the laser pulse self-focuses as it propagates in the gas jet, and its peak amplitude a_0 correspondingly increases. In the blow-out regime, this increase in a_0 leads to stronger ponderomotive force, and thus to a larger ion cavity. (As mentioned in section 1.1.4, the length of the cavity scales as $4k_p^{-1}\sqrt{a_0}$.[4]) The injection associated with this expansion of the cavity is known as *self-injection*.

[4]Note that, even when the wakefield is not in the blow-out regime (i.e. when the waist of the laser w is much larger than $2k_p^{-1}\sqrt{a_0}$; see section 1.1.4), the plasma period still increases with a_0 [Esarey et al., 2009]. In this case, the lengthening of the plasma period is not directly due to the transverse ponderomotive force, but rather to nonlinear relativistic effects. (Note that these nonlinear effects were not taken into account in the linear model of section 1.1.3.) Thus, in this regime also, a sudden increase in a_0 can lead to injection.

This effect is illustrated in fig. 3.4, which shows the results of a PIC simulation published in [Corde et al., 2013b]. In this simulation, a 30 fs laser pulse with an initial a_0 of 2 propagates through a gas jet with $n_0 \simeq 1 \times 10^{19}\,\mathrm{cm}^{-3}$. The left panel of fig. 3.4 shows the variations of a_0 during this propagation. In this panel, a_0 first rises (as a consequence of self-focusing) and then exhibits several oscillations (due to a competition between self-focusing and the natural diffraction of the pulse). As predicted by the above mechanism, self-injection is observed only when a_0 increases.

In addition, this simulation shows that the variations of a_0 can produce both longitudinal and transverse injection. In longitudinal injection (middle panel of fig. 3.4), the injected electrons are originally on-axis, and they go through the wakefield without a substantial transverse motion. On the contrary, in transverse injection (right panel), the electrons originate from off-axis positions, and they travel along the sheath and around the cavity before being injected. Thus, although the trajectories were essentially longitudinal in the case of a local perturbation (section 3.1.1), this figure shows that the injected trajectories can be transverse in the case of a global perturbation. In fact, transverse injection largely dominates over longitudinal injection in the case of fig. 3.4. The simulation indeed reveals that transverse injection leads to a 200 pC bunch whereas longitudinal injection leads only to 2 pC.

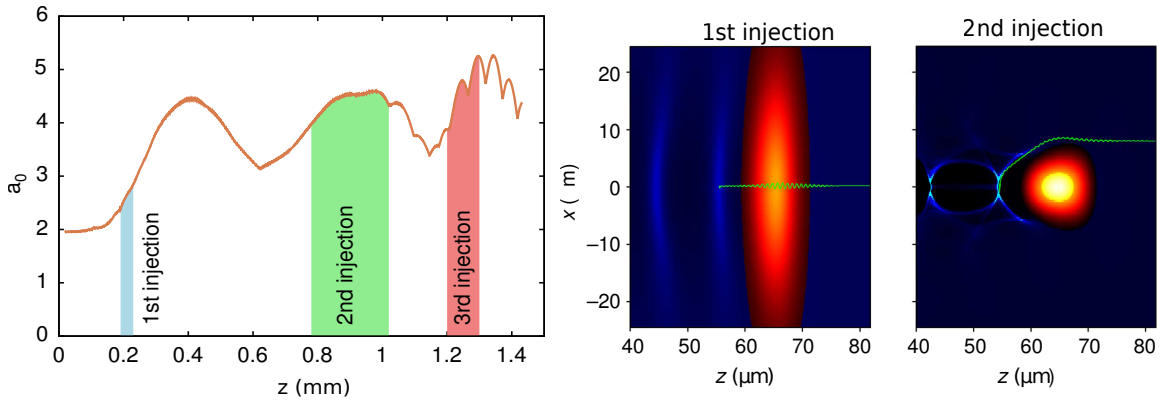

Figure 3.4: Results from a PIC simulation of self-injection. Left panel: Evolution of a_0 as the laser propagates in the gas jet. The colored areas correspond to several successive self-injections. Middle and right panels: representation of the aspect of the wakefield and of a typical injection trajectory during the first (middle panel) and second (right panel) injections. *From [Corde et al., 2013b].*

On the whole, the advantage of self-injection is that it is easy to obtain experimentally, since it can occur spontaneously. However, as suggested from the erratic variations of a_0 in fig. 3.4, self-injection is intrinsically difficult to control, and therefore it lacks stability. For this reason, it is sometimes preferable to controllably trigger the expansion of the ion cavity.

Density ramp injection. One way through which this expansion can be controlled is by forming a density downramp in the gas jet [Bulanov et al., 1998]. Because the length of the cavity scales as $4k_p^{-1}\sqrt{a_0}$ ($\propto n_0^{-1/2}$), the cavity expands as the laser pulse propagates into a lower density, and thus injection can occur. Notice that this mechanism is also possible in the linear regime, since the length of the plasma period in this regime is also proportional to $n_0^{-1/2}$.

The density downramp can correspond to the natural gradient at the end of the gas jet [Gonsalves et al., 2011; Geddes et al., 2008] or it can be purposedly created and tailored inside the gas jet. This has been done for instance by placing a knife edge [Schmid et al., 2010] or a thin wire [Burza et al., 2013] inside the gas jet, as well as by triggering a local thermal expansion with a second, transversely-propagating laser pulse [Chien et al., 2005; Faure et al., 2010].

Magnetic gradient injection. Another way to trigger a deformation of the cavity is through an external, transverse magnetic field [Vieira et al., 2011, 2012]. A transverse magnetic field can indeed induce an asymmetric deformation of the cavity. (In this case, one side of the cavity is shorter than the other.) Thus, when the laser pulse propagates in a magnetic downramp, this deformation progressively relaxes. As a result, one side of the cavity expands and triggers an asymmetric injection.

3.2 The mechanism of optical transverse injection

According to the previous section, several situations can lead to an expansion of the accelerating cavity and to a subsequent injection, but the situation of two colliding laser pulses was not considered to be one of them. As explained in section 3.1.1, the mechanism of colliding-pulse injection is indeed generally considered to happen in a *stationary wakefield*, which is only locally perturbed by the injection pulse. This is somewhat mitigated by the fact that, in some situations of colliding-pulse injection, the wakefield was observed to be non-stationary [Rechatin et al., 2007]. Yet in these cases, the deformation of the wakefield tends to prevent the injection rather than to enhance it – due to an effect known as *wakefield inhibition*.

On the contrary, it is shown here that there is a regime in which the accelerating cavity is strongly affected by the pulse collision, and in which this deformation leads to a new type of injection. In this regime, the colliding pulse indeed induces a transient expansion of the cavity, which then naturally triggers injection. This regime is thus considerably different from the previously-known mechanisms of optical injection, and in particular it leads to a transverse injection instead of a longitudinal one. For this reason, this new regime is referred to as *optical transverse injection* in the rest of this section.

3.2.1 Injection due to an expansion of the cavity

In order to illustrate this regime, fig. 3.5 shows the evolution of the cavity in a corresponding PIC simulation. This PIC simulation was run with the quasi-cylindrical code Calder Circ, using two azimuthal modes ($\ell = 0$ and $\ell = 1$) and a resolution defined by $\Delta z = 0.016\,\mu$m, $\Delta r = 0.16\,\mu$m and $c\Delta t = 0.96\Delta z$. Moreover, in order to avoid the spurious growth of emittance associated with the numerical Cherenkov effect, the Cherenkov-free algorithm of section 2.3.2 was used. In this simulation, a 1.0 J laser pulse with an FWHM duration $\tau_0 = 30\,$fs is focused to a waist $w_0 = 7.7\,\mu$m inside a gas jet of density $n_0 = 1.75 \times 10^{18}\,\mathrm{cm}^{-3}$. With these parameters, this laser pulse drives a strong, blown-out wakefield in the gas jet. Near its focal plane, this pulse collides with a counter-propagating pulse having the same waist and duration ($\tau_1 = \tau_0$, $w_1 = w_0$), but a much lower amplitude and thus a lower energy (2.5 mJ). The driving pulse and the counter-propagating pulse have opposite circular polarizations (i.e. their fields correspond to eq. (3.2) with $\epsilon = 0.5$), with $a_0 = 4$ and $a_1 = 0.2$ respectively. As a consequence, they produce a standing intensity modulation as they overlap. For convenience, the above parameters are grouped in table 3.1.

	Laser energy	FWHM duration	Waist at focus	Amplitude at focus
Driving pulse	1.0 J	$\tau_0 = 30\,\mathrm{fs}$	$w_0 = 7.7\,\mu\mathrm{m}$	$a_0 = 4$
Injection pulse	2.5 mJ	$\tau_1 = 30\,\mathrm{fs}$	$w_1 = 7.7\,\mu\mathrm{m}$	$a_1 = 0.2$

Table 3.1: Parameters of the two laser pulses in the PIC simulation of fig. 3.5.

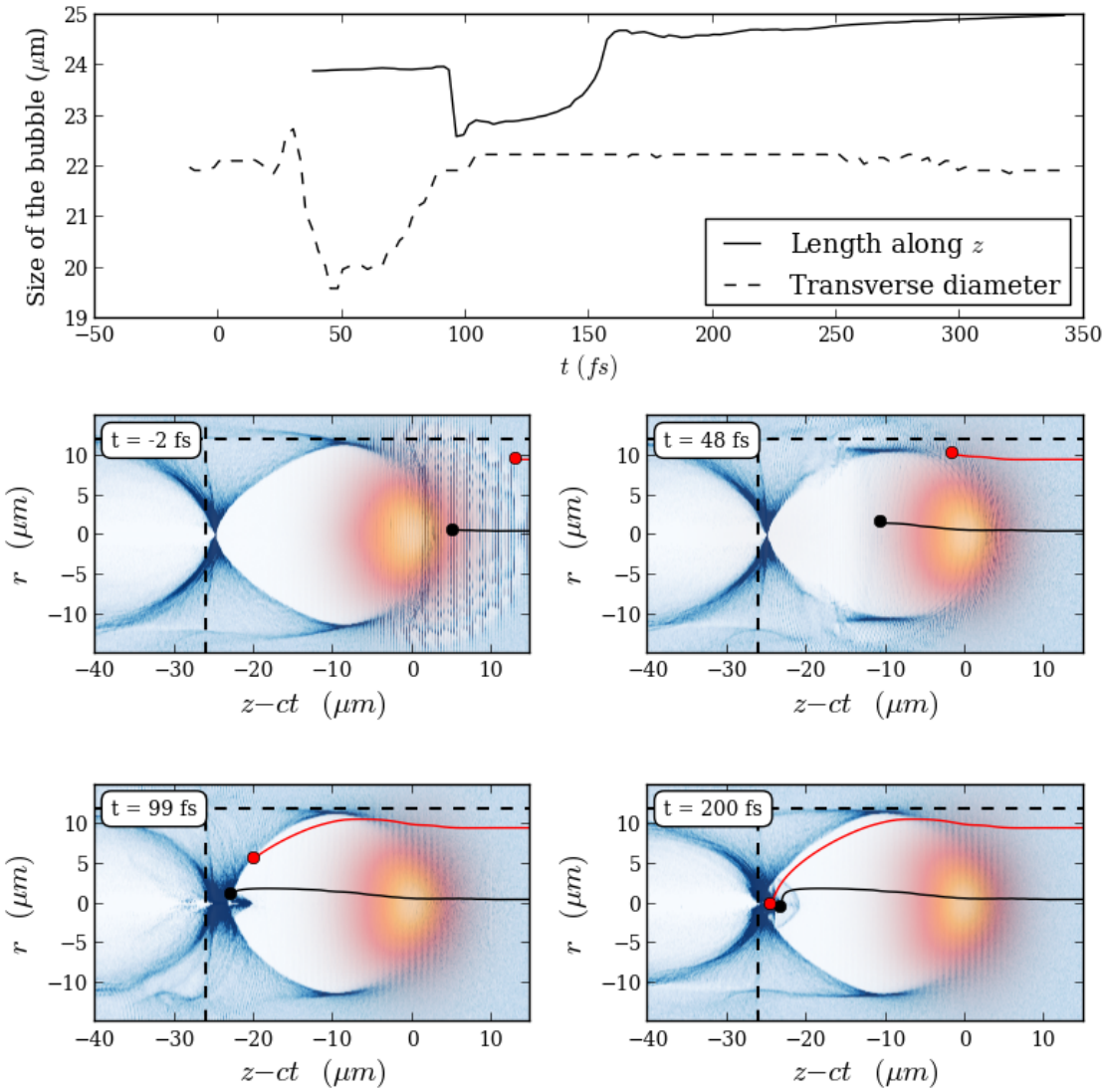

Figure 3.5: Top panel: Evolution of the size of the cavity in the transverse direction (dashed line) and longitudinal direction (solide line) versus time. Lower panels: Snapshots of the electron density and the driving laser pulse at different times. (The collision occurs at $t = 0$.) Notice that, because the counter-propagating pulse has a much lower amplitude than the driving pulse, it is not visible on these snapshots. The black dashed lines are visual aids that help evaluate the deformation of the cavity. The red and black curves represent the trajectory of an electron injected by *cold optical injection* (black line) and by *optical transverse injection* (red line).

As mentioned previously, the cavity is strongly affected by the pulse collision. Figure 3.5 displays the evolution of the transverse diameter (dashed line) and the longitudinal length (solid line) of the cavity (upper panel), along with four snapshots of the simulation corresponding to four different times. (The pulse collision occurs at $t = 0$.) As can be seen in both the upper panel and the snapshots, the cavity successively shrinks and reexpands – first radially (from $t = 40\,\mathrm{fs}$ to $t = 80\,\mathrm{fs}$) and then longitudinally (from $t = 100\,\mathrm{fs}$ to $t = 150\,\mathrm{fs}$). This traveling deformation is due to the electrons that were inside the laser pulse at $t = 0$ (i.e. during the collision) and then traveled along the sheath, towards the back of the cavity. The modified trajectory of these sheath electrons will be analyzed in the next section.

Note that two different types of injection occur shortly after the pulse collision. A typical trajectory for each of these two types of injection is represented in the fig. 3.5. In the first type of injection (black curve), the electron is injected just before the longitudinal expansion of the cavity, and its trajectory is essentially longitudinal (i.e. the electron was initially on-axis and went through the laser pulse, with relatively low variation of its transverse coordinate). This injection does not rely on the expansion of the cavity (since it occurs before this expansion), and it can in fact be interpreted by the mechanism of *cold optical injection* (see section 3.1.1). On the contrary, in the second injection (red curve), the trajectory is transverse and the electron reaches the back of the cavity *exactly as the cavity expands*. Moreover, no further injection occurs once the cavity stops expanding. This suggests that this injection is directly caused by the expansion of the cavity, and that its mechanism is very similar to that of density-ramp injection and transverse self-injection (see section 3.1.2). It is this second type of injection which is referred to as optical transverse injection.

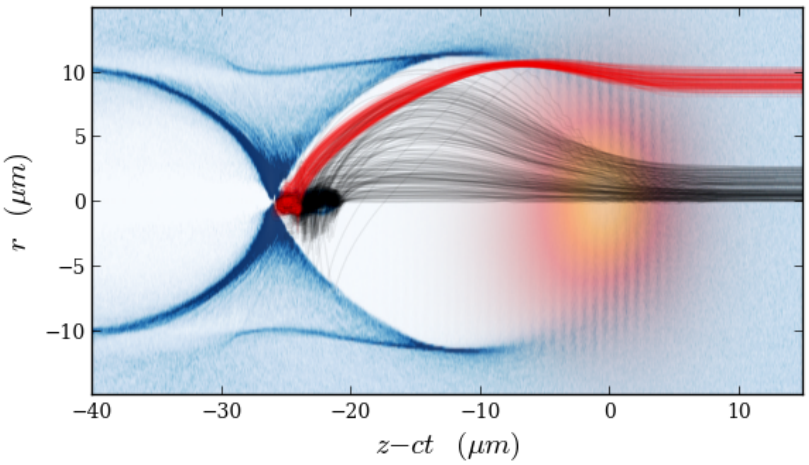

Figure 3.6: Representative sample of the trajectories of all the injected electrons, in the simulation corresponding to table 3.1. The trajectories corresponding to optical transverse injection and to cold optical injection have been colored in red and black respectively. Notice that, in the simulation, these trajectories are distributed in three dimensions around the cavity, with circular symmetry. Yet for a clearer visualization, they are all represented in the same plane here.

In addition, fig. 3.6 shows a representative sample of *all* the injected trajectories in the simulation. As can be seen in this figure, these trajectories can be divided into two well-separated groups, which correspond to the two above-mentioned mechanisms and have been colored ac-

cordingly. This confirms that these two mechanisms are different in nature, and not just two limiting cases of a unique and continuous mechanism.

All in all, this simulation shows that a pulse collision can lead to a transient deformation of the cavity, and that this can trigger an injection mechanism similar to that of density-ramp injection. However, while the expansion of the cavity in a density ramp is well-understood, it was not known that a pulse collision could cause the cavity to shrink and reexpand. This phenomenon is explained in the next section.

3.2.2 The laser-induced cavity expansion

In fact, the deformation of the cavity happens because, as will be shown in the rest of this section, the pulse collision transiently *reduces the impact of the transverse ponderomotive force.* As a result, the electrons that are inside the pulse at the time of the collision reach a lower transverse velocity than they would in the absence of a counter-propagating pulse. Therefore these electrons also reach a lower radius (i.e. the cavity shrinks transversely) and are also pulled faster towards the axis by the focusing fields of the cavity (and thus the cavity shrinks longitudinally). Once the collision is over, the ponderomotive force retrieves its initial impact, and the cavity recovers its orginal shape, i.e. it reexpands.

Origin of the reduced impact of the ponderomotive force. In order to explain the reduced impact of the transverse ponderomotive force during the collision, let us consider the equations of motion of a given background electron, inside the laser pulses. (In order to simplify the problem, the forces associated with the wakefield are neglected here.) When projected onto the radial and longitudinal direction (and when averaged over one laser period), the equations of motion read[5]

$$\frac{1}{c}\frac{dz}{dt} = \frac{u_z}{\gamma} \qquad \frac{1}{c}\frac{du_z}{dt} = -\frac{1}{2\gamma}\frac{\partial\langle \boldsymbol{a}_l^2\rangle}{\partial z} \tag{3.3}$$

$$\frac{1}{c}\frac{dr}{dt} = \frac{u_r}{\gamma} \qquad \frac{1}{c}\frac{du_r}{dt} = -\frac{1}{2\gamma}\frac{\partial\langle \boldsymbol{a}_l^2\rangle}{\partial r} \tag{3.4}$$

with $\gamma = \sqrt{1+\boldsymbol{u}^2+\langle \boldsymbol{a}_l^2\rangle}$ and where $\boldsymbol{u}$ is the slow component of the momentum of the electron considered. In these expressions, $\boldsymbol{a}_l$ represents the sum of the potential vectors of the two laser

[5] In eqs. (3.3) and (3.4), the expression $\boldsymbol{F} = -\frac{1}{2\gamma}\boldsymbol{\nabla}\langle \boldsymbol{a}_l^2\rangle$ was used for the ponderomotive force. However, this expression is not entirely rigorous here, since it was originally derived in the case of *one single laser pulse* (see section 1.1.2 and appendix A), and not in the case of *two counter-propagating pulses*. In order to verify the validity of eqs. (3.3) and (3.4), the trajectories derived from eqs. (3.3) and (3.4) were compared with the *numerical integration* of the more fundamental system of equations

$$\frac{1}{c}\frac{d\boldsymbol{u}_{tot}}{dt} = \frac{1}{c}\frac{\partial \boldsymbol{a}_l}{\partial t} - \frac{1}{\gamma}\boldsymbol{u}_{tot}\times(\boldsymbol{\nabla}\times\boldsymbol{a}_l) \qquad \frac{1}{c}\frac{d\boldsymbol{x}_{tot}}{dt} = \frac{1}{\gamma}\boldsymbol{u}_{tot}$$

(where the subscript *tot* refers to the sum of the slow and fast components of the motion), and a good agreement was found for the slow components of the motion. Thus this suggests that eqs. (3.3) and (3.4) are indeed valid for circular, counter-propagating pulses.

pulses, and it can be written as[6]:

$$\begin{aligned}\boldsymbol{a}_l =& \frac{a_0}{\sqrt{2}}[\,\cos(k_0 z-\omega_0 t)\boldsymbol{e}_x-\sin(k_0 z-\omega_0 t)\boldsymbol{e}_y\,]e^{-\frac{(z-ct)^2}{c^2\tau'^2}-\frac{r^2}{w_0^2}}\\ &+\frac{a_1}{\sqrt{2}}[\,\cos(k_0 z+\omega_0 t)\boldsymbol{e}_x+\sin(k_0 z+\omega_0 t)\boldsymbol{e}_y\,]e^{-\frac{(z+ct)^2}{c^2\tau'^2}-\frac{r^2}{w_1^2}}\end{aligned}$$

with $\tau'=\tau/\sqrt{2\log(2)}$ where τ denotes the FWHM duration of the pulse. (It is assumed that both pulses have the same duration here, although they can still have different waists.) Using this expression, the intensity pattern is given by:

$$\langle \boldsymbol{a}_l^2\rangle = \boldsymbol{a}_l^2 = \frac{a_0^2}{2}e^{-2\frac{(z-ct)^2}{c^2\tau'^2}-2\frac{r^2}{w_0^2}}+\frac{a_1^2}{2}e^{-2\frac{(z+ct)^2}{c^2\tau'^2}-2\frac{r^2}{w_1^2}}+a_0a_1\cos(2k_0z)e^{-2\frac{(z^2+c^2t^2)}{c^2\tau'^2}-\frac{r^2}{w_0^2}-\frac{r^2}{w_1^2}} \tag{3.5}$$

where the first two terms correspond to the envelopes of each pulse, and where the last term corresponds to the intensity modulation associated with their interference.

The equations of motion eqs. (3.3) and (3.4) can be simplified in two asymptotic cases. Firstly, *long before and long after* the collision ($t \ll -\tau'$ or $t \gg \tau'$), the colliding pulse is absent from the region of the driving pulse ($c(t-\tau') < z < c(t+\tau')$), and the last two terms of equation eq. (3.5) can be neglected when considering the motion of the electrons inside the driving pulse. Therefore, in this region, the ponderomotive force only depends on r and $\xi = ct - z$. As a result, $\gamma - u_z$ is a constant of motion[7], which equals 1 since the electrons are initially at rest. This in turn implies that $d\xi/dt = c/\gamma$ and thus the transverse equation of motion eq. (3.4) can be written in the form:

$$\frac{dr}{d\xi}=u_r \qquad \frac{du_r}{d\xi}=\frac{r}{w_0^2}\,a_0^2\,e^{-2\frac{\xi^2}{c^2\tau'^2}-2\frac{r^2}{w_0^2}} \tag{3.6}$$

Conversely, *during the collision* ($-\tau' < t < \tau'$ and $-c\tau' < z < c\tau'$), the colliding pulse cannot be neglected anymore and in fact the longitudinal ponderomotive force $\partial_z\langle \boldsymbol{a}_l^2\rangle$ is dominated by the derivative of the third term of eq. (3.5). (This is because the contribution of the third term to $\partial_z\langle \boldsymbol{a}_l^2\rangle$ is of order $k_0a_0a_1$, whereas that of the first term is of order $a_0^2(z-ct)/(c\tau')^2$, with $1/c\tau' \ll k_0$.) This longitudinal ponderomotive force corresponds to the longitudinal modulations of the intensity, and holds the electrons in the minimas of the interference pattern. Therefore, $dz/dt \simeq 0$ and $d\xi/dt \simeq c$. On the other hand, the radial ponderomotive force $\partial_r\langle \boldsymbol{a}_l^2\rangle$ is still dominated by the derivative of the first term of eq. (3.5) as long as $a_0 \gg a_1$, and thus eq. (3.4) can be written as:

$$\frac{dr}{d\xi}=\frac{1}{\gamma}u_r \qquad \frac{du_r}{d\xi}=\frac{1}{\gamma}\frac{r}{w_0^2}\,a_0^2\,e^{-2\frac{\xi^2}{c^2\tau'^2}-2\frac{r^2}{w_0^2}} \tag{3.7}$$

Both eq. (3.6) (which applies before and after the pulse collision) and eq. (3.7) (which applies during the collision) have to be integrated from the moment when an electron enters the pulse ($\xi < -c\tau'$) to the moment when it exits the pulse ($\xi > c\tau'$). However, due to the factors $\gamma > 1$

[6]Notice that, in this expression, the difference between the group velocity of the laser and the speed of light is neglected (i.e. $\beta_p = 1$), whereas it was shown previously that this difference is important when studying the injection in the wakefield. In reality, here the expression of $\boldsymbol{a}_l$ is used only for the motion of the electrons *inside the laser pulses*, and not for their subsequent injection in the wakefield. The difference between β_p and 1 is thus unimportant here.

[7]This is again a consequence of Noether's theorem. The set of equation eqs. (3.3) and (3.4) can indeed be derived from the Lagrangian $\mathcal{L} = -\sqrt{1+\langle \boldsymbol{a}_l^2\rangle}\times\sqrt{1-\boldsymbol{v}^2/c^2}$. In the case where no collision pulse is present, this Lagrangian is invariant under the transformation $(z, ct) \to (z+\epsilon, ct+\epsilon)$ and thus Noether's theorem applies.

in eq. (3.7), the electrons will exit the pulse with a lower transverse momentum u_r and a lower radius r, during the collision. Thus, eq. (3.6) corresponds to the regular impact of the transverse ponderomotive force (before and after the collision), while eq. (3.7) corresponds to a *reduced* impact of the transverse ponderomotive force (during the collision).

In essence, this reduced impact is simply due to the fact that the background electrons travel *faster* through the driving laser pulse during the collision ($d\xi/dt = c$) than before or after the collision ($d\xi/dt = c/\gamma$). Thus the electrons experience the transverse ponderomotive force for a shorter time during the collision, and its impact is therefore reduced.

Confirmation in PIC simulations. This interpretation is confirmed by PIC simulations. Figure 3.7 compares the trajectory of an electron of the sheath in two simulations: one in which a colliding pulse was present (solid line) and one in which there was no colliding pulse (dashed line).

The left panel of fig. 3.7 compares the longitudinal motion of the electron in these two cases. The colormap indicates the on-axis longitudinal profile of the laser as a function of time, in the case where a collision pulse is present. The standing intensity modulations are distinctively visible. In the case of a colliding pulse (solid line), the electron is trapped by the longitudinal ponderomotive force of these modulations, and remains roughly at the same z position. This is consistent with the hypothesis of our semi-quantative interpretation (i.e. $dz/dt = 0$, $d\xi/dt = c$ in the case of a colliding-pulse). On the other hand, in the absence of a colliding pulse (dashed line), there are no standing intensity modulations, and the electron is pushed forward by the longitudinal ponderomotive force associated with the envelope of the pulse ($d\xi/dt = c/\gamma$, in our semi-quantitative interpretation).

In parallel, the right panel of fig. 3.7 compares the radial motion of the same electron as a function of the copropagating coordinate $z - ct\,(= -\xi)$. As predicted by the factors $1/\gamma$ in eq. (3.7), r increases more slowly as a function of ξ in the presence of a colliding pulse than without it. As a consequence, the electron has a lower maximal radius, and it is then pulled faster towards the axis. On the whole, this confirms that the ponderomotive force is less effective during the pulse collision, and that this causes the cavity to shrink.

3.2.3 Conditions of existence

The existence of optical transverse injection is controlled by the different parameters of the laser pulses and of gas. In fact, it was found in the simulations that these parameters must satisfy two conditions for optical injection to occur.

Existence of a fully evacuated cavity. The first condition is that the driving laser pulse be intense and focused enough to generate a clear-cut, fully evacuated cavity (i.e. $a_0^2 \gg 1$ and $k_p w_0 \sim 2\sqrt{a_0}$, according to section 1.1.4). This condition can be interpreted again by the fact that the pulse collision reduces the impact of the transverse ponderomotive force. In the case where the cavity is fully evacuated, the consequence of this reduced impact is to transiently reduce the size of the cavity, as described in section 3.2.2. On the other hand, in the case where the cavity in only partially evacuated, the reduced impact of the ponderomotive force causes the cavity to be even less evacuated, and may in fact transiently prevent the generation of the wakefield. This effect, which is known as wake inhibition [Rechatin et al., 2007], is detrimental to the injection and should be avoided.

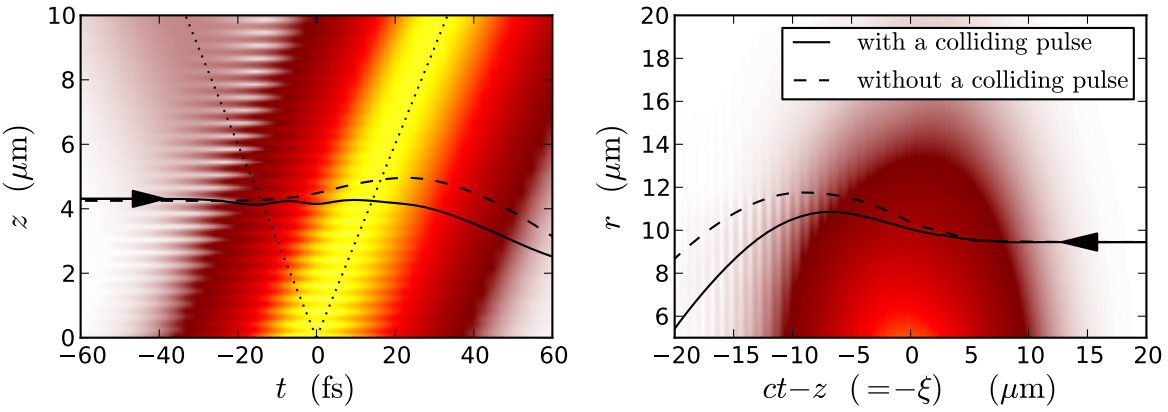

Figure 3.7: Longitudinal and transverse motion of one of the electrons that form the sheath, during the pulse collision (solid curve) and when no colliding pulse is present (dashed curve). The colormap in the left panel represents the on-axis laser intensity and its interference pattern – in the case where a colliding pulse is present. The position of the centroid of each pulse is materialized by a doted line. (Note that, in the case without a colliding pulse (dashed curve), the driving pulse is at the same position, but there is of course no interference pattern.) Right panel: The colormap represents the driving laser pulse in the (z, r) plane.

Perturbation of the whole cavity. Provided that the driving pulse satisfies the above condition, it is also necessary that the counter-propagating injection pulse provokes a deformation of the whole cavity. In the simulations, it was found that a global deformation of the cavity did occur under the condition $a_1 \gtrsim 0.1$ and $w_1 \gtrsim w_0$. The first condition simply expresses the fact that the counter-propagating pulse should be intense enough, while the second condition ensures that this pulse is wide enough to affect the motion of the off-axis electrons that will then form the sheath. If this second condition is not satisfied (i.e. $w_1 < w_0$), these off-axis electrons are weakly affected and the cavity hardly deforms at all. As a consequence, optical transverse injection is suppressed. Note however that, since the near-axis electrons are still affected by the collision for $w_1 < w_0$, cold optical injection is still present. Thus w_1 controls the transition between a regime in which only cold optical injection is present ($w_1 < w_0$) to a regime in which the two types of injection coexist ($w_1 \gtrsim w_0$). Incidentally, in this latter case, optical transverse injection tends to dominate in terms of charge. (For instance, in the simulation corresponding to the parameters of table 3.1, the charges injected through optical transverse injection and cold injection were 50 pC and 13 pC respectively.)

Importantly, as long as the two above conditions are satisfied, optical transverse injection was observed with both linear and circular polarizations (i.e. with $\epsilon = 0.5$ and $\epsilon = 1$ in eq. (3.2)).

3.3 Bunch quality in optical transverse injection

While the last section focused on the mechanism of optical transverse injection, this section emphasizes the properties of the bunches generated through this process. In particular, we explore the impact of the laser parameters on the final bunch quality.

3.3.1 General properties of the bunches in optical transverse injection

Let us thus start by summarizing the characteristics of the bunch obtained in the simulation corresponding to table 3.1. These characteristics will then serve as a reference when varying the laser parameters.

Figure 3.8 shows the longitudinal phase space of the injected electrons in this simulation, after 150 μm of acceleration. As can be seen, the phase space consists of a well-defined peak around 27 MeV and a long, diffuse distribution between 16 and 26 MeV. A comparison of the longitudinal positions in fig. 3.6 and in the left panel of fig. 3.8 reveals that the peak is due to optical transverse injection, while the diffuse distribution corresponds to cold optical injection.

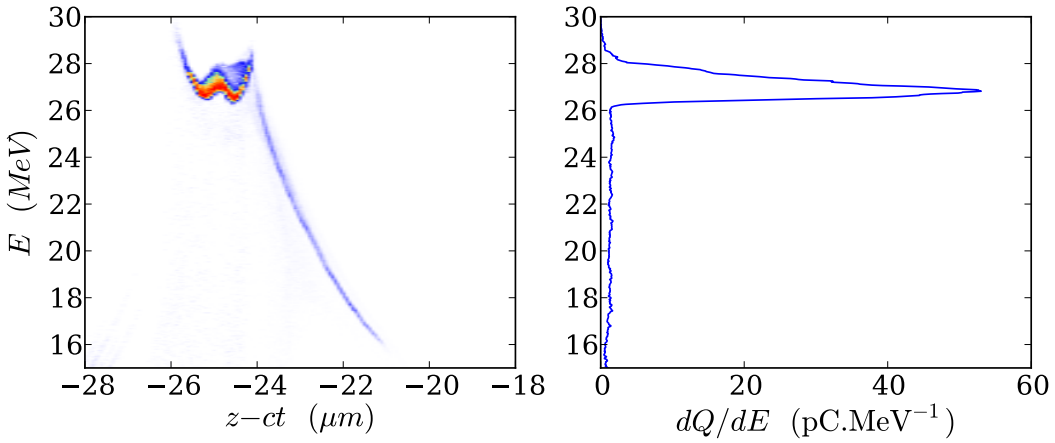

Figure 3.8: Phase space distribution of the injected electrons in the PIC simulation corresponding to table 3.1, after 150 μm of acceleration. The coordinates on the x axis of the left panel are the same as in fig. 3.6.

A further analysis of the electrons generated by optical transverse injection (i.e. those in the peak) showed that they present high-quality features. The RMS duration of the peak is 3 fs, its absolute RMS energy spread is 0.46 MeV (1.7 % relative energy spread at 27 MeV), and as mentioned before its total charge is 50 pC. Moreover, these electrons are characterized by a very low emittance: $\epsilon_x \simeq \epsilon_y \simeq 0.17\,\text{mm.mrad}$. By comparison, the emittance of the electrons between 16 MeV and 26 MeV is 1.9 mm.mrad. Notice also that the observation of a such a low emittance in the simulation was made possible only because the Cherenkov-free scheme of section 2.3.2 was used. (The emittance is otherwise observed to rapidly grow above this initial value.)

Thus optical transverse injection can produce electron bunches which have simultaneously a high charge, a short duration, a low energy spread and a low emittance. In fact, meeting all these requirements at the same time is generally considered to be challenging with other methods of injection. Since the low value of emittance obtained here is particularly remarkable, we give an interpretation of this value and study its dependence on the laser parameters in the next section.

3.3.2 Conditions for a low emittance

Here we suggest that the low emittance obtained in optical transverse injection is related to the fact that the electrons are injected at the very back of the cavity (see fig. 3.6). At the back of the cavity, the boundaries are not very wide apart, and the electrons may only perform low-amplitude betaton oscillations. Thus, the electrons that reach the back of the cavity with a high

radius or a high radial momentum are eventually ejected, since their betatron motion would not fit within the transverse boundaries of the cavity. This effect is illustrated in fig. 3.9, where the trajectories of a few electrons from the simulation of table 3.1 are represented. In this figure, the electrons having a low radius and a low momentum at the back of the cavity are injected (red trajectories), while the others are ejected (blue trajectories). Thus, this phenomenon effectively *filters* the particle and selects those which have a low-amplitude betatron motion, resulting thereby in a low emittance. Incidentally, this *filtering* effect can also explain why the electrons between 16 MeV and 26 MeV in fig. 3.8 have a large emittance (1.9 mm.mrad). As represented in fig. 3.6, these electrons are injected relatively far from the back of the cavity, where the boundaries are wider apart and lead to a lesser selection.

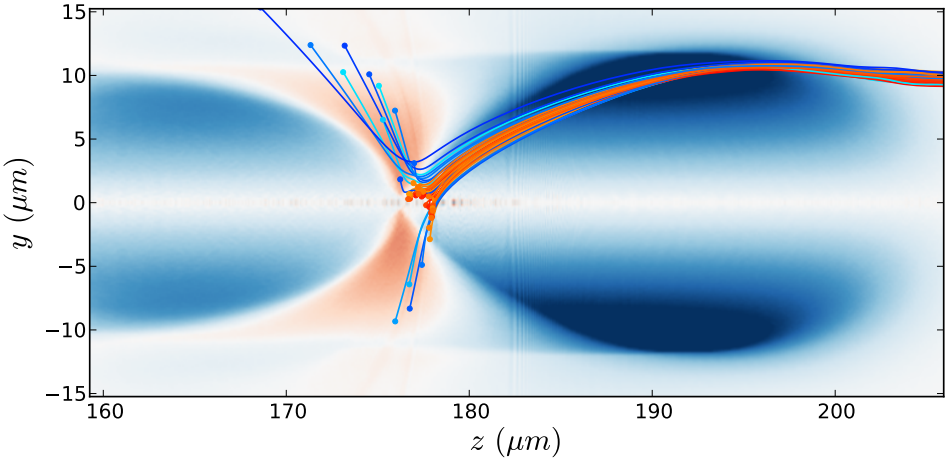

Figure 3.9: Trajectories of some particles in the simulation corresponding to table 3.1. The trajectories of the particles that are eventually injected (resp. ejected) are colored in red (resp. blue). The colored areas correspond to the values of the radial field $E_r - cB_\theta$ – which is approximately equal to the radial force felt by the particles: the areas of focusing (resp. defocusing) radial force are represented in blue (resp. red).

This interpretation also implies that the cavity should be as *narrow* as possible at its back, in order to have a low emittance. In the simutations, the profile of the back of the cavity was found to crucially depend on w_0 and a_0. This is illustrated in the left panel of fig. 3.10, which represents the profile of the back of the cavity for various values of w_0 (and a constant value of a_0). The back of the cavity is observed to grow wider and wider as w_0 increases. In parallel, the right panel shows the evolution of the emittance of the injected bunch when w_0 is increased. In agreement with the presumed filtering mechanism, the emittance grows as the back of the cavity becomes wider. Importantly, a similar evolution was found when varying a_0 (for $a_0 > 4$, and for a constant w_0). A high a_0 was observed to lead to a wide cavity, and to a relatively high emittance.

On the whole, these simulation results imply that the driving pulse should be focused to a low waist ($w_0 \sim 8\,\mu$m) in order to obtain a low emittance. In principle, one could operate at high gas density and rely on self-focusing in order to reach such a low waist. However, there is a risk that this would also trigger an undesired self-injection, on top of the optical injection. Therefore, it is in fact preferable to operate at low density – where both self-focusing and self-injection are much less important. At low density, one can rely only on the focusing optics of the laser system in order to reach $w_0 \sim 8\,\mu$m. Although this waist is low, it is within the focusing capabilities of

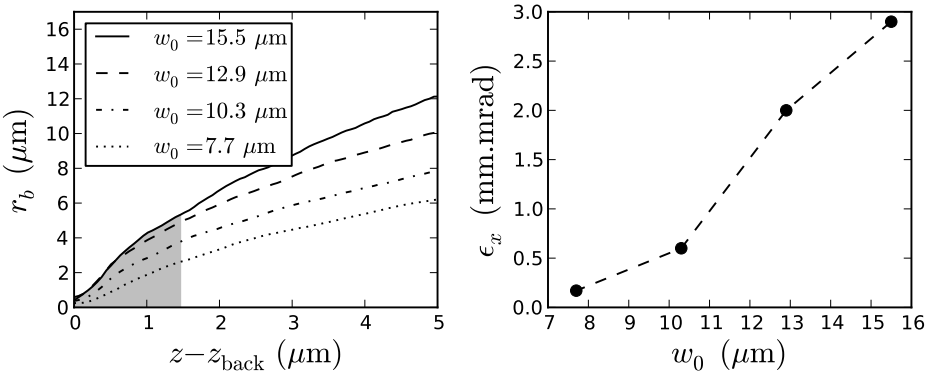

Figure 3.10: Results of PIC simulations, in which w_0 was gradually increased (while keeping $a_0 = 4$, $a_1 = 0.2$ and $w_0 = w_1$). Left panel: Profile of the back of the cavity for different values of w_0. The shaded area represents the typical area where electrons can be injected through optical transverse injection. Right panel: Emittance of the bunch injected through optical transvese injection, as a function of w_0.

existing laser system.

3.3.3 Final energy and final energy spread

In addition to the low emittance of the bunch, its low *absolute* energy spread is also an important feature. In fact, it is in a sense surprising to obtain a low energy spread here, since the electrons are injected at the very back of the cavity. At the back of the cavity, the electric field is indeed known to be very inhomogeneous [Lu et al., 2006b] and would normally cause the energy spread to increase. However, in our case the longitudinal electric field flattens out due to beamloading, and it can therefore preserve a low energy spread. This is illustrated in fig. 3.11, which compares the on-axis longitudinal electric field before and after the injection. (The position of the injected bunch is represented by red dots.)

The flattening of the electric field is however not perfect and the energy spread does increase – albeit slowly – at later times. There are solutions to avoid its increase, if the energy spread is to be preserved on a long acceleration distance. For instance, one could use a two-stage profile for the gas jet, whereby the density in the second stage is slighty lower than in the first stage. In this setup, the pulse collision occurs in the first stage, and the bunch is then mostly accelerated in the second stage. Because of the lower density in the second jet, the cavity is slightly larger than in the first jet and this effectively brings the electron bunch out of the zone in which the electric field is very inhomogenous.

Another important feature of optical transverse injection is that the final energy of the bunch is relatively low, in comparison with standard values for LWFA ($\sim$ 100 MeV – 1 GeV). This is because the driving laser pulse quickly diffracts after the pulse collision, as a consequence of its low waist and of the low density of the gas. This reduces the acceleration distance and limits the maximal energy of the electrons to a few tens of MeV. If a high energy is desired, this issue could in principle be avoided by guiding the laser pulse after the collision (for instance with a plasma channel). However, here we point out that low-energy bunches may also be of interest for certain applications. This is particularly true when designing compact free-electron laser scheme, for which a low-energy electron bunch can lead to a more robust growth than a high-energy bunch.

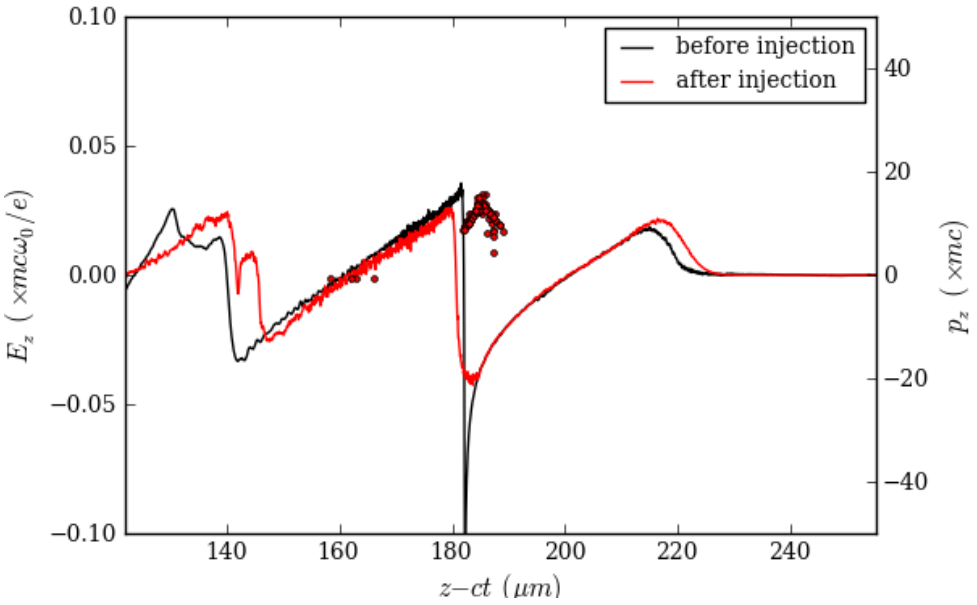

Figure 3.11: Representation of the on-axis longitudinal electric field in the simulation corresponding to table 3.1. The black (resp. red) line represents the electric field before (resp. after) the injection. The red dots represent the positions of a few injected electrons in longitudinal phase space (see the right axis).

This prospect is discussed further in chapter 5.

3.4 Conclusion

In conclusion, this section presented a new mechanism of colliding-pulse injection, which cannot be described with the concept of the two-dimensional separatrix. In this mechanism, the pulse collision transiently reduces the impact of the transverse ponderomotive force, and causes the accelerating cavity to temporarily shrink and reexpand. As the cavity reexpands, it triggers a sudden transverse injection.

Two conditions have to be met in order for this mechanism to occur. Firstly the driving pulse should be intense and focused enough to produce a fully-evacuated cavity, and secondly the counter-propagating pulse should be able to cause a global deformation of the cavity. These conditions are summarizing by the following inequalities

$$a_0^2 \gg 1 \qquad k_p w_0 \sim 2\sqrt{a_0} \qquad a_1 \gtrsim 0.1 \qquad w_1 \gtrsim w_0.$$

Moreover, within the range of parameters that satisfy the above conditions, it is preferable to choose relatively low values for w_0 and a_0, since this leads to a lower emittance. Finally, the density of the gas should be low enough for self-focusing and self-injection to be negligible. In practice, optical transverse injection was observed in simulations with densities ranging from $2 \times 10^{18}\,\mathrm{cm}^{-3}$ to $2 \times 10^{17}\,\mathrm{cm}^{-3}$, with no substantial self-focusing and no self-injection.

On the whole, the parameters required for this type of injection are within the reach of existing laser facilities. (In particular, the required energy and the required waist at focus have realistic values.) We note here that this regime of parameters has not yet been explored experimentally,

and that, compared with our simulations, previous experiments were carried out at higher density and with larger waists [Faure et al., 2006].

Finally, if the above conditions are met, optical transverse injection can lead to high-quality bunches with high charge, low energy spread and low emittance at the same time. Morever, this injection operates at low density and does not rely on self-focusing, which may make it more stable than other methods of injection. As will be shown in chapter 5, optical transverse injection can thus be particularly interesting for the design of innovative radiation sources. Yet here it should also be noted that, in spite of their low emittance, the bunches retain a relatively high divergence ($\sim$ 4 mrad in the simulations), which can be detrimental to these applications. Therefore, we address the general issue of beam divergence in the next chapter.

Chapter 4

The laser-plasma lens

In the previous chapter, transverse optical injection was shown to produce electron beams with a very low emittance, but with a relatively large divergence (several milliradians). It is in fact common for LWFA beams to have a large divergence – even with other injection methods. Yet for some applications, a high divergence can be a strong drawback, and thus the beam typically needs to be collimated. In this chapter, we propose a collimating scheme – the *laser-plasma* lens – which involves a second gas jet and takes advantage of the presence of the driving laser pulse. This scheme is studied through analytical models and PIC simulations. However, it is found that it is subject to several aberrations, and one of them (transverse beamloading) is modeled in details here. In order to avoid these aberrations, an alternative scheme involving two laser pulses is also proposed. In the end, simulations show that both schemes can substantially reduce the divergence in realistic experimental conditions, and thus the laser-plasma lens appears to be an interesting solution to the high divergence of LWFA beams.

Contents

4.1 Motivations for a laser-plasma lens

One of the most interesting features of LWFA bunches is their extremely high charge density. This high charge density is a direct consequence of both the small transverse size (∼1 μm) and short duration (∼1 fs) of these bunches, and it is in fact challenging for conventional accelerators to produce a similar density. As a result, it has been proposed to take advantage of this specificity of LWFA to produce very bright synchrotron sources. Here the idea is to send the accelerated electrons into a magnetic undulator (i.e. a series of alternating magnets which wiggle the electrons transversely), and thereby to force them to emit high-frequency radiation [Schlenvoigt et al., 2008]. In this situation, the brightness of the radiation is proportional to the charge density of the electrons. In fact, if the charge density is high enough, it can even give rise to a *free electron laser* effect, which dramatically enhances the brightness of the radiation. (This effect is discussed in more details in chapter 5.)

However, due to their large divergence, LWFA bunches naturally expand after exiting the accelerator, and their high charge density is very rapidly lost. For instance, a bunch having an initial transverse size $\sigma_x = 1\,\mu$m and an RMS divergence $\theta_x = 1$ mrad at the exit of the accelerator will see its transverse size increase ten-fold after only 1 centimeter of propagation. This implies that the charge density of the beam typically decreases by several orders of magnitude before entering the magnetic undulator, and as a consequence, the brightness of the emitted radiation is relatively low. Moreover, a large divergence further spoils the properties of the radiation by inducing a large angular and spectral distribution.

Because of this, it is paramount to reduce the divergence of the electron beam (i.e. to collimate the beam) before sending it into the undulator. For instance, Fuchs et al. [2009] collimated the bunch by using quadrupole lenses. However, this setup is not without drawbacks. First, a quadrupole lens (or a quadrupole doublet [Reiser, 2008]) is not convenient because the electrons are focused differently in the two transverse directions. In addition, because of the relatively low focusing fields of a quadrupole, the focal length of the device is typically tens of centimeter long. This means that the quadrupole lens has to be placed tens of centimeters behind the exit of the accelerator, and that the electrons will propagate freely over this distance. However, Khachatryan et al. [2007]; Migliorati et al. [2013] showed that the emittance of the beam can considerably degrade over such a long free propagation, especially if the energy spread of the beam is large. Moreover, after ten centimeters, the size of the beam is so large that it starts experiencing the high-radius aberrations of the quadupole lens, which results in a further increase in emittance. Thus, ideally, the beam should be collimated much sooner, i.e. before its transverse size and emittance increase too much.

A plasma lens [Chen, 1987] could a priori provide a solution to this issue. In a plasma lens, the electron bunch is sent into a gas jet, where its strong space-charge field ionizes a fraction of the atoms of the gas and radially expells the electrons produced. As a result, the bunch is surrounded by a focusing ion cavity, which can then collimate it. One advantage of the plasma lens is that its focusing fields are much higher than those of a quadrupole lens, and thus the corresponding focal length is much shorter. Plasma lenses have been studied extensively in the context of conventional accelerators [Chen et al., 1990; Su et al., 1990; Rosenzweig et al., 1991; Nakanishi et al., 1991; Hairapetian et al., 1994; Barov et al., 1998; Govil et al., 1999; Ng et al., 2001; Thompson et al., 2010]. However, they may not be appropriate in the case of laser-wakefield accelerators. This is because, in a plasma lens, there is always a finite length at the head of the bunch over which the focusing fields are very weak [Thompson et al., 2010; Barov et al., 1998; Rosenzweig et al., 1991]. This length corresponds to the distance that it takes to expell the plasma electrons. In the case of laser-wakefield acceleration, the bunch is so short that its length

can be comparable to that finite distance. In this case, a plasma lens would not be able to properly collimate the bunch.

Therefore, in this chapter we propose an alternative collimating scheme, which is referred to as the *laser-plasma* lens. As desired, this *laser-plasma lens* has a very short focal length and can be placed only about one millimeter behind the accelerator, and yet it does not suffer from the drawbacks of the plasma lens.

4.2 The single-pulse laser-plasma lens

4.2.1 Principle

As shown in figure fig. 4.1, the idea of the laser-plasma lens consists in placing a second, low-density gas jet behind the jet in which self-injection and acceleration took place. After exiting from the first jet, the laser and the electron bunch propagate freely in a millimeter-scale drift space. They then enter the second jet, in which the laser pulse again drives a wakefield. The focusing fields of this wakefield can then collimate the trailing electron bunch. On the whole, the phase space evolution of the bunch can be decomposed into three stages, which are represented in fig. 4.1 and described in the following paragraphs. (In fig. 4.1 and in the rest of this chapter, θ_x and θ_y denote the angles between the z axis and the velocity vector $\boldsymbol{v}$ of an individual electron, in the x and y plane respectively.)

First jet: Acceleration and betatron. In the first jet, the laser pulse self-focuses and the wakefield is typically in the blow-out regime. The density of this first jet is chosen high enough for self-injection to occur ($n_1 \sim 10^{19}\,\mathrm{cm}^{-3}$). In this case, the injected electron bunch is accelerated and focused by the fields of the ion cavity, and the individual electrons perform transverse betatron oscillations. When viewed in phase-space, these betatron oscillations roughly correspond to a rotation along a given ellipse. Due to the strong focusing fields of the cavity, this ellipse is elongated in the θ_x direction in fig. 4.1, and as a consequence the divergence of the bunch is typically high during these oscillations.

Drift space: Free propagation. In the drift space, the laser pulse is not self-focused anymore, and thus it diffracts freely. Also, there is no wakefield in the drift space and hence the electrons are not focused either. As a consequence of its high divergence, the bunch expands radially. In phase-space, this corresponds to the bunch stretching in the x direction, but along lines of constant θ_x (see fig. 4.1). As a result, the area covered by the beam becomes thinner and thinner in the θ_x direction[1].

Second jet: Collimation. In the second jet, the laser creates again a focusing wakefield. For reasons that will be explicited in section 4.2.3, the density of the second jet is chosen to be relatively low ($n_2 \sim 10^{18}\,\mathrm{cm}^{-3}$). It is also important to note that, in the second jet, the wakefield is typically in the linear regime. This is because the typical Rayleigh length after the first jet

[1] In the case of a monoergetic bunch with negligible space-charge, this can be seen as a consequence of the conservation of emittance. It is indeed easy to show that, if space-charge and energy-spread effects are negligible, the emittance of the bunch is conserved as it travels in vacuum. Here the emittance of the bunch can be written as $\epsilon_x = \frac{1}{mc}\sigma_x\sigma_{p_x-\alpha_{\mathrm{best}}x} = \gamma\sigma_x\sigma_{\theta_x-\alpha'_{\mathrm{best}}x}$ (see section 1.3.1 ; here $\alpha'_{\mathrm{best}} = \alpha_{\mathrm{best}}/(\gamma mc)$), where $\sigma_{\theta_x-\alpha'_{\mathrm{best}}x}$ is a measure of the thickness of the bunch along the θ_x direction, in phase-space. Since σ_x increases during the expansion of the bunch, and since ϵ_x remains constant, $\sigma_{\theta_x-\alpha'_{\mathrm{best}}x}$ necessarily decreases and the bunch becomes thinner in phase-space.

($Z_R \sim 200\,\mu$m) is much shorter than the millimeter-scale drift space, and thus the intensity of the laser pulse rapidly decreases before it reaches the second jet. Because the focusing fields in the linear regime are weaker than in the blow-out regime, the bunch rotates slower and along a wider ellipse in phase-space. At some point in this rotation, the bunch is aligned with the x axis and the divergence is minimal. This is where the second jet should end in order to properly collimate the beam. This shows that the length L_l of the second jet should be carefully tuned in relation with the other parameters of the setup (the density n_2 of the second jet and the drift distance L_d), in order to reach a minimal divergence. The next section explains quantitatively how these different parameters should be chosen. Notice also that, if these parameters are well-chosen, the final divergence is much smaller than the initial one (as a consequence of the bunch becoming thinner in the drift space) – which is indeed the aim of this setup.

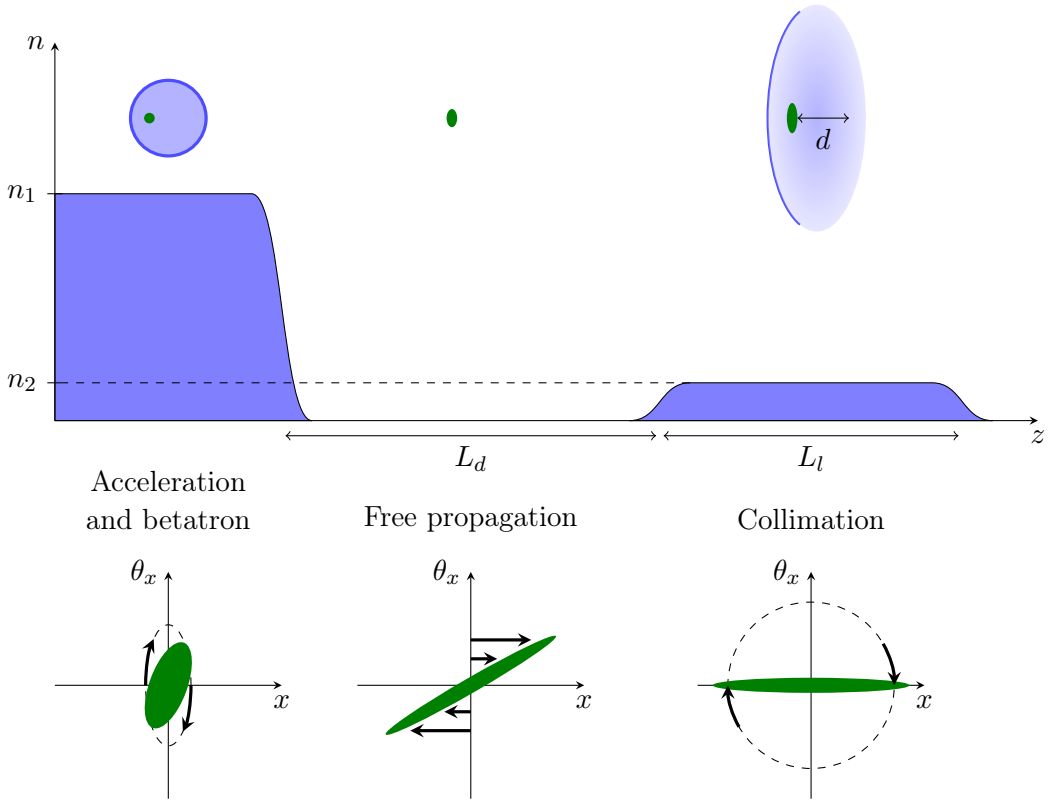

Figure 4.1: Schematic representation of the single-pulse laser-plasma lens. The blue curves represent the density profiles of the two jets. The above sketches represent the driving laser pulse (red), the laser-wakefield (blue) and the electron bunch (green), as they propagate through the two jets and the drift space. The plots in the lower panel represent the evolution of the electron bunch in transverse phase space.

4.2.2 A model for the laser-plasma lens

In order determine how the different parameters should be tuned, I built a simple model of the laser-plasma lens. In this simplified model, space-charge effects are neglected, and the laser-wakefield is explicitly assumed to be in the linear regime in the second jet. Moreover, the density gradients at the edges of the gas jets are considered to be infinitely steep. Thus the expression

of the gas density $n(z)$ is:

$$n(z) = \begin{cases} n_1 & \text{for } z < 0 \\ 0 & \text{for } 0 < z < L_d \\ n_2 & \text{for } L_d < z < L_d + L_l \end{cases}$$

(By convention, the end of the first jet is taken as the origin of the z axis.) In order to evaluate the impact of the lens on the divergence of the beam, we first study the trajectory of one individual electron, and then generalize the results to a whole bunch.

Trajectory of an individual electron. Let us thus consider an individual electron that exits from the first jet and let us calculate the evolution of its transverse position x and transverse angle θ_x as it goes through the drift space and the second jet,. At the end of the first jet, the initial transverse position and transverse angle of this electron are denoted as x_0 and θ_0.

As it travels in the drift space, the electron does not experience any force, and thus its transverse position and angle evolve as:

$$\begin{cases} x(z) = x_0 + \theta_0\, z \\ \theta_x(z) = \theta_0 \end{cases} \qquad \text{for } 0 < z < L_d \tag{4.1}$$

In particular, their values at the entrance of the second jet are $x(L_d) = x_0 + \theta_0\, L_d$ and $\theta_x(L_d) = \theta_0$. Once this electron enters the second jet, it experiences the focusing forces of the laser-wakefield. Thus, assuming that the laser pulse is Gaussian, one can use the linear wakefield expressions of section 1.1.3. In this case, the equations of transverse motion in the second jet are:

$$\frac{d\,p_x}{dt} = -\eta\, mc^2 \frac{a_0(z)^2}{w(z)^2} \sin(k_p d)\, x\, e^{-2(x^2+y^2)/w(z)^2} \qquad \frac{d\,x}{dt} = \frac{p_x}{\gamma m} \tag{4.2}$$

$$\text{with} \qquad k_p = \sqrt{4\pi r_e n_2} \qquad \text{and} \qquad \eta = \sqrt{\frac{\pi}{4\log(2)}} (ck_p\tau) \exp\left(-\frac{(ck_p\tau)^2}{16\log(2)}\right)$$

where η quantifies the efficiency with which the laser pulse drives the wakefield. In the above equations, $w(z)$ and $a_0(z)$ are the waist and the peak amplitude of the laser pulse, and τ is its FWHM duration. (a_0 and w depend on z because the laser progressively diffracts.) The quantity k_p denotes the plasma wavector in the second jet, and d is the distance between the electron bunch and the centroid of the laser pulse (see fig. 4.1).

These equations of motion can be integrated under a few approximations. First, since the drift space L_d is much longer than the Rayleigh length Z_R, the waist and amplitude of the laser pulse in the second jet evolve as $w(z) \simeq w(0) \times z/Z_R$ and $a_0(z) \simeq a_0(0) \times Z_R/z$ (where $a_0(0)$ and $w(0)$ are the amplitude and waist of the pulse at the exit of the first jet). Moreover, the electron is considered to travel approximately at the speed of light in the z direction ($z \simeq ct$, $p_x \simeq \gamma mc\,\theta_x$), and the variations of its Lorentz factor γ are neglected in the second jet. (This is because the accelerating electric field is relatively weak in the linear wakefield of the second jet.) Finally, it is assumed that the electron travels close enough to the axis for the exponential factor in eq. (4.2) to be approximated to 1 (i.e. it is assumed that $x(z), y(z) \ll w(z)$). With these approximation, the equations of motion can be rewritten as:

$$\frac{d^2x}{dz^2} = -\frac{Z_R^4}{z^4} k_{\text{foc}}^2\, x \qquad \text{with} \quad k_{\text{foc}}^2 = \frac{\eta\, a_0(0)^2}{\gamma\, w(0)^2} \sin(k_p d) \tag{4.3}$$

Taking into account the initial conditions $x(L_d)$ and $\theta_x(L_d)$, the solution of this equation is:

$$\begin{cases} x(z) = \chi\,\theta_0\,z\cos\left(\dfrac{k_{\rm foc}Z_R^2}{L_d} - \dfrac{k_{\rm foc}Z_R^2}{z} + \varphi\right) \\ \theta_x(z) = \chi\,\theta_0\left[\cos\left(\dfrac{k_{\rm foc}Z_R^2}{L_d} - \dfrac{k_{\rm foc}Z_R^2}{z} + \varphi\right) - \dfrac{k_{\rm foc}Z_R^2}{z}\sin\left(\dfrac{k_{\rm foc}Z_R^2}{L_d} - \dfrac{k_{\rm foc}Z_R^2}{z} + \varphi\right)\right] \end{cases} \tag{4.4}$$

where $\chi > 0$ and $\varphi \in [0, 2\pi[$ are defined by the relation

$$\chi e^{i\varphi} \equiv \left(1 + \frac{x_0}{\theta_0 L_d}\right) + i\frac{x_0}{k_{\rm foc}Z_R^2\theta_0} \tag{4.5}$$

These expressions (which are valid for $L_d < z < L_d + L_l$) and those of eq. (4.1) (which are valid for $0 < z < L_d$) are plotted as a function of z in fig. 4.2. In this figure, θ_x is indeed observed to progressively decrease in the second jet, as is desired. Notice that the evolution of θ_x becomes slower and slower as the particle travels into the jet. Mathematically, this is a consequence of the terms $1/z$ in eq. (4.4), while physically this is because the laser continues diffracting in the second jet, and because the focusing forces of the wakefield thus become weaker and weaker as a function of z. Note also that, at some point in the trajectory of the electron, θ_x becomes zero. Ideally, this is where the second jet should end. According to eq. (4.4), L_l should thus satisfy the condition:

$$\frac{k_{\rm foc}Z_R^2}{L_d + L_l}\tan\left(\frac{k_{\rm foc}Z_R^2}{L_d} - \frac{k_{\rm foc}Z_R^2}{L_d + L_l} + \varphi\right) = 1 \tag{4.6}$$

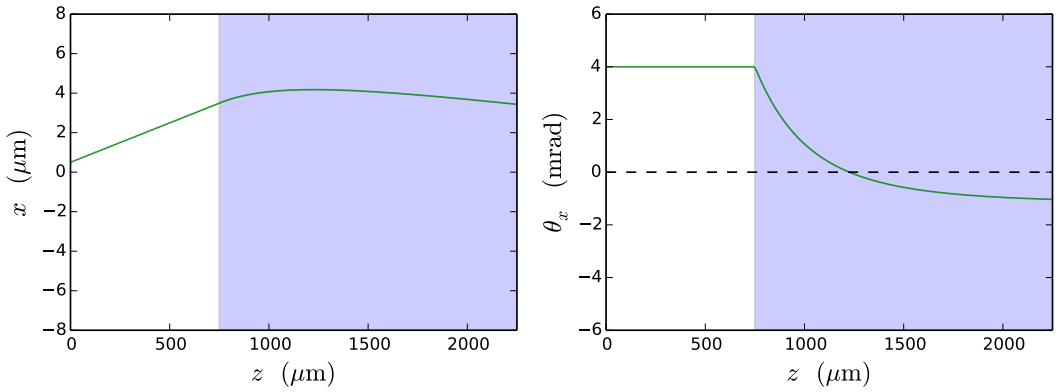

Figure 4.2: Evolution of x (left panel) and θ_x (right panel), as given by eq. (4.1) and eq. (4.4), for arbitrary initial conditions x_0 and θ_0 and for realistic parameters of the lens ($\gamma = 200$, $a_0(0) = 5$, $w(0) = 6\,\mu$m, $L_d = 750\,\mu$m, $d = 10\,\mu$m, $\tau = 30\,$fs). The white area represents the drift space, while the blue area represents the second jet.

Evolution for an electron bunch. Yet the above condition cannot be simultaneously satisfied for all the electrons of the bunch. This is because, according to eq. (4.5), φ depends on the transverse position x_0 and angle θ_0 of each individual electron. Therefore, as represented in fig. 4.3, the electrons of the bunch cannot reach $\theta_x = 0$ simultaneously, and the bunch will always have a non-zero divergence, regardless of the value of L_l. This result is not surprising

since, at any rate, the finite emittance of the bunch always prevents it from reaching a zero divergence.

Even though the final RMS divergence is not zero, fig. 4.3 shows that it can be considerably smaller than its initial value – if the parameters of the lens are well-chosen. A reasonable choice here is to adopt the parameters that satisfy the criterion

$$\frac{k_{\mathrm{foc}} Z_R^2}{L_d + L_l} \tan\left(\frac{k_{\mathrm{foc}} Z_R^2}{L_d} - \frac{k_{\mathrm{foc}} Z_R^2}{L_d + L_l} \right) = 1 \tag{4.7}$$

which is the condition eq. (4.6) for $\varphi = 0$. This is justified by the fact that, for typical laser-wakefield parameters, φ is close to zero for most of the electrons of the bunch. In practice, eq. (4.7) can be solved graphically in order to find one of the parameters of the lens when the others parameters are imposed. Here, this criterion is used to find the optimal length L_l of the second jet, while imposing the same parameters as in fig. 4.3. The result is plotted as a blue line in this figure. The divergence is indeed observed to be minimal around this position, and this confirms the validity of the criterion eq. (4.7).

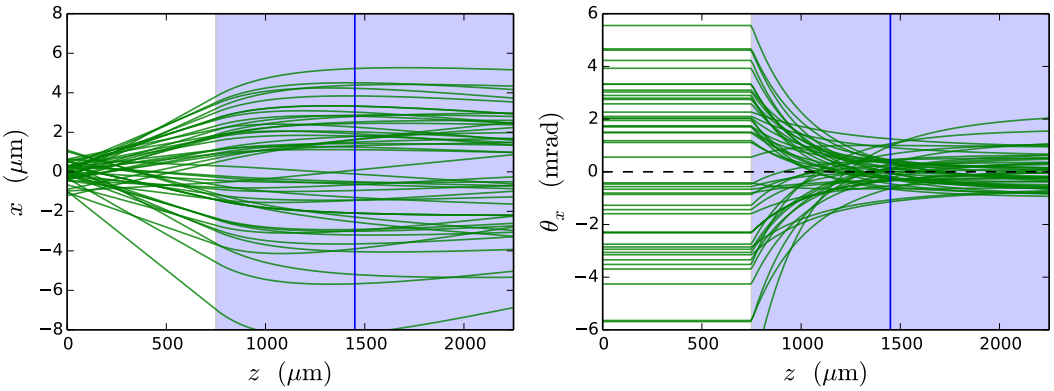

Figure 4.3: Evolution of x and θ_x for several electron of the bunch, as given by eq. (4.1) and eq. (4.4) for random values of x_0 and θ_0. The parameters of the lens are the same as in fig. 4.2 ($\gamma = 200$, $a_0(0) = 5$, $w(0) = 6\,\mu$m, $L_d = 750\,\mu$m, $d = 10\,\mu$m, $\tau = 30\,$fs, $n_2 = 1.7 \times 10^{18}\,\mathrm{cm}^{-3}$). The blue line represents the position at which the second jet should end, according to the criterion eq. (4.7).

4.2.3 Tuning the parameters of the lens

According to the model of the last section, the parameters of the lens should be tuned so as to satisfy eq. (4.7), in order to reach optimal collimation. Yet experimentally, several of the quantities that are involved in eq. (4.7) are known only approximately (e.g. Z_R, $w(0)$, d), and thus this criterion can only give an order of magnitude for the choice of the parameters. It is nonetheless still possible to reach optimal collimation experimentally, by scanning one of the parameters and by observing the corresponding evolution of the divergence. Experimentally, the parameters that can be most easily scanned are the density of the second jet (n_2) and the drift distance (L_d). (The quantity L_l is less easy to vary, since it is determined by the radius of the nozzle that produces the second jet.) It is therefore interesting to predict the evolution of the divergence when n_2 and L_d are scanned.

Scan in density (n_2). Figure 4.4 represents the RMS divergence of a typical electron bunch at the exit of the lens (here $L_l = 750\,\mu$m), as a function of n_2. This curve was obtained by generating a random set of x_0 and θ_0 (which represent the initial bunch – here with $\sqrt{\langle x_0^2 \rangle} = 0.5\,\mu$m and $\sqrt{\langle \theta_0^2 \rangle} = 3\,$mrad), and then by calculating the final θ_x analytically for each x_0 and θ_0, and by averaging these values to find the final RMS divergence $\sqrt{\langle \theta_x^2 \rangle}$. For the values of n_2 for which k_{foc}^2 is positive, the individual θ_x are given by eq. (4.4). On the other hand, for negative k_{foc}^2 (i.e. when k_{foc} is purely imaginary), eq. (4.4) is not valid anymore and another analytical expression[2] is used.

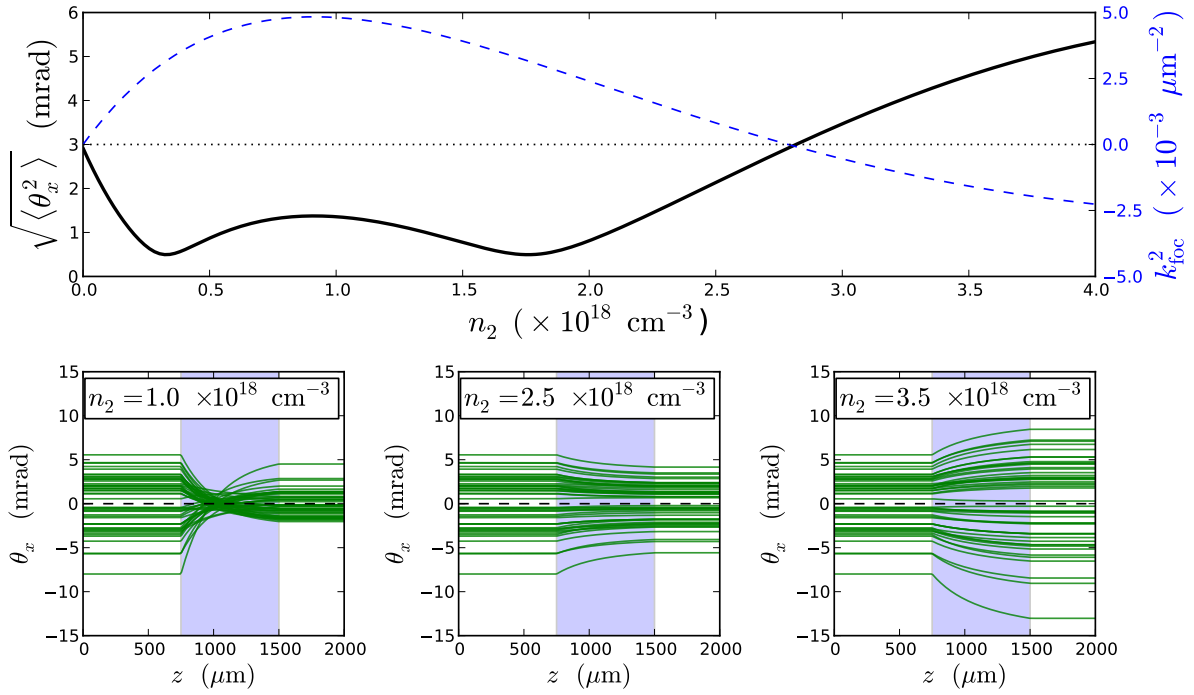

Figure 4.4: Top panel: Evolution of the final RMS divergence of the electron bunch (black solid line) and of the focusing parameter k_{foc}^2 (blue dashed line) as a function of the density n_2. The other parameters are fixed ($\gamma = 200$, $a_0(0) = 5$, $w(0) = 6\,\mu$m, $L_d = 750\,\mu$m, $L_l = 750\,\mu$m, $d = 10\,\mu$m, $\tau = 30\,$fs). The dotted line simultaneously marks the initial RMS divergence of the bunch $\sqrt{\langle \theta_0^2 \rangle} = 3\,$mrad (on the left axis) and the position of $k_{\text{foc}}^2 = 0$ (on the right axis). The bottom panels represent the evolution of θ_x for a few electrons as a function of z, for three different values of n_2.

Three regimes can be observed in fig. 4.4. First, for high densities k_{foc}^2 is negative (because of the term $\sin(k_p d)$ in eq. (4.3)), and the lens is defocusing. Physically, this is due to the fact that the plasma wavelength is very short for high values of n_2, and that, as a result, the electron bunch finds itself in the second half-period of the wakefield ($d > \lambda_p/2$). As mentioned in section 1.1.3, the second half-period is defocusing. In practice, this regime should definitely be avoided, since it results in a higher divergence than the initial one. In the experiments, this imposes to chose

[2] More precisely, in the case where k_{foc}^2 in negative, the solution of eq. (4.3) can be expressed with the functions cosh and sinh: $x(z) = \frac{(x_0+\theta_0 L_d)z}{L_d} \cosh\left(\frac{|k_{\text{foc}}|Z_R^2}{L_d} - \frac{|k_{\text{foc}}|Z_R^2}{z}\right) - \frac{x_0 z}{|k_{\text{foc}}|Z_R^2} \sinh\left(\frac{|k_{\text{foc}}|Z_R^2}{L_d} - \frac{|k_{\text{foc}}|Z_R^2}{z}\right)$ and $\theta_x = d_z x$.

a relatively low density:

$$n_2 < \frac{\pi}{4 r_e d^2} \tag{4.8}$$

For typical values of d ($d \sim 10\,\mu$m), this yields $n_2 < 2 \times 10^{18}\,\mathrm{cm}^{-3}$. In the range of n_2 which satisfy this condition, k_{foc}^2 is observed to go through a maximum. This is essentially because of the resonance of the term η in eq. (4.3) as a function of $ck_p\tau$ (see section 1.1.3). Two other regimes can be seen in this range of n_2. When k_{foc}^2 is low, the bunch is not focused strongly enough and the final divergence is relatively high. On the other hand, for a high k_{foc}^2, the bunch is overfocused and the final divergence can also be high. The optimal value of k_{foc} lies in between these two regimes, and it is given, again, by the criterion eq. (4.7). (Notice that, because k_{foc}^2 is not a bijective function of n_2, there are two values of n_2 which satisfy this criterion.)

Scan in position (L_d). As mentioned previously, it is also possible to scan the position L_d of the second jet. When doing so however, one must first choose a n_2 low enough for the electrons to be in a focusing phase of the wakefield (i.e. eq. (4.8) should be satisfied). Provided that this condition is satisfied, the evolution of the divergence as a function L_d will be similar to that of fig. 4.5.

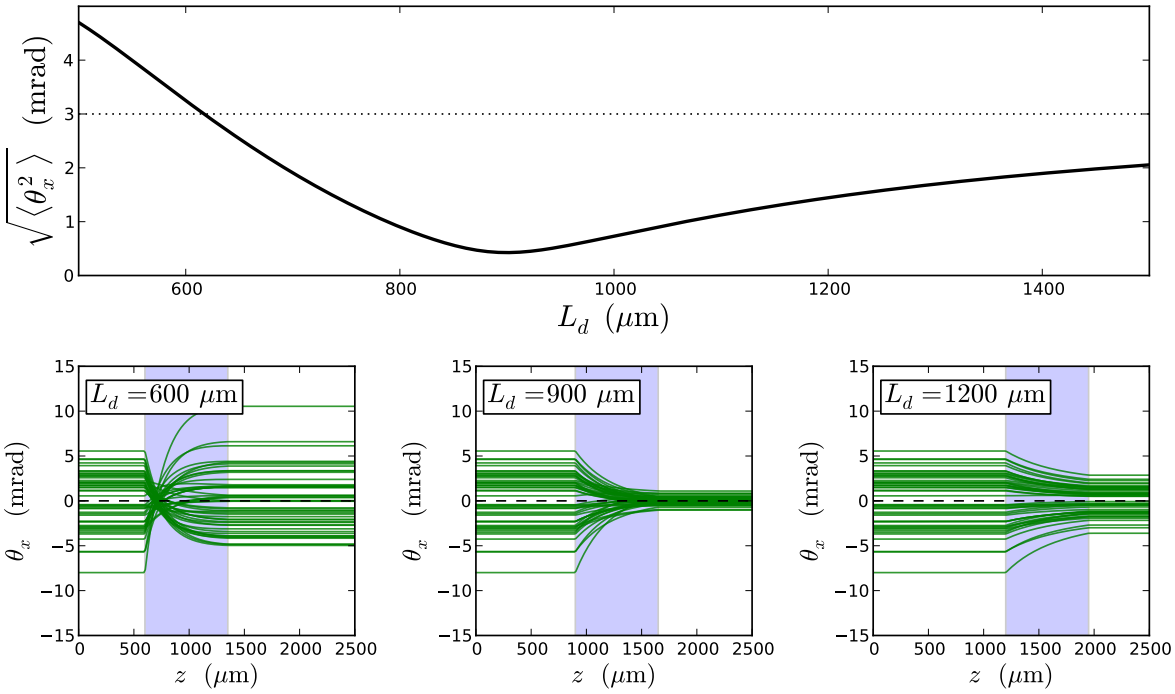

Figure 4.5: Top panel: Evolution of the final RMS divergence of the electron bunch (black solid line) as a function of the position of the second jet L_d. The other parameters are fixed ($\gamma = 200$, $a_0(0) = 5$, $w(0) = 6\,\mu$m, $n_2 = 1 \times 10^{18}\,\mathrm{cm}^{-3}$, $L_l = 750\,\mu$m, $d = 10\,\mu$m, $\tau = 30\,$fs). The dotted line marks the initial RMS divergence of the bunch $\sqrt{\langle\theta_0^2\rangle} = 3\,$mrad. The bottom panels represent the evolution of θ_x for a few electrons as a function of z, for three different values of L_d.

Two regimes can be observed in this figure. For high values of L_d, the bunch is not focused enough (see the lower right panel of fig. 4.5). This is because the laser diffracts considerably over the long distance L_d, and because it produces a relatively weak wakefield once it reaches

the second jet. On the opposite, the bunch is overfocused for low values of L_d (see the lower left panel of fig. 4.5), because the laser pulse has not diffracted enough and the wakefield is too strong[3]. Again, the optimal value of L_d lies in between these two regimes, and is given by eq. (4.7).

Conclusion on the model. On the whole, the model suggests that a laser-plasma lens can be realistically implemented in experiments. The required parameters for the second jet ($n_2 \sim 10^{18}\,\mathrm{cm}^{-3}$, $L_l \sim 1\,\mathrm{mm}$) are indeed quite standard. Moreover, the fact that the final divergence evolves smoothly as a function of n_2 and L_d in figs. 4.4 and 4.5 shows that this scheme does not require a very strong precision when tuning these parameters. Finally, according to the model, the divergence can be expected to be reduced by a factor ~ 6 with this scheme.

4.2.4 Confirmation by PIC simulations

In order to confirm the predictions of the model and to take into account the effects that it neglected (such as e.g. the finite density gradient of the jets), I ran PIC simulations of the laser-plasma lens. The simulations were run with the quasi-cylindrical code Calder Circ and, since the transverse quality of the beam is paramount here, the Cherenkov-free algorithm of section 2.3.1 was used (so as to limit any spurious growth of emittance). However, even with this scheme, the transverse dynamics of the electrons was still observed to be affected by numerical artifacts. I found that these artifacts were due to the interpolation of the $\boldsymbol{B}$ field in time, when calculating the Lorentz force at the positions of the macroparticles (see section 2.1.2). Because this interpolation is only second-order accurate in standard PIC codes, the electrons appeared to have a spuriously high interaction with the back of the laser pulse. I corrected this problem by using a third-order accurate interpolation in time (see appendix C for more details on this point). When using this correction, the observed artifacts vanished and the transverse dynamics of the electrons was physically consistent.

With the Cherenkov-free scheme and the third-order interpolation in time, PIC simulations confirmed the feasibility of the laser-plasma lens. In order to illustrate this, let us consider one of these simulations. In this particular simulation, a 0.7 J, 30 fs laser pulse is focused into a first gas jet having a density $n_1 = 8.8 \times 10^{18}\,\mathrm{cm}^{-3}$, which is then followed by a second jet having a density $n_2 = 1 \times 10^{18}\,\mathrm{cm}^{-3}$ (in accordance with the condition eq. (4.8)). The simulation was run with a resolution $\Delta z = 0.03\,\mu\mathrm{m}$, $\Delta r = 0.2\,\mu\mathrm{m}$ and $c\Delta t = 0.96\Delta z$, using two azimuthal modes ($\ell = 0$ and $\ell = 1$) and 20 macroparticles per cell.

The density profile is represented in the top panel of fig. 4.6, along with the evolution of the laser pulse. The laser self-focuses to a waist $w(0) \simeq 6\,\mu\mathrm{m}$ in the first jet and leads to the self-injection of a 70 pC, 1 fs electron bunch (black lines in fig. 4.6). This bunch is then accelerated up to $\gamma = 450$ (with a 10 % RMS energy spread) and reaches the drift space. Both the bunch and the laser pulse diverge in the drift space (the Rayleigh length of the laser is $Z_R = 150\,\mu\mathrm{m}$), and the bunch is then collimated in the second jet. The evolution of the RMS divergence of the bunch is represented in the bottom panel of fig. 4.6. The divergence oscillates in the first jet (as a consequence of the betatron oscillations of the individual electrons), remains constant in the drift space (as predicted by eq. (4.1)) and decreases in the second jet. In particular, as suggested by eq. (4.4), this decrease progressively slows down as a function of z. In the end, the

[3]Notice here that the hypothesis that the wakefield is in the linear regime may not be valid for low values of L_d. Therefore the results of the model may not be quantitatively exact, although the qualitative fact that the electrons are overfocused for small values of L_d is still expected to be correct.

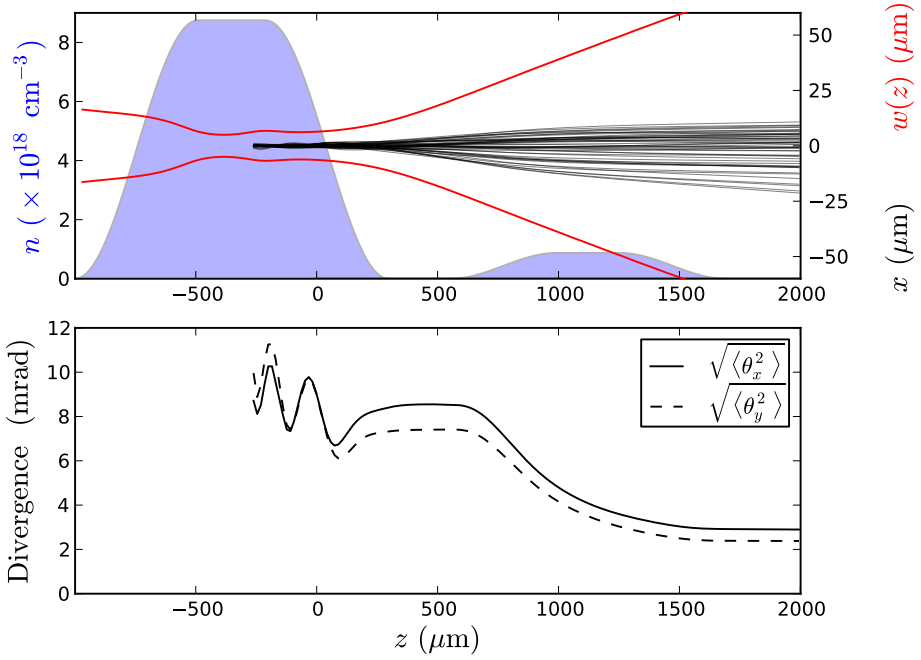

Figure 4.6: Results of the PIC simulation. Upper panel: density profile (blue), laser waist (red) and transverse positions of some of the injected electrons (black), as a function of the propagation coordinate z. Lower panel: RMS divergence of the electrons in the x and y directions. (The laser is polarized along x.)

final divergence is considerably smaller than the initial one, and this confirms the fact that the proposed laser-plasma lens can realistically collimate the electrons.

However, the reduction of the divergence (which corresponds roughly to a factor of 3 here) is not as high as one could have expected from the estimations of the model. This is due to *aberrations* of the laser-plasma lens, that were not considered in the initial model.

4.2.5 Aberrations of the single-pulse lens

As mentioned in section 4.2.2, the final non-zero divergence is due to the fact that the electrons cannot reach $\theta_x = 0$ (or $\theta_y = 0$) simultaneously. In the *ideal* model of section 4.2.2, this is due the fact that the different electrons have different initial x and θ_x, and thus the final divergence is limited by the initial emittance of the beam. Yet in reality, several aberrations induce an additional spread in the position z at which the electrons reach $\theta_x = 0$. As result, these aberrations increase the final divergence above the value predicted by the initial emittance. The next paragraphs describe these aberrations.

"Chromatic" aberrations. In the model of section 4.2.2, all electrons were considered to have the same energy. Yet in reality, the bunch can have a substantial energy spread. Since k_{foc}^2 depends on γ (see eq. (4.3)), the electrons with low energy experience a stronger focusing than the electrons with high energy. Thus the energy spread further prevents the electrons from simultaneously reaching $\theta_x = 0$.

High-radius aberrations. Equation (4.2) shows that the focusing forces e.g. in the x direction are proportional to $x\, e^{-2(x^2+y^2)/w(z)^2}$. In the model of section 4.2.2, it was assumed that the particles satisfied $x, y \ll w(z)$, and thus that the factor $e^{-2(x^2+y^2)/w(z)^2}$ was close to 1. However, in reality this assumption is not necessarily satisfied for all the electrons. Since the values of $x(z)$ and $w(z)$ at the entrance of the lens ($z = L_d$) are $x(L_d) \simeq \theta_0 L_d$ and $w(L_d) \simeq w(0) L_d / Z_R$, the condition $x(z) \ll w(z)$ in the second jet is essentially equivalent to

$$\theta_0 \ll \frac{w(0)}{Z_R}$$

The typical value of the right hand side is around 40 mrad, and thus the electrons of the bunch that have a divergence of the order of 10 mrad do not satisfy this condition. As a consequence of the factor $e^{-2(x^2+y^2)/w(z)^2}$, these electrons effectively feel a lower k_{foc}^2. This can be seen in fig. 4.7, which displays the transverse phase in the PIC simulation of section 4.2.4. As shown in this figure, the particles with a high initial divergence rotate slower in phase space than those with low divergence. Again, because of this, the electrons cannot reach $\theta_x = 0$ simultaneously, and the final divergence is higher than expected.

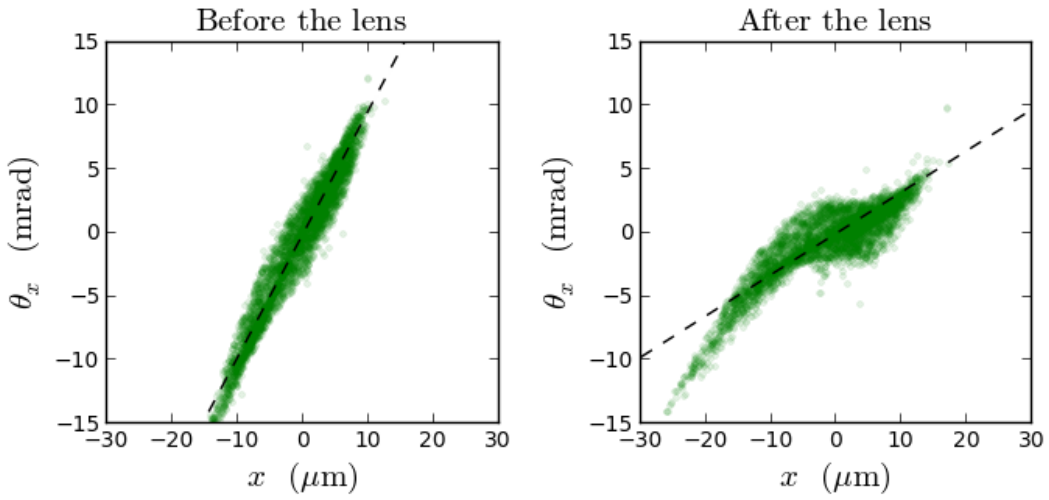

Figure 4.7: Representation of the phase space in the PIC simulation of section 4.2.4 before (left panel) and after (right panel) the lens. The dashed line represents the best linear fit to the phase space. As can be seen, the particles in the center of the plot rotate faster than this dashed line, while the particles with high initial divergence rotate slower.

Transverse beamloading. As the electron bunch propagates in the linear laser-wakefield of the second jet, it can drive a wakefield of its own, and thereby give rise to beamloading effects (see section 1.2.1). These effects are only important for long bunches with a high charge, and they were found to be negligible for the 1 fs, 70 pC bunch of the PIC simulation in section 4.2.4. However, they were observed in other simulations, and fig. 4.8 shows the results of one such simulation. This simulation was similar to that of section 4.2.4, but a higher laser energy (1.6 J) was used, and lead to the injection of more charge (130 pC). The upper left panel of fig. 4.8 shows the aspect of the wakefield in the second jet. The laser is observed to drive a weak, linear wakefield, while the high-charge bunch drives a strong wakefield of its own within the linear

wakefield. In this case, the electrons in the tail of the bunch (blue and green dots) effectively experience the focusing wakefield generated by the head of the bunch (red dots). As a result, the electrons in the tail undergo a stronger focusing than those in the head, and they rotate faster in phase space. This can be seen in the left panels of fig. 4.8, which represent the transverse phase space before and after the lens. Again, the fact that the particles rotate with different speed in phase space prevents them from being properly collimated, and results in a higher final divergence.

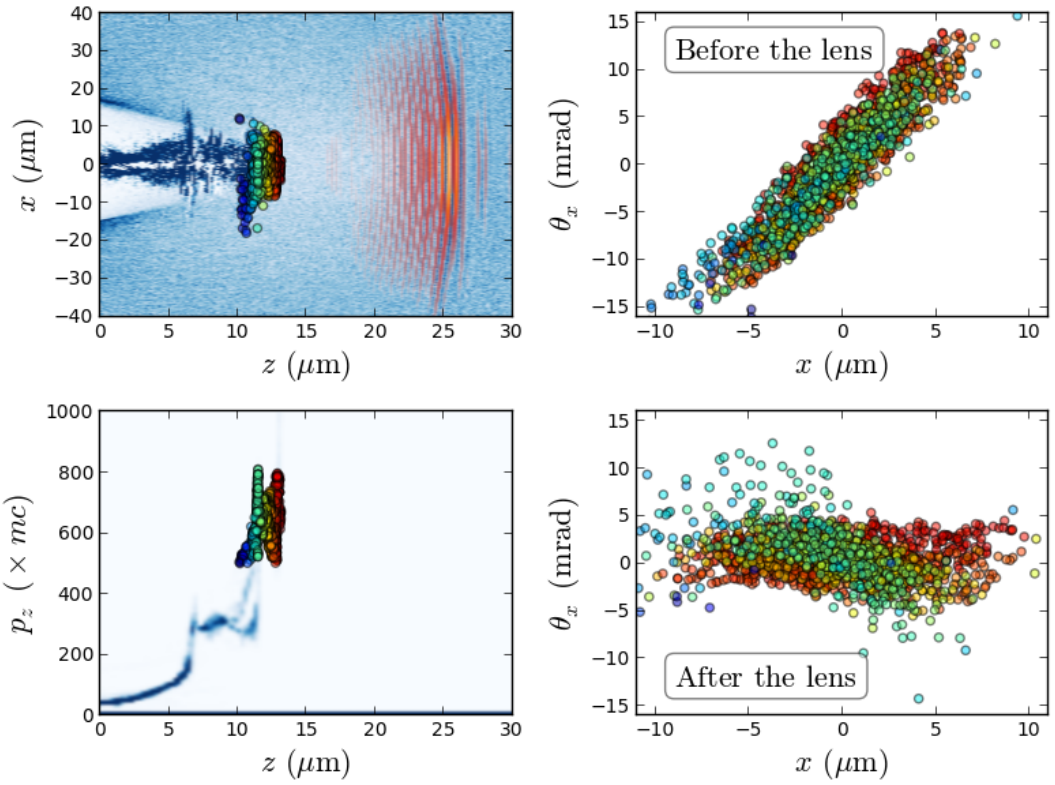

Figure 4.8: Upper left panel: Snapshot of a PIC simulation featuring a 130 pC bunch, in the second gas jet. Lower left panel: Longitudinal phase space at the same time in the simulation. The macroparticles in the higher energy part of the bunch (colored dots) are selected and followed in transverse phase space. (The color corresponds to their longitudinal position in the bunch.) Right panel: Position of these macroparticles in transverse phase space, before (upper panel) and after (lower panel) the lens.

From this simulation, it appears that transverse beamloading can potentially be an important aberration, but that it crucially depends on the charge and the geometry of the bunch. In order to determine the scaling of this aberration, I developed a model for nonlinear transverse beamloading in a linear laser-wakefield.

4.3 Transverse beamloading in the single-pulse lens

The aim of this section is thus to model the wakefield driven by a bunch within a linear laser-wakefield, and to calculate the focusing force that this wakefield produces on the bunch itself. In addition to the laser-plasma lens, this type of model can also be useful to other situations that may occur in laser-wakefield acceleration. For instance, in the context of two-stage laser-wakefield acceleration, it has been suggested to use a linear wakefield in the second stage, instead of a blown-out cavity [Schroeder et al., 2010; Paradkar et al., 2013]. In this case also, the head of the bunch can drive a wakefield which produces a focusing force on the tail of the bunch. As a result of this inhomogeneous focusing force, the emittance of the bunch can degrade during the acceleration (see section 1.3.2). Another important situation is that in which an unguided laser pulse propagates in a long gas jet. In this case, experiments [Corde et al., 2011] and simulations [Pae et al., 2010] showed that the laser-wakefield transitions from a blown-out cavity to a linear wakefield as the laser progressively diffracts. Here again, the trailing electron bunch can drive its own wakefield within the linear wakefield.

In view of these various situations, it is important to have a formalism to calculate the bunch-driven wakefield, within a linear laser-wakefield. Yet to date, there is no comprehensive satisfying formalism for this beamloading phenomenon. As mentioned in section 1.2.1, beamloading in a linear wakefield can be described analytically when the density perturbation produced by the bunch is small compared to the background density (linear beamloading). However, this is clearly not the case in fig. 4.8, where the bunch produces a strongly evacuated cavity in its wake. Alternatively, Rosenzweig et al. [1991] developed a model for this type of nonlinear bunch-driven wakefield, but their formalism is purely *electrostatic* and *non-relativistic*. Yet in the case of the laser-plasma lens, the bunch can be so intense that it can push the plasma electrons to relativistic energies. As a consequence, the plasma electrons gain inertia and become sensitive to the magnetic fields of bunch – and these effects are not taken into account in a classical and electrostatic model. Finally, Mora and Antonsen [1997] developed a *fully-relativistic* and *fully-electromagnetic* framework, which was summarized in section 1.1.2. Although Lu et al. [2006b]; Tzoufras et al. [2009] used this framework to describe nonlinear beamloading inside a *blown-out cavity*, it has not yet been applied to nonlinear beamloading inside a *linear wakefield*.

Thus, in this section, I use the framework of Mora and Antonsen [1997] to describe a nonlinear bunch-driven wakefield within a linear laser-driven wakefield.

4.3.1 Description of the model and governing equations

Overview. The situation modeled is represented schematically in fig. 4.9. A weak laser pulse (red) precedes the bunch and drives a weak wakefield (light red), in which the bunch (green) drives its own wakefield (light green). (Notice that the longitudinal coordinate in fig. 4.9 is $\xi = ct - z$, which is why the image appears inverted when compared with the upper left panel of fig. 4.8.) Here we are particularly interested in the region that immediately surrounds the electron bunch, and where the bunch-driven wakefield only starts to develop.

Three species are considered in the model:

- the motionless plasma ions, whose constant and uniform density is denoted n_i.
- the plasma electrons, whose density and dimensionless velocity are denoted n_p and $\boldsymbol{\beta}_p$. Notice that, because of the presence of the laser-driven wakefield, these electrons can already have a non-zero velocity when the bunch reaches them (i.e. at $\xi \simeq 0$ in fig. 4.9).

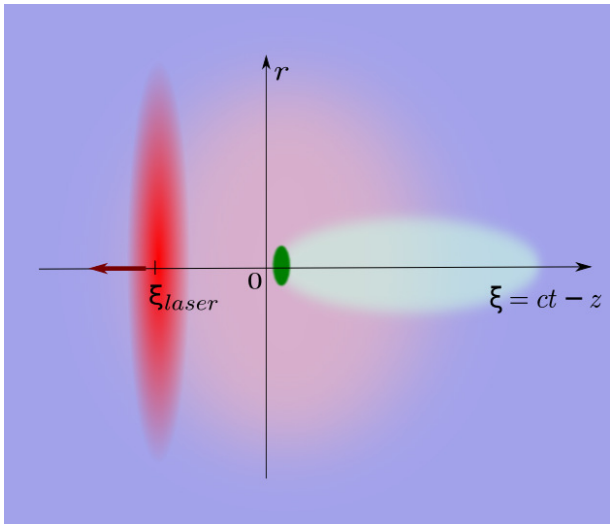

Figure 4.9: Schematic representation of the situation modeled. The electron density is represented in blue. Within this density, the laser pulse (red) and the ultrarelativistic bunch (green) drive their own wakefields (represented in light red and light green respectively).

- the ultrarelativistic electrons of the bunch, whose density and dimensionless velocity are denoted n_b and $\boldsymbol{\beta}_b$, and which satisfy $\beta_{b,z} \simeq 1$. In typical LWFA situations, the bunch is much denser than the surrounding plasma ($n_b \gg n_i, n_p$).

The laser pulse, the bunch and the wakefields are assumed to be cylindrically symmetric, and thus the problem is studied in cylindrical coordinates r, θ, z. In addition, both the laser pulse and the ultrarelativistic bunch are assumed to evolve on a timescale much longer than the crossing time of the plasma electrons. Thus the whole structure propagates essentially at the speed of light, and, when studying the motion of the electrons, all quantites are assumed to depend on z and t only through $\xi = ct - z$. (This is the *quasi-static* approximation which was introduced in section 1.1.2.) Finally, the trajectories of the plasma electrons are considered not to cross in the neighborhood of the driving bunch. In fact, PIC simulations tend to show that these trajectories usually cross a few microns behind the beam. Yet the length of the driving bunch is usually of the order of one micron, and thus trajectory crossing can be neglected when studying the dynamics of the driving bunch.

Governing equations With these approximations, the quasi-static ponderomotive formalism of section 1.1.2 can be used here. From eqs. (1.10) to (1.12), the field equations of this formalism read:

$$\frac{\partial}{\partial r}\left(\frac{1}{r}\frac{\partial\,(r\,a_r)}{\partial r}\right) = 4\pi r_e(n_p\beta_{p,r} + n_b\beta_{b,r}) \tag{4.9}$$

$$\frac{1}{r}\frac{\partial}{\partial r}\left(r\frac{\partial\,\phi}{\partial r}\right) = 4\pi r_e(n_p + n_b - n_i) \tag{4.10}$$

$$\frac{1}{r}\frac{\partial}{\partial r}\left(r\frac{\partial\,\psi}{\partial r}\right) = 4\pi r_e[\,n_p(1-\beta_{p,z}) + n_b(1-\beta_{b,z}) - n_i\,] \tag{4.11}$$

where ϕ and $\boldsymbol{a}$ are the dimensionless scalar potential and vector potential and where $\psi = \phi - a_z$. Compared to eqs. (1.10) to (1.12), the electron density n_e has been replaced by the sum of the

density of the plasma electrons n_p and the density of the electrons of the bunch n_b. Similarly, $\boldsymbol{j}_e$ has been replaced by $\boldsymbol{j}_p + \boldsymbol{j}_b$, and moreover $\boldsymbol{j}_p$ and $\boldsymbol{j}_b$ have been written as $n_p\boldsymbol{\beta}_p$ and $n_b\boldsymbol{\beta}_b$ respectively. This is because, since there is no trajectory crossing, there is a unique, well-defined velocity $\boldsymbol{\beta}_p$ (resp. $\boldsymbol{\beta}_b$) at each point in space.

Similarly, the motion of the plasma electrons in this quasi-static formalism is given by eqs. (1.14) and (1.15). These two equations can be combined into the following equation[4]:

$$\frac{d}{d\xi}(1+\psi)\frac{d\,r_p}{d\xi} = \frac{\partial a_r}{\partial \xi} + \frac{\partial \phi}{\partial r} + \left(\frac{\gamma_p}{1+\psi} - 1\right)\frac{\partial \psi}{\partial r} - \frac{1}{2(1+\psi)}\frac{\partial \langle \boldsymbol{a}_l^2\rangle}{\partial r} \tag{4.12}$$

Finally, eq. (1.19) expresses the radial focusing force experienced by the ultrarelativistic electrons of the bunch inside the wakefield:

$$F_{b,r} = mc^2\frac{\partial \psi}{\partial r} \tag{4.13}$$

Thus the field equations eqs. (4.9) to (4.11) and the equation of motion eq. (4.12) must be integrated jointly in order to find the wakefield quantity $\partial_r\psi$, which can then be used to calculate the force on the electrons of the bunch, through eq. (4.13). In order to do so, let us first take into account the specificities of the problem to simplify the above equations.

4.3.2 Approximate system

Field equations. As mentioned previously, the electron bunch is much denser than the plasma, i.e. $n_b \gg n_p, n_i$. This allows to neglect the terms n_p and n_i in the equation for ϕ (eq. (4.10)). On the other hand, because the bunch is ultrarelativistic ($1-\beta_{b,z} \ll 1$), the term $n_b(1-\beta_{b,z})$ is typically negligible compared to $n_p(1-\beta_{p,z})$ in the equation for ψ (eq. (4.11)). For instance, a 200 MeV, 100 pC bunch with a transverse and longitudinal size of 1 μm has a density $n_b = 2\times10^{20}\,\mathrm{cm}^{-3}$, but $n_b(1-\beta_{b,z}) = 2\times10^{15}\,\mathrm{cm}^{-3}$. By comparison, in the situations of interest here, the plasma has a density $n_p \sim 10^{18}\,\mathrm{cm}^{-3}$ and PIC simulations show that, in realistic conditions, $(1-\beta_{p,z}) > 10^{-1}$. Therefore, equations eqs. (4.9) to (4.11) are simplified in the following way:

$$\frac{\partial}{\partial r}\left(\frac{1}{r}\frac{\partial\,(r\,a_r)}{\partial r}\right) = 4\pi r_e(n_p\beta_{p,r} + n_b\beta_{b,r}) \tag{4.14}$$

$$\frac{1}{r}\frac{\partial}{\partial r}\left(r\frac{\partial\,\phi}{\partial r}\right) = 4\pi r_e n_b \tag{4.15}$$

$$\frac{1}{r}\frac{\partial}{\partial r}\left(r\frac{\partial\,\psi}{\partial r}\right) = 4\pi r_e[\,n_p(1-\beta_{p,z}) - n_i\,] \tag{4.16}$$

According to the above set of equations, ϕ corresponds to the space-charge fields that would be created by the ultrarelativistic bunch if it was in vacuum, while ψ represents the fields generated by the presence of the perturbed plasma (i.e. the wakefield).

Motion of the plasma electrons. Let us assess the importance of each term in the right-hand side of eq. (4.12). First of all, the term proportional to $\partial_r\langle \boldsymbol{a}_l^2\rangle$ represents the ponderomotive force of the laser pulse. This term can be neglected here, since we aim to study the dynamics of the plasma electrons *in the immediate neighborhood of the bunch*, and since the laser field is weak or even zero in this neighborhood. Similarly, the term proportional to $\partial_r\psi$ is negligible

[4]Here, as in chapter 1, we use the Lagrangian point of view as the natural point of view. However, the Eulerian point of view is equally valid, and it is in fact used in section 4.3.2 in order to calculate the density n_p. (This is done by using the correspondance between the Eulerian and Lagrangian point of view: $\boldsymbol{\beta_p}(\boldsymbol{r}_p) = \frac{1}{c}\frac{d\boldsymbol{r}_p}{dt}$)

compared to $\partial_r\phi$. This is because $n_b \gg n_p, n_i$ and thus, from eqs. (4.15) and (4.16), $|\phi| \gg |\psi|$. (In addition, the factor $\gamma_p/(1+\psi)-1$ is typically of order unity in realistic conditions, since the plasma electrons are only mildy relativistic.)

Finally, let us compare the terms $\partial_\xi a_r$ and $\partial_r\phi$ by integrating eqs. (4.14) and (4.15). Using the relations $a_r(r=0) = a_r(r=\infty) = 0$, $\partial_r a_r(r=\infty) = 0$ and $\partial_r\phi(r=0) = 0$ as boundary conditions, this integration leads to:

$$\frac{\partial\phi}{\partial r} = 4\pi r_e \left(\frac{1}{r}\int_0^r n_b(r',\xi) r'\, dr'\right)$$
$$\frac{\partial a_r}{\partial \xi} = -\frac{2\pi r_e}{r}\int_0^r \frac{\partial(n_b\beta_{b,r} + n_p\beta_{p,r})}{\partial\xi}(r')^2\, dr' - 2\pi r_e r \int_r^\infty \frac{\partial(n_b\beta_{b,r} + n_p\beta_{p,r})}{\partial\xi}\, dr'$$

If $\beta_\perp$ is the typical transverse velocity of the electrons of the bunch, R the typical radial size of the bunch and L its typical length scale along ξ, the order of magnitude of the ratio of these terms is

$$\frac{\partial_\xi a_r}{\partial_r\phi} \sim \frac{R}{L}\left(\beta_\perp + \frac{n_p}{n_b}\right)$$

where it was assumed that the radially expelled plasma electrons have $\beta_{p,r} \sim 1$. In typical situations, $\beta_\perp < 10^{-2}$ rad, $n_p/n_b < 10^{-2}$ and the aspect ratio of the bunch R/L usually satisfies $R/L < 10$. Thus the term $\partial_\xi a_r$ is typically negligible. On the whole, the term $\partial_r\phi$ dominates the right-hand side of eq. (4.12).

Let us now also evaluate the variation $\Delta\psi$ of the factor $1+\psi$ in the left-hand side of that equation. Note here that the quantity ψ is maximal on axis, inside the bunch-driven wakefield, and that its highest possible value is reached if the wake is fully evacuated. One may thus find an upper bound for $|\Delta\psi|$ by calculating the value $|\Delta\psi|_{\max}$ corresponding to a fully-blown wakefield of transverse size R. By integrating eq. (4.16), one finds $|\Delta\psi|_{\max} = \pi r_e n_i R^2 = k_p^2 R^2/4$, where $k_p = \sqrt{4\pi r_e n_i}$ is the plasma wavector associated with the ion density. For a bunch having a radius $R \sim 1\,\mu$m and $n_i = 10^{18}\,\mathrm{cm}^{-3}$, one has $|\Delta\psi_{\max}| \approx 3\times10^{-2}$. Since $|\Delta\psi|_{\max}$ is an upper bound for the variations of ψ, the factor $1+\psi$ can be considered to be constant along the trajectory of a plasma electrons, i.e. $1+\psi = 1+\psi_0$ where ψ_0 is the value of ψ at $\xi = 0$, before the electron has been reached by the bunch. While this approximation may be the least rigorous of the above set of approximations, it is nonetheless confirmed by PIC simulations – as will be seen in the next section.

Taking into account the above considerations, the equation of motion eq. (4.12) becomes

$$\frac{d^2 r_p}{d\xi^2} = \frac{4\pi r_e}{1+\psi_0}\left(\frac{1}{r_p}\int_0^{r_p} n_b(r',\xi) r'\, dr'\right) \tag{4.17}$$

A striking result here is that, although the plasma electrons can be pushed to relativistic energies by the space charge of the bunch, their equation of motion– when expressed as a function of ξ – is very similar to that of the *non-relativistic* and *electrostatic* model of Rosenzweig et al. [1991]. In this model, the equation of motion is $d_\xi^2 r_p = 4\pi r_e \left(\frac{1}{r_p}\int_0^{r_p} n_b(r',\xi) r'\, dr'\right) - 4\pi r_e n_i (r_p - r_0)$, where r_0 is the value of r_p at $\xi = 0$ (i.e. before the bunch reaches the electron). However, these two equations differ in two important ways.

- Equation (4.17) features a constant factor $1/(1+\psi_0)$. This factor takes into account the fact that the plasma electrons may already be mildly relativistic when the bunch reaches them, which slightly increases their inertia.

- The equation obtained with the non-relativistic and electrostatic model features an additional term $-4\pi r_e n_i (r_p - r_0)$. This term represents the impact of the restoring force of the ions on the motion of the plasma electrons. This restoring force is not present in eq. (4.17), essentially because the terms n_i and $n_p(1-\beta_{p,z})$ were neglected in eq. (4.16). Physically, this force is important when describing the bunch-driven wakefield *over a full plasma period*, as it is precisely this force which responsible for the plasma oscillations. Yet, when describing the wakefield over the small length of the driving bunch (which is much shorter than a plasma period), this force does not have enough time to have a substantial impact, and thus neglecting it is a good approximation.

Focusing force on the electrons of the bunch. According to eq. (4.13), the force experienced by the electrons of the bunch is $F_{b,r} = mc^2 \partial_r \psi$. The term $\partial_r \psi$ can be calculated by integrating eq. (4.16):

$$F_{b,r} = 4\pi r_e\, mc^2 \left[\left(\frac{1}{r} \int_0^r n_p(r',\xi) \left[\, 1 - \beta_{p,z}(r',\xi) \,\right] r'\, dr' \right) - \frac{n_i r}{2} \right]$$

The integral in the right-hand side can be calculated by noticing that the quantity $\int_0^{r_p(\xi)} n_p(r',\xi) \left[\, 1 - \beta_{p,z}(r',\xi) \,\right] dr'$ is independent of ξ for any plasma electron trajectory $r_p(\xi)$[5]. As a consequence,

$$\int_0^r n_p(r',\xi) \left[\, 1 - \beta_{p,z}(r',\xi) \,\right] r' dr' = \int_0^{r_0(r,\xi)} n_{p,0} \left[\, 1 - \beta_{p,z,0} \,\right] r' dr'$$

where $n_{p,0}$ and $\beta_{p,z,0}$ are the values of n_p and $\beta_{p,z}$ at $\xi = 0$, and where $r_0(r,\xi)$ is the radial position such that a plasma electron which is initially at $r_0(r,\xi)$ would reach the radial position r at ξ. In practice, in order to find $r_0(r,\xi)$, one needs to integrate eq. (4.17) to find $r_p(\xi, r_0)$ and invert the solution. The force experienced by the electrons of the bunch is then

$$F_{b,r} = 4\pi r_e\, mc^2 \left[\left(\frac{1}{r} \int_0^{r_0(r,\xi)} n_{p,0} \left[\, 1 - \beta_{p,z,0} \,\right] r'\, dr' \right) - \frac{n_i r}{2} \right] \tag{4.18}$$

This equation can be compared with the corresponding equations in other models. In the electrostatic model of Rosenzweig et al. [1991], the term $\int_0^{r_0} n_{p,0} \left[\, 1 - \beta_{p,z,0} \,\right] r'\, dr'$ is replaced by $\int_0^{r_0} n_{p,0}\, r'\, dr'$. This is because this type of model neglects the magnetic field generated by the plasma electrons. However, if the plasma electrons are relativistic ($|\beta_{p,z,0}| \approx 1$), they can produce a strong magnetic field, which can alter the Lorentz force experienced by the bunch. On the other hand, in a blown-out cavity [Lu et al., 2006b], the term $\int_0^{r_0} n_{p,0} \left[\, 1 - \beta_{p,z,0} \,\right] r'\, dr'$ is neglected altogether, since the cavity is completely void of electrons. In this case, the bunch feels a force $F_{b,r} = -2\pi r_e mc^2 n_i r = -mc^2 k_P^2 r/2$ associated with the bare ion cavity. Yet, in our

[5] This property is a consequence of the equation of continuity $\partial_t n_p + \boldsymbol{\nabla} \cdot (n_p c \boldsymbol{\beta}_p) = 0$, which can be rewritten as $\partial_\xi n_p (1-\beta_{p,z}) + \frac{1}{r}\partial_r (n_p \beta_{p,r}) = 0$ in the context of the quasistatic formalism that is used in this section. Using this equation, $\int_0^{r_p(\xi)} n_p (1-\beta_{p,z})\, r\, dr$ can be shown to be constant:

$$\begin{aligned}
\frac{d}{d\xi} \int_0^{r_p(\xi)} n_p\,(1-\beta_{p,z})\, r\, dr &= \int_0^{r_p(\xi)} \frac{\partial}{\partial \xi} \left[\, n_p\,(1-\beta_{p,z}) \,\right] r dr + \left(\frac{d\, r_p}{d\xi} \right) n_p(r_p,\xi) \left[\, 1 - \beta_{p,z}(r_p,\xi) \,\right] r_p \\
&= -\int_0^{r_p(\xi)} \frac{\partial}{\partial r} \left[\, r\, n_p\, \beta_{p,r} \,\right] dr + \left(\frac{1}{c} \frac{d\, r_p}{dt} \right) n_p(r_p,\xi)\, r_p \\
&= -r_p\, n_p(r_p,\xi)\, \beta_{p,r}(r_p,\xi) + \beta_{p,r}(r_p,\xi)\, n_p(r_p,\xi)\, r_p \qquad = 0
\end{aligned}$$

model, the bunch travels in a partially evacuated cavity, and the term $\int_0^{r_0} n_{p,0}[\,1-\beta_{p,z,0}\,]\,r'\,dr'$ represents the shielding effect of the plasma electrons over the ions.

On the whole, for a given bunch profile $n_b(r,\xi)$, eq. (4.17) should be integrated, so as to find $r_p(\xi,r_0)$. Then this solution should be inverted to find $r_0(r,\xi)$ and injected into eq. (4.18). Let us illustrate this procedure in the case of a flat-top bunch.

4.3.3 Application to a flat-top bunch in a linear laser-wakefield

Here let us consider a flat-top bunch of the form

$$n_b(r,\xi) = \begin{cases} n_{b,0} & \text{if } 0<r<L \text{ and } r<R \\ 0 & \text{otherwise} \end{cases}$$

which travels behind a sine-like laser pulse of the form

$$\boldsymbol{a} = \begin{cases} a_0 \cos[\,k_0(\xi-\xi_{\text{laser}})\,] \cos\left(\frac{\pi}{2}\frac{(\xi-\xi_{\text{laser}})}{c\tau}\right) \exp\left(-\frac{r^2}{w^2}\right) & \text{if } |\xi-\xi_{\text{laser}}|<c\tau \\ 0 & \text{otherwise} \end{cases}$$

with $\xi_{\text{laser}}<0$ (as represented in fig. 4.9) and $a_0^2 \ll 1$ (linear wakefield). As before, w denotes the waist of the laser and τ its FWHM duration. It is further assumed that $R \ll w$, and thus the high-radius effects that were described in section 4.2.5 are not taken into account here.

In this case, the laser-driven wakefield that forms ahead of the bunch ($\xi<0$) can be calculated analytically (see section 1.1.3). For the above model, the quantities of interest are:

$$\beta_{p,r} = \left(\frac{\eta\, a_0^2\, r}{k_p w^2}\right) \cos[\,k_p(\xi-\xi_{\text{laser}})\,]$$

$$\beta_{p,z} = -\frac{\eta\, a_0^2}{4} \sin[\,k_p(\xi-\xi_{\text{laser}})\,]$$

$$n_p(1-\beta_{p,z}) = n_i - n_i \frac{2\,\eta\, a_0^2}{k_p^2 w^2} \sin[\,k_p(\xi-\xi_{\text{laser}})\,]$$

$$\psi = \frac{\eta\, a_0^2}{4} \sin[\,k_p(\xi-\xi_{\text{laser}})\,]$$

where $\eta = \pi^2 \sin(\omega_p\tau)/[\,\pi^2-(\omega_p\tau)^2\,]$ quantifies how efficiently the laser drives its wakefield. Here again, $k_p = \sqrt{4\pi r_e n_i}$ is the plasma wavevector associated with the background ion density and $\omega_p = ck_p$. Note that, in the above equations, the expression of the laser wakefield has been simplified, by using the assumption $R \ll w$.

Motion of the plasma electrons. With the above hypotheses, eq. (4.17) becomes

$$\frac{d^2 r_p}{d\xi^2} = \frac{{k'_b}^2}{2} r_p \qquad \text{with} \quad {k'_b}^2 = \frac{k_b^2}{1+\frac{\eta\, a_0^2}{4}\sin(\,k_p|\xi_{\text{laser}}|\,)} \quad \text{and} \quad k_b^2 = 4\pi r_e n_{b,0} \tag{4.19}$$

where k_b is the plasma wavevector associated with the density of the bunch, and where $k'_b = k_b/\sqrt{1+\psi_0}$ takes into account the fact that the plasma electrons can initially be mildly relativistic, due to the laser-wakefield.[6]

[6] Here, the difference between k_b and k'_b may seem very small and possibly insignificant, since $a_0^2 \ll 1$. However, it turns out that k'_b later appears in the argument of an exponentially-growing function (see eq. (4.20)), and thus the small difference between k_b and k'_b can have a substantial impact on the final result. Consistently, we observed that it was important to retain the term k'_b in order to have a good agreement with the simulations.

Let us consider a plasma electron which is initially at r_0 for $\xi = 0$. The initial value of the derivative of r_p is $d_\xi r_p|_{\xi=0} = d_t r_p|_{\xi=0}/[\,c(1-\beta_{p,z,0})\,] = \beta_{p,r,0}/(1-\beta_{p,z,0})$. With these initial conditions, the solution of eq. (4.19) reads

$$r_p = r_0 \cosh\left(\frac{k'_b \xi}{\sqrt{2}}\right) + r_0 \left(\frac{\sqrt{2}\,\eta\, a_0^2 k'_b}{k_b^2 k_p w^2}\right) \cos(k_p \xi_{\text{laser}}) \sinh\left(\frac{k'_b \xi}{\sqrt{2}}\right) \tag{4.20}$$

This expression is valid as long as the electron remains inside the bunch ($0 < \xi < L$, $r_p < R$). This solution is plotted in the left panel of fig. 4.10, for different values of r_0 and for the parameters of table 4.1.

Laser parameters	Bunch and plasma parameters
$w = 10\,\mu$m	$R = 1\,\mu$m
$c\tau = 9\,\mu$m	$L = 1\,\mu$m
$\xi_{\text{laser}} = -10\,\mu$m	$n_{b,0} = 2\times10^{20}\,\text{cm}^{-3}$ $\quad (Q_{\text{bunch}} = 100\,\text{pC})$
$a_0 = 0.5$	$n_i = 1\times10^{18}\,\text{cm}^{-3}$

Table 4.1: Typical laser wakefield parameters, used for the analytical calculations of fig. 4.10 and for the PIC simulations of fig. 4.11.

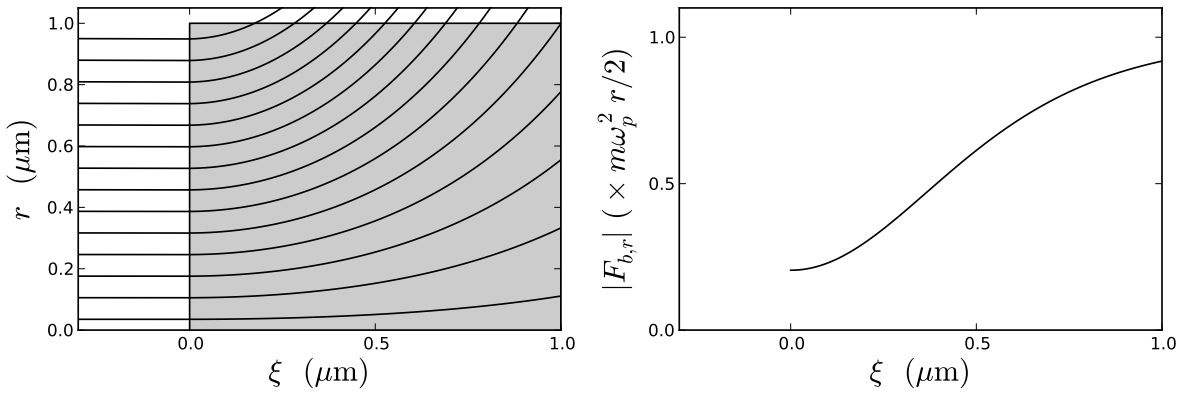

Figure 4.10: Left panel: Trajectories of the plasma electrons as given by eq. (4.20) and for the parameters of table 4.1. The gray rectangle represents the flat-top electron bunch. Right panel: Focusing force experienced by the electrons of the bunch, at a given radius $r < R$ (solid line). On both panels, the head of the bunch is on the left ($\xi = 0\,\mu$m) and its tail is on the right ($\xi = 1\,\mu$m).

Focusing force on the electrons of the bunch. In order to calculate the force $F_{b,r}$ on the electrons of the bunch, let us invert eq. (4.20):

$$r_0(r_p, \xi) = \frac{r_p}{\cosh\left(\frac{k'_b \xi}{\sqrt{2}}\right) + \frac{\sqrt{2}\,\eta\, a_0^2\, k'_b}{k_b^2 k_p w^2} \cos(k_p \xi_{\text{laser}}) \sinh\left(\frac{k'_b \xi}{\sqrt{2}}\right)}$$

When injecting this expression into eq. (4.18), along with the expression $n_{p,0}(1-\beta_{p,z,0})$ from the laser-wakefield formulas, the focusing force $F_{b,r}$ reads:

$$F_{b,r} = -\frac{m\omega_p^2}{2}\, r \left(1 - \frac{1 + \left(\frac{2\,\eta\, a_0^2}{k_p^2 w^2}\right) \sin(k_p \xi_{\text{laser}})}{\left[\cosh\left(\frac{k_b' \xi}{\sqrt{2}}\right) + \left(\frac{\sqrt{2}\,\eta\, a_0^2 k_b'}{k_b^2 k_p w^2}\right) \cos(k_p \xi_{\text{laser}}) \sinh\left(\frac{k_b' \xi}{\sqrt{2}}\right)\right]^2} \right) \tag{4.21}$$

This force is linear in r, but has on a nonlinear dependency on ξ. The variation of $F_{b,r}$ as a function of ξ is represented in the right panel of fig. 4.10. As can be seen in this figure, the force transitions from a weak focusing force (due to the laser-driven wakefield) at the head of the bunch ($\xi = 0$) to a strong focusing force (due to bunch-driven wakefield) at the tail of the bunch ($\xi = 1\,\mu$m).

Confirmation by PIC simulations. In order to validate the above predictions and the corresponding approximations, I ran a high-resolution PIC simulation of a flat-top bunch traveling behind a weak laser pulse. The parameters of the laser, the bunch and the plasma are those of table 4.1. The simulation was run with the quasi-cylindrical code Calder Circ and the Cherenkov-free algorithm of section 2.3.2. Two azimuthal modes were used, and the resolution was $\Delta z = 1.3 \times 10^{-2}\,\mu$m, $\Delta r = 2.5 \times 10^{-2}$ and $c\Delta t = \Delta z$[7].

As mentioned in section 4.3.2, the space-charge fields generated by the plasma electrons (which are contained in ψ) are much weaker than the fields generated by the bunch (which are contained in ϕ). However, in this simulation, we are particularly interested in the fields generated by the plasma electrons, since it is those fields that determine the focusing force on the bunch. This imposes to reduce the numerical noise as much as possible, since any source of noise can easily exceed these weak fields. For this reason, the macro-particles were initialized in a regularly-spaced manner – with 64 macro-particles per cell – and high-order shape factors where used when interpolating and projecting the fields on the grid.

At the beginning of the simulation, the relativistic flat-top bunch is initialized in vacuum (with $\gamma_b = 400$ and no radial velocity), and its initial space-charge fields are obtained by using the matrix-inversion method of Cowan et al. [2013].[8] Shortly after initialization, the laser and the bunch enter a pre-ionized plasma. The trajectories of a few plasma electrons are represented in the left panel of fig. 4.11, and compared with the theoretical predictions of eq. (4.20). As can be seen, the agreement between the predictions and the simulation results is excellent. Notice that the electrons do reach relativistic energies as they are expelled by the bunch ($\gamma_p \sim 3$). This justifies the relativistic approach that has been adopted throughout this section.

[7] In section 2.3.3, it was mentioned that $c\Delta t = \Delta z$ lead to a high level of Nyquist noise. However, in this particular simulation, the Nyquist noise appeared to be relatively low, and did not impact the simulation significantly. This was probably because of the high resolution of this simulation, and because additional measures where taken in order to reduce the overall noise of the simulation.

[8] More precisely, in order to initialize the space-charge fields of the bunch, Cowan et al. [2013] pointed out that the fields of a bunch propagating at a constant speed $\boldsymbol{\beta} = \beta \boldsymbol{e}_z$ satisfy:

$$\frac{\partial^2 \phi}{\partial x^2} + \frac{\partial^2 \phi}{\partial y^2} + \frac{1}{\gamma^2}\frac{\partial^2 \phi}{\partial z^2} = 4\pi r_e n_e \qquad \frac{\partial^2 \boldsymbol{a}}{\partial x^2} + \frac{\partial^2 \boldsymbol{a}}{\partial y^2} + \frac{1}{\gamma^2}\frac{\partial^2 \boldsymbol{a}}{\partial z^2} = 4\pi r_e n_e \beta \boldsymbol{e}_z$$

(These equations can be derived from the propagation equations eqs. (1.1) and (1.2) by using the fact that, for a bunch propagating at a constant speed $\boldsymbol{\beta}$: $\frac{1}{c}\frac{\partial \phi}{\partial t} = -\beta \frac{\partial \phi}{\partial z}$ and $\frac{1}{c}\frac{\partial \boldsymbol{a}}{\partial t} = -\beta \frac{\partial \boldsymbol{a}}{\partial z}$.) The above equations can then be discretized on the grid of a PIC code. In this case, the differential operators can be represented as matrix operations, and the above equations can be solved for ϕ and $\boldsymbol{a}$ on the whole grid by using a matrix-inversion algorithm (for instance the conjugate gradient algorithm). Finally, once ϕ and $\boldsymbol{a}$ are known on the grid, the fields $\boldsymbol{E}$ and $\boldsymbol{B}$ can be obtained from the discretized version of the equations $\boldsymbol{E} = \frac{mc^2}{e}\left(-\boldsymbol{\nabla}\phi + \beta \frac{\partial \boldsymbol{a}}{\partial z}\right)$ and $\boldsymbol{B} = \frac{mc}{e}\boldsymbol{\nabla}\times\boldsymbol{a}$.

The force felt by the electrons of the bunch is plotted in the right panel of fig. 4.11. In the simulation, this force is evaluated by calculating the radial acceleration of the macroparticles of the bunch: $F_{b,r}^{\text{evaluated}} \equiv \gamma_b m d_t^2 r_b$. There is a significant disagreement between the simulation results and the predictions of eq. (4.21) (solid lines) at the very head ($\xi = 0\,\mu$m) and the very tail ($\xi = 1\,\mu$m) of the bunch. This local discrepancy is presumably due to numerical noise, which was observed to accumulate at the edges of the bunch in the simulations. Apart from this local discrepancy, the predictions and the simulation results are in good agreement. In particular, eq. (4.21) predicts that the focusing force near the head of the bunch is non-zero, due to the laser-wakefield. In order to highlight this point, fig. 4.11 also features the predictions of eq. (4.21) in the case *without a laser pulse* ($a_0 = 0$; dashed line in fig. 4.11). As can be seen in the figure, the simulation results agree with the solid lines and do feature this non-zero focusing force at the head of the bunch.

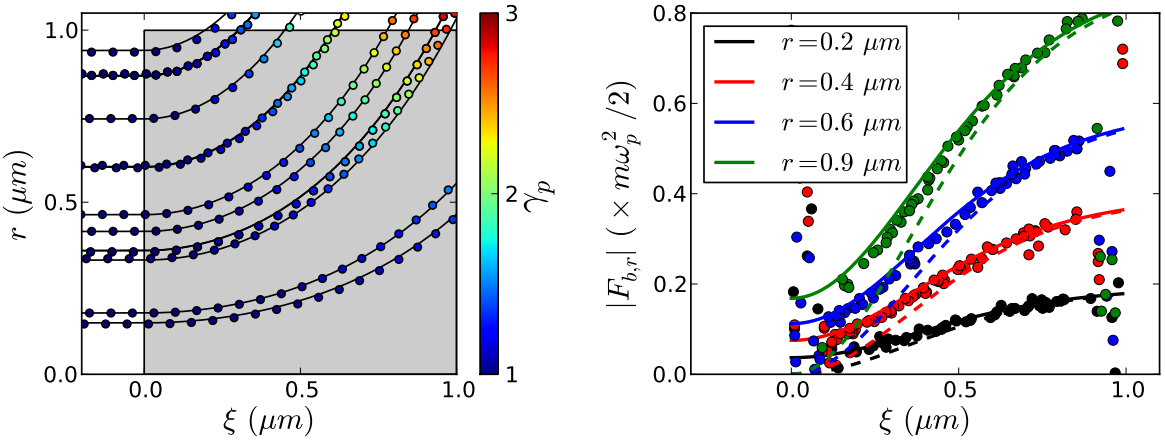

Figure 4.11: Left panel: Trajectories of a few randomly-chosen plasma electrons in the PIC simulation. The colored dots correspond to the successive positions of the macroparticles in the simulations (the colorscale corresponds to the Lorentz factor γ_p of the electrons), while the black line represents the prediction of eq. (4.20) based on the initial radius r_0 of each macroparticle. Right panel: Force experienced by the electrons of the bunch. The results are plotted for different radii r, and each dot corresponds to one macroparticle. (Only the macroparticles lying close to either $r = 0.2$, 0.4, 0.6 or 0.9 μm have been represented.) The predictions of eq. (4.21) are plotted for $a_0 = 0.5$ (solid lines) and, for comparison, for $a_0 = 0$ (dashed lines).

On the whole, the model that was developed in this section is in good agreement with PIC simulations. As mentioned in the introduction of this section, this model can be useful in several situations associated with laser-wakefield acceleration, and these results were recently published in [Lehe et al., 2014].

4.3.4 Implications for the single-pulse laser-plasma lens

Although eq. (4.21) was derived for a flat-top bunch, some of its qualitative feature can be generalized to other bunch profiles. One of these features is the qualitative evolution of the focusing force $F_{b,r}$ along the bunch. As mentioned in the previous section, this force transitions between two regimes depending on the value of ξ.

- For $k_b\xi \ll 1$, a Taylor expansion of eq. (4.21) (considering also $a_0^2 \ll 1$) yields:

$$F_{b,r} = -mc^2\eta r\frac{a_0^2}{w^2}\sin[\, k_p(\xi - \xi_{\text{laser}})\,] - mc^2\frac{k_p^2 k_b^2\xi^2}{2}r \tag{4.22}$$

  In this expression, the first term represents the focusing force associated with the laser-driven wakefield (which was also used in the model of section 4.2.2), while the second term represents the corrections due to transverse beamloading.

- For $k_b\xi \gg 1$, the focusing force reduces to $F_{b,r} = -m\omega_p^2 r/2$. This is the focusing force associated with a blown-out cavity (see section 1.1.4) – which means that the plasma electrons have been completely evacuated at this longitudinal position ξ.

Therefore, the overall transverse dynamics of the bunch strongly depends on whether the bunch is long enough to experience the second regime. The key parameter here is k_bL, where L is the typical length of the bunch. This parameter can be expressed as:

$$k_bL = 2.6\left(\frac{Q_{\text{bunch}}}{100\,\text{pC}}\right)^{1/2}\left(\frac{L}{1\,\mu\text{m}}\right)^{1/2}\left(\frac{R}{1\,\mu\text{m}}\right)^{-1} \tag{4.23}$$

In the context of the laser-plasma lens, the parameter k_bL determines the importance of the aberrations associated with transverse beamloading. If $k_bL \gg 1$, the tail of the bunch experiences the strong fields of the bare ion cavity, while the head of the bunch experiences the weak forces of the laser-wakefield. In this case, the head and the tail cannot be simultaneously collimated by the lens, and the final divergence after the lens will be high. On the other hand, for $k_bL \ll 1$, eq. (4.22) applies to the whole bunch. In this equation, the correction term $-mc^2k_b^2k_p^2\xi^2/2$ grows from the head to the tail of the bunch, and thus beamloading effects may still be important if this corrective term is comparable to the first term, at $\xi = L$. Therefore, for these aberrations to have a low impact, the bunch must satisfy the criterion

$$k_bL \ll 1 \qquad \text{and} \qquad k_bL < \sqrt{2\eta\sin(k_pd)}\frac{a_0}{k_pw} \tag{4.24}$$

where d is the distance from the bunch to the centroid of the laser pulse, and where the second inequality ensures that the corrective term is negligible.

This criterion is confirmed by the PIC simulations of sections 4.2.4 and 4.2.5. In the simulation of section 4.2.4, self-injection lead to a bunch with $Q_{\text{bunch}} = 70\,\text{pC}$, $L = 0.3\,\mu\text{m}$ and $R = 10\,\mu\text{m}$ at the entrance of the lens, for which beamloading effects were found to be negligible. This is consistent with the above analysis, since $k_bL \simeq 0.1$ for this bunch and thus the above criterion is satisfied. (For this simulation, $\sqrt{2\eta\sin(k_pd)} \times a_0/(k_pw) \simeq 0.26$ at the entrance of the lens.) On the other hand, another simulation in section 4.2.5 lead to a bunch with $Q_{\text{bunch}} = 130\,\text{pC}$, $L = 2.5\,\mu\text{m}$ and $R = 5\,\mu\text{m}$, for which beamloading aberrations were observed to be strong. Again, this is consistent, since $k_bL \simeq 0.9$ for this bunch and hence the criterion eq. (4.24) is not satisfied.

Thus, according to this criterion, the electron bunch should have a low charge, a short duration and a large radius in order to avoid the beamloading aberrations in the single-pulse laser-plasma lens. However, it is not always possible for the electron bunch to satisfy these conditions and, as will be seen in the next section, there are other means to prevent these aberrations.

4.4 The two-pulse laser-plasma lens

4.4.1 Principle

In order to limit the impact of the aberrations of the single-pulse scheme, we propose an alternative scheme for the laser-plasma lens. As depicted in fig. 4.12, the idea of this alternative scheme is to use a *second, copropagating laser pulse* in order to produce a blown-out cavity in the second jet. While the first pulse (represented in red in fig. 4.12) is focused into the first gas jet, the second pulse (represented in orange) is focused into the second gas jet. Because of its low waist and high intensity at focus, this second pulse can thus generate a fully-evacuated cavity in the second jet (see section 1.1.4).

In addition, this second pulse is chosen to precede the first one by a few tens of femtoseconds.[9] In this way, the second pulse does not experience the strong wakefield of the first pulse in the first jet – which would otherwise perturb its propagation and its focal position. Finally, the second jet is chosen to have a low density ($n_2 \sim 10^{18}\,\mathrm{cm}^{-3}$), so that the blown-out cavity is large enough to encompass the electron bunch.

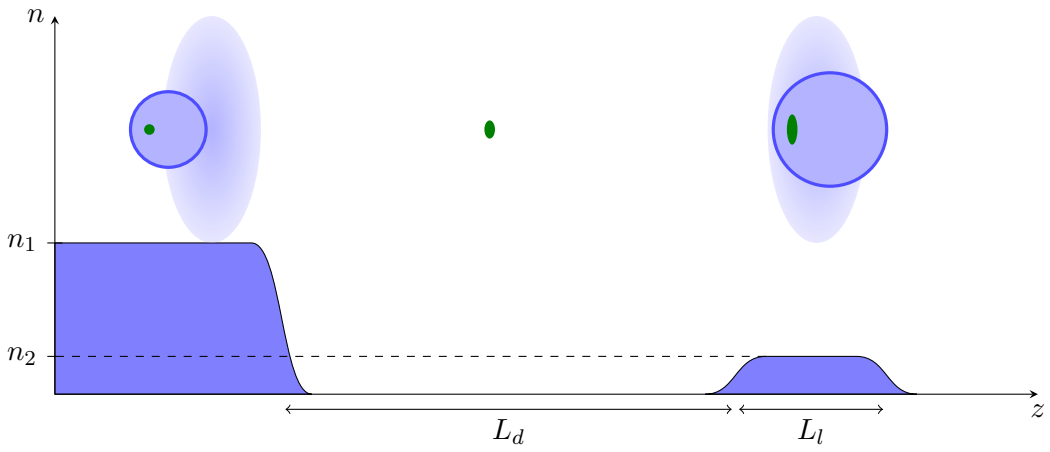

Figure 4.12: Schematic representation of the two-pulse laser-plasma lens. The blue curves represent the density profiles of the two jets. The above sketches represent the first (red) and second (orange) laser pulse, the electron bunch (green) and the aspect of the wakefield (blue) as they propagate through the two jets. (Although the two laser pulses are represented with different colors here, they have physically the same wavelength $\lambda_0 = 0.8\,\mu$m.)

The motivation for this two-pulse scheme is that a fully-evacuated cavity induces less aberrations than the linear wakefield of the single-pulse scheme. For instance, the focusing force along x in the cavity is exactly proportional to x (instead of $x\,e^{-2(x^2+y^2)/w^2}$ in the linear wakefield), and thus there are no high-radius aberrations. In addition, since the cavity is completely void of electrons (except from the high-energy electron bunch), the bunch itself cannot drive its own wakefield anymore. As a consequence, the aberrations associated with transverse beamloading are absent in the two-pulse scheme. Thus, on the whole, the two-pulse scheme is only subject to the "chromatic" aberrations (i.e. those associated with the finite energy-spread of the bunch).

The phase space evolution of the electron bunch in this scheme is qualitatively similar to that of the single-pulse scheme (see fig. 4.1). Yet quantitatively, the focusing forces are stronger in

[9] Although it is experimentally relatively challenging, producing two copropagating laser pulses separated by only a few tens of femtoseconds is within the capabilities of current laser facilities.

the blown-out cavity than in the linear wakefield. As a result, the electrons rotate faster in phase space in the two-pulse scheme than in the single-pulse scheme, and one should therefore make the second jet shorter – if it is to end at the position where the electrons reach their minimal divergence. In the next section, a model predicts how to quantitatively choose the length of the second jet (as well as the other parameters of the lens).

4.4.2 Model and choice of parameters

Here let us follow a similar reasoning as for the single-pulse laser-plasma lens (section 4.2.2). First, the evolution of θ_x is derived analytically for an individual electron, and then on this basis, a criterion is derived which minimizes the RMS divergence $\sqrt{\langle\theta_x^2\rangle}$ of a full bunch of electrons. Again, space-charge effects are neglected and the density gradients are considered to be infinitely steep. Because the second jet is short and has a low density, the variations of the electrons' γ factor inside this jet are also neglected.

Trajectory of an individual electron. Let us consider an individual electrons having a transverse position x_0 and a divergence θ_0, as it exits from the first jet. Then, as in section 4.2.2, the trajectory of this electron in the drift space is

$$\begin{cases} x(z) = x_0 + \theta_0\, z \\ \theta_x(z) = \theta_0 \end{cases} \qquad \text{for } 0 < z < L_d \tag{4.25}$$

However, the equation of transverse motion in the second jet differs from that of section 4.2.2, since the expression of the focusing force in the blown-out cavity is different from that of the linear wakefield. Inside the blown-out cavity, the equation of transverse motion reads (see section 1.2.2)

$$\frac{d^2\,x}{dz^2} = -{k'_{\text{foc}}}^2\, x \qquad \text{with} \quad k'_{\text{foc}} = \frac{k_p}{\sqrt{2\gamma}} \quad \text{and} \quad k_p = \sqrt{4\pi r_e n_2}$$

Notice that k'_{foc} is in fact the *betatron* wavevector in the second jet ($k'_{\text{foc}} = \omega_\beta/c$, where ω_β is defined in section 1.2.2). The above equation is easily integrated and, with the initial conditions $x(L_d)$ and $\theta(L_d)$ given by eq. (4.25), one finds

$$\begin{cases} x(z) = (x_0 + \theta_0 L_d)\cos[\, k'_{\text{foc}}(z - L_d)\,] + \dfrac{\theta_0}{k'_{\text{foc}}}\sin[\, k'_{\text{foc}}(z - L_d)\,] \\ \theta_x(z) = \theta_0\cos[\, k'_{\text{foc}}(z - L_d)\,] - k'_{\text{foc}}(x_0 + \theta_0 L_d)\sin[\, k'_{\text{foc}}(z - L_d)\,] \end{cases} \tag{4.26}$$

Thus x and θ_x perform sinusoidal oscillations in the second jet. Ideally, the second jet should end at a position where the electron reaches $\theta_x = 0$. According to the above expression of θ_x, this corresponds to

$$\left(1 + \frac{x_0}{\theta_0 L_d}\right) k'_{\text{foc}} L_d \tan(k'_{\text{foc}} L_l) = 1 \tag{4.27}$$

Choice of the parameters of the lens. However, the above relation cannot be satisfied simultaneously by all the electrons of the bunch. This is due to the finite spread in x_0 and θ_0 (i.e. the finite emittance), but also to the finite spread in γ (i.e. the finite energy spread) which induces a corresponding spread in k'_{foc}. Nonetheless, a reasonable choice for the parameters of the lens would be to satisfy

$$\bar{k}'_{\text{foc}} L_d \tan(\, \bar{k}'_{\text{foc}} L_l\,) = 1 \qquad \text{with} \quad \bar{k}'_{\text{foc}} = \frac{k_p}{\sqrt{2\langle\gamma\rangle}} \tag{4.28}$$

where the brackets denote an average over the electron bunch. Note that the factor $1+x_0/(\theta_0 L_d)$ of eq. (4.27) has been dropped in eq. (4.28), since, in typical LWFA bunches, this factor is close to 1 for most electrons.

Because of the periodicity of the tangent function, the criterion eq. (4.28) has several solutions. For instance, when searching for L_l as a function of the other parameters, one finds

$$L_l = \frac{1}{\bar{k}'_{\mathrm{foc}}} \arctan\left(\frac{1}{\bar{k}'_{\mathrm{foc}} L_d}\right) + n\frac{\pi}{\bar{k}'_{\mathrm{foc}}} \tag{4.29}$$

where n is an integer. This is confirmed by fig. 4.13, in which the formulas eq. (4.25) and eq. (4.28) were applied to a set of randomly-distributed initial conditions x_0, θ_0, γ representing a typical electron bunch. (This bunch had an initial RMS divergence $\sqrt{\langle\theta_0^2\rangle} = 3\,\mathrm{mrad}$, an initial RMS transverse size $\sqrt{\langle x_0^2\rangle} = 0.5\,\mu\mathrm{m}$ and a Gaussian energy distribution around $\gamma = 800$ with a 10 % energy spread.) As can be seen in this figure, there are indeed several positions at which the divergence is minimal. Moreover, the positions of these minima are in good agreement with the predictions of eq. (4.29) and thus confirm the validity of the criterion eq. (4.28).

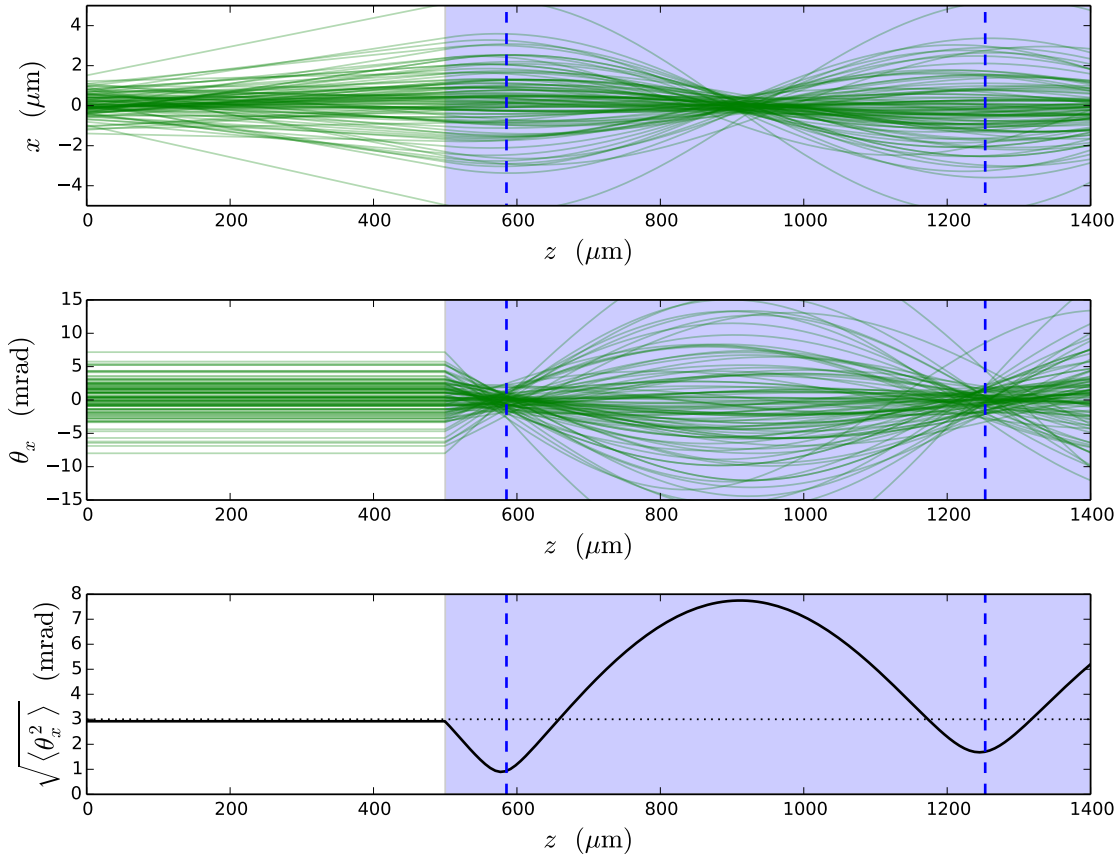

Figure 4.13: Top and middle panel: evolution of x and θ_x as given by eq. (4.26) for a given bunch of electrons. Bottom panel: evolution of their RMS divergence $\sqrt{\langle\theta_x^2\rangle}$. The blue area represents the second jet (here with $n_2 = 1\times10^{18}\,\mathrm{cm}^{-3}$ and $L_d = 500\,\mu\mathrm{m}$). The blue dashed lines mark the optimal values for L_l, as predicted by eq. (4.29) (for $n = 0$ and $n = 1$). (Here the bunch was initialized with $\sqrt{\langle x_0^2\rangle} = 0.5\,\mu\mathrm{m}$, $\sqrt{\langle\theta_0^2\rangle} = 3\,\mathrm{mrad}$, $\langle\gamma\rangle = 800$ and a 10 % energy spread.)

However, fig. 4.13 also shows that the successive local minima of the divergence are not equivalent. In fact, the minimal divergence progressively grows with the index n of the minimum. This is due to the energy spread of the electrons, and to the related spread in their individual oscillation frequency k'_{foc}. Because of this spread, the more oscillations the electrons perform inside the second jet, the more incoherent they become, and the less simultaneous are the moments when each of them reaches $\theta_x = 0$. (This effect can be seen in middle panel of fig. 4.13.) Thus, for the sake of the final divergence, it is best to choose the solution corresponding to $n = 0$:

$$L_l = \frac{1}{\bar{k}'_{\mathrm{foc}}} \arctan\left(\frac{1}{\bar{k}'_{\mathrm{foc}} L_d}\right) \qquad = \frac{\sqrt{2\langle\gamma\rangle}}{k_p} \arctan\left(\frac{\sqrt{2\langle\gamma\rangle}}{k_p L_d}\right)$$

Notice however that this solution implies that the second jet should be very short. For instance, for $\langle\gamma\rangle = 800$ and $n_2 = 1 \times 10^{18}\,\mathrm{cm}^{-3}$, L_l is of the order of 100 μm. Experimentally, such a short gas jet cannot be produced with a standard nozzle. However, preliminary hydrodynamic simulations show that it can realistically be generated with a leaking capillary. Of course, with such a short gas jet, the density gradients at the edges of the jet become very important, and the model – which assumes the gradients to be infinitely steep – only provides an approximative estimate for the parameters of the lens. Therefore, experimentally, it is suggested to install a leaking capillary with a $\sim 100\,\mu$m diameter behind the first jet, and then again to scan the gas density n_2 or the drift distance L_d in order reach the optimal divergence.

Tuning the density and drift distance. Although the previous model neglects the density gradients, it is reasonable to think that the evolution of the divergence as a function of n_2 and L_d in this model is qualitatively correct. Let us thus examine its predictions, so as to gain insight into the evolution that may be observed experimentally.

Figure 4.14 shows the evolution of the RMS divergence of the bunch when the density n_2 is varied. Because the focusing parameter k'_{foc} is a growing function of the density n_2, the bunch is overfocused at high density (and thus diverges), while it is not focused enough at low density (see the lower panels of fig. 4.14). As can be predicted through eq. (4.28), the optimal density is $n_2 \simeq 0.8 \times 10^{18}\,\mathrm{cm}^{-3}$. Notice that the evolution of the divergence is qualitatively different from that of the single-pulse scheme (fig. 4.4). This is essentially because the focusing forces increase monotonically with n_2 in the blown-out cavity of the two-pulse scheme, while they go through a resonance for a certain n_2 in the linear wakefield of the single-pulse scheme.

Similarly, fig. 4.15 displays the evolution of the divergence as a function of the drift distance L_d. As can be seen in the lower panels, the electrons are focused too weakly for low values of L_d, and too strongly for high values of L_d. Qualitatively, this is because the focusing force in the second jet is proportional to the transverse coordinate x of the electrons. A large value of L_d allows the electrons to considerably diverge in the drift space, and thus to enter the second jet with a large transverse position x, thereby experiencing a strong focusing force. Interestingly, this behaviour is inverted in the single-pulse scheme (fig. 4.5), where the electrons are overfocused at low L_d and underfocused at high L_d. In the case of the single-pulse scheme, this is explained by the fact that the intensity of the diffracting laser decreases faster than the transverse position x increases.

Notice finally that the optimal drift distance in fig. 4.14 is quite low ($L_d \simeq 400\,\mu$m). This short distance is rather a disadvantage, since it limits the final reduction of divergence – even for a monoenergetic bunch. For a monoenergetic bunch one can indeed show that the final divergence necessarily satisfies $\sqrt{\langle\theta_x^2\rangle} \geq \epsilon_x/(\gamma\sqrt{\langle x^2\rangle})$ (see section 1.3.1). Since the emittance ϵ_x remains constant in the linear fields of the cavity, one should let $\sqrt{\langle x^2\rangle}$ increase in order to be

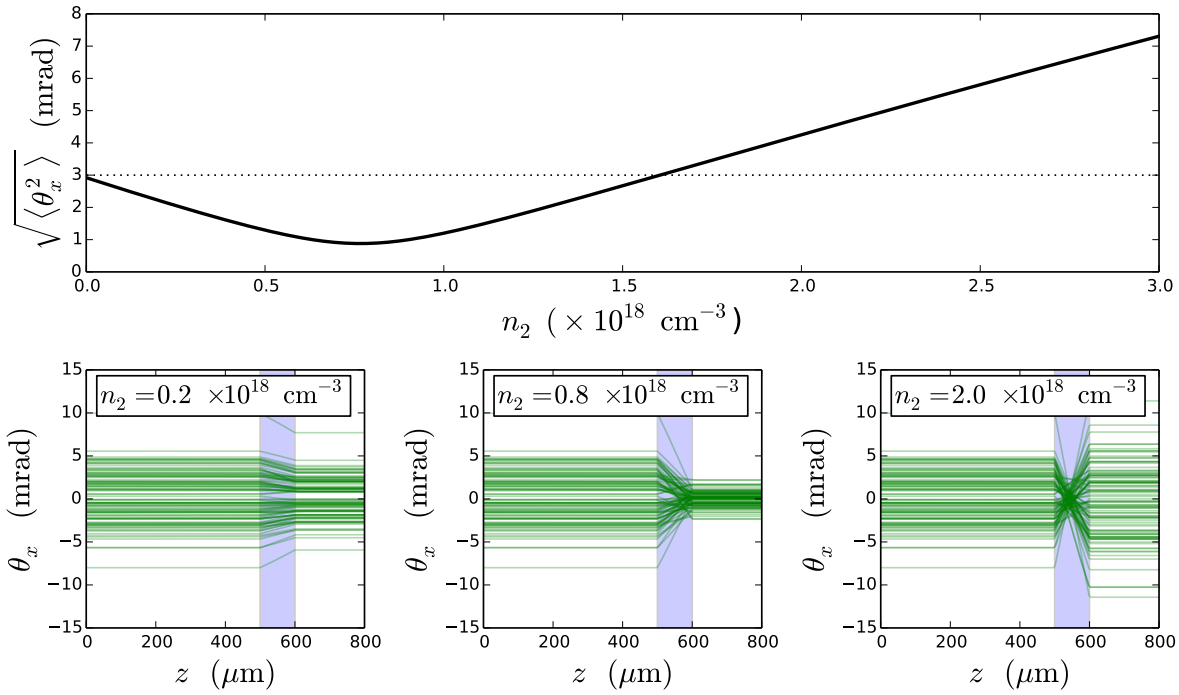

Figure 4.14: Top panel: Evolution of the final RMS divergence of the electron bunch as a function of n_2. The other parameters are fixed ($L_d = 500\,\mu$m, $L_l = 100\,\mu$m, and the bunch is initially characterized by $\sqrt{\langle\theta_0^2\rangle} = 3$ mrad, $\sqrt{\langle x_0^2\rangle} = 0.5\,\mu$m, $\langle\gamma\rangle = 800$, and a 10 % energy spread). The dotted line marks the initial RMS divergence of the bunch. Bottom panel: Evolution of θ_x for a few electrons as a function of z, for three different values of n_2.

able to reduce $\sqrt{\langle\theta_x^2\rangle}$. This is the role of the drift space, and thus a relatively short drift space prevents a strong reduction of the divergence. Nonetheless, fig. 4.15 shows that, even with this short drift space, a reduction of a factor 3 is still possible.

4.4.3 Confirmation by PIC simulations

In order to confirm the above predictions, I ran PIC simulations of the two-pulse laser-plasma lens. There are indeed a few important effects that were not taken into account in the previous model, but which can have a substantial impact on the two-pulse scheme. For instance, the second pulse may experience significant self-focusing in the first jet, and that can perturb its propagation and shift its focal plane away from the second jet. In addition, in the first jet, the presence of the second pulse ahead of the first pulse may perturb – or even inhibit – self-injection.

In order to assess these effects, I simulated a typical two-pulse laser-plasma lens experiment. In accordance with the results of the previous section, the second jet is chosen to have a peak density $n_2 = 1 \times 10^{18}\,\text{cm}^{-3}$, a length $L_l \simeq 100\,\mu$m (with realistic density gradients at the edges of the jet), and to be located 500 μm behind the first jet. (The density profiles of the two jets are represented in the upper right panel of fig. 4.16.) The first pulse is a 1.6 J, 30 fs laser pulse, which is focused into the first jet. The second pulse contains 1 J and is purposedly focused in such a way that its focal plane would lie 500 μm after the second jet, if the pulse had propagated in vacuum. (This is done in anticipation of its self-focusing in the first jet.) Finally, the simulation

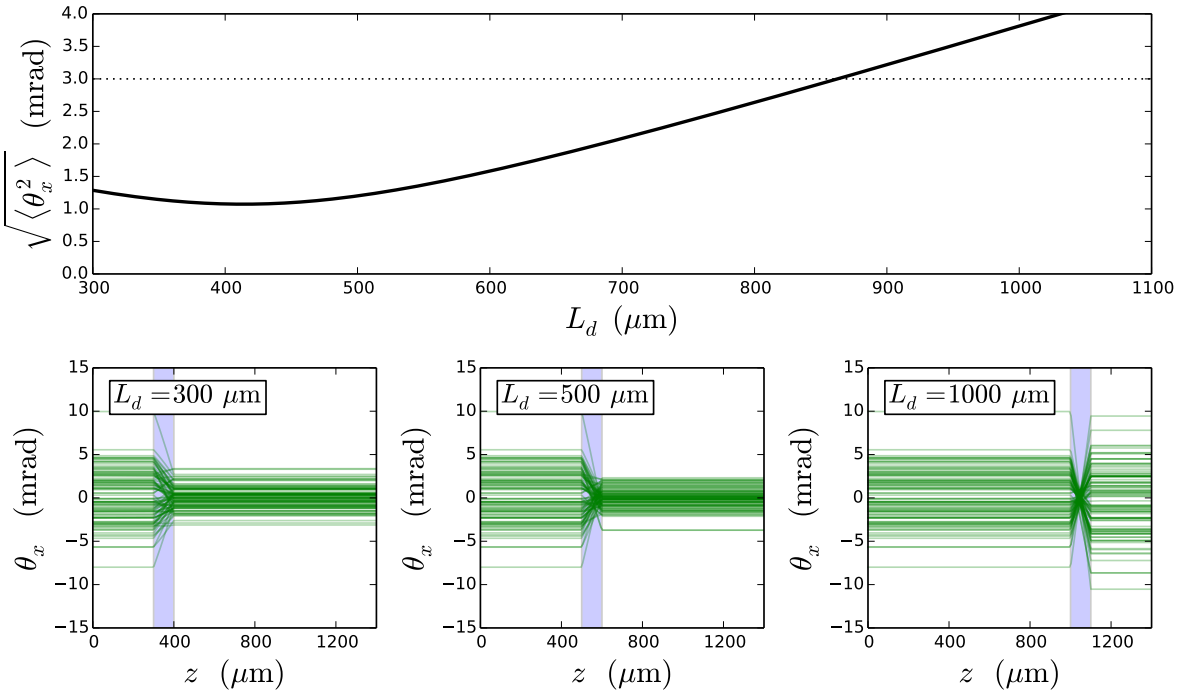

Figure 4.15: Top panel: Evolution of the final RMS divergence of the electron bunch as a function of L_d. The other parameters are fixed ($n_2 = 1\times10^{18}\,\mathrm{cm}^{-3}$, $L_l = 100\,\mu$m, and the bunch is initially characterized by $\sqrt{\langle\theta_0^2\rangle} = 3\,$mrad, $\sqrt{\langle x_0^2\rangle} = 0.5\,\mu$m, $\langle\gamma\rangle = 800$, and a 10 % energy spread). The dotted line marks the initial RMS divergence of the bunch. Bottom panel: Evolution of θ_x for a few electrons as a function of z, for three different values of n_2.

is run with the quasi-cylindrical code Calder Circ, using the Cherenkov-free algorithm of chapter 2 and a third-order accurate interpolation of the B field in time (see appendix C). Two azimuthal modes are used ($\ell = 0$ and $\ell = 1$), and the resolution is $\Delta z = 0.03\,\mu$m, $\Delta r = 0.2\,\mu$m and $c\Delta t = 0.96\Delta z$.

The evolution of the laser waists in the simulation are shown in the upper right panel of fig. 4.16. The first pulse (red line) self-focuses in the first jet and then diverges in the drift space. The second pulse (dashed orange line) only self-focuses at the end of the first jet, and it reaches the second jet with a low waist, as desired. Self-injection does take place in the first jet, and leads to the acceleration of a high-charge electron bunch. This bunch has a large energy distribution however (see fig. 4.17), and here we concentrate on the high-energy part of this bunch (shaded area in fig. 4.17). The evolution of the divergence of this part of the bunch is shown in the bottom right panel of fig. 4.16. As a consequence of the acceleration, the divergence is observed to progressively decrease in the first jet (θ_x and θ_y evolve on average as $\gamma^{-3/4}$; see section 1.2.2). It then remains constant in the drift space, before suddenly dropping as the bunch travels through the second jet. On the whole, the simulation confirms that the divergence can be reduced by roughly a factor 3.

The very steep reduction of the divergence suggests that the electron bunch indeed experiences the strong fields of a blown-out cavity in the second jet. This is confirmed by the left panel of fig. 4.18, which shows that the second laser pulse is indeed able to drive a blown-out cavity in

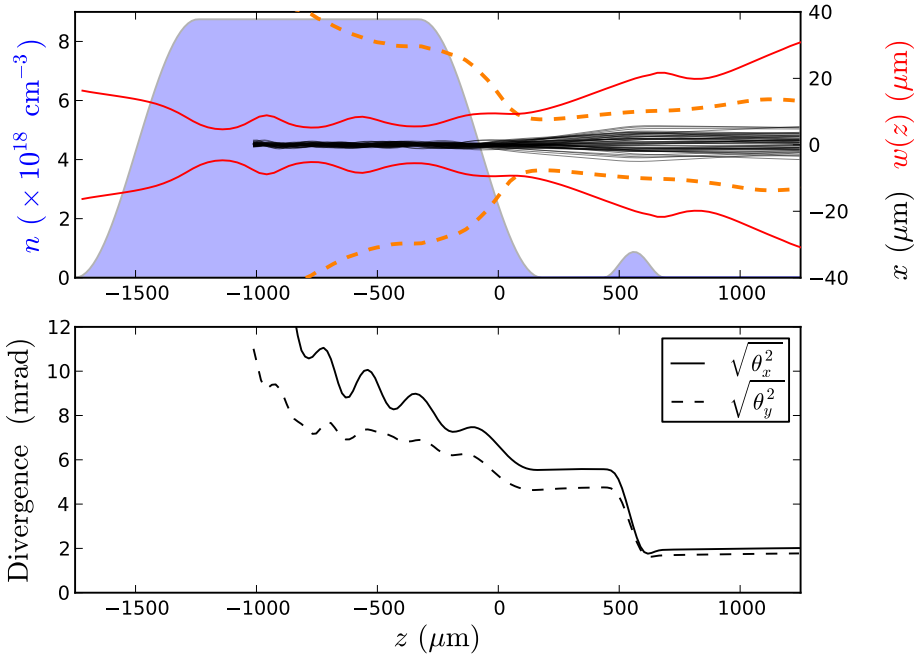

Figure 4.16: Upper right panel: Density profile of the two jets (blue) and evolution of the waist of the first (red line) and second (dashed orange line) laser pulses. The black lines represent the trajectories of a few electrons from the high-energy part of the bunch (see fig. 4.17). Lower right panel: Evolution of the RMS divergence of the electrons in the high-energy part of the bunch.

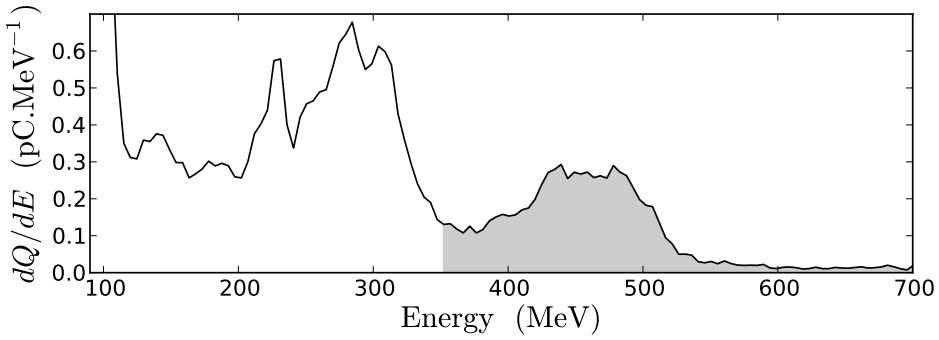

Figure 4.17: Energy spectrum of the electron bunch, at the entrance of the second jet. The shaded area corresponds to the high-energy part of the bunch. It is the divergence of this part of the bunch which is represented in fig. 4.16.

the second jet. For comparison, the right panel of fig. 4.18 shows the results of a simulation with the same density profile, but with *no second pulse*. In this panel, the first pulse alone drives only a weak, quasi-linear wakefield. As expected, while the electron bunch is able to drive a wakefield of its own in the single-pulse case (right panel), it cannot do so in the two-pulse case (left panel), since the blown-out cavity is entirely void of electrons. This confirms that there are no transverse beamloading effects in the two-pulse scheme.

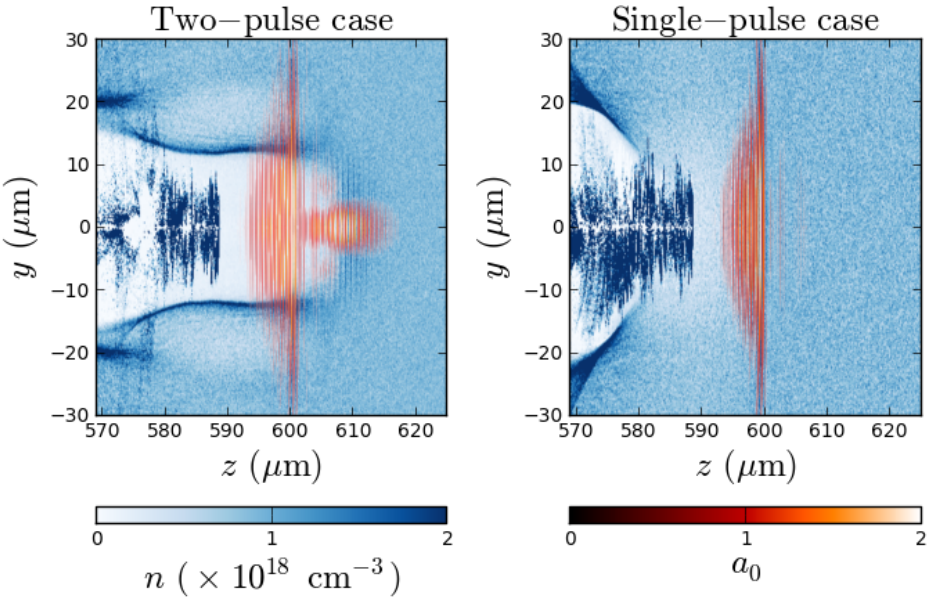

Figure 4.18: Left panel: Snapshot of the PIC simulation at a time when the two pulses are in the second jet. Right panel: Snapshot of a similar simulation, but in which there was *no second pulse*.

4.5 Conclusion: pros and cons of the single-pulse and two-pulse schemes

Let us conclude this chapter by summarizing the characteristics of each scheme, along with their advantages and drawbacks. In the single-pulse scheme, the parameters of the lens should satisfy

$$\frac{k_{\rm foc}Z_R^2}{L_d+L_l}\tan\left(\frac{k_{\rm foc}Z_R^2}{L_d}-\frac{k_{\rm foc}Z_R^2}{L_d+L_l}\right)=1 \qquad \text{and} \qquad n_2<\frac{\pi}{4r_e d^2} \tag{4.30}$$

in order to properly collimate the bunch (see sections 4.2.2 and 4.2.3). The advantage of this scheme is that it is easy to implement experimentally. However, this scheme is subject to high-radius aberrations and beamloading aberrations, which limit the final divergence. These aberrations are negligible if $\theta_0 \ll \frac{w(0)}{Z_R}$ and $k_b L \ll \sqrt{2\eta\sin(k_p d)}\frac{a_0}{k_p w(L_d)}$ (from sections 4.2.5 and 4.3.4), but in practice the self-injected bunch may not satisfy these conditions.

On the other hand, in the two-pulse scheme the parameters of the lens should verify

$$\bar{k}'_{\rm foc}L_d\tan(\,\bar{k}'_{\rm foc}L_l\,)=1 \tag{4.31}$$

(see section 4.4.2). This scheme is more challenging to implement experimentally, since it requires a very short gas jet and imposes to align and synchronize two separate laser pulses. Moreover, it may be less stable than the single-pulse scheme, due to the self-focusing of the second pulse in the first jet and due to the impact of this pulse on self-injection. This scheme is not affected by the high-radius aberration or the beamloading aberration, but on the other hand the final divergence is limited by the relatively short drift space. Thus, although this scheme was originally developed to prevent the aberrations, it may not lead to a stronger reduction of divergence in practice.

Both schemes are however complementary from another point of view: while the single-pulse scheme is well-adapated to low-energy bunches ($\gamma \sim 200$–400), the two-pulse scheme is well-suited for high-energy bunches ($\gamma \sim 800$). This is because the relatively weak focusing fields of the single-pulse scheme may not be sufficient to fully collimate high-energy bunches, due to their higher inertia (i.e. in some conditions, the first equation of eq. (4.30) cannot be satisfied for high-energy bunches). On the other hand, the criterion eq. (4.31) imposes impractical parameters for low-energy bunches (either $L_l < 100\,\mu$m which is difficult to obtain experimentally, or $n_2 < 10^{18}\,\mathrm{cm}^{-3}$ which makes the second jet so faint that it risks being eclipsed by the potentially far-reaching end gradient of the first jet).

In the end, both schemes can realistically lead to a reduction of the divergence by a factor 3. It is in fact currently planned to implement these schemes in future experiments at LOA.

Chapter 5

Towards a compact free-electron laser

This chapter focuses on the design of a prospective free-electron laser based on an LWFA. Compact free-electron lasers are indeed one of the most interesting potential applications of LWFA. Here, after summarizing the basics of free-electron laser physics, we discuss the specific issues that arise when using an LWFA. In particular, the results of previous chapters are put into context, and it is shown how they can contribute to overcoming those issues. Finally, a new concept of ultra-compact free-electron laser is presented (the *nanowire* undulator). By using a simplified model, I show that gain lengths of $\sim$100 μm could in principle be obtained with this concept. However, there are important effects that are not considered in the model, and I discuss their potential impact at the end of the chapter.

Contents

5.1 Physics of FEL

5.1.1 Qualitative picture

A Free Electron Laser (FEL) is a device that can produce extremely bright radiation over a wide range of wavelengths, and in particular at very short wavelengths. In fact, some existing FELs can even reach the hard X-ray range (down to angstrom wavelengths), and are therefore known as *XFEL*s. The working principle of an FEL consists in sending a relativistic electron bunch into an undulator. The purpose of the undulator is to force the electrons to oscillate transversely, and thereby to emit radiation. All currently operating FELs use magnetic undulators, i.e. undulators that consist of an arrangement of alternating magnets, and which can produce a periodic magnetic field of the order of 1 Tesla with a centimeter-scale period. Yet, many other undulator concepts have been proposed (e.g. Whittum et al. [1990]; Joshi et al. [1987]; Gea-Banacloche et al. [1987]; Danly et al. [1987]). In particular, an interesting concept that will also be considered in this section is that of a laser undulator [Gea-Banacloche et al., 1987], in which a counterpropagating CO_2 or Ti:Sapph laser pulse is used in order to wiggle the electrons.

The principle of an FEL is represented in fig. 5.1 (in the case of a magnetic undulator). As the relativistic electrons are wiggled, they emit Doppler-shifted, short-wavelength radiation along the axis of the undulator. However this radiation is relatively weak at the entrance of the undulator. This is because the electrons are initially randomly distributed within the bunch. As a consequence of this random distribution, the electromagnetic waves emitted by each individual electron are randomly phased. On average, these waves do not interfere neither constructively nor destructively, and the corresponding radiation power is relatively low.

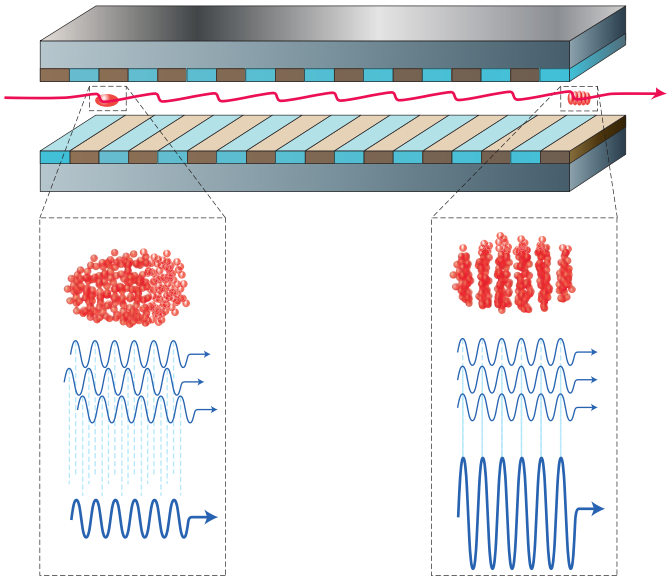

Figure 5.1: Schematic representation of the working principle of an FEL. A relativistic electron bunch (represented in red) travels through an undulator, and performs a transverse wiggling motion. As a result of this motion, each electron emits an electromagnetic wave, but these waves (which are represented by blue lines) are initially incoherent. However, as the electrons propagate in the undulator, they progressively micro-bunch, and they eventually emit coherent high-power radiation. *From McNeil and Thompson [2010].*

However, as the radiation copropagates with the bunch in the undulator, it tends to group the electrons into sub-bunches. (This phenomenon is known as *micro-bunching*.) These sub-bunches are separated by approximately one wavelength, and thus the waves emitted by the individual electrons interfere constructively on average. This creates a positive feedback loop and triggers an instability in which both the radiation and the micro-bunching grow exponentially. As a result, the *coherent* radiation power emitted at the end of the undulator is many orders of magnitude higher than the *incoherent* power emitted at its entrance! In fact, no other existing X-ray source matches the FEL in terms of peak power. As a consequence of this unique feature, FELs enable unprecented applications in many areas of science, including atomic and molecular science, biochemistry and solid-state physics.

5.1.2 Cold fluid theory of the FEL instability

Historically, the original idea of the FEL was proposed and demonstrated by J. Madey and colleagues [Madey, 1971; Deacon et al., 1977], and it was later cast into the formalism of an instability starting from incoherent radiation (e.g. [Kondratenko and Saldin, 1980]). Here, let us examine the nature of this instability in the simplified case of an electron bunch with negligible temperature [Liu and Tripathi, 1994]. In this case the dynamics of the electron bunch can be described by cold fluid theory. The bunch is also assumed to be sufficiently long and wide for edge effects to be neglected. Finally, we assume that space-charge effects are negligible, and thus that the only forces that the electrons experience are those associated with the fields of the undulator and of the emitted radiation. Both the fields of the undulator and of the radiation are described by their vector potential $\boldsymbol{A}$, in the Lorenz gauge.

Governing equations. Using dimensionless quantities, the equations of this system are[1]:

$$\frac{1}{c}\frac{\partial n}{\partial t} + \boldsymbol{\nabla}\cdot\left(\frac{n\boldsymbol{u}}{\gamma}\right) = 0 \qquad \text{(Conservation of charge)} \qquad (5.1)$$

$$\frac{1}{c}\frac{\partial}{\partial t}(\boldsymbol{u}-\boldsymbol{a}) + \frac{1}{\gamma}(\boldsymbol{u}\cdot\boldsymbol{\nabla})(\boldsymbol{u}-\boldsymbol{a}) = -\frac{1}{\gamma}(\boldsymbol{u}\cdot\boldsymbol{\nabla}\boldsymbol{a}) \qquad \text{(Equation of dynamics)} \qquad (5.2)$$

$$\boldsymbol{\nabla}^2\boldsymbol{a} - \frac{1}{c^2}\frac{\partial^2\boldsymbol{a}}{\partial t^2} = 4\pi r_e\frac{n\boldsymbol{u}}{\gamma} \qquad \text{(From the Maxwell equations)} \qquad (5.3)$$

where $n = \rho/(-e)$ is the electron density, $\boldsymbol{u} = \boldsymbol{p}/mc$ is the normalized momentum, and $\boldsymbol{a} = \boldsymbol{a}_u + \boldsymbol{a}_r = e\boldsymbol{A}_u/mc + e\boldsymbol{A}_r/mc$ is the sum of the normalized vector potentials of the undulator and the radiation. Here, let us consider a helical undulator of the form

$$\boldsymbol{a}_u = \frac{\boldsymbol{a}_{u,0}}{2}e^{ik_u z + i\omega_u t} + \frac{\boldsymbol{a}_{u,0}^*}{2}e^{-ik_u z - i\omega_u t}$$

with $\boldsymbol{a}_{u,0} = a_{u,0}(x,y)(\boldsymbol{e}_x + i\boldsymbol{e}_y)$. Then, as a function of z, the vector potential $\boldsymbol{a}_u$ rotates in the transverse plane, with a constant amplitude $a_{u,0}$ and with a period $\lambda_u = 2\pi/k_u$. The above expression can represent either a magnetic undulator or a counterpropagating laser. In the case of a magnetic undulator, $\omega_u = 0$ and $a_{u,0} = eB_{u,0}/(mck_u)$, while in the case of a counterpropagating laser pulse, $\omega_u = ck_u$.

[1] Here, by definition, $(\boldsymbol{u}\cdot\boldsymbol{\nabla}\boldsymbol{a}) \equiv (\boldsymbol{u}\cdot\partial_x\boldsymbol{a})\boldsymbol{e}_x + (\boldsymbol{u}\cdot\partial_y\boldsymbol{a})\boldsymbol{e}_y + (\boldsymbol{u}\cdot\partial_z\boldsymbol{a})\boldsymbol{e}_z$. The equation of dynamics has been obtained from the more standard equation $\frac{1}{c}\partial_t\boldsymbol{u} + \frac{1}{\gamma}(\boldsymbol{u}\cdot\boldsymbol{\nabla})\boldsymbol{u} = -\frac{e}{mc^2}(\boldsymbol{E} + \boldsymbol{v}\times\boldsymbol{B}) = \frac{1}{c}\partial_t\boldsymbol{a} - \frac{1}{\gamma}\boldsymbol{u}\times(\boldsymbol{\nabla}\times\boldsymbol{a})$ by using the vector identity $\boldsymbol{u}\times(\boldsymbol{\nabla}\times\boldsymbol{a}) = (\boldsymbol{u}\cdot\boldsymbol{\nabla}\boldsymbol{a}) - (\boldsymbol{u}\cdot\boldsymbol{\nabla})\boldsymbol{a}$

Since the electron bunch travels relativistically along the axis of the undulator, the components of $\boldsymbol{u}$ satisfy $u_z \gg |\boldsymbol{u}_\perp|$. This implies that, in the equation of dynamics, the term $(\boldsymbol{u}\cdot\boldsymbol{\nabla})\boldsymbol{a}$ is much greater than $(\boldsymbol{u}\cdot\boldsymbol{\nabla}\boldsymbol{a}) = (\boldsymbol{u}_\perp\cdot\boldsymbol{\nabla}\boldsymbol{a})$. If, in a first approach, this latter term is neglected, the equation of dynamics leads to[2] $D_t(\boldsymbol{u}_\perp - \boldsymbol{a}) \approx 0$ and thus $\boldsymbol{u}_\perp \approx \boldsymbol{a}$, if the initial transverse momentum of the bunch (before entering the undulator) is negligible. Using this relation in the unapproximated equation of motion eq. (5.2) leads to

$$\frac{1}{c}\frac{\partial}{\partial t}(\boldsymbol{u}-\boldsymbol{a}) + \frac{1}{\gamma}(\boldsymbol{u}\cdot\boldsymbol{\nabla})(\boldsymbol{u}-\boldsymbol{a}) = -\frac{1}{2\gamma}\boldsymbol{\nabla}\boldsymbol{a}^2 \tag{5.4}$$

As can be seen from the above considerations, the presence of the undulator or of the radiation ($\boldsymbol{a} \neq 0$) results in a transverse wiggling of the electrons ($\boldsymbol{u}_\perp \approx \boldsymbol{a}$) and, on a longer timescale, in a ponderomotive force term ($-\frac{1}{2\gamma}\boldsymbol{\nabla}\boldsymbol{a}^2$). Depending on the transverse profile of $\boldsymbol{a}$, the transverse component of this ponderomotive term can focus or defocus the electron bunch. In the case of a magnetic undulator for instance, it leads to a phenomenon known as *natural focusing* [Huang and Kim, 2007]. However, since the transverse ponderomotive force acts on a long timescale and is in fact not essential to the FEL process, it will be neglected in the rest of this section and the discussion of its effect will be postponed until section 5.1.3. On the opposite, the longitudinal ponderomotive force $-\frac{1}{2\gamma}(\partial_z\boldsymbol{a}^2)\boldsymbol{e}_z$ is paramount here as it is this force which micro-bunches the electrons.

Linearized system. As explained in section 5.1.1, the radiation is initially weak, and in fact $|\boldsymbol{a}_r| \ll 1$ at the entrance of the undulator. On the other hand, in standard undulators, $|\boldsymbol{a}_u|$ is of order unity[3]. Therefore, the radiation field $\boldsymbol{a}_r$ can be considered as a small perturbation on top of the undulator field, and the system can be linearized with respect to this quantity.

In the zeroth-order system ($\boldsymbol{a}_r = \boldsymbol{0}$), the longitudinal ponderomotive force is zero, since $\boldsymbol{a}^2 = \boldsymbol{a}_u^2 = a_{u,0}(x,y)^2$ does not depend on z. Therefore, there cannot be any micro-bunching, and the stationary zeroth-order solution is:

$$u_{z,0} = const. \tag{5.5}$$
$$\boldsymbol{u}_{\perp,0} = \boldsymbol{a}_u \tag{5.6}$$
$$\gamma_0 = \sqrt{1+\boldsymbol{a}_{u,0}^2+u_{z,0}^2} = const. \tag{5.7}$$
$$\beta_{z,0} = \frac{u_{z,0}}{\gamma_0} \approx 1 - \frac{1+a_{u,0}^2}{2\gamma_0^2} = const. \tag{5.8}$$
$$n_0 = const. \tag{5.9}$$

where we used the fact that $a_{u,0}^2 \ll u_{z,0}$, since the electron bunch is relativistic and since $|\boldsymbol{a}_u| \sim 1$. Thus the electrons travel through the undulator with a constant longitudinal velocity $\beta_{z,0}$, which, incidentally, is lower than $1 - 1/2\gamma_0^2$ due to their transverse wiggling.

Let us now perturb this stationary solution with $\boldsymbol{a}_r \neq \boldsymbol{0}$. In this case, $\boldsymbol{a}^2 = (\boldsymbol{a}_u + \boldsymbol{a}_r)^2$ is not constant anymore and a longitudinal ponderomotive force can arise. This force affects the longitudinal momentum and drives a density modulation: $u_z = u_{z,0} + \delta u$, $n = n_0 + \delta n$.

[2] By definition, the notation D_t represents the operator $\partial_t + \frac{1}{\gamma}(\boldsymbol{u}\cdot\boldsymbol{\nabla})$.

[3] For instance, for a magnetic undulator with $B_{u,0} = 1\,\mathrm{T}$ and $\lambda_u = 2\,\mathrm{cm}$, the undulator parameter is $|\boldsymbol{a}_u| = 1.86$.

Linearizing eqs. (5.1), (5.3) and (5.4) with respect to $\boldsymbol{a}_r$, δu and δn leads to:

$$\left[\frac{1}{c}\frac{\partial}{\partial t}+\beta_{z,0}\frac{\partial}{\partial z}\right]\frac{\delta n}{n_0}=-\frac{(1+\boldsymbol{a}_u^2)}{\gamma_0^3}\frac{\partial \delta u}{\partial z}+\frac{\beta_{z,0}}{\gamma_0^2}\frac{\partial \boldsymbol{a}_u\cdot\boldsymbol{a}_r}{\partial z} \tag{5.10}$$

$$\left[\frac{1}{c}\frac{\partial}{\partial t}+\beta_{z,0}\frac{\partial}{\partial z}\right]\delta u=-\frac{1}{\gamma_0}\frac{\partial \boldsymbol{a}_u\cdot\boldsymbol{a}_r}{\partial z} \tag{5.11}$$

$$\left[\frac{\partial^2}{\partial z^2}-\frac{1}{c^2}\frac{\partial^2}{\partial t^2}-\frac{k_p^2}{\gamma_0}\right]\boldsymbol{a}_r=\frac{k_p^2}{\gamma_0}\frac{\delta n}{n_0}\boldsymbol{a}_u-\frac{k_p^2}{\gamma_0^3}(\boldsymbol{a}_u\cdot\boldsymbol{a}_r)\boldsymbol{a}_u-\beta_{z,0}\frac{k_p^2}{\gamma_0^2}\delta u\,\boldsymbol{a}_u \tag{5.12}$$

where $k_p^2=4\pi r_e n_0$.

Resonant growing mode. In order to find the eigenmodes of this linear system, we search for $\boldsymbol{a}_r$ in the form[4]

$$\boldsymbol{a}_r=\frac{\boldsymbol{a}_{r,0}}{2}e^{ikz-i\omega t}+\frac{\boldsymbol{a}_{r,0}^*}{2}e^{-ikz+i\omega t}\qquad\text{with}\qquad\boldsymbol{a}_{r,0}=a_{r,0}(\boldsymbol{e}_x-i\boldsymbol{e}_y)$$

Then, the ponderomotive terms in eqs. (5.10) and (5.11) are proportional to $e^{i(k+k_u)z-i(\omega-\omega_u)t}$ (or its complex conjugate), and they drive density and velocity perturbations of the form

$$\delta n=\frac{\delta n_0}{2}e^{i(k+k_u)z-i(\omega-\omega_u)t}+\frac{\delta n_0^*}{2}e^{-i(k+k_u)z+i(\omega-\omega_u)t} \tag{5.13}$$

$$\delta u=\frac{\delta u_0}{2}e^{i(k+k_u)z-i(\omega-\omega_u)t}+\frac{\delta u_0^*}{2}e^{-i(k+k_u)z+i(\omega-\omega_u)t} \tag{5.14}$$

Substituting these expressions into eqs. (5.10) to (5.12) leads to the following dispersion relation.

$$\omega^2-c^2k^2-\frac{c^2k_p^2}{\gamma_0'}=\frac{c^4k_p^2a_{u,0}^2}{4\gamma_0^3}\left(\frac{1+a_{u,0}^2}{\gamma_0^2}+2\beta_{z,0}-2\frac{(\omega-\omega_u)}{c(k+k_u)}\right)\left(\beta_{z,0}-\frac{(\omega-\omega_u)}{c(k+k_u)}\right)^{-2} \tag{5.15}$$

where $\gamma_0'=\gamma_0(1-(1+a_{u,0}^2)/4\gamma_0^2)^{-1}\approx\gamma_0$. The left-hand side of eq. (5.15) is essentially the dispersion relation of an electromagnetic wave propagating in a relativistic beam of energy γ_0. The right-hand side takes into account the coupling of this type of wave with the undulator, through the combined ponderomotive force $\propto -\partial_z(\boldsymbol{a}_r\cdot\boldsymbol{a}_u)$. However, since $\gamma_0\gg a_{u,0}$, this coupling term is negligible for most values of k. In this case, the mode satisfies $\omega^2\approx c^2k^2+c^2k_p^2/\gamma_0'$ and simply represents a wave propagating along with the beam, without any growth.

The only values of k for which there can be significant coupling are those for which the factor $\beta_{z,0}-(\omega-\omega_u)/c(k+k_u)$ nearly cancels, and thus makes the right-hand side large. The signification of this resonant-coupling condition can be understood by noticing that $(\omega-\omega_u)/(k+k_u)$ is the phase velocity of the ponderomotive force term $-\partial_z(\boldsymbol{a}_r\cdot\boldsymbol{a}_u)$. Only when this velocity equals the velocity of the beam $c\beta_{z,0}$ (i.e. when the ponderomotive term is stationary in the beam frame) can the ponderomotive force have a substantial, lasting micro-bunching effect on the beam. This resonance condition can be rewritten $\omega=c\beta_{z,0}(k+k_u')$ with

$$k_u'=k_u+\frac{\omega_u}{c\beta_{z,0}} \tag{5.16}$$

[4]The right ($\boldsymbol{a}_r=a_{r,0}(\boldsymbol{e}_x+i\boldsymbol{e}_y)$) and left ($\boldsymbol{a}_r=a_{r,0}(\boldsymbol{e}_x-i\boldsymbol{e}_y)$) polarization are not coupled by eqs. (5.10) to (5.12) and thus they can be treated separately. Performing the same calculations with $\boldsymbol{a}_r=a_{r,0}(\boldsymbol{e}_x+i\boldsymbol{e}_y)$ leads to no predicted growth, meaning that the right polarization is not amplified here.

and is represented in fig. 5.2. According to the above analysis, significant coupling can only occur for $\omega \approx \omega_r$, $k \approx k_r$, where k_r and ω_r satisfy the relations

$$\begin{cases} \omega_r &= c\beta_{z,0}(k_r + k'_u) \\ \omega_r^2 &= c^2 k_r^2 + c^2 k_p^2/\gamma'_0 \approx c^2 k_r^2 \end{cases}$$

As represented in fig. 5.2, when $\beta_{z,0}$ is close to 1, the solution of this system lies at a very

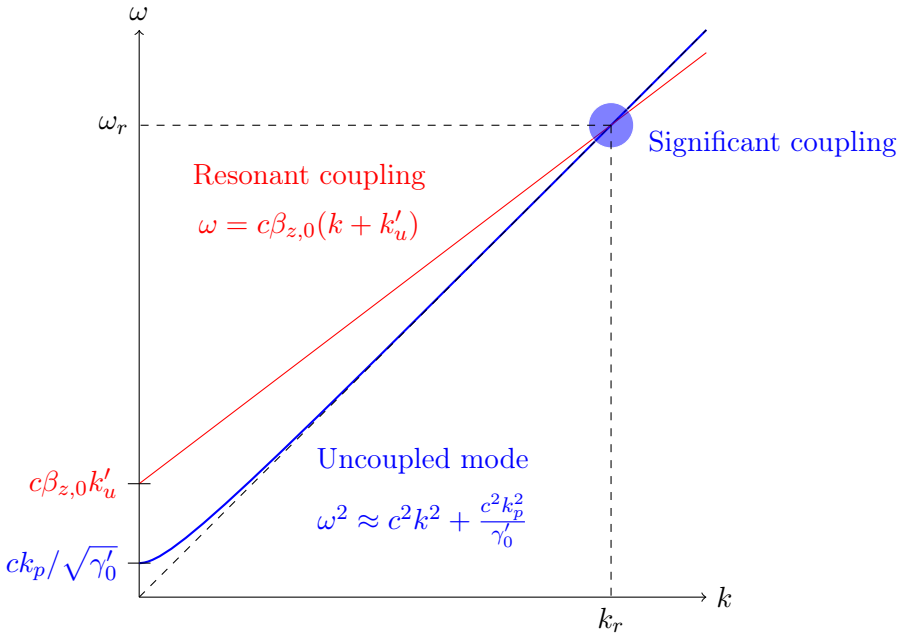

Figure 5.2: Schematic representation of the conditions for significant coupling in eq. (5.15).

high frequency $k_r \gg k_p/\sqrt{\gamma'_0}$, and this justifies the approximation in the latter equation of the system. The above system leads to

$$\omega_r = \frac{c\beta_{z,0}k'_u}{1-\beta_{z,0}} \approx \frac{2\gamma_0^2 ck'_u}{(1+a_{u,0}^2)} \qquad k_r = \omega_r/c \tag{5.17}$$

This result is indeed natural. Since $c\beta_{z,0}k'_u$ is the frequency at which the electrons wiggle, $\omega_r = c\beta_{z,0}k'_u/(1-\beta_{z,0})$ can be interpreted as the Doppler-shifted frequency of the radiation that they emit along the axis of the undulator. Equation (5.17) also shows that $k_r \gg k_u$, and as a result that the density modulation in eq. (5.13) (i.e. the micro-bunching) have a wavelength that is essentially equal to the radiation wavelength $\lambda_r = 2\pi/k_r$.

However, $\omega = \omega_r$, $k = k_r$ is not in itself a solution of eq. (5.15). Therefore, we search for a proper solution in the form $\omega = \omega_r$, $k = k_r + \delta k$, where $\delta k \ll k_0$. In this case, there are three roots δk to the dispersion relation, of which two are complex: $\delta k = \rho k'_u(1 \pm i\sqrt{3})$, with

$$\rho = \frac{1}{\gamma_0}\left(\frac{a_{u,0}^2\, k_p^2}{32\, k_u'^2}\right)^{1/3} \tag{5.18}$$

One of these roots corresponds to an exponentially growing $\boldsymbol{a}_r$ as a function of z:

$$\boldsymbol{a}_r = \left[\frac{\boldsymbol{a}_{r,0}}{2}e^{i(k_r+\rho k'_u)z - i\omega_r t} + \frac{\boldsymbol{a}^*_{r,0}}{2}e^{-i(k_r+\rho k'_u)z + i\omega_r t}\right]\exp(\sqrt{3}\rho k'_u z) \qquad \boldsymbol{a}_{r,0} = a_{r,0}(\boldsymbol{e}_x - i\boldsymbol{e}_y) \tag{5.19}$$

with a corresponding Poynting flux

$$\Pi = \frac{mc\omega_r^2 a_{r,0}^2}{4\pi r_e} \exp(z/L_{g,0}) \qquad L_{g,0} = \frac{1}{2\sqrt{3}\rho k'_u} \tag{5.20}$$

This solution corresponds to the radiation amplified by the FEL.

Generalization. Importantly, all the above expressions are valid both for a magnetic undulator ($k'_u = k_u$) and for a counterpropagating laser pulse ($k'_u \approx 2k_u$). These expressions are however restricted to the case of a helical undulator ($\boldsymbol{a}_{u,0} = a_{0,u}(\boldsymbol{e}_x \pm i\boldsymbol{e}_y)$). In the case of a planar undulator ($\boldsymbol{a}_u = \frac{a_{u,0}}{2}(e^{ik_u z + i\omega_u t} + e^{-ik_u z + i\omega_y t})\boldsymbol{e}_x$), the analysis is complicated by the fact the zeroth-order velocity is not constant:

$$\beta_{z,0}^{\text{planar}} = 1 - \frac{2 + a_{u,0}^2}{4\gamma_0^2} - \frac{a_{u,0}^2}{4\gamma_0^2}\cos(2k_u z + 2\omega_u t) \tag{5.21}$$

As a consequence of these velocity oscillations, a planar FEL can amplify radiation at several discrete harmonics. When considering only the fundamental harmonic for instance, the above results can be transposed by replacing eq. (5.17) and eq. (5.18) by

$$\omega_r^{planar} = ck_r^{planar} = \frac{4\gamma_0^2 ck'_u}{(2 + a_{u,0}^2)} \tag{5.22}$$

$$\rho^{planar} = \frac{1}{\gamma_0}\left(\frac{a'^2_{u,0}\, k_p^2}{32\, k'^2_u}\right)^{1/3} \qquad \text{where} \qquad a'_{u,0} = a_{u,0}\left[J_0\left(\frac{a_{u,0}^2}{4 + 2a_{u,0}^2}\right) - J_1\left(\frac{a_{u,0}^2}{4 + 2a_{u,0}^2}\right)\right] \tag{5.23}$$

To summarize the results of this section, an FEL amplifies radiation at the natural Doppler-shifted frequency ω_r given in eq. (5.17) (helical undulator) or eq. (5.22) (planar undulator). According to these expressions, the emitted frequency ω_r can be rather easily tuned, either by changing the energy γ_0 of the injected electrons, or by changing the strength of the undulator $a_{u,0}$. In particular, in order to reach a very high radiation frequency, XFELs need very energetic electrons.

The radiation is amplified with a characteristic *gain length* $L_{g,0}$, whose expression is given in eq. (5.20), and which crucially depends on the *Pierce parameter* ρ given in eq. (5.18) (helical undulator) or eq. (5.23) (planar undulator). This exponentionally growing radiation originates from a positive feedback loop. A small-level radiation starts micro-bunching the electrons at the radiation wavelength λ_r, which therefore emit with greater coherence and produce a stronger radiation, which in turn produce stronger micro-bunching. Physically, the energy of the emitted radiation is taken from the kinetic energy of the electrons.

5.1.3 Degrading effects

In the previous section, it was assumed that the electron bunch was initially cold (both longitudinally and transversely) and that the impact of its finite transverse and longitudinal size could be neglected. When these assumptions are no longer valid, the gain of the FEL process tends to be degraded (i.e. the actual gain length L_g tends to be larger than $L_{g,0}$).

One of the main impacts of transverse temperature (i.e. non-zero emittance) is that the electron beam diverges. This can have major consequences for the FEL process, since the density n_0 of a diverging beam progressively decreases, and so does the corresponding plasma vector

$k_p^2 = 4\pi n_0 r_e$ and the crucial Pierce parameter $\rho \propto k_p^{2/3}$. In order to keep the transverse size of the beam small, transverse focusing has to be applied. In conventional magnetic undulator, this is partly done by natural focusing (i.e. by the transverse, focusing ponderomotive force of the magnetic field of the undulator) and partly by the use of quadrupole magnets [Huang and Kim, 2007]. As a result of this focusing, individual electrons perform betatron oscillations while propagating through the undulator. The strength of the focusing elements is usually tuned so that the beam, as a whole, keeps a nearly constant transverse size throughout the undulator. (The beam is said to be *matched*.) Yet, even when the transverse size of the beam is constant, the FEL gain can still be degraded.

An exact calculation of the degrading impact of finite temperature and finite size requires a 3D kinetic formalism (e.g. [Saldin, 1999; Huang and Kim, 2007]). Using this formalism, Xie [2000] derived the degraded gain length in the case of a matched, cylindrically-symmetric Gaussian beam. A convient fitting formula for his analytic results is commonly used [Huang and Kim, 2007; Xie, 2000]:

$$L_g = L_{g,0}[\,1 + \Lambda(\eta_d, \eta_\epsilon, \eta_\gamma)\,] \qquad \text{where} \qquad \eta_d = \frac{L_{g,0}}{2k_r\sigma_x^2} \qquad \eta_\epsilon = 2\sigma_\theta^2 k_r L_{g,0} \qquad \eta_\gamma = \frac{1}{\sqrt{3}\rho}\frac{\sigma_\gamma}{\gamma} \tag{5.24}$$

where ρ can be rewritten from eq. (5.18) and eq. (5.23), as

$$\rho = \frac{1}{\gamma_0}\left(\frac{a_{u,0}'^2\, I}{16\, I_A\, k_u'^2 \sigma_x^2}\right)^{1/3} \qquad \text{where} \qquad \begin{cases} a'_{u,0} = a_{u,0} & \text{(helical)} \\ a'_{u,0} = a_{u,0}\left[J_0\left(\frac{a_{u,0}^2}{4+2a_{u,0}^2}\right) - J_1\left(\frac{a_{u,0}^2}{4+2a_{u,0}^2}\right)\right] & \text{(planar)} \end{cases} \tag{5.25}$$

In the above expressions, $L_{g,0}$ is the ideal gain length from eq. (5.20), I is the peak curent of the electron bunch and $I_A = ec/r_e = 17\,\text{kA}$, $\sigma_x = \sqrt{\langle x^2\rangle} = \sqrt{\langle y^2\rangle}$ is the transverse RMS size of the cylindrically-symmetric bunch, $\sigma_\theta = \sqrt{\langle\theta_x^2\rangle} = \sqrt{\langle\theta_y^2\rangle}$ is its RMS divergence, and $\sigma_\gamma = \sqrt{\langle\gamma^2\rangle - \langle\gamma\rangle^2}$ its RMS energy spread. Λ is a growing function of η_d, η_ϵ and η_γ, and is given by the fitted expression:

$$\Lambda = a_1\,\eta_d^{a_2} + a_3\,\eta_\epsilon^{a_4} + a_5\,\eta_\gamma^{a_6} + a_7\,\eta_\epsilon^{a_8}\eta_\gamma^{a_9} + a_{10}\,\eta_d^{a_{11}}\eta_\gamma^{a_{12}} + a_{13}\,\eta_d^{a_{14}}\eta_\epsilon^{a_{15}} + a_{16}\,\eta_d^{a_{17}}\eta_\epsilon^{a_{18}}\eta_\gamma^{a_{19}} \tag{5.26}$$

$$\begin{array}{lllll} a_1 = 0.45 & a_2 = 0.57 & a_3 = 0.55 & a_4 = 1.6 & a_5 = 3 \\ a_6 = 2 & a_7 = 0.35 & a_8 = 2.9 & a_9 = 2.4 & a_{10} = 51 \\ a_{11} = 0.95 & a_{12} = 3 & a_{13} = 5.4 & a_{14} = 0.7 & a_{15} = 1.9 \\ a_{16} = 1140 & a_{17} = 2.2 & a_{18} = 2.9 & a_{19} = 3.2 & \end{array}$$

Thus the gain length equals the ideal gain length $L_{g,0}$ for $\eta_d = \eta_\epsilon = \eta_\gamma = 0$, and it is larger when these quantities are non-zero (i.e. the FEL process is degraded). Let us give a qualitative interpretation for this fact.

Diffractive loss (η_d). In section 5.1.2, the transverse profile of the radiation was ignored. However, if the electron beam has a finite transverse size σ_x, the width of the radiation profile is also of the order σ_x. Therefore, the radiation diffracts and its amplitude decreases on a characteristic length $Z_R = k_r\sigma_x^2/2$ (Rayleigh length). If Z_R is short compared to $L_{g,0}$, the FEL amplification is not fast enough to compensate for this decrease in amplitude. Therefore the impact of diffraction is quantified by the ratio

$$\frac{L_{g,0}}{Z_R} = \frac{2L_{g,0}}{k_r\sigma_x^2} \propto \eta_d$$

Decoherence due to finite energy spread (η_γ). If the bunch has a finite energy spread, the electrons have different longitudinal velocities. From eq. (5.8), the corresponding velocity spread is $\Delta\beta_{z,0} = \sigma_\gamma(1+a_{u,0}^2)/\gamma_0^3$. Thus, if the electrons are micro-bunched at some point, this spread in velocity tends to smear out the micro-bunching pattern at later times. This effect starts impacting the coherence of the FEL process when the corresponding widening of the micro-bunches Δz is comparable to the wavelength of the density modulation: $k_r\Delta z = 1$. The characteristic propagation length L_{coh} over which this happens can be found from $k_r\Delta\beta_{z,0}L_{coh} = 1$, and yields

$$L_{coh} = \frac{\gamma_0^3}{(1+a_{u,0}^2)k_r\sigma_\gamma}$$

There is therefore a competition between the ponderomotive force, which tends to micro-bunch the electrons over a characteristic length $L_{g,0}$, and the energy spread, which tends to erase the micro-bunching over a characteristic length L_{coh}. The FEL process will be strongly degraded if the ratio $L_{g,0}/L_{coh}$ is large. Using eq. (5.20) and the above expression,

$$\frac{L_{g,0}}{L_{coh}} = \frac{1}{\sqrt{3}\rho}\frac{\sigma_\gamma}{\gamma_0} = \eta_\gamma$$

and thus η_γ can be interpreted a measure of the degradation due to the energy spread.

Degradation by finite emittance (η_ϵ). If an electron of energy γ_0 propagates with an average[5] angle θ with respect to the axis of the undulator, its longitudinal velocity is reduced and can be expressed as

$$\beta_{z,0} = 1 - \frac{1+a_{u,0}^2}{2\gamma_0^2} - \frac{\theta^2}{2}$$

Therefore, the angular spread of the beam σ_θ also leads to a longitudinal velocity spread $\Delta\beta_{z,0} = \sigma_\theta^2/2$. Again, this tends to smear out the micro-bunching pattern, and coherence is lost after a propagation distance $L_{coh} = 1/(\Delta\beta_{z,0}k_r) = 2/(k_r\sigma_\theta^2)$. As before, the FEL process is strongly affected if the characteristic distance for ponderomotive micro-bunching $L_{g,0}$ is larger than L_{coh}. The impact of the angular spread is thus quantified by the ratio

$$\frac{L_{g,0}}{L_{coh}} = \frac{k_r L_{g,0}\sigma_\theta^2}{2} \propto \eta_\epsilon$$

Quite importantly, all three degrading coefficients η_d, η_γ and η_ϵ are inversely proportional to the Pierce parameter ρ. This means that an FEL with a high Pierce parameter will be less sensitive to diffraction, high energy spread or high emittance, i.e. that a large Pierce parameter improves the robustness of the FEL process.

5.1.4 Space-charge effects

A large Pierce parameter requires an intense electron bunch (through the factor I/σ_x^2 in eq. (5.25)). However, very intense bunches can be affected by space-charge effects (i.e. the fact that the electrons of the bunch repel each other), which can also degrade the FEL process in three ways.

[5] Due to the transverse wiggling motion of the electron, the angle between the trajectory and the axis of the undulator is not constant. Thus θ represents the average of this angle over one wiggling period.

Short-range longitudinal space-charge. Longitudinally repelling space-charge forces tend to oppose the micro-bunching ponderomotive force, through a phenomenon that is related to the longitudinal plasma oscillations. For a relativistic bunch, the frequency of the longitudinal plasma oscillations is $\omega_p/\gamma_0^{3/2}$ (due to the relativistic inertia of the electron in the longitudinal direction), and thus the propagation length over which space-charge forces impact micro-bunching is $\gamma_0^{3/2}k_p^{-1}$. Thus the importance of space-charge effects can be quantified by the ratio

$$\frac{k_p L_{g,0}}{\gamma^{3/2}} \propto \frac{\sqrt{\rho}}{a'_{u,0}}$$

where $a'_{u,0}$ is given in eq. (5.25). Marcus et al. [2011] derived a fitting formula of the same type as that of Xie [2000], which shows that the gain length is indeed increased when this ratio is large.

Long-range longitudinal space-charge. Longitudinal space-charge forces can also have an impact at the scale of the whole bunch. They tend to accelerate the head of the bunch and decelerate its tail, over a characteristic propagation distance [Grüner et al., 2009]

$$L_{sp,\parallel} = 2\pi\gamma^2\sqrt{2\sigma_x\sigma_z\frac{I_A}{I}} \tag{5.27}$$

This induces an energy chirp across the bunch which, if it becomes comparable to $\gamma_0\rho$, can significantly affect the FEL process.

Transverse space-charge. Similarly, the transverse space-charge fields tend to radially blow-out the bunch. This leads to an increase of the transverse size σ_x and of the angular spread σ_θ, which degrade the FEL process through the coefficient η_ϵ and through a decrease of the Pierce parameter ρ. This blowout happens on a characteristic propagation distance [Reiser, 2008; Grüner et al., 2009]

$$L_{sp,\perp} = 2\pi\gamma^{3/2}\sigma_x\sqrt{\frac{2I_A}{I}} \tag{5.28}$$

5.1.5 Saturation

No instability can grow indefinitely, and at some point a limiting non-linear effect saturates the amplitude. In the case of FEL amplification, this effect is a type of non-linear phase-mixing. As the amplitude of the radiation grows, the longitudinal ponderomotive force substantially accelerates and decelerates the electrons (depending on their longitudinal position), and thus creates stronger and stronger energy modulations across the bunch. In the linear regime, these energy modulations are directly correlated with the longitudinal position z and are part of the FEL process. However, when the modulations are too large, they start distorting these correlations, through the non-linear equations of motion. Figure 5.3 shows these energy modulations in the linear regime (lower left panel) and their distortion in the non-linear regime (lower right panel).

The details of this phenomenon are intricate and an exact description essentially requires numerical simulations. Yet, for a rough analysis of the saturation, the decorrelated energy modulations can be seen as an effective energy spread. Then, according to section 5.1.3, the FEL process will effectively saturate when these energy modulations reach $\delta\gamma \sim \gamma_0\rho$. The amplitude of the radiation at this point can be estimated by using the relation between $a_{r,0}$ and

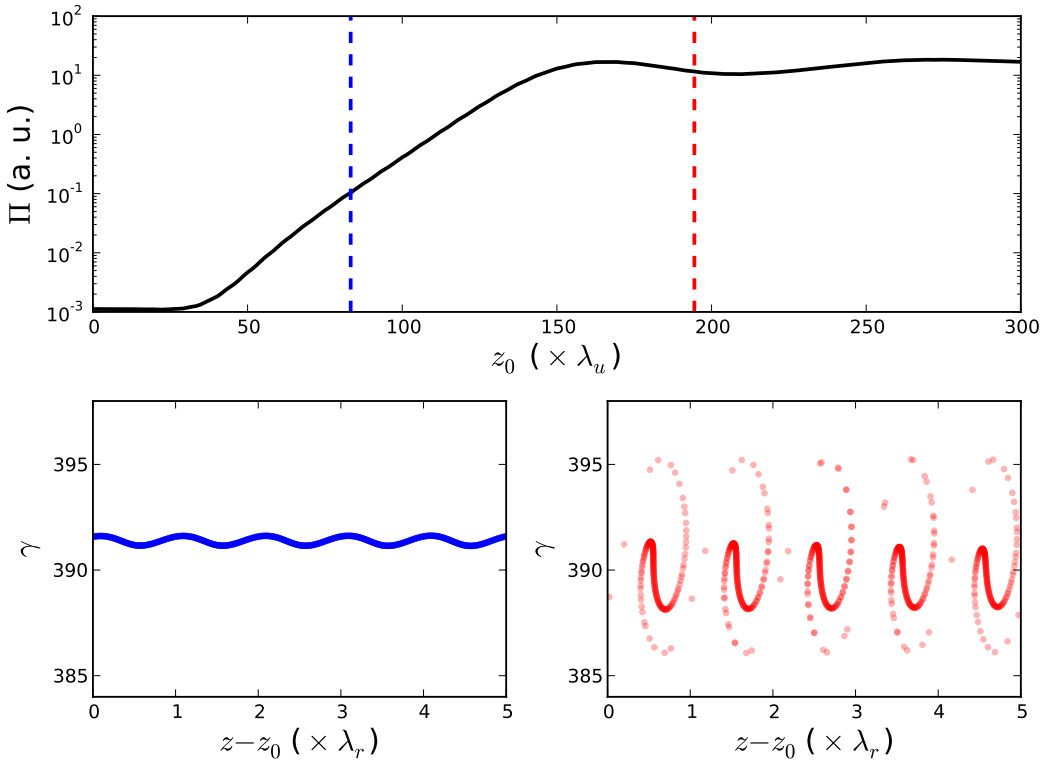

Figure 5.3: Simulation results showing the saturation of the FEL process, for a planar magnetic undulator with $a_{u,0} = 2$ and an electron bunch with $\gamma_0 = 392$. Top: Evolution of the Poynting flux Π with the propagation distance in the undulator z_0. Bottom: Zoom on the energy modulation of the beam, at two different positions in the undulator. Each dot represents a macro-electron of the simulation. (The scale of the z axis in the lower plots is very different than that in the top plot, since $\lambda_r \ll \lambda_u$.) *Simulation run with the FEL spectral code* PLARES *by Andriyash et al. [2014b]*

$\delta u_0 \approx \delta\gamma$ in the linear regime described by section 5.1.2. This yields[6] $a_{r,0} \sim (\gamma_0\rho)^2 k'_u/k_r$ at saturation, which corresponds to a saturated Poynting flux

$$\Pi_{sat} \sim \rho \times (\gamma_0 mc^2) n_0 c.$$

Here $n_0 c$ can be identified as the flux of electrons in the undulator. The above equation implies that an FEL amplifies radiation until it has extracted a fraction $\sim \rho$ of the initial kinetic energy of the electrons. At that point the FEL process saturates and the radiation is no longer amplified.

[6] More precisely, injecting eq. (5.14) and eq. (5.19) in eq. (5.11) yields $a_{r,0} = -\frac{\gamma_0\beta_{z,0}\rho k'_u(1-i\sqrt{3})}{(k_r+k_u+\rho k'_u(1-i\sqrt{3}))a_{u,0}}\delta u_0 \approx \gamma_0 \frac{k'_u}{a_{u,0}k_r}(1-i\sqrt{3})\delta u_0$. From the above analysis, $\delta u_0 \approx \delta\gamma \sim \gamma_0\rho$ at saturation and thus $a_{r,0} \sim (\gamma_0\rho)^2 k'_u/k_r$.

5.2 A prospective study of an LWFA-based FEL

5.2.1 Motivation and specific features of an LWFA-based FEL

Although FELs are unique sources due to their brightness, coherence and short wavelength, they are also very large and costly facilities. This is particularly true of FELs that operate in the UV and X-ray range, and which require a long accelerator to provide the necessary GeV-level electrons. For instance, the accelerator of SACLA – the most compact existing XFEL – is 750 m long [Tanaka and Shintake, 2005] (see fig. 5.4), and the accelerator of the European XFEL, currently under construction in Germany, will even reach 2.1 km [Altarelli, 2006]. In view of these numbers, the possibility to accelerate electrons to the same energies in a meter-scale distance (and using a ten-meter scale laser system) is indeed attractive.

Figure 5.4: The accelerator (left) and magnetic undulator (right) of the free-electron laser SACLA, during a visit organized for the FEL2012 conference.

However, when designing an LWFA-based FEL, the particular features of the electron bunches have to be duly taken into account. As shown in table 5.1, some of the characteristics of these bunches are very different than those for conventional accelerator. One the one hand, LWFA-generated bunches typically have a much higher peak current – which is favorable to the FEL process since it increases the Pierce parameter ρ. On the other hand, they are also characterized by a relatively large energy spread – which, as explained previously, can seriously affect the FEL process. Similarly, although conventional accelerator and LWFA tend to produce bunches with comparable emittance, LWFA-generated bunches have much smaller transverse size and much higher divergence. Again, a smaller transverse size leads to a higher Pierce parameter, but a larger divergence threatens the FEL process.

When considering the above parameters, it is clear that the design of a conventional FEL has

	Peak current	Bunch length	σ_γ/γ_0	$\epsilon_\perp$	σ_x	σ_θ
Conventional	∼0.1 – 1 kA	∼0.1 – 1 mm	∼0.01 %	∼1 mm.mrad	∼1 mm	∼1 μrad
LWFA	∼10 kA	∼1 μm	∼1 %	∼1 mm.mrad	∼1 μm	∼1 mrad

Table 5.1: Typical orders of magnitude for the characteristics of an electron bunch produced either by a conventional accelerator or an LWFA.

to be re-adapted in order to accomodate the specific features of LWFA-generated bunches, and that actually reaching FEL amplification may in fact be challenging. On the other hand, these parameters also suggest that LWFA bunches might be better suited to other types of undulators (i.e. non-magnetic) than their conventional counterparts. Keeping this in mind, in the rest of this section we search for the condition that would allow a *proof-of-concept* FEL amplification, with an LWFA bunch. In particular, we consider the undulator parameters $a_{u,0}$ and $\lambda'_u = 2\pi/k'_u$ as free parameters, in order to determine which type of undulator would be best suited for an LWFA-generated bunch.

Figure 5.5 illustrates this approach. In this figure, the efficiency of the FEL process is estimated as function of the undulator parameters $a_{u,0}$, λ'_u, for a typical LWFA bunch ($E \approx$ 200 MeV, $\epsilon_\perp = 0.5$ mm.mrad, $\sigma_x = 1$ μm, I=30 kA). In order to quantify this efficiency, we use the ratio $L_{g,0}/L_g = 1/[\ 1 + \Lambda(\eta_d, \eta_\epsilon, \eta_\gamma)\ ]$, as given by the Xie formula (eqs. (5.24) and (5.26)) in the case of a planar undulator. For $L_{g,0}/L_g \approx 1$ there is robust FEL amplification and the gain length is relatively short, whereas for $L_{g,0}/L_g \ll 1$, the FEL process is strongly degraded and it is extremely uncertain whether there will be any FEL amplification at all. The left panel is a colormap of $L_{g,0}/L_g$. The right panel indicates the zones where diffraction ($\eta_d > 1$, red area), emittance ($\eta_\epsilon > 1$, green area) or energy spread ($\eta_\gamma > 1$, blue area) seriously degrade the FEL process, and thus provides a semi-quantitative explanation for the aspect of the left panel. Several types of undulator are represented on this figure, including magnetic undulators ($a_{u,0} \sim 1$, $\lambda'_u \sim 1cm$), plasma wave undulators [Joshi et al., 1987; Williams et al., 1993; Corde and Ta Phuoc, 2011] ($a_{u,0} \sim 0.5$, λ'_u ranges from $\sim 10\,\mu$m to $\sim 100\,\mu$m depending on the plasma density), and picosecond laser undulators [Tomassini et al., 2003; Bacci et al., 2008; Petrillo et al., 2008] (according to section 5.1.2, $\lambda'_u = \lambda_u/2$ for a laser pulse, thus λ'_u is 5 μm for a CO_2 laser pulse and 0.4 μm for a Ti:Sapph laser).

On the whole, fig. 5.5 shows that, in the case of a laser or plasma undulator, the FEL process is strongly degraded, due to finite energy spread and emittance. Similarly, as a result of the small beam size and high divergence, diffraction and finite emittance seriously affect an FEL based on a magnetic undulator. This conclusion can however be modified by manipulating the beam before it enters the undulator.

5.2.2 Magnetic undulator

In fact, the estimation provided by the Xie formula is incomplete in the case of a magnetic undulator. Because of the high divergence of the LWFA bunch, its transverse size σ_x will quickly grow over the meter-scale drift distance beetween the accelerator and undulator, and then over the length of the undulator. This reduces the Pierce parameter and makes degradation by finite emittance even more serious. Therefore, in order for FEL amplification to occur, the beam has to be collimated before entering the undulator. Collimation reduces the divergence σ_θ and the associated degradation parameter η_ϵ, while ensuring at the same time that the Pierce parameter does not decrease along the undulator. Using quadrupole magnets, the beam can be collimated to a transverse size of $\sim 100\,\mu$m and, assuming that the emittance is preserved, to a divergence

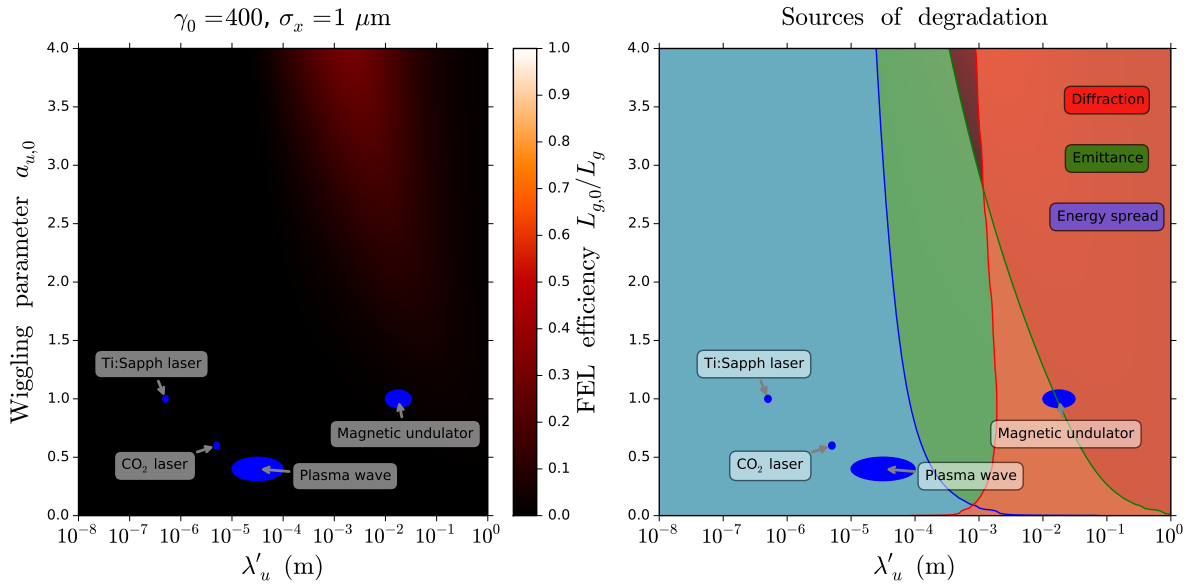

Figure 5.5: Estimation of the efficiency of the FEL process for a typical LWFA bunch ($I = 30$ kA, $\epsilon_\perp = 0.5$ mm.mrad, $\gamma_0 = 400$, $\sigma_\gamma/\gamma = 1\%$, $\sigma_x = 1\,\mu$m), based on the Xie formula (eqs. (5.24) and (5.26)). The colored areas on the right panel indicates the zones where $\eta_d > 1$ (red area), $\eta_\epsilon > 1$ (green area) or $\eta_\gamma > 1$ (blue area).

of $\sim$10 μrad.

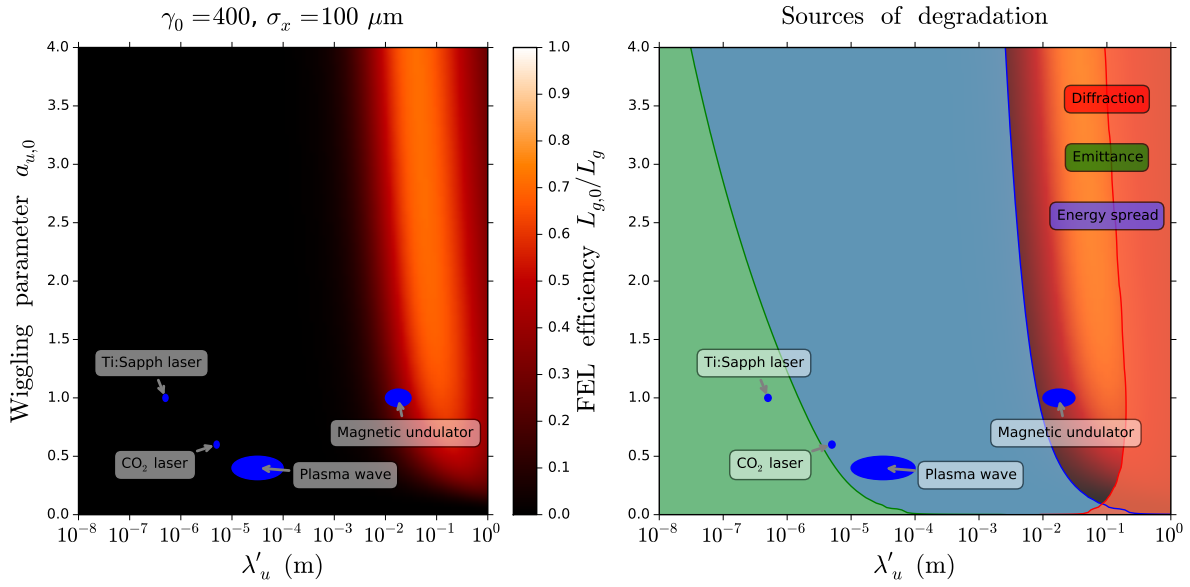

Figure 5.6: Estimation of the efficiency of the FEL process for a *collimated* LWFA bunch. ($I = 30$ kA, $\epsilon_\perp = 0.5$ mm.mrad, $\gamma_0 = 400$, $\sigma_\gamma/\gamma = 1\%$, $\sigma_x = 100\,\mu$m).

The FEL efficiency associated with a collimated beam is plotted in fig. 5.6. As shown in this figure, FEL amplification now seems realistic, in the case of a magnetic undulator. The

dominant source of degradation here is the finite energy spread of the bunch, and it can still seriously degrade the FEL process if the actual bunch quality is lower than that considered here. In order to alleviate the impact of energy spread and to make the FEL amplification more robust, Maier et al. [2012] and Loulergue [2013] proposed to use a magnetic chicane before the undulator. The corresponding setup is represented in fig. 5.7. The effect of the chicane is to sort the electrons longitudinally, depending on their energy. (The most energetic electrons are placed at the head of the bunch, while the low energy electrons trail at the back.) This results in a lower effective energy spread, but also come at the cost of a longer bunch duration and thus a lower peak current. For well-chosen chicane parameters, this scheme greatly improves the robustness of FEL amplification. It is now at the heart of the LUNEX5 project [Couprie et al., 2013], a collaboration which involves several research centers, including LOA and the SOLEIL synchrotron, and which aims at an experimental demonstration of an LWFA-based FEL.

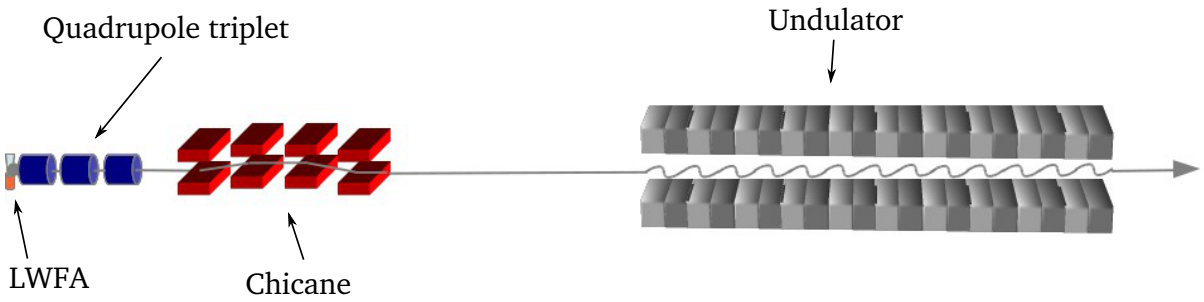

Figure 5.7: Schematic representation of the setup considered for an FEL based on an LWFA beam and a magnetic undulator. A quadrupole triplet collimates the beam after the exit of the accelerator. It is followed by a magnetic chicane, which decompresses the bunch longitudinally. *Courtesy of A. Loulergue*

One of the remaining issues of this scheme lies in the transport of the bunch from the accelerator to the undulator. The transport and collimation are indeed made difficult by the high divergence of the bunch, at the exit of the accelerator. Because of this divergence, the transverse size of the bunch is very large when it reaches the collimating quadrupole magnets. As a result, the electrons experience the high-radius aberrations of these magnets, and their emittance is strongly affected. In addition, a large divergence also implies that the electrons have a considerable spread in longitudinal velocity, and therefore that the bunch will spread longitudinally during its propagation from the accelerator to the undulator. This effect reduces the peak current (thereby reducing the Pierce parameter) and moreover makes it more difficult to longitudinally sort the electrons with the chicane. Calculations and simulations by Alexandre Loulergue showed that, for a bunch with an initial divergence of 2 mrad, the peak current can be 20 times lower and the emittance 100 times higher, after transport and collimation. With these parameters, FEL amplification is again degraded.

Calculations also show that this increase in emittance and decrease in peak current depend quadratically on the initial divergence. This means that reducing the initial divergence is paramount here, and that even a moderate reduction can have substantial benefits. Although divergence can in principle be reduced by accelerating the electrons to higher energies (see section 1.2.2), a higher energy also reduces the Pierce parameter (see eq. (5.25)), and thus one must find other means to improve divergence. In this context, the results of chapter 4 can provide a solution. In that chapter, it was shown that a laser-plasma lens can significantly reduce the divergence of the bunch. Importantly, this reduction of divergence occurs only about one millimeter

after the exit of the accelerator i.e. before the initial divergence can induce substantial bunch lengthening. Thus placing a laser-plasma lens after the accelerator and before the quadrupole triplet would greatly facilitate the subsequent transport of the beam and would ultimately lead to a more robust FEL process.

It should nonetheless be mentioned that, although the laser-plasma would substantially facilitate the transport of the beam, it is not strictly necessary for a first proof-of-principle experiment, within the LUNEX5 collaboration. In addition to the magnetic chicane, recent progress in the design of the experiment (including the *super-matching* transport scheme by Alexandre Loulergue) are likely to make the amplification much more robust. In addition, the use of a *seeding* radiation (e.g. [Yu et al., 2000; Togashi et al., 2011]) will allow to use a shorter undulator [Lambert et al., 2008; Labat et al., 2011]. Simulations currently suggest that, in these conditions, an FEL gain can realistically be observed, and a first experiment is planned to take place at LOA within the next few years.

5.2.3 Laser and plasma undulator

Although magnetic undulators are a robust and efficient technology, other undulator concepts have also been proposed. As mentioned before, these concepts include laser and plasma undulators [Whittum et al., 1990; Joshi et al., 1987; Gea-Banacloche et al., 1987; Danly et al., 1987]. With the development of high-power femtosecond lasers – and their ability to generate high fields in plasmas – these alternative concepts have recently attracted much interest. Compared to a magnetic undulator, laser undulators and plasma undulators have a much higher wiggling field and a much shorter undulator period. This gives them several advantages over the conventional magnetic undulators. First, due to their micron-scale undulator period, laser and plasma undulators can be orders of magnitude shorter than magnetic undulators. They could thus drastically reduce the size of the overall FEL setup. Moreover, in contrast to a magnetic undulator, a laser undulator or plasma undulator can be placed almost immediately after the accelerator, and thereby eliminates the need for beam transport.

However, figs. 5.5 and 5.6 show that, with a standard LWFA beam, the FEL efficiency of these undulator is close to zero. This is due to their short undulator period λ'_u, which makes the Pierce parameter ρ very low (see eq. (5.18)) and leads to tighter requirements on the bunch quality. In order to compensate for this, one could consider using a lower-energy electron bunch, since ρ increases when γ_0 decreases. Here it should be noted that in principle low-energy bunches are more sensitive to deleterious space-charge effects. This however is partly compensated by the shorter length of a laser or plasma undulator, which implies that these effects have less time to develop.

In chapter 3, it was shown that optical transverse injection could precisely provide low-energy bunches with low emittance, low energy spread and high current. Thus these bunches appear to be good candidates for a laser or plasma undulator. The corresponding FEL efficiency (for the bunch of section 3.3.1) is plotted in fig. 5.8. As can be seen, the situation is partly improved compared to figs. 5.5 and 5.6. In particular, this type of bunch would be well suited for an undulator with $\lambda'_u \sim 10\ \mu\text{m}$ –$100\ \mu\text{m}$ and $a_{u,0} \gtrsim 1$, and this is the motivation for the undulator that is proposed in section 5.3. However, regarding a laser or a plasma undulator, degradation by energy spread and emittance is still too strong.

In fact, a laser or plasma undulator requires even lower energy. In the rest of this section, we consider the set of beam parameters of table 5.2, which corresponds to $\gamma = 20$ with a percent-level energy spread, and which could realistically lead to amplification with a CO_2 laser undulator or plasma undulator. Although these parameters have not yet been achieved, they provide a

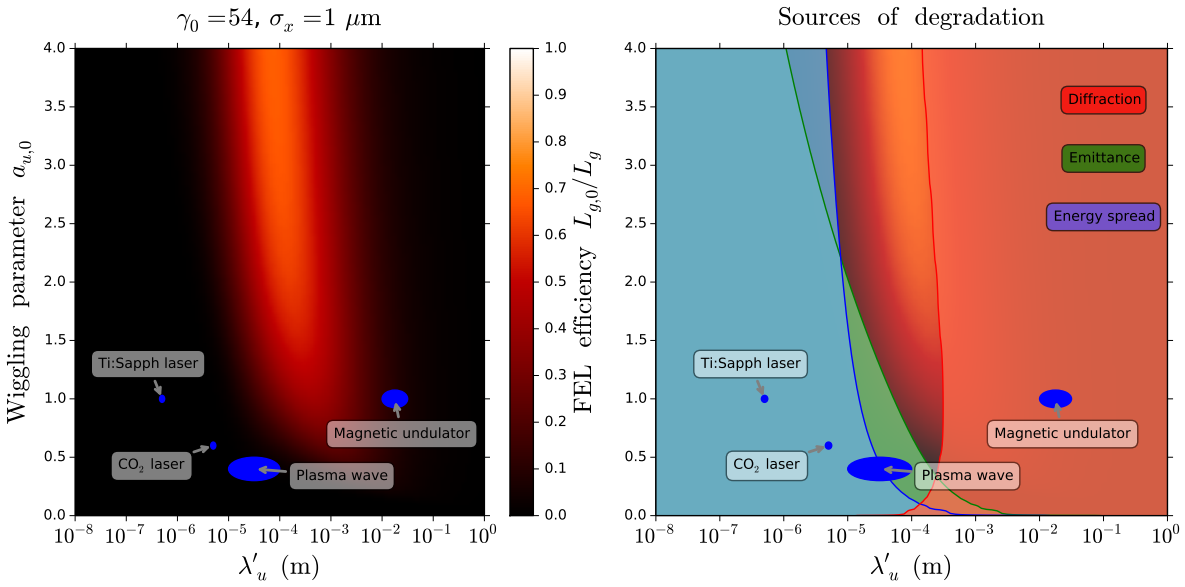

Figure 5.8: Estimation of the efficiency of the FEL process for a bunch *obtained by optical transverse injection* in section section 3.3.1 (I = 10 kA, $\epsilon_\perp$ = 0.17 mm.mrad, γ_0 = 54, σ_γ/γ = 1.7%, $\sigma_x = 1\,\mu$m).

reasonable objective for simulations and ultimately for experiments. Apart from the lower energy and energy spread, these values are close to those obtained by optical transverse injection, and scanning the parameters of the injection (plasma density, laser energy) could potentially lead to similar parameters. Alternatively, low-energy gradient injection [Geddes et al., 2008; Schmid et al., 2010] is also a possible candidate to meet the requirements of table 5.2.

Q	γ	σ_γ	$\epsilon_\perp$	σ_x	σ_z
100 pC	20	0.2	0.17 mm.mrad	2 μm	1 μm

Table 5.2: Set of parameters considered for FEL amplification with a CO_2 laser undulator or a plasma undulator.

The efficiency of the FEL process for the parameters of table 5.2 is represented in fig. 5.9. As a result of the lower energy and the higher associated Pierce parameter, these parameter seem indeed favorable to a plasma undulator or a CO_2 laser undulator.

5.2.4 The particular case of the CO_2 laser undulator

Due to its short undulator period, the CO_2 laser undulator is a particularly attractive option [Petrillo et al., 2008]. In a CO_2 laser undulator, the electron bunch travels through a long (∼100 ps) and energetic (∼100 J) counterpropagating laser pulse. In this configuration, the electric and magnetic fields of the pulse force the electrons to oscillate, and can potentially lead to an FEL instability. In this section, we evaluate the potential of a CO_2 undulator with the beam parameters of table 5.2, by taking into account additional degrading effects that were neglected in the previous section. Three important additional effects have to be considered here, that are not assessed by the Xie formula.

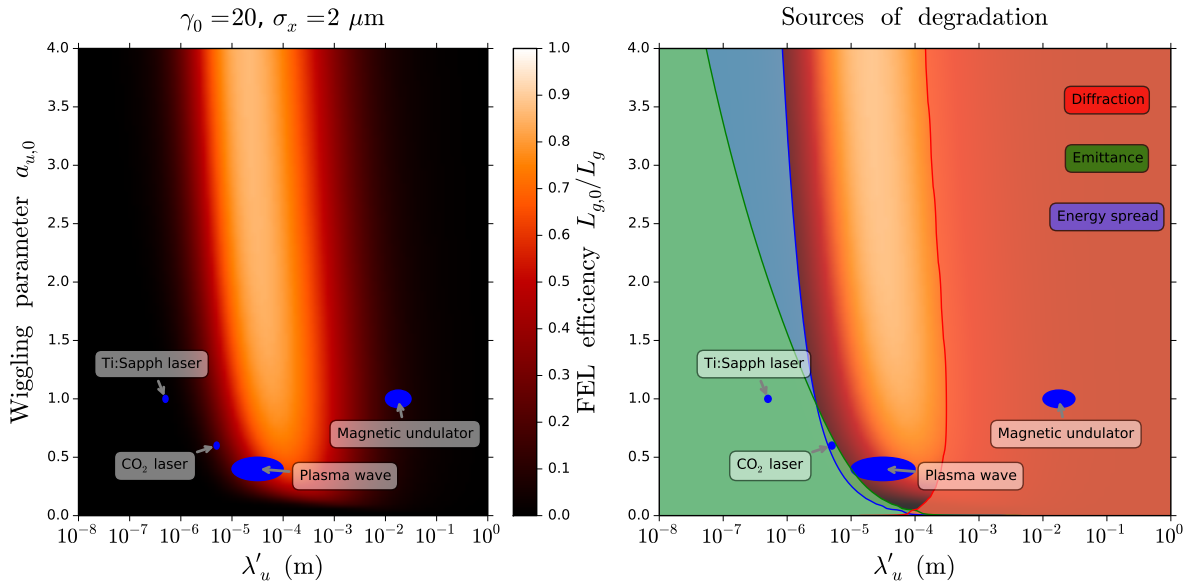

Figure 5.9: Estimation of the efficiency of the FEL process for the *hypothetical* bunch of table 5.2. A Gaussian profile is assumed longitudinally, and thus the peak current is $I = 12$ kA.

The first one is the fact that the bunch naturally diverges while propagating in the laser undulator. Therefore the density of the bunch decreases along the undulator, and this has to be accounted for. A second important effect is the impact of space charge. As explained in section 5.1.4, space-charge effects tend to make bunching more difficult, and they can be substantial for low-energy electron bunches. Finally, the third effect is the non-uniformity of the undulator. As the electrons propagate through the counterpropagating CO_2 laser pulse, the wiggling parameter $a_{u,0}$ that they experience changes. This is due partly to the finite duration of the laser pulse, and partly to its finite Rayleigh length. In this section, we will consider UCLA's "MARS" laser, which can deliver 200 J pulses with 170 ps duration focused to a waist $w_0 = 80\,\mu$m (which corresponds to $a_{u,0} = 0.7$ in the focal plane). In this case, the length of the laser pulse is about 50 mm, while the Rayleigh length is 2 mm. Thus the non-uniformity of the laser is dominated by the finite Rayleigh length:

$$a_{u,0}(z) = \frac{a_{u,0}}{\sqrt{1 + \frac{(z-z_{foc})^2}{Z_R^2}}}$$

where z_{foc} is the longitudinal position of the focal plane and Z_R is the Rayleigh length.

In order to take these effects into account, we performed GENESIS simulations[7] [Reiche, 1999] with the bunch parameters of table 5.2. These simulations consistently take into account the divergence of the bunch, the non-uniformity of the undulator, and the short-range space-charge effects. The results of these simulations are shown in fig. 5.10, and they reveal that FEL amplification indeed does take place. As a result of the growing σ_x (which lowers the Pierce parameter) and of the decreasing $a_{u,0}$ (which detunes the resonant wavelength), FEL

[7]Strictly speaking, GENESIS only features a magnetic undulator. Yet, according to section 5.1.2, the FEL equations are the same for a laser undulator with a wavelength λ_0 and for a magnetic undulator with a period $\lambda_u = \lambda_0/2$. Thus the simulations were performed for an equivalent magnetic undulator having $\lambda_u = 5\,\mu m$. A similar approach was used by Petrillo et al. [2008], but they did not consider the non-uniformity of the undulator.

amplification stops after 1.5 mm of propagation. Nonetheless, the radiation emitted before this point already has interesting properties. The simulations predict that the electrons emit 4 μJ of radiation at $\lambda_r = 8.5$ nm (146 eV), with a peak power of 700 MW.

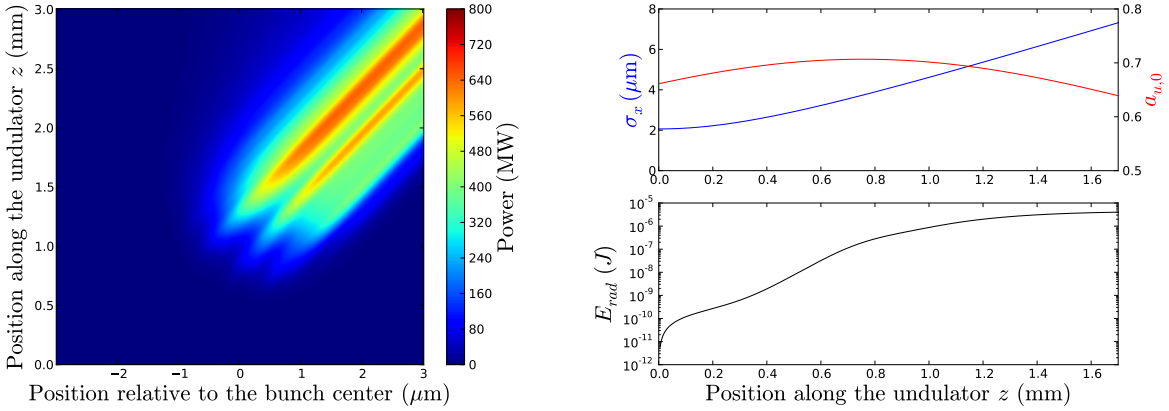

Figure 5.10: Results of GENESIS simulations for the bunch parameters of table 5.2 and for a laser undulator corresponding to UCLA's 'MARS' laser. Left panel: Radiation power along the undulator. The radiation *slips* with respect to the center of the bunch, due to the relatively low energy of the electrons. Right panel: evolution of the transverse size of the bunch σ_x, the wiggling parameter $a_{u,0}$ and the total radiated energy E_{rad}, along the undulator. The energy stops growing after ∼1.5 mm of propagation.

Here, it should however be noted that GENESIS simulations do not take into account transverse space-charge effects. As explained in section 5.1.4, tranverse space-charge can lead to an increase in emittance, which can potentially degrade the FEL process. With the bunch parameters considered here, the characteristic length over which these effects develop is $L_{sp,\perp} \approx 1.5$ mm (see eq. (5.28)), and is thus comparable to the length over wich FEL amplification takes place. The impact of these effects can be estimated by using eq. (1.45). Assuming that the bunch evolves from a transversely Gaussian profile to a transversely uniform profile during its propagation, the corresponding increase in emittance evaluates as

$$\epsilon_{x,f} = \sqrt{\epsilon_{x,i}^2 + \frac{\sigma_x^2}{4\gamma_0}\frac{I}{I_A}U_{Gauss}} \qquad \text{with} \qquad U_{Gauss} = 0.154$$

With an initial emittance $\epsilon_{x,i} = 0.17$ mm.mrad and with $\sigma_x = 2$ μm, the final emittance $\epsilon_{x,f}$ is 0.19 mm.mrad. Thus the emittance is only slightly increased, and the transverse space-charge effects are unlikely to seriously degrade the FEL operation.

On the whole, the above estimates and the results of GENESIS simulations are quite positive. Thus the parameters of table 5.2 can indeed be considered as an objective for future parametric studies of optical transverse injection. Reaching this objective would allow FEL amplification with currently available laser undulators.

5.3 Nanowire undulator

5.3.1 Presentation and motivation

As mentioned in section 5.2.3, the electron bunches produced by optical transverse injection would be ideally suited for an undulator with $\lambda_u \sim 10\ \mu\text{m} - 100\ \mu\text{m}$ and $a_{u,0} \gtrsim 1$. However, such undulators are not currently available. For this reason, we proposed a new type of undulator, with which it is hoped to reach the equivalent of $a_{u,0} \gtrsim 1$. The basic idea is to place an array of nano-fabricated wires, immediately after a laser-wakefield accelerator. As represented in fig. 5.11, in this scheme the driving laser pulse propagates through this array after exiting the gas jet. As the pulse hits the wires, it ionizes them and strips them of a fraction of their electrons. As a result, the wires become positively charged and generate a strong space-charge field. PIC simulations by Agustin Lifschitz and Igor Andriyash at LOA showed that electrostatic fields of the order of 1 TV.m^{-1} can be generated in this way.

These electrostatic fields can then influence the trajectories of the trailing electrons, after they exit from the accelerator. The nanowires are arranged in a checker-board pattern, so that they pull the electrons in alternate directions, effectively forcing them to wiggle. In this scheme, the nanowires are ∼10 microns long and ∼0.5 μm wide, and they are separated by ∼10 microns. These specifications are within the capabilities of current nano-fabrication techniques with silicon substrates.

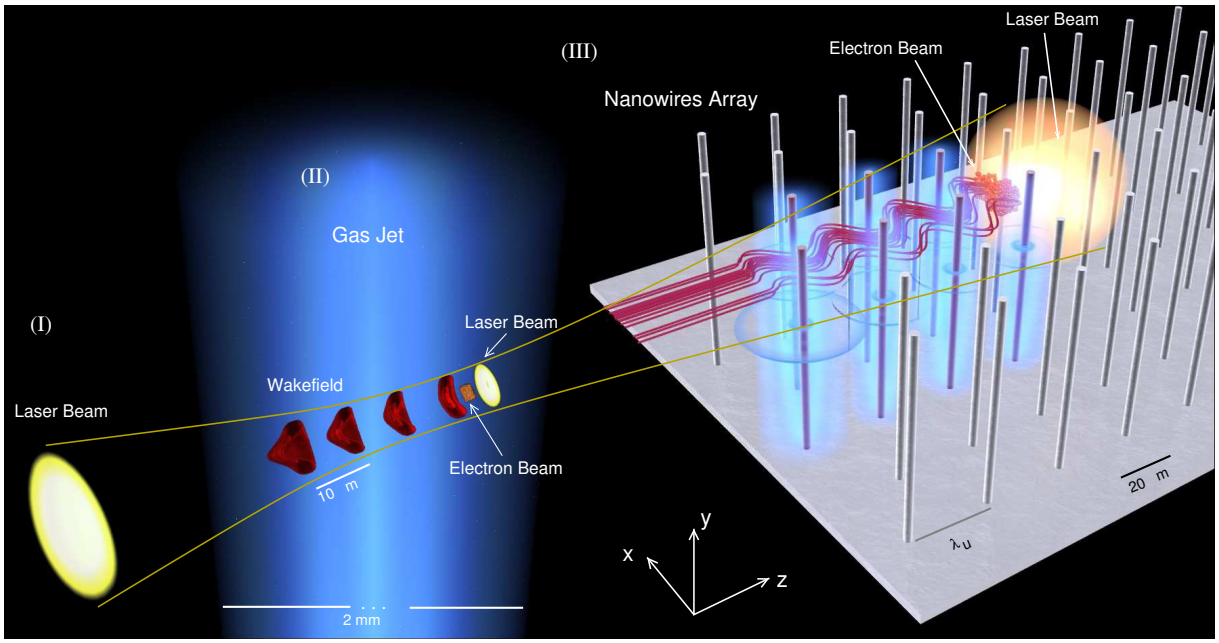

Figure 5.11: Representation of the proposed nanowire undulator. After exiting the accelerator, the driving laser pulse ionizes the wires, and repels a fraction of the electrons. This creates a strong space charge field around the nanowires, which can wiggle the trailing electron bunch. *(Courtesy of A. Lifschitz)*

In order to study this undulator, we use a simplified model in sections 5.3.2 to 5.3.4. In this model, which is represented in fig. 5.12, the undulator consists of two infinite rows of identical, positively-charged and infinitely-long wires. We chose to consider only two rows because the rows lying closer to the path of the laser are the most strongly charged, and they are the ones

that determine in practice the motion of the electrons. In section 5.3.5, we examine to which extent the other approximations of this model are valid, and we discuss how the results of the model are modified when considering a more realistic undulator.

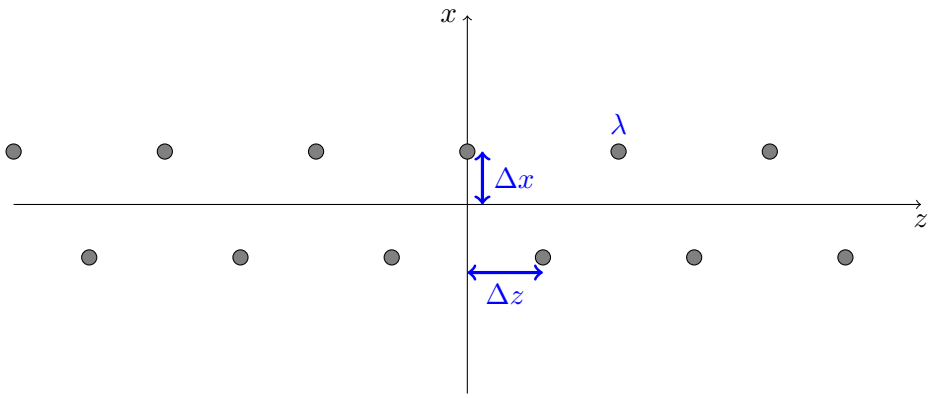

Figure 5.12: Representation of the simplified model considered in sections 5.3.2 to 5.3.4. The parameters of the model are the longitudinal and transverse spacing between the wires (Δz and Δx), and the linear charge density λ of each individual wire.

In studying the FEL process, we use a cold-fluid approach similar to that of section 5.1.2. The electric field inside the undulator is calculated in section 5.3.2, and the zeroth-order motion of the electrons in this field (i.e. their motion in the absence of radiation) is studied in section 5.3.3. The amplified radiation is considered in section 5.3.4, and we derive the gain length for a certain range of parameters.

5.3.2 The fields inside the undulator

The electric field created by an individual, infinitely-long wire has a well-known expression.

$$\boldsymbol{E} = \frac{2mc^2 r_e}{e^2}\left(\frac{\lambda}{r}\right)\boldsymbol{e}_r = 2\frac{mc^2}{e}\tilde{\lambda}\left(\frac{x-x_0}{(x-x_0)^2+(z-z_0)^2}\boldsymbol{e}_x + \frac{z-z_0}{(x-x_0)^2+(z-z_0)^2}\boldsymbol{e}_z\right) \quad (5.29)$$

where r is the distance from the axis of the wire, and where (x_0, y_0) is the position of the wire in cartesian coordinates. λ is the linear charge density of the wire, and $\tilde{\lambda} \equiv \lambda r_e/e$ is the corresponding dimensionless parameter. In our case, $\tilde{\lambda}$ can be reexpressed as

$$\tilde{\lambda} = \pi R^2 r_e Z \alpha n_{\text{at}} \qquad = 6.2\times 10^3\ \alpha\, R[\mu\text{m}]^2 \quad \text{for silicon}$$

where R is the radius of the wire, n_{at} is the density of atoms in the wire, Z the atomic number of these atoms and α the overall fraction of electrons that have been removed by the laser. PIC simulations reveal that α is of the order of 10^{-3}, and thus for $R \approx 0.5\,\mu$m, $\tilde{\lambda}$ is of order unity.

By linear superposition, the total electric field in the undulator can be written as a sum over the wires:

$$E_z = \frac{2\tilde{\lambda}mc^2}{e}\sum_{n=-\infty}^{\infty}\frac{z-n\Delta z}{[\,z-n\Delta z\,]^2+[\,x-(-1)^n\Delta x\,]^2}$$

$$E_x = \frac{2\tilde{\lambda}mc^2}{e}\sum_{n=-\infty}^{\infty}\frac{x-(-1)^n\Delta x}{[\,z-n\Delta z\,]^2+[\,x-(-1)^n\Delta x\,]^2}$$

Compact expression of the fields. Due to the presence of an infinite sum, the above expression are not very convenient. It is however possible to rewrite them in a more compact form, by an appropriate use of the residue theorem (see appendix D):

$$E_z = -\pi\tilde{\lambda}\frac{mc^2}{e\Delta z}\left[\frac{\sin\left(\frac{\pi}{\Delta z}z\right)}{\left[\cosh\left(\frac{\pi}{\Delta z}(\Delta x + x)\right) + \cos\left(\frac{\pi}{\Delta z}z\right)\right]} - \frac{\sin\left(\frac{\pi}{\Delta z}z\right)}{\left[\cosh\left(\frac{\pi}{\Delta z}(\Delta x - x)\right) - \cos\left(\frac{\pi}{\Delta z}z\right)\right]}\right] \tag{5.30}$$

$$E_x = \pi\tilde{\lambda}\frac{mc^2}{e\Delta z}\left[\frac{\sinh\left(\frac{\pi}{\Delta z}(\Delta x + x)\right)}{\left[\cosh\left(\frac{\pi}{\Delta z}(\Delta x + x)\right) + \cos\left(\frac{\pi}{\Delta z}z\right)\right]} - \frac{\sinh\left(\frac{\pi}{\Delta z}(\Delta x - x)\right)}{\left[\cosh\left(\frac{\pi}{\Delta z}(\Delta x - x)\right) - \cos\left(\frac{\pi}{\Delta z}z\right)\right]}\right] \tag{5.31}$$

In addition, it is also possible to express the associated dimensionless potential $\phi = e\Phi/mc^2$ (which, by definition, satisfies the relations $E_z = -mc^2/e \times \partial_z\phi$, $E_x = -mc^2/e \times \partial_x\phi$).

$$\phi = -\tilde{\lambda}\log\left[4e^{-2\frac{\pi\Delta x}{\Delta z}}\left(\cosh\left(\frac{\pi(\Delta x + x)}{\Delta z}\right) + \cos\left(\frac{\pi z}{\Delta z}\right)\right)\left(\cosh\left(\frac{\pi(\Delta x - x)}{\Delta z}\right) - \cos\left(\frac{\pi z}{\Delta z}\right)\right)\right]$$

These compact expressions are particularly useful in some numerical FEL simulations, in which the expression of the external undulator fields is treated as an input. They are also convenient when graphically representing the fields, as it is done in fig. 5.13.

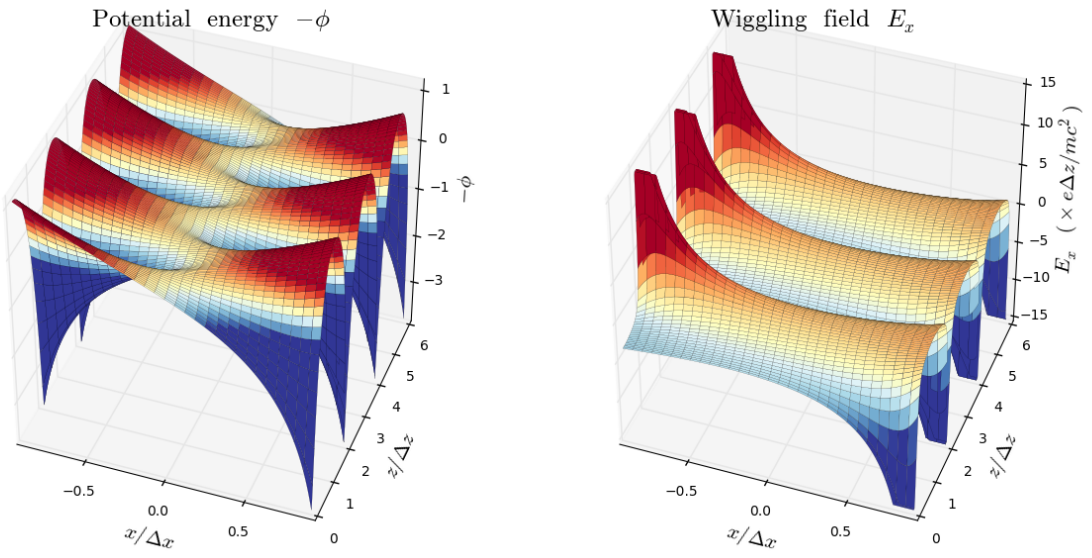

Figure 5.13: Representation of the periodic fields along the undulator for $\tilde{\lambda} = 1$ and $\Delta x = 0.5\Delta z$. Left panel: representation of $-\phi$, which is proportional to the potential energy of the electrons in the undulator. Right panel: representation of the transverse electric field.

Expression of the fields as a Fourier series. Since the fields are periodic along the z axis, they can also be expressed as a Fourier series. Inside the undulator ($|x| < \Delta x$), the corresponding

expressions are (see appendix D):

$$E_z = 2\pi\tilde{\lambda}\frac{mc^2}{e\Delta z}\sum_{k=1}^{\infty} e^{-\frac{k\pi\Delta x}{\Delta z}}\left[e^{\frac{k\pi x}{\Delta z}} + (-1)^k e^{-\frac{k\pi x}{\Delta z}}\right]\sin\left(\frac{k\pi z}{\Delta z}\right) \tag{5.32}$$

$$E_x = -2\pi\tilde{\lambda}\frac{mc^2}{e\Delta z}\sum_{k=1}^{\infty} e^{-\frac{k\pi\Delta x}{\Delta z}}\left[e^{\frac{k\pi x}{\Delta z}} - (-1)^k e^{-\frac{k\pi x}{\Delta z}}\right]\cos\left(\frac{k\pi z}{\Delta z}\right) \tag{5.33}$$

$$\phi = 2\tilde{\lambda}\sum_{k=1}^{\infty}\frac{e^{-\frac{k\pi\Delta x}{\Delta z}}}{k}\left[e^{\frac{k\pi x}{\Delta z}} + (-1)^k e^{-\frac{k\pi x}{\Delta z}}\right]\cos\left(\frac{k\pi z}{\Delta z}\right) \tag{5.34}$$

These expressions are convenient when integrating the equations of motion for the electrons. Importantly, it can be seen from these expressions that the average of $E_x(x,z)$ over one period in z is zero (for any fixed value of x). This implies that, if a relativistic electron propagated on a straight line (fixed x), the average transverse field would be neither focusing, nor defocusing. However, electrons do not propagate on straight lines here, but instead they wiggle about their average trajectory. As will be seen in the next section, this gives rise to a transverse ponderomotive force.

5.3.3 Motion of the electron in the absence of radiation

In the absence of radiation ($\boldsymbol{a} = \boldsymbol{0}$), the zeroth-order equation of motion for the electrons is:

$$\frac{1}{c}\frac{\partial \boldsymbol{u}_0}{\partial t} + \frac{1}{\gamma_0}(\boldsymbol{u}_0\cdot\boldsymbol{\nabla})\boldsymbol{u}_0 = \boldsymbol{\nabla}\phi$$

Since ϕ does not depend on t, this equation preserves the quantity $\gamma_0 - \phi$.

$$\gamma_0 = \bar{\gamma}_0 + \phi \quad = \bar{\gamma}_0 + 2\tilde{\lambda}\sum_{k=1}^{\infty}\frac{e^{-\frac{k\pi\Delta x}{\Delta z}}}{k}\left[e^{\frac{k\pi x}{\Delta z}} + (-1)^k e^{-\frac{k\pi x}{\Delta z}}\right]\cos\left(\frac{k\pi z}{\Delta z}\right) \tag{5.35}$$

where $\bar{\gamma}_0$ is the average value of γ_0, and is a constant here.

Wiggling motion. In order to study the transverse wiggling motion, we rewrite the equation of transverse motion as

$$\frac{1}{c}\frac{\partial u_{x,0}}{\partial t} + \frac{\partial u_{x,0}}{\partial z} - \frac{\partial\phi}{\partial x} = \left(1 - \frac{u_{z,0}}{\gamma_0}\right)\frac{\partial u_{x,0}}{\partial z} - \frac{u_{x,0}}{\gamma_0}\frac{\partial u_{x,0}}{\partial x} \tag{5.36}$$

where part of the term $(\boldsymbol{u}_0\cdot\boldsymbol{\nabla})u_{x,0}$ has been brought to the right-hand side. These right-hand side terms can in fact be neglected as a first approximation. This is because, for relativistic electrons propagating along the z axis, $u_{z,0}/\gamma_0 = \beta_{z,0} \approx 1$ and $u_{x,0}/\gamma_0 = \beta_{x,0} \ll 1$. In addition, since ϕ does not depend on t, it is natural to assume that $\boldsymbol{u}_0$ does not depend on t either. Upon neglecting the right-hand side terms and suppressing the time derivative, eq. (5.36) becomes

$$\frac{\partial u_{x,0}}{\partial z} - \frac{\partial\phi}{\partial x} = 0 \tag{5.37}$$

Using the Fourier expression of ϕ (eq. (5.34)), this leads to:

$$u_{x,0} = \bar{u}_{x,0} + 2\tilde{\lambda}\sum_{k=1}^{\infty}\frac{e^{-\frac{k\pi\Delta x}{\Delta z}}}{k}\left[e^{\frac{k\pi x}{\Delta z}} - (-1)^k e^{-\frac{k\pi x}{\Delta z}}\right]\sin\left(\frac{k\pi z}{\Delta z}\right) \tag{5.38}$$

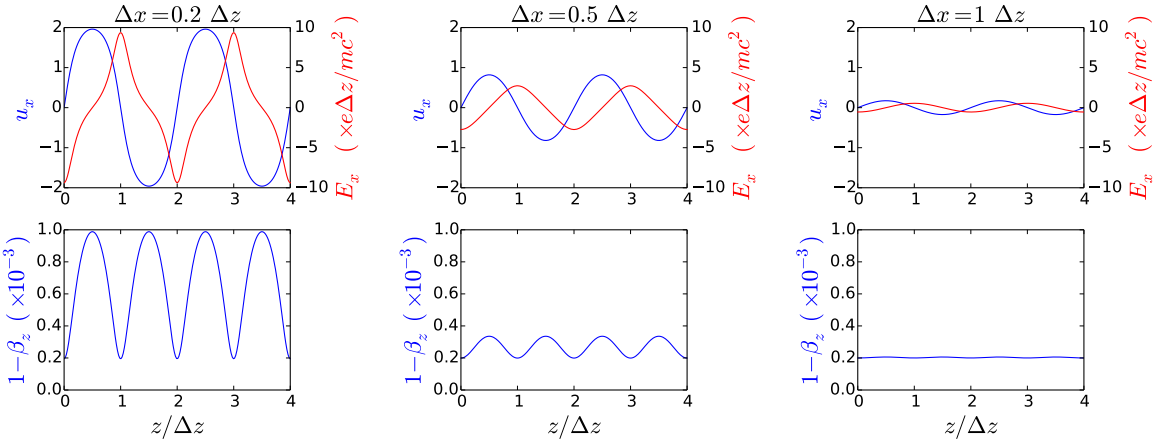

Figure 5.14: Plots of $u_{x,0}$, E_x and $1-\beta_{z,0}$ for different values of Δx. These quantities are plotted on-axis ($x = 0$), for $\bar{u}_{x,0} = 0$, and with fixed values for $\tilde{\lambda}$ and $\bar{\gamma}_0$ ($\tilde{\lambda} = 1$, $\bar{\gamma}_0 = 50$).

where $\bar{u}_{x,0}$ is the average of u_x over one period. Using eqs. (5.35) and (5.38), it is possible to obtain $\beta_{z,0}$ from the relation

$$\beta_{z,0} = 1 - \frac{(1 + u_{x,0}^2)}{2\gamma_0^2} \tag{5.39}$$

The quantities $u_{x,0}$ and $\beta_{z,0}$ are plotted on-axis ($x = 0$) in fig. 5.14 for different values of the ratio $\Delta x/\Delta z$ and for the same value of $\tilde{\lambda}$. As can be seen from these plots, the motion is nearly sinusoidal and has a relatively low amplitude for $\Delta x/\Delta z \gtrsim 0.5$. On the contrary, it is anharmonic and has a larger amplitude for $\Delta x/\Delta z \lesssim 0.5$. This behavior is also clearly apparent in the Fourier components of $u_{x,0}$ and γ_0 (eqs. (5.35) and (5.38)), through their exponentional dependence on $\Delta x/\Delta z$.

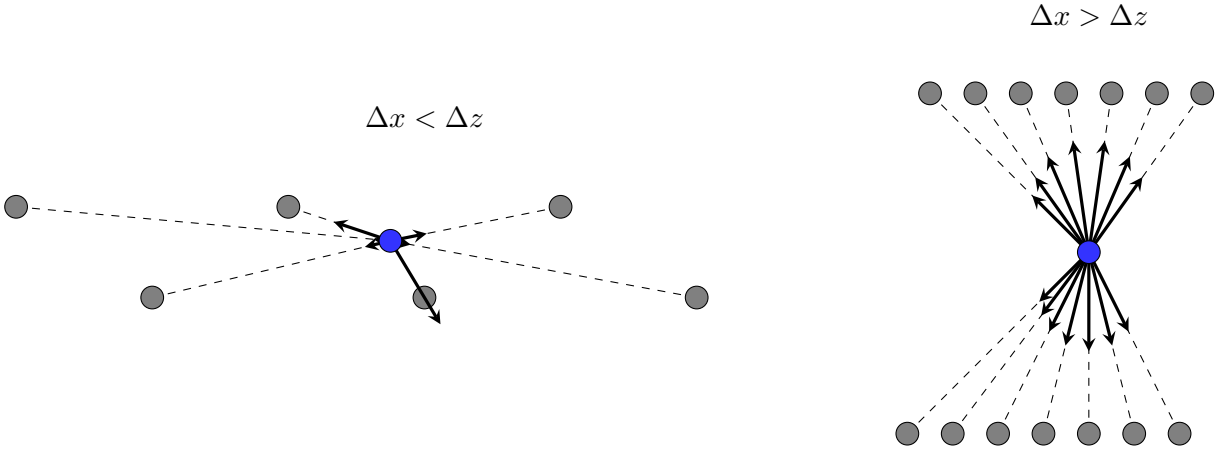

Figure 5.15: Schematic representation of the forces experienced by an electron in the undulator, for the cases $\Delta x < \Delta z$ and $\Delta x > \Delta z$. The blue dot represents the electron and the black arrows represent the forces exerted by the individual wires. In the case $\Delta x > \Delta z$, these force compensate each other for the most part.

The observed fact that the amplitude of E_x and $u_{x,0}$ rapidly decrease when the ratio $\Delta x/\Delta z$

increases can be understood qualitatively. As shown in fig. 5.15, in the case $\Delta x < \Delta z$, the wires are relatively far apart, and a given electron essentially feels the force of each individual wires *successively in time*. On the contrary, for $\Delta x > \Delta z$, a given electron is at a similar distance from many distinct wires. Thus at any time, it *simultaneously* feels the force of the two rows of wires. These forces cancel each other for the most part, and hence the total wiggling force is very low.

Transverse ponderomotive force. In eq. (5.37), we neglected the right-hand side terms of eq. (5.36), and as a result $\bar{u}_{x,0}$ was considered a constant in the final solution (eq. (5.38)). However, although it is typically small, the right-hand side of eq. (5.36) can have long-term effects, and it can in particular induce slow variations of $\bar{u}_{x,0}$. Assuming again $|u_{x,0}| \ll \gamma_0$, the average of eq. (5.36) over one period reads[8]:

$$\frac{1}{c}\frac{\partial \bar{u}_{x,0}}{\partial t} + \frac{\partial \bar{u}_{x,0}}{\partial z} + \frac{\bar{u}_{x,0}}{\bar{\gamma}_0}\frac{\partial \bar{u}_{x,0}}{\partial x} \approx -\frac{1}{2\bar{\gamma}_0}\frac{\partial}{\partial x}\langle (u_{x,0} - \bar{u}_{x,0})^2 \rangle \tag{5.40}$$

where the brackets denote an average over one period. The right-hand size can now be interpreted as a transverse ponderomotive force $F_x = -mc^2/2\bar{\gamma}_0 \times \partial_x \langle (u_{x,0} - \bar{u}_{x,0})^2 \rangle$. From eq. (5.38), one can obtain

$$\langle (u_{x,0} - \bar{u}_{x,0})^2 \rangle = +2\tilde{\lambda}^2 \sum_{k=1}^{\infty} \frac{1}{k^2} \left(e^{\frac{-k\pi(\Delta x - x)}{\Delta z}} - (-1)^k e^{-\frac{k\pi(\Delta x + x)}{\Delta z}} \right)^2$$

and thus the expression of the ponderomotive force is

$$\begin{aligned} F_x &= -\frac{mc^2}{2\bar{\gamma}_0}\frac{\partial}{\partial x}\langle (u_{x,0} - \bar{u}_{x,0})^2 \rangle \\ &= -\frac{2\pi\tilde{\lambda}^2}{\bar{\gamma}_0}\frac{mc^2}{\Delta z}\sum_{k=1}^{\infty}\frac{1}{k}\left[e^{\frac{-2k\pi(\Delta x - x)}{\Delta z}} - e^{\frac{-2k\pi(\Delta x + x)}{\Delta z}} \right] \\ &= -\frac{2\pi\tilde{\lambda}^2}{\bar{\gamma}_0}\frac{mc^2}{\Delta z}\log\left(\frac{e^{\frac{2\pi}{\Delta z}\Delta x} - e^{-\frac{2\pi}{\Delta z}x}}{e^{\frac{2\pi}{\Delta z}\Delta x} - e^{\frac{2\pi}{\Delta z}x}} \right) \end{aligned}$$

where the power series of the logarithm was used in order to obtain the final expression. This expression is negative when $x > 0$ and positive when $x < 0$, and hence this ponderomotive force is focusing. This is not surprising since ponderomotive effects typically push particles away from areas of high wiggling field, and since, in the case of the nanowires, the wiggling field is higher off-axis than on-axis, as shown in fig. 5.13. For the purpose of the FEL process, this focusing force is rather beneficial, as it focuses the diverging electron beam. It should however be remarked that this force operates only in the x-z plane and that the electrons will still diverge in the y-z plane.

Close to the axis, the ponderomotive force F_x can be linearized.

$$F_x = -\frac{8\pi^2\tilde{\lambda}^2}{\bar{\gamma}_0}\frac{mc^2}{\Delta z^2}\frac{x}{\left(1 + e^{\frac{2\pi\Delta x}{\Delta z}}\right)} \tag{5.41}$$

Under the influence of this force, the electrons will perform sinusoidal betatron oscillations. The corresponding betatron wavelength is

$$\lambda_\beta = \frac{\bar{\gamma}_0 \Delta z}{\tilde{\lambda}\sqrt{2}}\sqrt{1 + e^{\frac{2\pi\Delta x}{\Delta z}}} \tag{5.42}$$

[8] In obtaining this average equation, we neglected the term proportional to $(1 - u_{z,0}/\gamma_0)$ and made the approximations $\gamma_0 \approx \bar{\gamma}_0$. Relaxing these approximations leads to additional terms of the order $u_{x,0}^2/\bar{\gamma}_0^2 \times \partial_z u_{x,0}$ and $u_{x,0}^3/\bar{\gamma}_0^3 \times \partial_x u_{x,0}$, which are indeed negligible compared to the terms of order $u_{x,0}/\bar{\gamma}_0 \times \partial_x u_{x,0}$.

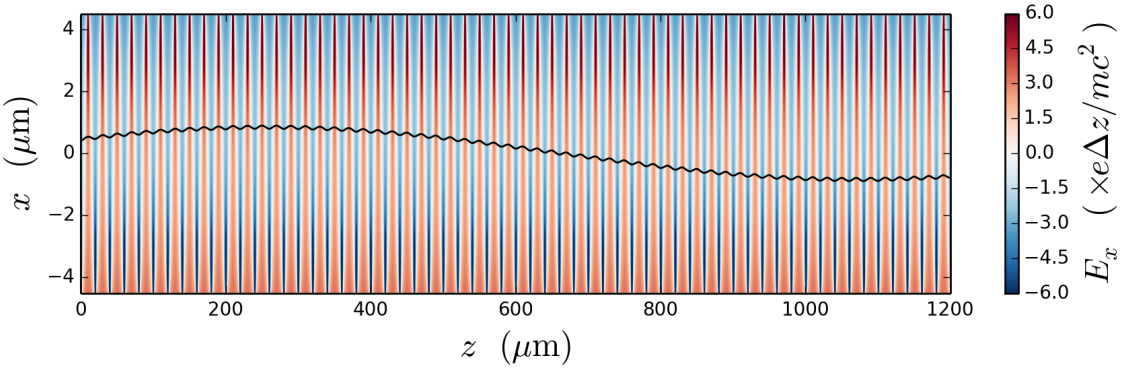

Figure 5.16: Trajectory of a single electron (black lines), obtained by numerical integration of the equations of motion, in the fields given by eqs. (5.30) and (5.31). The colormap corresponds to the wiggling field E_x. The parameters used here are $\bar{\gamma}_0 = 50$, $\Delta z = 10$ μm, $\Delta x = 5$ μm, $\tilde{\lambda} = 1$.

These predictions can be confirmed by numerically integrating the equations of motion for a single electron, in the electric field given by the compact expressions eqs. (5.30) and (5.31). The numerically-integrated trajectory is plotted in fig. 5.16, in the case $\bar{\gamma}_0 = 50$, $\Delta z = 10$ μm, $\Delta x = 5$ μm, $\tilde{\lambda} = 1$. The short-term wiggling motion and the long-term betatron oscillations can be clearly seen. The results of the numerical integration are in good agreement with the predictions of this section, since the betatron wavelength of the trajectory in fig. 5.16 is $\lambda_\beta = 1.6\,\text{mm}$, while eq. (5.42) predicts $\lambda_\beta = 1.7\,\text{mm}$.

5.3.4 FEL amplification

In the presence of co-propagating radiation, the zeroth-order motion is perturbed and, in a similar way as that decribed in section 5.1.2, this pertubation can lead to micro-bunching and amplification. In fact, when $\Delta x \gtrsim 0.5\Delta z$ and $|x| \ll \Delta x$, the motion is nearly sinusoidal and the situation is indeed identical to that of a planar magnetic undulator. The only difference lies in the fact that γ_0 remains constant in the case of a magnetic undulator whereas it oscillates about its mean value $\bar{\gamma}_0$ in the case of the nanowire undulator. However, these oscillations are of the order of $\tilde{\lambda}$, which is typically small compared to $\bar{\gamma}_0$, and they will be neglected here[9].

Thus a complete analogy can be drawn with a planar magnetic undulator, when $\Delta x \gtrsim 0.5\Delta z$ and $|x| \ll \Delta x$. As mentioned above, the motion is sinusoidal with these parameters, and the higher harmonics can be neglected in the expression of $u_{x,0}$ (eq. (5.38)):

$$u_{x,0} = 4\tilde{\lambda} e^{-\frac{\pi\Delta x}{\Delta z}} \sin\left(\frac{\pi z}{\Delta z}\right)$$

The parameters of the equivalent magnetic undulator are

$$a_{u,0} = 4\tilde{\lambda} e^{-\frac{\pi\Delta x}{\Delta z}} \qquad k_u = \frac{\pi}{\Delta z}$$

[9]Indeed the variations that the oscillations of γ_0 induce on $1 - \beta_{z,0}$ (which is an important quantity here since it determines the Doppler shift) are typically of the order of $\tilde{\lambda}/\bar{\gamma}_0^3$ (according to eq. (5.39)). By contrast, the variations induced by the oscillations of $u_{x,0}$ are of the order of $\tilde{\lambda}^2/\bar{\gamma}_0^2$. Thus, for $\tilde{\lambda} \gg 1/\bar{\gamma}_0$ (which is commonly satisfied), the oscillations of γ_0 have a negligible impact.

Using this analogy, the predicted radiation wavelength and the predicted gain length are:

$$\lambda_r = \frac{\lambda_u(1+a_{u,0}^2/2)}{2\bar{\gamma}_0^2} = \frac{\Delta z}{\bar{\gamma}_0^2}(1+8\tilde{\lambda}^2 e^{-\frac{2\pi\Delta x}{\Delta z}}) \qquad L_{g,0} = \frac{1}{2\sqrt{3}\rho k_u} = \frac{\Delta z}{2\pi\sqrt{3}\rho} \tag{5.43}$$

where

$$\rho = \frac{1}{\bar{\gamma}_0}\left(\frac{k_p^2\Delta z^2\tilde{\lambda}^2[JJ]^2}{2\pi^2}\right)^{1/3} e^{-\frac{2\pi\Delta x}{3\Delta z}} \qquad [JJ] = J_0\left(\frac{4\tilde{\lambda}^2}{e^{\frac{2\pi\Delta x}{\Delta z}}+8\tilde{\lambda}^2}\right) - J_1\left(\frac{4\tilde{\lambda}^2}{e^{\frac{2\pi\Delta x}{\Delta z}}+8\tilde{\lambda}^2}\right)$$

The crucial result here is that the Pierce parameter – and thus the gain length – have an exponential dependence on the geometrical ratio $\Delta x/\Delta z$. This implies that Δx should be chosen very small in order to have robust and fast FEL amplification. On the other hand, the sinusoidal approximation is not justified for very small Δx and the FEL process may then behave differently.

In order to confirm these predictions, I compared them with numerical FEL simulations. The FEL code Genesis cannot be used here, since it intrinsically assumes that the wiggling field is purely magnetic and sinusoidal. On the contrary, the code PlaRes by Andriyash et al. [2014b] integrates the equations of motion in user-specified wiggling fields. Thus PlaRes was used here, with the compact expressions of the wiggling fields eqs. (5.30) and (5.31). I simulated a cylindrical flat-top electron bunch of density $n_e = 3\times10^{19}$ cm^{-3} (a typical order of magnitude for LWFA bunches) and energy $\bar{\gamma}_0 = 50$, propagating through a nanowire undulator with $\tilde{\lambda} = 1$ and $\Delta z = 10\,\mu$m. The transverse spacing of the undulator Δx is varied and the radius of the electron bunch is modified accordingly ($R = 0.1\Delta x$), so as to always satisfy the condition of validity for the sinusoidal approximation $|x| \ll \Delta x$. The simulated electron beam is *ideal* in the sense that its initial energy spread and emittance are zero.

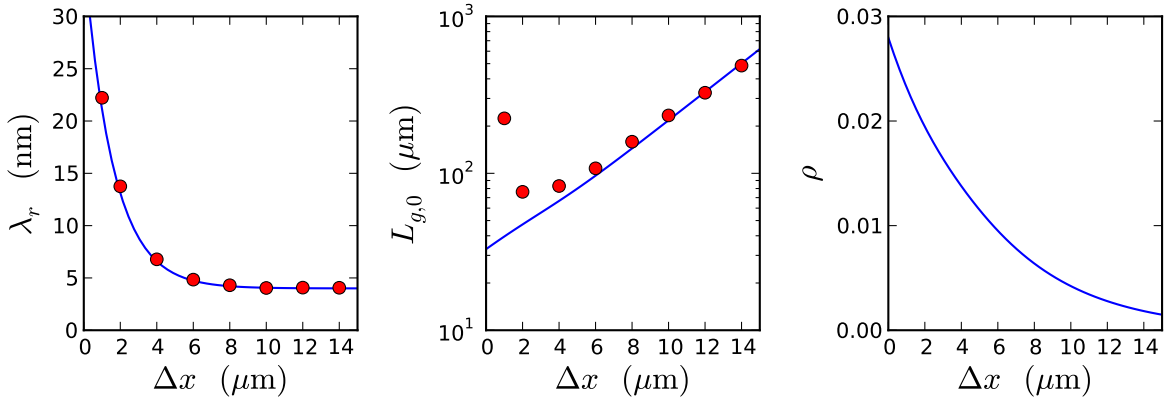

Figure 5.17: Comparison of the predictions of eq. (5.43) (blue curves) with the results of 2D PlaRes simulations (red dots). The left panel shows the central radiation wavelength λ_r while the middle panel shows the gain length $L_{g,0}$. The predicted Pierce parameter is indicated in the right panel, as an additional information.

The results of these simulations are shown in fig. 5.17. The agreement is very good for $\Delta x > 5\,\mu$m, and confirms that the gain length increases exponentially with the ratio $\Delta x/\Delta z$. The simulation results depart from the theoretical predictions for $\Delta x < 5\,\mu$m. This could be because the sinusoidal approximation of eq. (5.38) is not valid anymore for these values of Δx.

Another possibility is that this discrepancy is due to degradation by diffraction, which can be strong for small Δx (since the size of the electron beam is proportional to Δx here).

The case $\Delta x = 4\,\mu$m has the advantage of having a relatively short gain length, while satisfying $\Delta x \gg \sigma_x$ with typical values of σ_x for LWFA beams. Therefore, the PLARES simulation is re-run with a *realistic* bunch (i.e. with finite energy spread and emittance, and a larger transverse size). The parameters of the bunch are again those obtained in simulations of optical transverse injection ($\bar{\gamma}_0 = 54$, $\sigma_x = 1\,\mu$m, $\sigma_z = 1\,\mu$m, $Q = 50\,$pC, $\sigma_\gamma/\gamma = 1.7$ %, $\epsilon_\perp = 0.17$ mm.mrad). The results are shown in fig. 5.18 and compared with that of an ideal bunch (same parameters, except for $\sigma_\gamma = 0$, $\epsilon_\perp = 0$). Although the FEL amplification is degraded in the case of the realistic beam, there is still a very clear exponential increase of the radiated energy. Thus, FEL amplification does take place and, as was suggested by the colormaps of section 5.2.3, a nanowire undulator is in principle well-adapted for the bunches obtained by transverse optical injection.

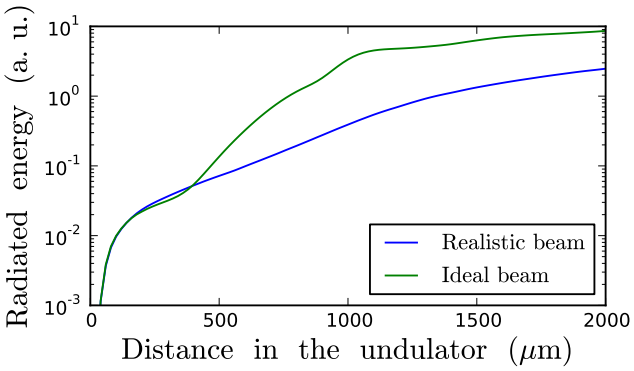

Figure 5.18: Energy radiated by an electron bunch as a function of the distance in the nanowire undulator. The blue curve corresponds to a realistic bunch ($\sigma_\gamma/\gamma = 1.7$ %, $\epsilon_\perp = 0.17$ mm.mrad), while the green curve corresponds to an ideal bunch ($\sigma_\gamma/\gamma = 0$ %, $\epsilon_\perp = 0$ mm.mrad). The other parameters of the bunch are $\bar{\gamma}_0 = 54$, $\sigma_x = 1\,\mu$m, $\sigma_z = 1\,\mu$m, $Q = 50\,$pC.

5.3.5 Discussion for a realistic undulator

Although the results from our simplified model are encouraging, there are a number of important effects that have not been taken into account. Unfortunately, these effects can seriously affect the FEL process, and we discuss them in this section.

Finite size of the wires In our simplified model, the wires were considered to be infinitely long and uniformly charged. Yet in reality, their length is of course finite, and moreover the laser pulse only creates charge separation over a certain fraction of this length (due to its finite waist). The effect of the finite size of the charge-separation zone can be estimated by considering uniformly-charged wires having a finite length L. Then the expression of the electric field created

by one individual wire (in its bisecting plane) is

$$\boldsymbol{E} = 2\frac{mc^2 r_e}{e^2}\frac{\lambda}{r}\frac{L}{\sqrt{4r^2+L^2}}\boldsymbol{e}_r \tag{5.44}$$

$$= 2\frac{mc^2}{e}\frac{\tilde{\lambda}}{(x-x_0)^2+(z-z_0)^2}\frac{L}{\sqrt{4(x-x_0)^2+4(z-z_0)^2+L^2}}[\,(x-x_0)\boldsymbol{e}_x+(z-z_0)\boldsymbol{e}_z\,] \tag{5.45}$$

where again r is the distance from the axis of the wire, where (x_0, y_0) is its position in cartesian coordinates, and where λ is its linear charge density. As can be expected, this expression reduces to the expression for an infinite wire (eq. (5.29)) for $r \ll L$. On the other hand, for $r \gg L$ the field decreases faster than that of an infinite wire ($|\boldsymbol{E}| \propto r^{-2}$ instead of r^{-1}). This can have important implications for the total field of the undulator.

As mentioned in section 5.3.2, the total field of the undulator is the sum of the fields of the individual wires. Yet, when the field of an individual wire is given by eq. (5.45), it is not possible to use the same techniques as in section 5.3.2 and to rewrite the total field in a compact form or as a Fourier series. It is nonetheless possible to calculate at the least the average of the total wiggling field over one undulator period:

$$\langle E_x \rangle = \frac{2mc^2}{e\Delta z}\tilde{\lambda}\left[\arctan\left(\frac{2(\Delta x - x)}{L}\right) - \arctan\left(\frac{2(\Delta x + x)}{L}\right)\right]$$

In agreement with the results of section 5.3.2, this expression goes to zero in the case of infinite wires ($L = \infty$). However, in the case of finite-sized wires, $\langle E_x \rangle$ is non-zero, and an analysis of its sign reveals that it is defocusing for electrons. Therefore this effect competes with the focusing ponderomotive force. Close to the axis, the expression of the average defocusing force is

$$F_x = \frac{8mc^2\tilde{\lambda}}{L\Delta z}\frac{x}{(1+4\Delta x^2/L^2)}$$

For realistic values of the parameters ($\tilde{\lambda} \sim 1$, $\bar{\gamma}_0 \sim 50$, $L \sim 10\,\mu$m, $\Delta x \sim 5\,\mu$m, $\Delta z \sim 10\,\mu$m), this force largely dominates over the ponderomotive force (eq. (5.41)), and the electron bunch will defocus as it travels through the undulator. However, it should be noticed that this defocusing effect only operates along the x direction. On the contrary, the average electric field along the y direction is expected to be focusing and to bring the electrons in the bisecting plane of the wires. This can partially compensate the impact that the defocusing fields in x have on the bunch density.

Diffuse electron density As the laser removes a fraction of the electrons from the wires, it scatters them around and thus generates a diffuse distribution of negative charges inside the undulator. Although this distribution was not taken into account in our simplified model, it can partially screen the positive charge of the wires. This typically causes the electric field of individual wires to decrease faster with r than they would in the absence of electrons. In this sense, the impact of a diffuse electron density is similar to that of the finite length of the wires. It is thus expected that this distribution of electron will also lead to an average defocusing force in the x-z. Building an accurate model of the electron density and of the corresponding defocusing force can be quite complicated. Yet estimations by PIC simulations suggest that it can have a substantial effect. These simulations showed that the bunch can indeed defocus over a length as short as ~ 200 μm [Andriyash et al., 2014a]. Yet the exact dependency of this length with respect to the laser and undulator parameters remains to be established.

Finite length of the undulator In the simplified model, the undulator was considered to be infinite in the longitudinal direction. In reality, the wires that are ahead of the laser pulse, at a given time, are not charged yet. Since the electron bunch travels not far behind the laser pulse, there will be a larger number of positively-charged wires *behind* the electron bunch than *ahead* of it. In this case, the average longitudinal electric field over one undulator period is expected to be non-zero and to pull the electrons back. Although it is unlikely to actually stop the electron bunch, it can still progressively reduce its energy. The exact amplitude of this effect depends on the range of the electric field produced by individual wires, and thus on their length and on the surrounding electron distribution. PIC simulations tend to show that the relative decrease of the mean bunch energy is at the percent level, but again a study of its dependence with respect to the parameters of the undulator has to be carried out.

Evolution of the laser pulse As the laser pulse propagates through the undulator, it progressively loses energy. This occurs because it gives energy to the electrons as it pulls them from the wires, but also because a fraction of the laser energy diffracts on the wires and is lost transversely. PIC simulations suggest that these effects cause the laser field to decrease exponentially, as a function of the propagation distance. In these simulations, the characteristic length of this phenomenon is $\sim$400 μm.

As a consequence of its decreasing field, the laser pulse removes less and less electrons from each wire as it propagates through the undulator. Therefore the successive wires are not identical, as it was assumed in the simplified model, but instead their individual charge decreases across the undulator. This situation is analog to that of a tapered undulator [Huang and Kim, 2007]. In principle, tapered undulators can, if their taper is well-chosen, increase the total energy radiated by the bunch in the undulator. However, it is unclear to which extent the taper can be controlled in our case, and it could just as well lead to detrimental detuning effects if its value is not well-adapted.

Conclusion and future work The results of the simplified model suggest that FEL amplification could in principle take place, even with realistic bunch parameters. However, this section shows that a number of effects can seriously degrade the FEL process in practice. These effects should be studied systematically, in the hope that a regime of parameters can be found in which they are not limiting. Alternatively, variations of the original undulator concept could be considered, so as to make it less sensitive to the above mentioned effects. For instance, it theoretically possible to use a secondary electron bunch in order to remove the electrons from the wires, instead of a laser pulse. Although a laser pulse tends to scatter the electrons around the wires, an electron bunch tends to repell them radially. Thus such an electron bunch would generate less diffuse electron density inside the undulator, and would thus reduce the defocusing forces.

Conclusion

Summary of the results

This section summarizes the main results of this thesis.

Firstly, I showed in chapter 2 that standard PIC simulations of laser-wakefield acceleration can sometimes overestimate the emittance of the accelerated bunch. This occurs mostly for very intense bunches, and I showed that this overestimation is, to a large extent, due to the numerical Cherenkov effect. Because of this artifact, the electrons emit a spurious radiation, which then interacts with the bunch itself and artificially increases its emittance. I then proposed a modified numerical scheme, which suppresses the Cherenkov radiation and results in a lower final emittance. Importantly, this scheme is applicable to both three-dimensional Cartesian grids and quasi-cylindrical grids.

Using this algorithm, I showed in chapter 3 that a new regime of colliding-pulse injection can lead to low-emittance bunches. In this new regime – which arises for low densities and tightly-focused laser pulses – the pulse collision causes the accelerating cavity to shrink and reexpand. The rapid expansion of the cavity then triggers a sharp transverse injection. This *optical transverse injection* contrasts with previously-known mechanisms of colliding-pulse injection, which were longitudinal and conceptually relied on a stationary wakefield. Importantly, optical transverse injection can lead to low-energy bunches ($\sim$ 25 MeV) with a high charge ($\sim$ 50 pC) and a low energy spread ($\sim$ 2 %), in addition to their low emittance ($\sim$ 0.2 mm.mrad).

In chapter 4, we propose an interesting setup (the *laser-plasma lens*) which substantially reduces the divergence of the electrons after they exit the accelerator. In this setup, a second, well-chosen gas jet is placed after the accelerator. When the driving laser pulse (or a second, dedicated laser pulse) propagates through this jet, it generates a wakefield which can collimate the trailing electrons. While the single-pulse version of this scheme is well-adapted to low-energy electrons ($\sim$ 100 MeV), the two-pulse version may be better suited to high-energy electrons ($\sim$ 400 MeV). Through PIC simulations (for which an additional artifact was corrected in appendix C), it is shown that both versions of this scheme can realistically reduce the final divergence by a factor 3.

Finally, in chapter 5, I consider the combination of a laser-wakefield accelerator with several types of undulators. In particular, it is shown that low-energy electron bunches could be advantageously combined with short-period laser-plasma undulators, and may result in ultra-compact FELs. In this context, an innovative *nanowires undulator* is proposed. Through a simplified

model, I show that, when combined with typical bunches from optical transverse injection, this nanowires undulator could lead to FEL amplification, with a gain length of the order of 100 μm.

Future prospects

These results open up several prospects, both regarding the numerical modeling of relativistic plasmas and regarding the short-term and long-term prospects of laser-wakefield acceleration.

Towards a better numerical description of laser-plasma experiments. Although PIC codes can accurately describe many aspects of laser-plasma interactions, I showed here that it is in some cases still challenging to correctly describe the transverse dynamics of relativistic beams. For this reason, several methods were introduced in order to improve this description, in particular by avoiding the numerical Cherenkov effect (chapter 2) as well as by correcting an inaccurate compensation of the $\boldsymbol{E}$ and $\boldsymbol{B}$ fields (appendix C). These methods were used in the case of optical transverse injection and of the laser-plasma lens, but in principle they have a broader field of application, and they may in fact be used in many situations in which the transverse dynamics of the bunch is important. Recently, we used for instance the Cherenkov-free algorithm in order to study the evolution of the angular momentum of the accelerated bunch [Thaury et al., 2013]. This algorithm has also been used lately by Xavier Davoine (CEA DAM) and Serge Kalmykov (University of Nebraska Lincoln) in simulations of Compton scattering with a laser-accelerated bunch. In this case, preliminary results showed that the spectrum of the Compton radiation is much narrower when the spurious growth of the bunch emittance is suppressed.

In addition, the results concerning the numerically-inaccurate compensation of $\boldsymbol{E}$ and $\boldsymbol{B}$ at the back of the laser pulse (appendix C) may have implications for simulations of laser-enhanced betatron motion. Some simulations indeed suggest that the betatron oscillations of the accelerated electrons can be amplified by their interaction with the back of the laser pulse [Németh et al., 2008; Cipiccia et al., 2011]. However, as shown in appendix C, this interaction can sometimes be numerically overestimated, and it would thus be interesting to run these simulations with higher-order time interpolation of the $\boldsymbol{B}$ field.

Finally, the above methods could also be used to simulate the influence of space charge forces on the bunch itself (including e.g. the growth of emittance due to space charge). It is indeed difficult for PIC codes to accurately reproduce this space-charge force, since this situation is prone to both the numerical Cherenkov effect (the particles propagate close to c) and to the numerically-inaccurate compensation of $\boldsymbol{E}$ and $\boldsymbol{B}$. (physically, the bunch-generated $\boldsymbol{E}$ and $\boldsymbol{B}$ fields should compensate with a precision of $1/\gamma^2$). It is thus important to study precisely to which extent PIC codes can correctly capture this space-charge force.

Mitigation of numerical instabilities in flowing-plasma simulations. The numerical Cherenkov effect can also have a dramatic impact in flowing-plasma simulations (i.e. simulations in which the whole plasma travels at a relativistic speed). In this case, the numerical Cherenkov effect leads to a growing instability, which rapidly disrupts the simulation [Xu et al., 2013]. This instability appears for instance in simulations of relativistic astrophysical shocks [Spitkovsky, 2008; Keshet et al., 2009] and in boosted-frame simulations [Vay, 2007; Martins et al., 2010] (i.e. simulations that reduce the computational cost by considering a moving frame of reference). For three-dimensional PIC simulations, several methods have already been developed in order to mitigate this instability [Xu et al., 2013; Vay et al., 2011], but the Cherenkov-free algorithm

of chapter 2 could nevertheless complement these methods. In fact, preliminary research has been carried out along these lines, in collaboration with the group of Luís Silva at the Instituto Superior Técnico (Lisbon). These first investigations revealed that the Cherenkov-free algorithm can supress the primary Cherenkov instability, although it is still subject to a secondary, slowly-growing Cherenkov instability (known as the *aliased* Cherenkov instability).

More importantly, this Cherenkov-free algorithm could also be used in quasi-cylindrical PIC simulations of flowing plasmas. Contrary to *three-dimensional* PIC simulations, no methods have been developed so far in order to mitigate the Cherenkov instability in *quasi-cylindrical* simulations. Thus, if the Cherenkov-free algorithm is successful in suppressing the Cherenkov instability in this case, it would allow to carry out *quasi-cylindrical boosted-frame simulations* for the first time. These simulations would cumulate the reductions in computational load associated with both the boosted-frame technique and the quasi-cylindrical grid, and would thus be extremely fast.

Multi-stage linear colliders. In the longer term, the results of this thesis could contribute to the development of several potential applications of LWFA, and in particular to prospective compact colliders. In the most recent proposals for LWFA-based colliders (e.g. [Schroeder et al., 2010]), the electron beam is accelerated in a series of staged gas-filled capillaries. At the end of each stage, the depleted driving laser pulse is replaced by a fresh pulse, which continues accelerating the electron bunch in the next stage. Also, in this design, the laser-wakefield is typically in the linear or quasi-linear regime inside the gas-filled capillaries.

Although the development of multi-stage linear colliders was only briefly mentioned in this thesis, several of our results could be applied in this context. Firstly, optical transverse injection could be used as a low-energy, high-quality injector, just before the first stage. Moreover, the laser-plasma lens could refocus the electron bunch inbetween two consecutive stages. The bunch indeed tends to diverge in the drift space between two stages, and its emittance later degrades if it is not refocused before entering the next stage [Mehrling et al., 2012]. Finally, the nonlinear beamloading calculations of section 4.3 could be applied to the accelerated bunch, within the linear wakefield of each stage. Using these calculations, one could in particular evaluate the growth of emittance due to transverse beamloading, over the long acceleration distance of the collider. These evaluations could then help design the collider, by predicting the maximal charge and the optimal geometry of the bunch that would keep emittance at a low level.

Plasma-based X-ray sources. Our results can also contribute to the long-term development of incoherent X-ray sources (i.e. synchrotron-type sources) and coherent X-ray sources (i.e. free-electron lasers). Regarding incoherent sources, the laser-plasma lens could facilitate the coupling between a laser-wakefield accelerator and a magnetic undulator. As mentioned in chapter 4, the associated reduction in divergence would indeed reduce the width of the emitted spectrum, and increase the brightness of the radiation. In addition, the development of innovative plasma-based undulators (such as the nanowire undulator) could lead to drastically more compact synchrotron sources. In this context, it is for instance planned to experimentally observe the first incoherent radiation from a nanowire undulator within the next year at LOA.

These developments are also important in the case of coherent sources. In this context, the laser-plasma lens could be integrated into the FEL design of the Lunex5 project – which combines an LWFA with a magnetic undulator. Here the lens could help preserve the emittance and duration of the bunch, throughout the transport line from the exit of the accelerator to the entrance of the undulator. Finally, chapter 5 contributed to show that low-energy, high-quality

bunches (similar to those produced by optical transverse injection) could possibly lead to an FEL effect when combined with a compact undulator (such as the laser undulator or the nanowire undulator). This opens exciting prospects for ultra-compact FELs, in which both the accelerator and the undulator have a centimeter-scale length (although they would still require a ten-meter size laser system). However, there is still much work to be done in this direction. In particular, it would be necessary to build more realistic models of the nanowire undulator, so as to confirm that it can robustly lead to an FEL effect. It might also be advantageous to explore different geometries for the array of nano-wires, as well as to consider the possibly to activate them with an electron bunch instead of a laser pulse.

More generally, this thesis is part of a much larger effort towards higher-quality laser-accelerated beams, and towards innovative LWFA-based applications. Although an actual compact collider may still lie a few decades away from now, several other applications could become available on a shorter term. This includes for instance LWFA-based tomography, phase-contrast imaging, and electron diffraction in crystals. In addition, thanks to recent developments in the LUNEX5 collaboration (including super-matching, the design of a magnetic chicane and the design of a seeding beam), a soft X-ray LWFA-based FEL now seems achievable within the next few years. If successful, this experiment would pave the way for cheaper and more wide-spread FEL facilities, which would then open many new opportunities in atomic physics, biochemistry, and material science.

Appendix A

Ponderomotive formalism

This section gives a short version of the demonstration of the ponderomotive equations by Mora and Antonsen [1997]. We refer the reader to this article for a more rigorous derivation.

Equations of motion : Let us consider a given electron in the plasma. Its motion in the potentials $\boldsymbol{a}_{tot}$ and ϕ_{tot} is determined by the electromagnetic Lagrangian

$$\mathcal{L} = -\sqrt{1-\boldsymbol{\beta}_{tot}^2} - \boldsymbol{\beta}_{tot}\cdot\boldsymbol{a}_{tot} + \phi_{tot} \quad \text{where} \quad \boldsymbol{\beta}_{tot} \equiv \frac{1}{c}\frac{d\boldsymbol{x}_{tot}}{dt}.$$

This Lagrangian results in the following equations of motion

$$\frac{1}{c}\frac{d\boldsymbol{x}_{tot}}{dt} = \frac{\boldsymbol{u}_{tot}}{\gamma_{tot}} \qquad \frac{1}{c}\frac{d}{dt}(\boldsymbol{u}_{tot}-\boldsymbol{a}_{tot}) = \boldsymbol{\nabla}\phi_{tot} - (\boldsymbol{\nabla}\cdot\boldsymbol{a}_{tot})\cdot\frac{\boldsymbol{u}_{tot}}{\gamma_{tot}} \tag{A.1}$$

with $\gamma_{tot} = 1/\sqrt{1-\boldsymbol{\beta}_{tot}^2} = \sqrt{1+\boldsymbol{u}_{tot}^2}$. Equation (A.1) can also be re-written in the form of eqs. (1.4) and (1.5). Moreover, as explained in section 1.1, we make the quasi-static assumption i.e. we assume that $\boldsymbol{a}_{tot}$ and ϕ_{tot} are only functions of $\xi = ct-z$ and $\boldsymbol{x}_\perp$. Therefore the Lagrangian $\mathcal{L}$ is invariant under the transformation $(ct, z) \to (ct+\epsilon, z+\epsilon)$, and Noether's theorem states that there is a corresponding constant of motion $\mathcal{H}$:

$$\mathcal{H} = \frac{\partial\mathcal{L}}{\partial\boldsymbol{\beta}_{tot}}\cdot\boldsymbol{\beta}_{tot} - \mathcal{L} - \frac{\partial\mathcal{L}}{\partial\beta_{z,tot}} = \gamma_{tot} - u_{z,tot} - \psi_{tot}$$

where $\psi = \phi - a_z$. Now before the electron has been reached by the laser pulse, it is at rest and does not experience any field. Therefore $\mathcal{H} = 1$, which leads to the relation

$$\gamma_{tot} - u_{z,tot} = 1 + \psi_{tot} \tag{A.2}$$

As suggested in section 1.1, let us now decompose the quantities in eqs. (A.1) and (A.2) into their fast and slow components (e.g. $\boldsymbol{a}_{tot} = \boldsymbol{a}_f + \boldsymbol{a}_s$). The fast components oscillate in time at the laser frequency ω_0 (and multiples thereof) and hence vanish when averaging over one laser period (e.g. $\langle\boldsymbol{a}_f\rangle = 0$), while the slow components vary much more slowly and are essentially constant over a laser period (e.g. $\langle\boldsymbol{a}_s\rangle = \boldsymbol{a}_s$).

Fast component of $\boldsymbol{u}_\perp$: The fast, transverse component of eq. (A.1) reads

$$\frac{1}{c}\frac{d}{dt}(\boldsymbol{u}_{\perp,f} - \boldsymbol{a}_{\perp,f}) = \boldsymbol{\nabla}_\perp\phi_f - \left[(\boldsymbol{\nabla}_\perp\cdot\boldsymbol{a}_{tot})\cdot\frac{\boldsymbol{u}_{tot}}{\gamma_{tot}}\right]_f$$

This gives an order of magnitude for $\boldsymbol{u}_{\perp,f} - \boldsymbol{a}_{\perp,f}$: $|\boldsymbol{u}_{\perp,f} - \boldsymbol{a}_{\perp,f}| \sim \frac{|\boldsymbol{a}_{tot}|}{k_0\sigma_\perp}, \frac{\phi_f}{k_0\sigma_\perp}$ where k_0 is the wavevector of the laser and $\sigma_\perp$ is the transverse size of the laser. In typical situations, $k_0\sigma_\perp \gg 1$, and thus

$$\boldsymbol{u}_{\perp,f} \simeq \boldsymbol{a}_{\perp,f} \tag{A.3}$$

Slow components of γ and u_z : The fast component of the Lorenz gauge condition reads

$$\frac{\partial \psi_f}{\partial \xi} + \boldsymbol{\nabla}_\perp \cdot \boldsymbol{a}_{\perp,f} = 0$$

and therefore, in order of magnitude, $\psi_f \sim \frac{|\boldsymbol{a}_{\perp,f}|}{k_0\sigma_\perp}$. As a result, ψ_f can be essentially neglected, and eq. (A.2) becomes :

$$\gamma_{tot} - u_{z,tot} = \gamma_s - u_{z,s} = 1 + \psi_s \tag{A.4}$$

Injecting the above results $\gamma_{tot} = u_{z,tot} + \gamma_s - u_{z,s}$ and $\boldsymbol{u}_{\perp,f} = \boldsymbol{a}_{\perp,f}$ into the relation $\gamma_{tot}^2 = 1 + \boldsymbol{u}_{tot}^2$ yields :

$$\gamma_s^2 + u_{z,s}(u_{z,s} - 2u_{z,tot}) + 2\gamma_s(u_{z,tot} - u_{z,s}) = 1 + \boldsymbol{u}_{\perp,s}^2 + 2\boldsymbol{u}_{\perp,s} \cdot \boldsymbol{a}_{\perp,f} + \boldsymbol{a}_{\perp,f}^2$$

Averaging this equation over one laser period provides an expression for γ_s, and therefore also for $u_{z,s}$.

$$\gamma_s = \sqrt{1 + \boldsymbol{u}_s^2 + \langle \boldsymbol{a}_{\perp,f}^2 \rangle} \qquad u_{z,s} = \sqrt{1 + \boldsymbol{u}_s^2 + \langle \boldsymbol{a}_{\perp,f}^2 \rangle} - 1 - \psi_s \tag{A.5}$$

Slow component of the equation of motion : Another by-product of eq. (A.4) is a relation between the variables ξ and t : $\frac{d\xi}{dt} \equiv 1 - \beta_{z,tot} = \frac{1+\psi_s}{\gamma_{tot}}$. This allows to express the equations of motion eq. (A.1) as a function of ξ :

$$\begin{aligned} \frac{d\boldsymbol{x}_{tot}}{d\xi} = \frac{\boldsymbol{u}_{tot}}{1+\psi_s} \qquad \frac{d}{d\xi}(\boldsymbol{u}_{tot} - \boldsymbol{a}_{tot}) &= \frac{\gamma_{tot}\boldsymbol{\nabla}\phi_{tot}}{1+\psi_s} - \frac{(\boldsymbol{\nabla}\boldsymbol{a}_{tot}) \cdot \boldsymbol{u}_{tot}}{1+\psi_s} \\ &= \frac{\gamma_{tot}\boldsymbol{\nabla}\psi_{tot}}{1+\psi_s} + \frac{(\gamma_{tot} - u_{z,tot})\boldsymbol{\nabla}a_{z,tot}}{1+\psi_s} - \frac{(\boldsymbol{\nabla}\boldsymbol{a}_{\perp,tot}) \cdot \boldsymbol{u}_{\perp,tot}}{1+\psi_s} \\ &= \frac{\gamma_{tot}\boldsymbol{\nabla}\psi_s}{1+\psi_s} + \frac{(\gamma_s - u_{z,s})\boldsymbol{\nabla}a_{z,tot}}{1+\psi_s} - \frac{(\boldsymbol{\nabla}\boldsymbol{a}_{\perp,tot}) \cdot \boldsymbol{u}_{\perp,tot}}{1+\psi_s} \end{aligned} \tag{A.6}$$

This last expression isolates most of the fast components, and averaging over one laser period is more amenable. When doing so, the equations become :

$$\begin{aligned} \frac{d\boldsymbol{x}_s}{d\xi} &= \frac{\boldsymbol{u}_s}{1+\psi_s} \\ \frac{d}{d\xi}(\boldsymbol{u}_s - \boldsymbol{a}_s) &= \frac{\gamma_s\boldsymbol{\nabla}\psi_s}{1+\psi_s} + \frac{(\gamma_s - u_{z,s})\boldsymbol{\nabla}a_{z,s}}{1+\psi_s} - \frac{(\boldsymbol{\nabla}\boldsymbol{a}_{\perp,s}) \cdot \boldsymbol{u}_{\perp,s}}{1+\psi_s} - \frac{\langle(\boldsymbol{\nabla}\boldsymbol{a}_{\perp,f}) \cdot \boldsymbol{a}_{\perp,f}\rangle}{1+\psi_s} \\ &= \frac{\gamma_s\boldsymbol{\nabla}\phi_s}{1+\psi_s} - \frac{(\boldsymbol{\nabla}\boldsymbol{a}_s) \cdot \boldsymbol{u}_s}{1+\psi_s} - \frac{1}{2(1+\psi_s)}\boldsymbol{\nabla}\langle \boldsymbol{a}_{\perp,f}^2 \rangle \end{aligned}$$

Thus the equations of motion for the slow components are the same as the standard equations of motion eq. (A.6), except for the additional *ponderomotive* term $-\frac{1}{2(1+\psi_s)}\boldsymbol{\nabla}\langle \boldsymbol{a}_{\perp,f}^2 \rangle$.

Appendix B

The coefficients of the Cherenkov-free algorithms

In section 2.3, two modified PIC algorithm are proposed, whose properties strongly depend on a set of coefficients. This appendix explains how these coefficients were chosen.

B.1 Coefficients for the Cartesian algorithm

In the case of the proposed Cartesian algorithm, the numerical dispersion relation is

$$\begin{aligned}\frac{s_t^2}{c^2\Delta t^2} =& \frac{s_x^2}{\Delta x^2} + \frac{s_y^2}{\Delta y^2} + \frac{s_z^2}{\Delta z^2} - 4\left(\delta_x \frac{s_x^4}{\Delta x^2} + \delta_y \frac{s_y^4}{\Delta y^2} + \delta_z \frac{s_z^4}{\Delta z^2}\right) \\ &- 4\left(\frac{1}{\Delta x^2}\beta_{x,y} + \frac{1}{\Delta y^2}\beta_{y,x}\right) s_x^2 s_y^2 \\ &- 4\left(\frac{1}{\Delta y^2}\beta_{y,z} + \frac{1}{\Delta z^2}\beta_{z,y}\right) s_y^2 s_z^2 \\ &- 4\left(\frac{1}{\Delta z^2}\beta_{z,x} + \frac{1}{\Delta x^2}\beta_{x,z}\right) s_z^2 s_x^2 \end{aligned} \tag{B.1}$$

where $s_t = \sin(\omega\Delta t/2)$ and $s_u = \sin(k_u \Delta u/2)$ for $u = x, y, z$. As mentioned in section 2.3.1, the β and δ coefficients should be chosen so as to avoid numerical Cherenkov radiation for particles propagating along the z axis ($\boldsymbol{v} = v\boldsymbol{e}_z$). In other words, these coefficients should be chosen in such a way that no wavevector $\boldsymbol{k}$ can simultaneously satisfy the above numerical dispersion relation and the resonant condition $\omega = vk_z$.

The choice of δ_z. In order to ensure this property, let us first impose it for wavevectors of the form $\boldsymbol{k} = k_z\boldsymbol{e}_z$. Since v can be extremely close to c for an ultrarelativistic bunch, we impose $\omega(\boldsymbol{k} = k_z\boldsymbol{e}_z) \geq ck_z$, for all k_z in $[0, \pi/\Delta z]$. Using the above numerical dispersion relation, this becomes

$$\omega = \frac{2}{\Delta t}\arcsin\left(\frac{c\Delta t}{\Delta z} s_z \sqrt{1 - 4\delta_z s_z^2}\right) \geq ck_z \tag{B.2}$$

Decreasing δ_z increases the left-hand side (even for negative values of δ_z). This is represented in fig. B.1. As can be seen in this figure, once δ_z reaches the value $\delta_{z,0}$ for which eq. (B.2) is

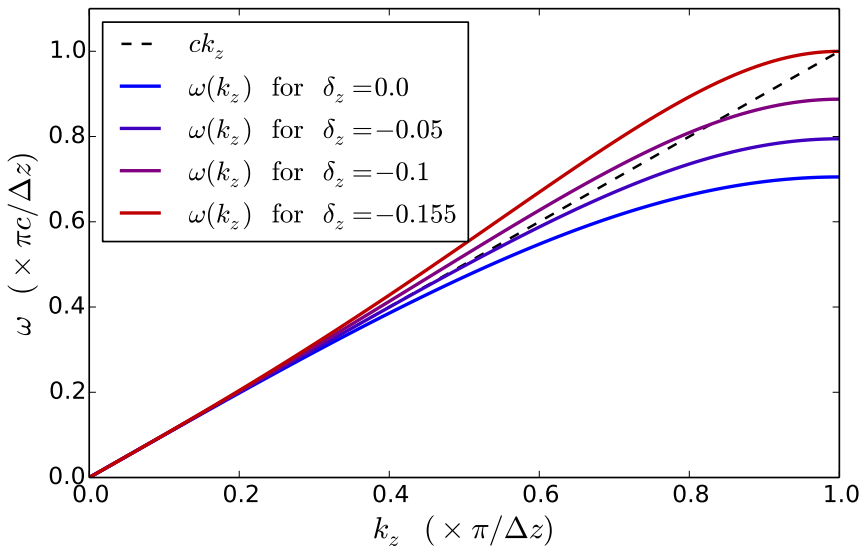

Figure B.1: Representation of the numerical dispersion relation for wavectors of the form $\boldsymbol{k} = k_z \boldsymbol{e}_z$, for different (negative) values of δ_z. The dashed line represents the quantity ck_z.

satisfied at $k_z = \pi/\Delta z$, then eq. (B.2) is satisfied for all k_z in $[0, \pi/\Delta z]$. With this definition, $\delta_{z,0}$ can be found from the relation

$$\frac{2}{\Delta t} \arcsin\left(\frac{c\Delta t}{\Delta z}\sqrt{1 - 4\delta_{z,0}}\right) = \frac{c\pi}{\Delta z}$$

which yields

$$\delta_{z,0} = -\frac{1}{4}\left[\frac{\Delta z^2}{c^2\Delta t^2}\sin^2\left(\frac{\pi c\Delta t}{2\Delta z}\right) - 1\right].$$

Thus, as long as $\delta_z \leq \delta_{z,0}$, the condition eq. (B.2) is satisfied. However, it must be noticed that $\omega(\boldsymbol{k} = \frac{\pi}{\Delta z}\boldsymbol{e}_z)$ becomes a complex number for $\delta_z < -\frac{1}{4}\left(\frac{\Delta z^2}{c^2\Delta t^2} - 1\right)$, which means that the numerical scheme becomes unstable. In order to avoid this, I chose to use

$$\delta_z = \delta_{z,0}$$

since $\delta_{z,0}$ always satisfies $\delta_{z,0} \geq -\frac{1}{4}\left(\frac{\Delta z^2}{c^2\Delta t^2} - 1\right)$.

The choice of the other β and δ coefficients. With the above choice of δ_z, ω is real for all wavevectors of the form $\boldsymbol{k} = k_z\boldsymbol{e}_z$. However it can still be complex for other wavevectors $\boldsymbol{k}$, and thus the stability of the scheme is not yet guaranteed. This is best seen by considering the numerical dispersion relation eq. (B.1) for $\boldsymbol{k} = \frac{\pi}{\Delta x}\boldsymbol{e}_x + \frac{\pi}{\Delta z}\boldsymbol{e}_z$. In this case, the numerical dispersion equation leads to

$$\sin^2\left(\frac{\omega\Delta t}{2}\right) = \sin^2\left(\frac{\pi c\Delta t}{2\Delta z}\right) + \frac{c^2\Delta t^2}{\Delta x^2}\left(1 - 4\delta_x - 4\beta_{x,z} - 4\frac{\Delta x^2}{\Delta z^2}\beta_{z,x}\right)$$

If $\beta_{x,z}$, $\beta_{z,x}$ and δ_x are chosen to be zero, then the right-hand side can easily be greater than 1 (for typical values of Δt, Δx and Δz), which again leads to a complex ω. In order to prevent

this, I chose

$$\beta_{x,z} = \frac{1}{8} \qquad \beta_{z,x} = \frac{\Delta z^2}{8\Delta x^2} \qquad \delta_x = 0 \tag{B.3}$$

which ensures that the right-hand side of eq. (B.3) always remains lower than 1. A similar reasoning for $\boldsymbol{k} = \frac{\pi}{\Delta y}\boldsymbol{e}_y + \frac{\pi}{\Delta z}\boldsymbol{e}_z$ leads to

$$\beta_{y,z} = \frac{1}{8} \qquad \beta_{z,y} = \frac{\Delta z^2}{8\Delta y^2} \qquad \delta_y = 0$$

Finally, for simplicity, $\beta_{x,y}$ and $\beta_{y,x}$ are chosen to be zero.

Resulting dispersion relation With this choice of coefficients, the numerical dispersion relation eq. (B.1) becomes

$$\frac{s_t^2}{c^2\Delta t^2} = \frac{s_z^2}{\Delta z^2}(1 - 4\delta_{z,0}s_z^2) + \frac{s_x^2}{\Delta x^2}(1 - s_z^2) + \frac{s_y^2}{\Delta y^2}(1 - s_z^2) \tag{B.4}$$

An analysis of this dispersion relation reveals that the corresponding scheme is numerically stable, provided that

$$\frac{1}{c^2\Delta t^2} \geq \max\left(\frac{1}{\Delta x^2} + \frac{1}{\Delta y^2} \ , \ \frac{1}{\Delta z^2} \right)$$

In addition, no wavevector $\boldsymbol{k}$ can satisfy the resonant condition $\omega = vk_z$ with this dispersion relation. This can be seen by remarking that, from eq. (B.4):

$$\begin{aligned}
\omega &= \frac{2}{\Delta t}\arcsin\left(\sqrt{\frac{s_z^2}{\Delta z^2}(1 - 4\delta_{z,0}s_z^2) + \frac{s_x^2}{\Delta x^2}(1 - s_z^2) + \frac{s_y^2}{\Delta y^2}(1 - s_z^2)}\right) \\
&\geq \frac{2}{\Delta t}\arcsin\left(\sqrt{\frac{s_z^2}{\Delta z^2}(1 - 4\delta_{z,0}s_z^2)}\right) \\
&\geq ck_z \\
&> vk_z
\end{aligned}$$

where the results of the first paragraph (choice of δ_z) were used when going from the second to the third line. Since $\omega > vk_z$ for all $\boldsymbol{k}$, this numerical scheme avoids the numerical Cherenkov effect (for particles traveling along z). Thus, as was desired, the scheme is both stable and Cherenkov-free.

Notice however that the above choice of coefficients is by no means unique. For instance, choosing the alternative set of coefficients

$$\begin{cases} \delta_x = 0 \qquad \delta y = 0 \qquad \delta_z = \delta_{z,0} \\ \beta_{x,z} = \dfrac{1}{4} \qquad \beta_{y,z} = \dfrac{1}{4} \qquad \beta_{z,x} = \beta_{z,y} = \beta_{x,y} = \beta_{y,x} = 0 \end{cases} \tag{B.5}$$

leads to the exact same numerical dispersion relation (i.e. eq. (B.4) is unchanged). Thus this choice of coefficients also leads to a stable, Cherenkov-free numerical scheme.

B.2 Coefficients for the quasi-cylindrical algorithm

As mentioned in section 2.3.2, the numerical dispersion relation cannot be found analytically in the case of the quasi-cylindrical algorithm. Therefore, contrary to the case of the Cartesian algorithm, it is not possible to theoretically predict the values of the β and δ coefficients which will prevent the numerical Cherenkov effect. Instead, one has to resort to a heuristic choice for these coefficients, and then to verify through test simulations that this choice does suppress the numerical Cherenkov effect. Here, in order to make this heuristic choice, I drew an analogy between the quasi-cylindrical scheme and the alternative Cartesian scheme defined by eq. (B.5). This is motivated by the fact that the coefficients of these two scheme play similar roles in the definition of the numerical operators, as shown in figs. B.2 and B.3.

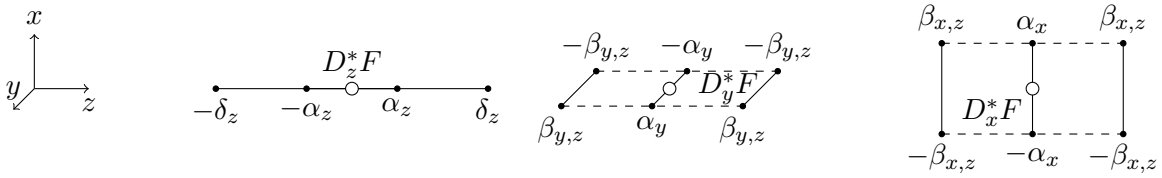

Figure B.2: Graphical representation of the role of the coefficients from eq. (B.5) in the definition of the numerical operators D_z^*, D_y^*, D_z^*. The coefficients that have a zero value (i.e. δ_x, δ_y, $\beta_{z,x}$, $\beta_{z,y}$, $\beta_{x,y}$, $\beta_{y,x}$) have not been represented.

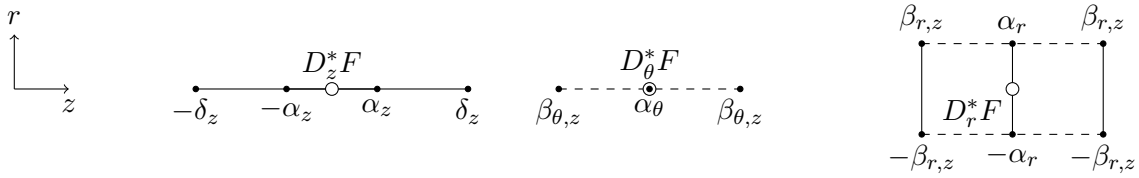

Figure B.3: Graphical representation of the coefficients of the proposed quasi-cylindrical scheme, in the definition of the numerical operators D_z^*, D_r^*, D_θ^*.

Moreover, these coefficients have to satisfy similar relations in order to ensure that the corresponding numerical operators are second-order accurate:

$$\begin{cases} \alpha_z + 3\delta_z = 1 \\ \alpha_y + 2\beta_{y,z} = 1 \\ \alpha_x + 2\beta_{x,z} = 1 \end{cases} \qquad \begin{cases} \alpha_z + 3\delta_z = 1 \\ \alpha_\theta + 2\beta_{\theta,z} = 1 \\ \alpha_r + 2\beta_{r,z} = 1 \end{cases}$$

Therefore, a natural heuristic choice for the quasi-cylindrical scheme is to mirror the coefficients of eq. (B.5) and choose:

$$\begin{cases} \delta_z = \delta_{z,0} \quad \left(= -\frac{1}{4}\left[\frac{\Delta z^2}{c^2\Delta t^2}\sin^2\left(\frac{\pi c\Delta t}{2\Delta z}\right) - 1\right] \right) \\ \beta_{r,z} = \frac{1}{4} \qquad \beta_{\theta,z} = \frac{1}{4} \end{cases}$$

This choice of coefficients was then tested in typical simulations, and the corresponding numerical scheme proved to be stable and Cherenkov-free.

Appendix C

Spurious interaction between the electrons and the laser pulse

In standard PIC simulations of the laser-plasma lens (chapter 4), the divergence and emittance of the electrons were observed to substantially grow in the direction of the laser polarization. This appendix explains why this growth is a numerical artifact, and how I suppressed it in the numerical simulations.

C.1 Observation of an unphysical interaction with the laser

In order to illustrate this growth of divergence, let us consider the simulation results of fig. C.1. This figure shows the evolution of the transverse position (upper panels) and transverse momenta (lower panels) of the accelerated electrons in the x and y directions. Note that, in this simulation, the laser pulse was linearly polarized along the x direction. (The simulation was run with Calder Circ and the Cherenkov-free scheme, with two azimuthal modes and with $\Delta z = 0.03\,\mu$m, $\Delta r = 0.2\,\mu$m and $c\Delta t = 0.96\Delta z$.)

In the drift space, in fig. C.1, the y components of the momenta (p_y) appear to remain roughly constant, but the x components (p_x) vary considerably. Since there is no wakefield in the drift space, the only force that the electrons can experience are their own space-charge force, and the force associated with the $\boldsymbol{E}$ and $\boldsymbol{B}$ fields in the back of the laser pulse. (Since the electrons progressively catch up with the laser pulse during their acceleration, they can in some cases reach the back of its intensity distribution.) However, the fact that only p_x exhibits high variations suggests that these variations are due to the force associated with the linearly-polarized laser. This is confirmed by fig. C.2, which shows that the electrons indeed experience the fields of the back of the pulse. (This figure even shows that the bunch is *modulated* at the laser wavelength.)

In theory, the field of the laser pulse can certainly accelerate the electrons along its polarization axis, and cause their momenta to vary. However, the amplitude of these variations is surprisingly high in fig. C.1. Notice that, if these variations were indeed physical, they would represent a serious hurdle for the laser-plasma lens. As can be seen by comparing the lower left and lower right panel of fig. C.1, the fact that p_x varies in the drift space prevents the lens from properly collimating the electrons.

In order to determine whether the variations of p_x are of physical or numerical origin, let us evaluate the force that the electrons should physically experience. For a given electron, the

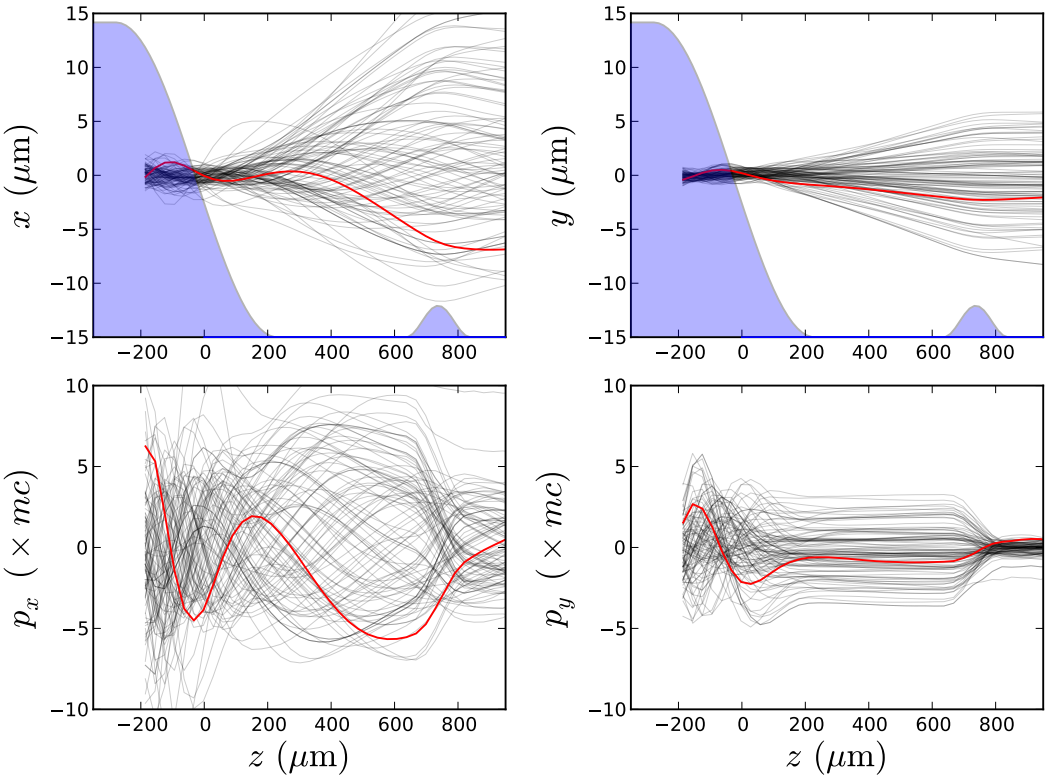

Figure C.1: Results of a typical PIC simulation of the laser-plasma lens. Upper panels: Density profile of the two jets (blue curves) and evolution of the transverse coordinates x (left panel) and y (right panel) for some of the accelerated electrons (black lines). (In the simulation the laser is polarized along x.) Lower panels: Evolution of the transverse momenta p_x (left panel) and p_y (right panel) for the same electrons. For more clarity, the trajectory of one of these electrons has been singled out and colored in red.

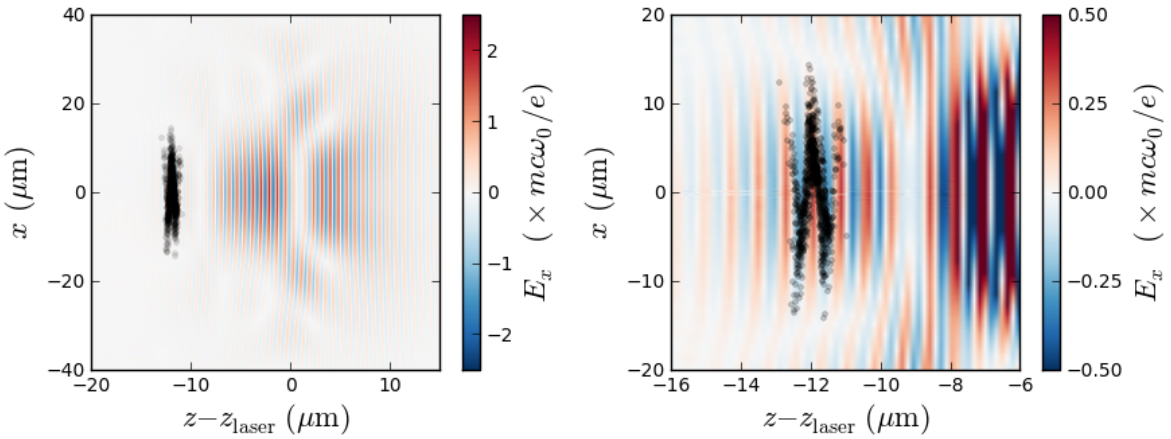

Figure C.2: Left panel: Snapshot of the simulation at $z = 550\,\mu$m (i.e. inside the drift space), showing the laser pulse (red and blue) and the trailing electron bunch (black dots). Right panel: Zoom on the electron bunch. (Notice that the electric field E_x has been rescaled.)

equation of motion along the x direction reads:

$$\frac{d\,p_x}{dt} = -e(E_x - v_z B_y + v_y B_z)$$

Since the laser propagates along the z axis and in vacuum, its fields satisfy $B_z = 0$ and $B_y = E_x/c$. This yields

$$\frac{d\,p_x}{dt} = -eE_x(1 - \beta_z) \quad \sim -\frac{eE_x}{2\gamma^2}$$

where $\beta_z = v_z/c$ and where $1 - \beta_z$ was estimated by assuming that the electrons propagate essentially along the z axis. Thus, for relativistic electrons, the force of the laser is reduced by a factor $2\gamma^2$, which can be very high since the Lorentz factor of the electrons is around $\gamma = 300$. Using the above estimation, one can evaluate an order of magnitude of the *physical* variation of p_x across the drift space. Since the electrons experience an electric field $|E_x| \sim 0.5\, mc\omega_0/e$ (see fig. C.2) over a propagation distance $L_d \sim 500\,\mu$m, this yields $\Delta p_x \sim 10^{-2}\, mc$. This is 500 times lower than the typical variation observed in the simulation: $\Delta p_x \sim 5\, mc$ (see fig. C.1)! This shows that, due to a numerical artifact, the laser force felt by the electrons in the simulation is unphysically high. Importantly, this unphysical force was observed both with the Cherenkov-free algorithm and the standard algorithm.

C.2 Origin of the spurious force

In the above physical calculation, the terms E_x and $v_z B_y$ cancel each other almost entirely ($E_x - v_z B_y$ is of the order of $10^{-5}\, E_x$). In PIC codes, this implies that E_x and $v_z B_y$ should be calculated with a precision of about 10^{-5}. While this precision is much coarser than machine precision, the intrinsic discretization of the equations in a PIC code can still introduce errors of this order of magnitude. For instance, Vay [2008] showed that, assuming that B_y is accurately calculated in PIC codes (i.e. that B_y equals E_x/c with a very good precision), the discretization error on v_z can lead to an important error on the final force $E_x - v_z B_y$. However, in the case of the simulation of fig. C.1, this error was estimated analytically and found to be negligible.

Since the observed error does not come from the discretization error on v_z, it must come from the calculation of B_y, i.e. from the fact that B_y does not equal E_x/c with enough precision in the simulation. Here it is important to note that, in the standard PIC algorithm, it can be shown that the relation $B_y = E_x/c$ is satisfied exactly *on the grid*[10] for a sinusoidal wave propagating along z. However, when calculating the force $E_x - v_z B_y$, the fields E_x and B_y are interpolated from the grid to the macroparticles. In particular, the magnetic field B_y has to be interpolated in time, since B_y is defined at half-timesteps on the grid whereas the force $E_x - v_z B_y$ is calculated at integer timesteps. As explained in section 2.1.2, this interpolation in time is done by simply averaging the fields in time, i.e. the field B_y^n at integer timestep $n\Delta t$ is calculated through $B_y^n = (B_y^{n+1/2} + B_y^{n-1/2})/2$. As represented in fig. C.3, this method of interpolation typically introduces an error in the calculation of B_y^n, and thus B_y^n does not equal E_x^n/c when interpolated on the macroparticles.

[10] More precisely, one can show that the expressions ${E_x}^n_{i+\frac{1}{2},j,k} = E_0 \cos[\, n\omega_0\Delta t - \omega_0 k\Delta z/c\,]$ and ${B_y}^{n+\frac{1}{2}}_{i,j+\frac{1}{2},k+\frac{1}{2}} = B_0 \cos\left[\, \left(n+\frac{1}{2}\right)\omega_0\Delta t - \omega_0\left(k+\frac{1}{2}\right)\Delta z/c\,\right]$ on the grid are solution of the discretized Maxwell equations, provided that $B_0 = E_0/c$. This is true in the standard PIC scheme, but not exactly true in the Cherenkov-free scheme. However, the difference between B_0 and E_0/c in the Cherenkov-free scheme can be evaluated, and it is negligible for the laser of fig. C.2.

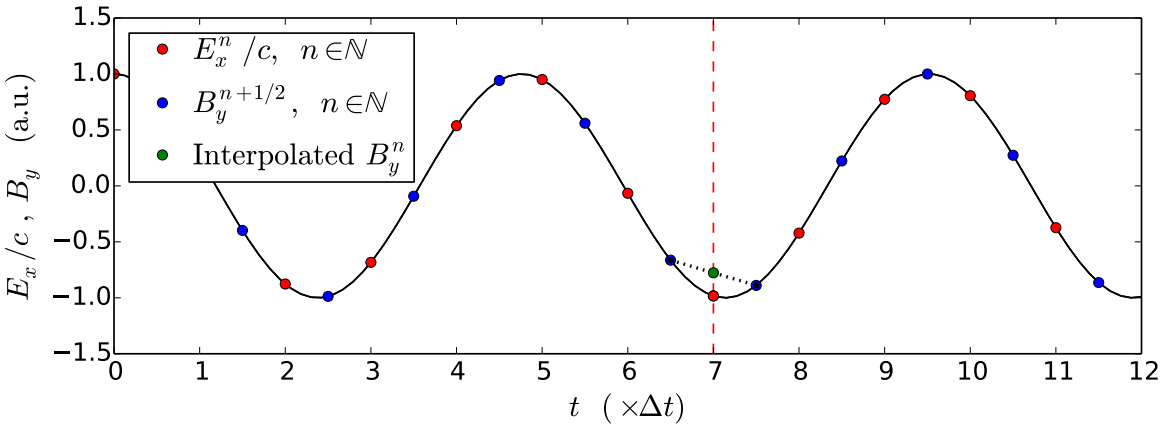

Figure C.3: Schematic representation of the evolution of the E_x and B_y fields for a sinusoidal wave in a PIC simulation. It can be shown that, in the standard PIC algorithm, the discrete fields E_x^n/c (red dots) and $B_y^{n+\frac{1}{2}}$ (blue dots) lie exactly on the same sinusoid. However, when interpolating the B_y field to an integer time (dashed red line), the obtained field B_y^n is not on the sinusoid (green dot), and thus the E_x and B_y fields do not compensate exactly in the Lorentz force.

This error can be directly estimated by a Taylor expansion. Assuming that the fields E_x^n and $B_y^{n+1/2}$ are of the form $E_x^n = E_0 \cos[\,\omega_0 n\Delta t\,]$, $B_y^{n+1/2} = \frac{E_0}{c}\cos[\,\omega_0(n+\frac{1}{2})\Delta t\,]$, the interpolated field at integer timestep B_y^n is of the form:

$$B_y^n = \frac{B_y^{n+1/2} + B_y^{n-1/2}}{2} = \frac{E_0}{c}\cos[\,\omega_0 n\Delta t\,] \times \left(1 - \frac{(\omega_0\Delta t)^2}{8}\right) + O(\Delta t^3)$$

where ω_0 is the laser frequency. Thus B_y^n is only second-order accurate in Δt. The corresponding force on the electrons is

$$F_x^n = -e(E_x^n - v_z B_y^n) = -eE_0(1-\beta_z)\cos[\,\omega_0 n\Delta t\,] - eE_0\beta_z\frac{(\omega_0\Delta t)^2}{8}\cos[\,\omega_0 n\Delta t\,]$$

Here the second term (which is typically much greater than the first one) is unphysical, and it can explain why the electrons were strongly accelerated along x in fig. C.1.

C.3 Correction with a third-order accurate interpolation method

In order to reduce this spurious force, I implemented a third-order accurate interpolation method instead of the standard second-order accurate method. As represented in fig. C.4, this method uses the fields $B_y^{n-3/2}$, $B_y^{n-1/2}$ and $B_y^{n+1/2}$ to calculate B_y^n. The exact expression of the interpolated field is

$$B_y^n = \frac{3}{8}B_y^{n+1/2} + \frac{3}{4}B_y^{n-1/2} - \frac{1}{8}B_y^{n-3/2}$$

where the coefficients have been chosen so as to have third-order accuracy. When performing a Taylor expansion of the above equation (and considering the half-timestep fields to have the

same sinusoidal expression as before), it can indeed be shown that

$$B_y^n = \frac{E_0}{c}\cos[\,\omega_0 n\Delta t\,] + \frac{E_0}{c}\frac{(\omega_0\Delta t)^3}{16}\sin[\,\omega_0 n\Delta t\,]$$

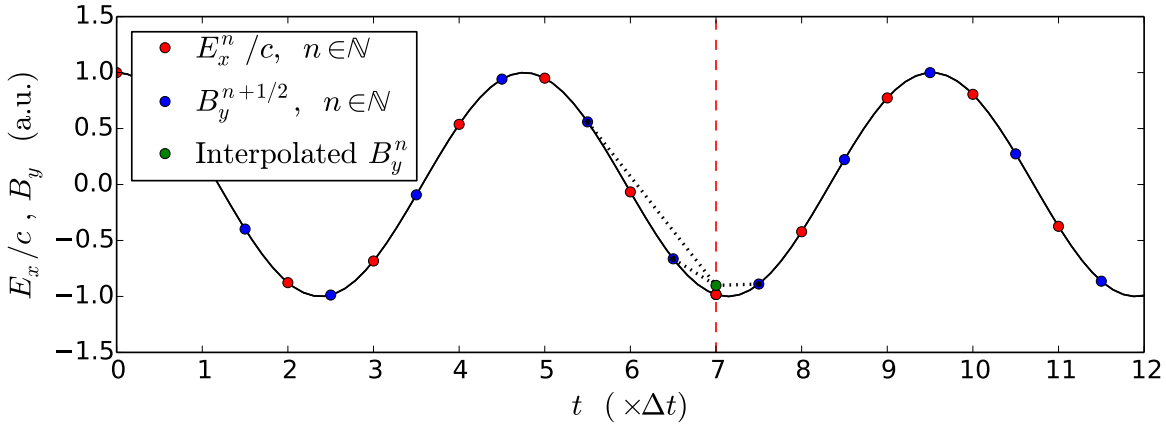

Figure C.4: Schematic representation of the third-order accurate interpolation method. This method is more precise than the standard second-order accurate interpolation method, and thus the interpolated field lies closer to the sinusoid than in fig. C.3.

I reran the simulation of section C.1 with this interpolation method. The simulation results for the second-order accurate and third-order accurate method are shown in figs. C.5 and C.6. The bunch still lies in the back of the laser pulse with the third-order method (see fig. C.6), but the variations of p_x in the drift space are almost negligeable (see fig. C.5). Notice that the proposed interpolation method does not attempt to explicitly reduce the force of the laser, but only to calculate the B field with more accuracy. Thus, the results of fig. C.5 confirm that the variations of p_x observed in section C.1 were unphysical, and that they were in fact due to an inaccurate interpolation of the B field in time and a lack compensation of the $\boldsymbol{E}$ and $\boldsymbol{v}\times\boldsymbol{B}$ term in the Lorentz force.

In addition, the lower right panel of fig. C.5 shows that the laser-plasma lens can now properly collimate the electrons in the x direction. This implies that the impact of the laser field on the electron bunch is in reality too weak to represent a serious hurdle for the laser-plasma lens concept.

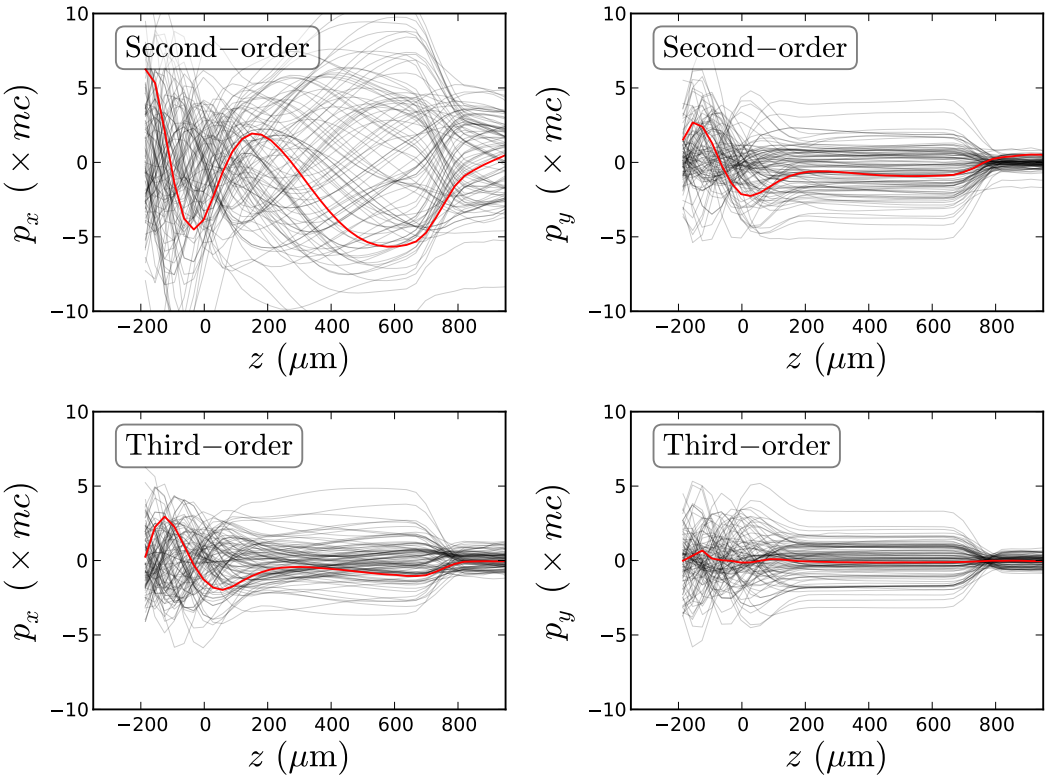

Figure C.5: Comparison of the simulation results with second-order accurate interpolation (top panels) and with third-order accurate interpolation (lower panels). The plots show the evolution of the transverse momenta p_x (left panels) and p_y (right panels) of the accelerated electrons throughout the simulation.

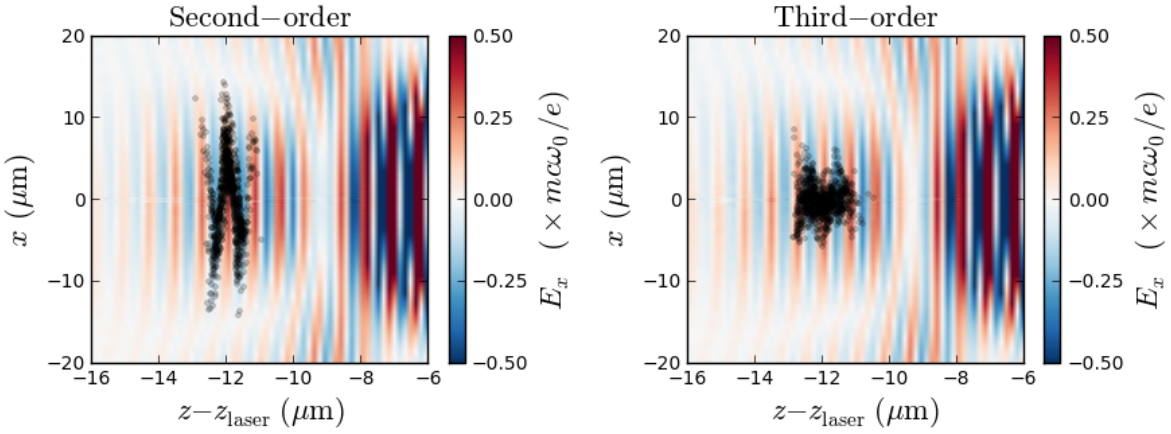

Figure C.6: Snapshot of the simulation at $z = 550\,\mu$m with the second-order accurate (left panel) and third-order accurate (right panel) methods. The electric field of the laser is virtually unchanged with the third-order method, but the electrons (black dots) experience a weaker force.

Appendix D

Expression of the fields in the nanowires undulator

In this appendix, the expressions used in section 5.3 are derived.

D.1 Expression of the fields as a Fourier series

D.1.1 Expression of E_z.

E_z is a $2\Delta z$-periodic odd function of z, and can therefore be expressed as a Fourier series :

$$E_z = 2\tilde{\lambda}\frac{mc^2}{e}\sum_{n=-\infty}^{\infty}\frac{z-n\Delta z}{[\,z-n\Delta z\,]^2+[\,x-(-1)^n\Delta x\,]^2} = \sum_{k=1}^{\infty} a_k \sin\left(\frac{k\pi z}{\Delta z}\right)$$

$$\text{where}\quad a_k = \frac{1}{i\Delta z}\int_{-\Delta z}^{\Delta z} dz\, e^{i\frac{k\pi z}{\Delta z}} \times 2\tilde{\lambda}\frac{mc^2}{e}\sum_{n=-\infty}^{\infty}\frac{z-n\Delta z}{[\,z-n\Delta z\,]^2+[\,x-(-1)^n\Delta x\,]^2}$$

By decomposing the sum over n into even and odd values of n, a_k can be written as a sum of integrals over *contiguous* intervals, and thus as an integral from $-\infty$ to ∞.

$$\begin{aligned} a_k = \quad & 2\tilde{\lambda}\frac{mc^2}{ie\Delta z}\sum_{p=-\infty}^{\infty}\int_{-\Delta z}^{\Delta z} dz\, e^{i\frac{k\pi z}{\Delta z}} \times \frac{z-2p\Delta z}{[\,z-2p\Delta z\,]^2+[\,x-\Delta x\,]^2} \\ & + 2\tilde{\lambda}\frac{mc^2}{ie\Delta z}\sum_{p=-\infty}^{\infty}\int_{-\Delta z}^{\Delta z} dz\, e^{i\frac{k\pi z}{\Delta z}} \times \frac{z-(2p+1)\Delta z}{[\,z-(2p+1)\Delta z\,]^2+[\,x+\Delta x\,]^2} \\ \\ = \quad & 2\tilde{\lambda}\frac{mc^2}{ie\Delta z}\sum_{p=-\infty}^{\infty}\int_{-\Delta z-2p\Delta z}^{\Delta z-2p\Delta z} dz\, e^{i\frac{k\pi z}{\Delta z}} \times \frac{z}{z^2+[\,x-\Delta x\,]^2} \\ & + (-1)^k 2\tilde{\lambda}\frac{mc^2}{ie\Delta z}\sum_{p=-\infty}^{\infty}\int_{-\Delta z-(2p+1)\Delta z}^{\Delta z-(2p+1)\Delta z} dz\, e^{i\frac{k\pi z}{\Delta z}} \times \frac{z}{z^2+[\,x+\Delta x\,]^2} \\ \\ = \quad & 2\tilde{\lambda}\frac{mc^2}{ie\Delta z}\left[\int_{-\infty}^{\infty} dz \frac{z\, e^{i\frac{k\pi z}{\Delta z}}}{z^2+[\,x-\Delta x\,]^2} + (-1)^k\int_{-\infty}^{\infty} dz \frac{z\, e^{i\frac{k\pi z}{\Delta z}}}{z^2+[\,x+\Delta x\,]^2}\right] \end{aligned}$$

These integrals can be calculated by using the residue theorem (along with Jordan's lemma).

$$a_k = 2\pi\tilde{\lambda}\frac{mc^2}{e\Delta z}\left[e^{-\frac{k\pi}{\Delta z}|\Delta x - x|} + (-1)^k e^{-\frac{k\pi}{\Delta z}|\Delta x + x|}\right]$$

And thus, inside the undulator ($|x| < \Delta x$):

$$E_z = 2\pi\tilde{\lambda}\frac{mc^2}{e\Delta z}\sum_{k=1}^{\infty} e^{-\frac{k\pi\Delta y}{\Delta z}}\left[e^{\frac{k\pi x}{\Delta z}} + (-1)^k e^{-\frac{k\pi x}{\Delta z}}\right]\sin\left(\frac{k\pi z}{\Delta z}\right)$$

D.1.2 Expression of E_x

Similarly, E_x is a periodic, even function of z and thus it can be written as:

$$E_x = 2\tilde{\lambda}\frac{mc^2}{e}\sum_{n=-\infty}^{\infty}\frac{x-(-1)^n\Delta x}{[\,z-n\Delta z\,]^2+[\,x-(-1)^n\Delta x\,]^2} = \frac{b_0}{2} + \sum_{k=1}^{\infty} b_k\cos\left(\frac{k\pi z}{\Delta z}\right)$$

where

$$b_k = \frac{1}{\Delta z}\int_{-\Delta z}^{\Delta z} dz\, e^{i\frac{k\pi z}{\Delta z}} \times\ 2\tilde{\lambda}\frac{m}{c}^2 e\sum_{n=-\infty}^{\infty}\frac{x-(-1)^n\Delta x}{[\,z-n\Delta z\,]^2+[\,x-(-1)^n\Delta x\,]^2}$$

By using similar techniques as in the previous section, b_k can be expressed as

$$b_k = -2\pi\tilde{\lambda}\frac{mc^2}{e\Delta z}\left[\frac{\Delta x - x}{|\Delta x - x|}e^{-\frac{k\pi}{\Delta z}|\Delta x - x|} - \frac{\Delta x + x}{|\Delta x + x|}(-1)^k e^{-\frac{k\pi}{\Delta z}|\Delta x + x|}\right]$$

Using the above expression of b_k, the expression of E_x inside the undulator is:

$$E_x = -2\pi\tilde{\lambda}\frac{mc^2}{e\Delta z}\sum_{k=1}^{\infty} e^{-\frac{k\pi\Delta x}{\Delta z}}\left[e^{\frac{k\pi x}{\Delta z}} - (-1)^k e^{-\frac{k\pi x}{\Delta z}}\right]\cos\left(\frac{k\pi z}{\Delta z}\right)$$

D.1.3 Expression of ϕ

By integrating the equations $\partial_z\phi = -eE_z/mc^2$, $\partial_x\phi = -eE_x/mc^2$, one can find the expression of ϕ.

$$\phi = 2\tilde{\lambda}\sum_{k=1}^{\infty}\frac{e^{-\frac{k\pi\Delta x}{\Delta z}}}{k}\left[e^{\frac{k\pi x}{\Delta z}} + (-1)^k e^{-\frac{k\pi x}{\Delta z}}\right]\cos\left(\frac{k\pi z}{\Delta z}\right) + K$$

Here K is an integration constant, which determines the origin of the potentials. If, by convention, this constant is chosen so that the average of ϕ over one period is zero, then

$$\phi = 2\tilde{\lambda}\sum_{k=1}^{\infty}\frac{e^{-\frac{k\pi\Delta x}{\Delta z}}}{k}\left[e^{\frac{k\pi x}{\Delta z}} + (-1)^k e^{-\frac{k\pi x}{\Delta z}}\right]\cos\left(\frac{k\pi z}{\Delta z}\right) \tag{D.1}$$

D.2 Compact expression of the fields

D.2.1 Expression of E_x.

By separating odd and even values of n in E_x, its expression can be written as

$$\begin{aligned} E_x &= 2\tilde{\lambda}\frac{mc^2}{e}\sum_{n=-\infty}^{\infty}\frac{x-(-1)^n\Delta x}{[\,z-n\Delta z\,]^2+[\,x-(-1)^n\Delta x\,]^2} \\ &= 2\tilde{\lambda}\frac{mc^2}{e}\left[\sum_{k=-\infty}^{\infty}\frac{x+\Delta x}{[(\,z-\Delta z)-2k\,\Delta z\,]^2+[\,x+\Delta x\,]^2} + \sum_{k=-\infty}^{\infty}\frac{x-\Delta x}{[\,z-2k\,\Delta z\,]^2+[\,x-\Delta x\,]^2}\right] \end{aligned}$$

Let us thus obtain a compact expression for the sum

$$f(u,v) = \sum_{k=-\infty}^{\infty} \frac{1}{(u - 2k\,\Delta z)^2 + v^2}$$

$f(u,v)$ can in fact be written as a sum of residues for a well-chosen holomorphic function $g(z)$:

$$f(u,v) = \sum_{k=-\infty}^{\infty} \mathrm{Res}[\, g(z)\ ,\ z = 2k\,\Delta z\,] \qquad g(z) = \frac{\frac{\pi}{2\Delta z}}{\tan\left(\frac{\pi z}{2\Delta z}\right)} \frac{1}{[\,(u-z)^2 + v^2\,]}$$

Using the residue theorem, $f(u,v)$ can also be written as a sum of integrals of $g(z)$ over successive closed contours.

$$f(u,v) = \frac{1}{2i\pi} \sum_{k=-\infty}^{\infty} \oint_{\mathcal{C}_k} g(z)dz$$

These closed contours are represented in the following figure (blue circle). The singularities of g are represented on the same figure (black dots).

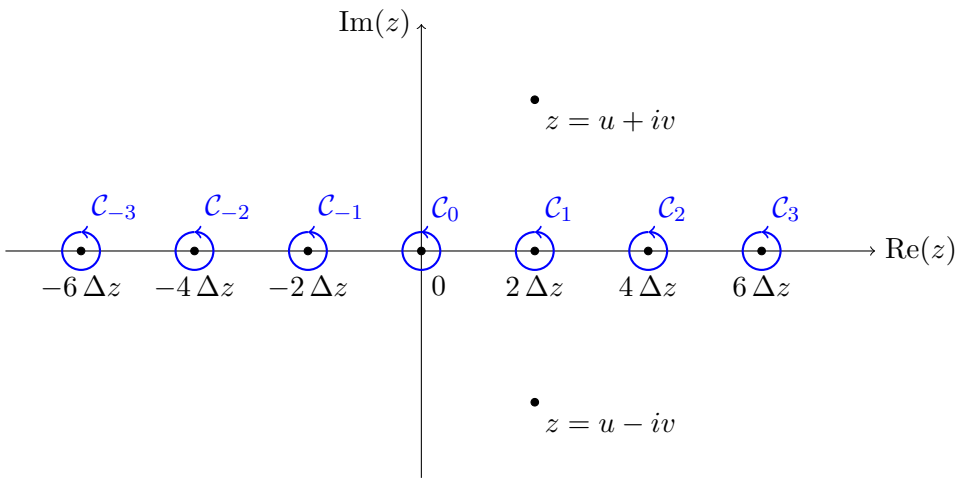

These contours can be reshaped into two new contours (see the following figure), one lying in the upper plane ($\mathcal{C}_+$) and the other one in the lower plane ($\mathcal{C}_-$). This deformation does not change the value of the associated integral, since the contributions of the red portions cancel each other, and since the contributions of the green ones vanish when the contour goes to infinity.

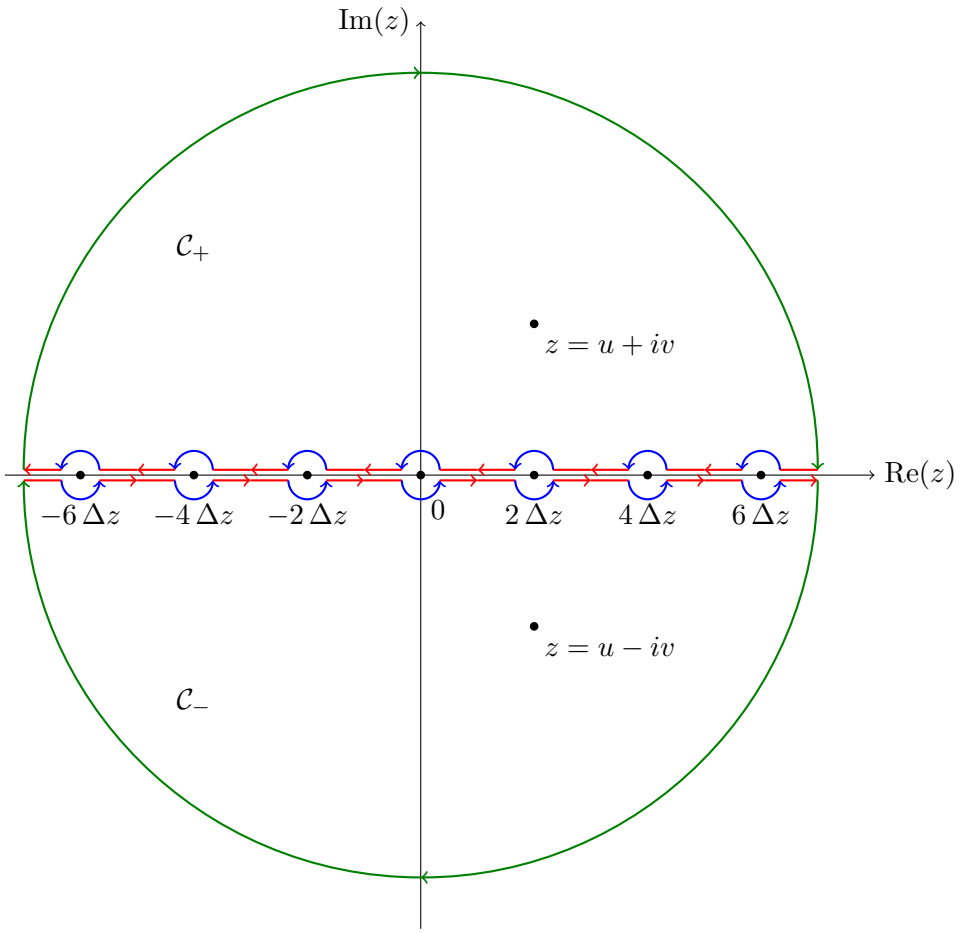

Thus $f(u,v)$ can be expressed as:

$$f(u,v) = \frac{1}{2i\pi}\left(\oint_{\mathcal{C}_+} g(z)dz + \oint_{\mathcal{C}_-} g(z)dz\right)$$

and by using the residue theorem:

$$\begin{aligned} f(u,v) &= -\text{Res}[\, g(z)\ ,\ z = u + iv\,] - \text{Res}[\, g(z)\ ,\ z = u - iv\,] \\ &= -\frac{\pi}{4v\Delta z}\left(\frac{e^{\pi(iu-v)/2\Delta z} + e^{-\pi(iu-v)/2\Delta z}}{e^{\pi(iu-v)/2\Delta z} - e^{-\pi(iu-v)/2\Delta z}} - \frac{e^{\pi(iu+v)/2\Delta z} + e^{-\pi(iu+v)/2\Delta z}}{e^{\pi(iu+v)/2\Delta z} - e^{-\pi(iu+v)/2\Delta z}}\right) \\ &= \frac{\pi}{2v\Delta z}\frac{\sinh\left(\frac{\pi}{\Delta z}v\right)}{\left[\,\cosh\left(\frac{\pi}{\Delta z}v\right) - \cos\left(\frac{\pi}{\Delta z}u\right)\,\right]} \end{aligned}$$

Using the above relation, E_x can be expressed in a relatively compact form:

$$E_x = \pi\tilde{\lambda}\frac{mc^2}{e\Delta z}\left[\frac{\sinh\left(\frac{\pi}{\Delta z}(\Delta x + x)\right)}{\left[\,\cosh\left(\frac{\pi}{\Delta z}(\Delta x + x)\right) + \cos\left(\frac{\pi}{\Delta z}z\right)\,\right]} - \frac{\sinh\left(\frac{\pi}{\Delta z}(\Delta x - x)\right)}{\left[\,\cosh\left(\frac{\pi}{\Delta z}(\Delta x - x)\right) - \cos\left(\frac{\pi}{\Delta z}z\right)\,\right]}\right]$$

D.2.2 Expression of the potential ϕ.

The dimensionless potential ϕ can be obtained from E_x by integrating the relation $E_x = -mc^2/e \times \partial_x \phi$. This yields

$$\phi = -\tilde{\lambda} \log \left[\left(\cosh\left(\frac{\pi(\Delta x + x)}{\Delta z}\right) + \cos\left(\frac{\pi z}{\Delta z}\right)\right) \left(\cosh\left(\frac{\pi(\Delta x - x)}{\Delta z}\right) - \cos\left(\frac{\pi z}{\Delta z}\right)\right) \right] + F(z) \tag{D.2}$$

where F is an undetermined function. F can however be obtained from the Laplace equation $\partial_z^2 \phi + \partial_x^2 \phi = 0$, which is valid in between the wires (since it is assumed that there is no charge present, apart from the wires themselves). Injecting the above expression of ϕ in the Laplace equation yields $F''(z) = 0$, and thus $F(z) = \alpha z + \beta$. Since the infinite array of nanowires is invariant by a translation of $2\Delta z$ along the z axis, the constant α is necessarily zero. In addition, the constant β is a global constant that determines the origin of potentials. This constant must be chosen in such a way that the present expression of ϕ (eq. (D.2)) matches that of the previous section (eq. (D.1)). The constant β can thus be determined by evaluating both expressions at $x = 0$, $z = 0$:

$$\begin{aligned} -2\tilde{\lambda} \log\left[\sinh\left(\frac{\pi \Delta x}{\Delta z}\right)\right] + \beta &= 4\tilde{\lambda} \sum_{k=1}^{\infty} \frac{e^{-\frac{2k\pi\Delta x}{\Delta z}}}{2k} \\ &= -2\tilde{\lambda} \log\left(1 - e^{-\frac{2\pi\Delta x}{\Delta z}}\right) \end{aligned}$$

and the resulting expression of ϕ is:

$$\phi = -\tilde{\lambda} \log \left[4e^{-2\frac{\pi\Delta x}{\Delta z}} \left(\cosh\left(\frac{\pi(\Delta x + x)}{\Delta z}\right) + \cos\left(\frac{\pi z}{\Delta z}\right)\right) \left(\cosh\left(\frac{\pi(\Delta x - x)}{\Delta z}\right) - \cos\left(\frac{\pi z}{\Delta z}\right)\right) \right]$$

D.2.3 Expression of E_z.

The electric field E_z can be easily obtained from the above expression and the relation $E_z = -mc^2/e \times \partial_z \phi$:

$$E_z = -\pi\tilde{\lambda} \frac{mc^2}{e\Delta z} \left[\frac{\sin\left(\frac{\pi}{\Delta z} z\right)}{\left[\, \cosh\left(\frac{\pi}{\Delta z}(\Delta x + x)\right) + \cos\left(\frac{\pi}{\Delta z} z\right) \,\right]} - \frac{\sin\left(\frac{\pi}{\Delta z} z\right)}{\left[\, \cosh\left(\frac{\pi}{\Delta z}(\Delta x - x)\right) - \cos\left(\frac{\pi}{\Delta z} z\right) \,\right]} \right]$$

Appendix E

List of publications and conference contributions

Publications

A laser-plasma lens for laser-wakefield accelerators
R. Lehe, C. Thaury, E. Guillaume, A.F. Lifschitz, V. Malka
Submitted to Physical Review Letters

A spectral unaveraged algorithm for free electron laser simulations
I.A. Andriyash, R. Lehe, V. Malka
Submitted to Journal of Computational Physics

An ultra-compact X-rays source based on a laser-plasma undulator
I. A. Andriyash, R. Lehe, A. Lifshitz, C. Thaury, J.-M. Rax, K. Krushelnik, V. Malka
Nat. Comm. 5 (2014) 4736

Transverse dynamics of an intense bunch traveling through a pre-ionized plasma
R. Lehe, C. Thaury, A.F. Lifschitz, J. M. Rax, V. Malka
Physics of Plasmas 21 (2014) 043104

Optical transverse injection in laser-plasma acceleration
R. Lehe, A.F. Lifschitz, X. Davoine, C. Thaury, V. Malka
Phys. Rev. Lett. 111 (2013) 085005

Angular-momentum evolution in laser-plasma accelerators
C. Thaury, E. Guillaume, S. Corde, R. Lehe, M. Le Bouteiller, K. Ta Phuoc, X. Davoine, J. M. Rax, A. Rousse, V. Malka
Phys. Rev. Lett. 111 (2013) 135002

Numerical growth of emittance in simulations of laser-wakefield acceleration
R. Lehe, X. Davoine, A.F. Lifschitz, C. Thaury, V. Malka
Phys. Rev. ST Accel. Beams 16 (2013) 021301

Observation of longitudinal transverse self-injections in laser-plasma accelerators

S. Corde, C. Thaury, A.F. Lifschitz, G. Lambert, K. Ta Phuoc, X. Davoine, R. Lehe, D. Douillet, A. Rousse V. Malka
Nat. Comm. 4 (2013) 1501

The LUNEX5 project in France
M.E. Couprie et al.
Journal of Physics : Conference Series 425 (2013) 072001

Conference contributions

Injection optique transverse dans l'accélération laser-plasma
R. Lehe, A.F. Lifschitz, X. Davoine, C. Thaury, V. Malka
Poster - Journées Accélérateurs de la SFP, 14-15 October 2013, Roscoff, France

Numerical Cherenkov effect in simulations of laser-wakefield acceleration
R. Lehe, A.F. Lifschitz, X. Davoine, C. Thaury, V. Malka
Oral presentation - Laser and Plasma Accelerator Workshop, 2-6 September 2013, Goa, India

Optical Transverse Injection : A New Mechanism of Injection in Laser-Wakefield Acceleration
R. Lehe, A.F. Lifschitz, X. Davoine, C. Thaury, V. Malka
Oral presentation -1st European Advanced Accelerator Concepts Workshop, 2-7 June 2013, Isola d'Elba, Italy

Optical transverse injection in laser-wakefield acceleration
R. Lehe, A.F. Lifschitz, X. Davoine, C. Thaury, V. Malka
Oral presentation - Physics and Applications of High Brightness Beams, 25-28 March 2013, San Juan, Puerto Rico

Numerical study of an FEL based on LWFA electrons a laser-plasma wiggler
R. Lehe, X. Davoine, G. Lambert, A.F. Lifschitz, J.-M. Rax, V. Malka
Poster & conference proceeding - Free Electron Laser conference, 25-31 August 2012, Nara, Japan

Bibliography

Albert, F., Shah, R., Phuoc, K. T., Fitour, R., Burgy, F., Rousseau, J.-P., Tafzi, A., Douillet, D., Lefrou, T., and Rousse, A. (2008). Betatron oscillations of electrons accelerated in laser wakefields characterized by spectral x-ray analysis. *Phys. Rev. E*, 77:056402.

Altarelli, M. (2006). *XFEL: The European X-ray Free-electron Laser : Technical Design Report*. DESY (Series). DESY XFEL Project Group.

Amiranoff, F., Baton, S., Bernard, D., Cros, B., Descamps, D., Dorchies, F., Jacquet, F., Malka, V., Marquès, J. R., Matthieussent, G., Miné, P., Modena, A., Mora, P., Morillo, J., and Najmudin, Z. (1998). Observation of laser wakefield acceleration of electrons. *Phys. Rev. Lett.*, 81:995–998.

Andriyash, I. A., Lehe, R., Lifschitz, A., Thaury, C., Rax, J. M., Krushelnick, K., and Malka, V. (2014a). An ultracompact x-ray source based on a laser-plasma undulator. *Nat Commun*, 5.

Andriyash, I. A., Lehe, R., and Malka, V. (2014b). Spectral time-domain algorithm for non-averaged modeling of the coherent amplification in free electron lasers (fels). *Submitted to Computer Physics Communications*.

Bacci, A., Maroli, C., Petrillo, V., Rossi, A., Serafini, L., and Tomassini, P. (2008). Compact x-ray free-electron laser based on an optical undulator. *Nucl. Instrum. Methods Phys. Rev. A*, 587:388 – 397.

Barov, N., Conde, M. E., Gai, W., and Rosenzweig, J. B. (1998). Propagation of short electron pulses in a plasma channel. *Phys. Rev. Lett.*, 80:81–84.

Ben-Ismail, A., Lundh, O., Rechatin, C., Lim, J. K., Faure, J., Corde, S., and Malka, V. (2011). Compact and high-quality gamma-ray source applied to 10 μm-range resolution radiography. *Applied Physics Letters*, 98(26):264101.

Birdsall, C. and Langdon, A. (2004). *Plasma Physics via Computer Simulation*. Series in Plasma Physics. Taylor & Francis.

Boris, J. (1970). Relativistic plasma simulation-optimization of a hybrid code. In *Proceeding of the Fourth Conference on Numerical Simulations of Plasmas*. Naval Research Laboratory.

Bourgeois, N., Cowley, J., and Hooker, S. M. (2013). Two-pulse ionization injection into quasi-linear laser wakefields. *Phys. Rev. Lett.*, 111:155004.

Bulanov, S., Naumova, N., Pegoraro, F., and Sakai, J. (1998). Particle injection into the wave acceleration phase due to nonlinear wake wave breaking. *Phys. Rev. E*, 58:R5257–R5260.

Burza, M., Gonoskov, A., Svensson, K., Wojda, F., Persson, A., Hansson, M., Genoud, G., Marklund, M., Wahlström, C.-G., and Lundh, O. (2013). Laser wakefield acceleration using wire produced double density ramps. *Phys. Rev. ST Accel. Beams*, 16:011301.

Chen, M., Esarey, E., Geddes, C. G. R., Schroeder, C. B., Plateau, G. R., Bulanov, S. S., Rykovanov, S., and Leemans, W. P. (2013). Modeling classical and quantum radiation from laser-plasma accelerators. *Phys. Rev. ST Accel. Beams*, 16:030701.

Chen, P. (1987). A possible final focusing mechanism for linear colliders. *Particle Accelerators*, 20:171–182.

Chen, P., Oide, K., Sessler, A. M., and Yu, S. S. (1990). Plasma-based adiabatic focuser. *Phys. Rev. Lett.*, 64:1231–1234.

Chien, T.-Y., Chang, C.-L., Lee, C.-H., Lin, J.-Y., Wang, J., and Chen, S.-Y. (2005). Spatially localized self-injection of electrons in a self-modulated laser-wakefield accelerator by using a laser-induced transient density ramp. *Phys. Rev. Lett.*, 94:115003.

Cipiccia, S., Islam, M. R., Ersfeld, B., Shanks, R. P., Brunetti, E., Vieux, G., Yang, X., Issac, R. C., Wiggins, S. M., Welsh, G. H., Anania, M.-P., Maneuski, D., Montgomery, R., Smith, G., Hoek, M., Hamilton, D. J., Lemos, N. R. C., Symes, D., Rajeev, P. P., Shea, V. O., Dias, J. M., and Jaroszynski, D. A. (2011). Gamma-rays from harmonically resonant betatron oscillations in a plasma wake. *Nat Phys*, 7(11):867–871.

Clayton, C. E., Marsh, K. A., Dyson, A., Everett, M., Lal, A., Leemans, W. P., Williams, R., and Joshi, C. (1993). Ultrahigh-gradient acceleration of injected electrons by laser-excited relativistic electron plasma waves. *Phys. Rev. Lett.*, 70:37–40.

Corde, S. and Ta Phuoc, K. (2011). Plasma wave undulator for laser-accelerated electrons. *Physics of Plasmas (1994-present)*, 18(3):033111.

Corde, S., Ta Phuoc, K., Lambert, G., Fitour, R., Malka, V., Rousse, A., Beck, A., and Lefebvre, E. (2013a). Femtosecond x rays from laser-plasma accelerators. *Rev. Mod. Phys.*, 85:1–48.

Corde, S., Thaury, C., Lifschitz, A., Lambert, G., Ta Phuoc, K., Davoine, X., Lehe, R., Douillet, D., Rousse, A., and Malka, V. (2013b). Observation of longitudinal and transverse self-injections in laser-plasma accelerators. *Nat Commun*, 4.

Corde, S., Thaury, C., Phuoc, K. T., Lifschitz, A., Lambert, G., Faure, J., Lundh, O., Benveniste, E., Ben-Ismail, A., Arantchuk, L., Marciniak, A., Stordeur, A., Brijesh, P., Rousse, A., Specka, A., and Malka, V. (2011). Mapping the x-ray emission region in a laser-plasma accelerator. *Phys. Rev. Lett.*, 107:215004.

Couprie, M. E., Benabderrahmane, C., Betinelli, P., Bouvet, F., Buteau, A., Cassinari, L., Daillant, J., Denard, J. C., Eymard, P., Gagey, B., Herbeaux, C., Labat, M., Lagarde, B., Lestrade, A., Loulergue, A., Marchand, P., Marlats, J. L., Miron, C., Morin, P., Nadji, A., Polack, F., Pruvost, J. B., Ribeiro, F., Ricaud, J. P., Roy, P., Tanikawa, T., Roux, R., Bielawski, S., Evain, C., Szwaj, C., Lambert, G., Lifschitz, A., Malka, V., Lehe, R., Rousse, A., Phuoc, K. T., Thaury, C., Devanz, G., Luong, M., CarrÃ©, B., LeBec, G., Farvacque, L., Dubois, A., and LÃŒning, J. (2013). The lunex5 project in france. *Journal of Physics: Conference Series*, 425(7):072001.

Cowan, B. M., Bruhwiler, D. L., Cary, J. R., Cormier-Michel, E., and Geddes, C. G. R. (2013). Generalized algorithm for control of numerical dispersion in explicit time-domain electromagnetic simulations. *Phys. Rev. ST Accel. Beams*, 16:041303.

Danly, B., Bekefi, G., Davidson, R., Temkin, R., Tran, T., and Wurtele, J. (1987). Principles of gyrotron powered electromagnetic wigglers for free-electron lasers. *Quantum Electronics, IEEE Journal of*, 23(1):103–116.

Davidson, A., Tableman, A., An, W., Tsung, F. S., Lu, W., Vieira, J., Fonseca, R. A., Silva, L. O., and Mori, W. B. (2014). Implementation of a hybrid particle code with a PIC description in r-z and a gridless description in ϕ into OSIRIS. *ArXiv e-prints*.

Davoine, X., Beck, A., Lifschitz, A., Malka, V., and Lefebvre, E. (2010). Cold injection for electron wakefield acceleration. *New Journal of Physics*, 12(9):095010.

Davoine, X., Lefebvre, E., Rechatin, C., Faure, J., and Malka, V. (2009). Cold optical injection producing monoenergetic, multi-gev electron bunches. *Phys. Rev. Lett.*, 102:065001.

Deacon, D. A. G., Elias, L. R., Madey, J. M. J., Ramian, G. J., Schwettman, H. A., and Smith, T. I. (1977). First operation of a free-electron laser. *Phys. Rev. Lett.*, 38:892–894.

Esarey, E., Hubbard, R. F., Leemans, W. P., Ting, A., and Sprangle, P. (1997). Electron injection into plasma wakefields by colliding laser pulses. *Phys. Rev. Lett.*, 79:2682–2685.

Esarey, E., Krall, J., and Sprangle, P. (1994). Envelope analysis of intense laser pulse self-modulation in plasmas. *Phys. Rev. Lett.*, 72:2887–2890.

Esarey, E., Schroeder, C. B., and Leemans, W. P. (2009). Physics of laser-driven plasma-based electron accelerators. *Rev. Mod. Phys.*, 81:1229–1285.

Esarey, E., Shadwick, B. A., Catravas, P., and Leemans, W. P. (2002). Synchrotron radiation from electron beams in plasma-focusing channels. *Phys. Rev. E*, 65:056505.

Esirkepov, T. (2001). Exact charge conservation scheme for particle-in-cell simulation with an arbitrary form-factor. *Computer Physics Communications*, 135(2):144 – 153.

Faure, J., Glinec, Y., Pukhov, A., Kiselev, S., Gordienko, S., Lefebvre, E., Rousseau, J.-P., Burgy, F., and Malka, V. (2004). A laser-plasma accelerator producing monoenergetic electron beams. *Nature*, 431(7008):541–544.

Faure, J., Rechatin, C., Lundh, O., Ammoura, L., and Malka, V. (2010). Injection and acceleration of quasimonoenergetic relativistic electron beams using density gradients at the edges of a plasma channel. *Physics of Plasmas (1994-present)*, 17(8):083107.

Faure, J., Rechatin, C., Norlin, A., Lifschitz, A., Glinec, Y., and Malka, V. (2006). Controlled injection and acceleration of electrons in plasma wakefields by colliding laser pulses. *Nature (London)*, 444:737–739.

Fourmaux, S., Corde, S., Phuoc, K. T., Lassonde, P., Lebrun, G., Payeur, S., Martin, F., Sebban, S., Malka, V., Rousse, A., and Kieffer, J. C. (2011). Single shot phase contrast imaging using laser-produced betatron x-ray beams. *Opt. Lett.*, 36(13):2426–2428.

Fubiani, G., Esarey, E., Schroeder, C. B., and Leemans, W. P. (2004). Beat wave injection of electrons into plasma waves using two interfering laser pulses. *Phys. Rev. E*, 70:016402.

Fuchs, M., Weingartner, R., Popp, A., Major, Z., Becker, S., Osterhoff, J., Cortrie, I., Zeitler, B., Horlein, R., Tsakiris, G. D., Schramm, U., Rowlands-Rees, T. P., Hooker, S. M., Habs, D., Krausz, F., Karsch, S., and Gruner, F. (2009). Laser-driven soft-x-ray undulator source. *Nat Phys*, 5(11):826–829.

Gea-Banacloche, J., Moore, G., Schlicher, R., Scully, M., and Walther, H. (1987). Soft x-ray free-electron laser with a laser undulator. *Quantum Electronics, IEEE Journal of*, 23(9):1558–1570.

Geddes, C. G. R., Nakamura, K., Plateau, G. R., Toth, C., Cormier-Michel, E., Esarey, E., Schroeder, C. B., Cary, J. R., and Leemans, W. P. (2008). Plasma-density-gradient injection of low absolute-momentum-spread electron bunches. *Phys. Rev. Lett.*, 100:215004.

Geddes, C. G. R., Toth, C., van Tilborg, J., Esarey, E., Schroeder, C. B., Bruhwiler, D., Nieter, C., Cary, J., and Leemans, W. P. (2004). High-quality electron beams from a laser wakefield accelerator using plasma-channel guiding. *Nature*, 431(7008):538–541.

Godfrey, B. B. (1974). Numerical cherenkov instabilities in electromagnetic particle codes. *Journal of Computational Physics*, 15(4):504 – 521.

Gonsalves, A. J., Nakamura, K., Lin, C., Panasenko, D., Shiraishi, S., Sokollik, T., Benedetti, C., Schroeder, C. B., Geddes, C. G. R., van Tilborg, J., Osterhoff, J., Esarey, E., Toth, C., and Leemans, W. P. (2011). Tunable laser plasma accelerator based on longitudinal density tailoring. *Nat. Phys.*, 7:862–866.

Gorbunov, L. M. and Kirsanov, V. I. (1987). Excitation of plasma waves by an electromagnetic wave packet. *Sov. Phys. JETP*, 66:290–294.

Govil, R., Leemans, W. P., Backhaus, E. Y., and Wurtele, J. S. (1999). Observation of return current effects in a passive plasma lens. *Phys. Rev. Lett.*, 83:3202–3205.

Greenwood, A. D., Cartwright, K., Baca, E., and Luginsland, J. (2002). On the use of fdtd to simulate systems with charged particles. *Proc. IEEE Antennas and Propagation*, pages 268–271.

Greenwood, A. D., Cartwright, K. L., Luginsland, J. W., and Baca, E. A. (2004). On the elimination of numerical cerenkov radiation in pic simulations. *Journal of Computational Physics*, 201(2):665 – 684.

Grüner, F. J., Schroeder, C. B., Maier, A. R., Becker, S., and Mikhailova, J. M. (2009). Space-charge effects in ultrahigh current electron bunches generated by laser-plasma accelerators. *Phys. Rev. ST Accel. Beams*, 12:020701.

Hairapetian, G., Davis, P., Clayton, C. E., Joshi, C., Hartman, S. C., Pellegrini, C., and Katsouleas, T. (1994). Experimental demonstration of dynamic focusing of a relativistic electron bunch by an overdense plasma lens. *Phys. Rev. Lett.*, 72:2403–2406.

He, Z., Thomas, A., Beaurepaire, B., Nees, J. A., Hou, B., Malka, V., Krushelnick, K., and Faure, J. (2013). Diffraction of electron pulses generated in a laser-wakefield accelerator at 0.5 khz. In *CLEO: 2013*. Optical Society of America.

Hockney, R. and Eastwood, J. (1988). *Computer Simulation Using Particles*. Taylor & Francis.

Huang, Z. and Kim, K.-J. (2007). Review of x-ray free-electron laser theory. *Phys. Rev. ST Accel. Beams*, 10:034801.

Humphries, S. (1990). *Charged particle beams*. A Wiley-Interscience publication. Wiley.

Jackson, J. D. (1998). *Classical Electrodynamics Third Edition*. Wiley, third edition.

Johnson, L. C. and Chu, T. K. (1974). Measurements of electron density evolution and beam self-focusing in a laser-produced plasma. *Phys. Rev. Lett.*, 32:517–520.

Joshi, C., Katsouleas, T., Dawson, J., Yan, Y. T., and Slater, J. (1987). Plasma wave wigglers for free-electron lasers. *Quantum Electronics, IEEE Journal of*, 23(9):1571–1577.

Kalmykov, S., Yi, S. A., Khudik, V., and Shvets, G. (2009). Electron self-injection and trapping into an evolving plasma bubble. *Phys. Rev. Lett.*, 103:135004.

Karkkainen, M., Gjonaj, E., Lau, T., and Weiland, T. (2006). Low-dispersion wake field calculation tools. In *Proceedings of ICAP 2006*, volume 1, page 35, Chamonix, France.

Katsouleas, T., Wilks, S., Chen, P., Dawson, J. M., and Su, J. J. (1987). Beam loading in plasma accelerators. *Particle Accelerators*, 22:81–99.

Keshet, U., Katz, B., Spitkovsky, A., and Waxman, E. (2009). Magnetic field evolution in relativistic unmagnetized collisionless shocks. *The Astrophysical Journal Letters*, 693(2):L127.

Khachatryan, A. G., Irman, A., van Goor, F. A., and Boller, K. J. (2007). Femtosecond electron-bunch dynamics in laser wakefields and vacuum. *Physical Review Special Topics - Accelerators and Beams*, 10(12):121301+.

Kim, H. T., Pae, K. H., Cha, H. J., Kim, I. J., Yu, T. J., Sung, J. H., Lee, S. K., Jeong, T. M., and Lee, J. (2013). Enhancement of electron energy to the multi-gev regime by a dual-stage laser-wakefield accelerator pumped by petawatt laser pulses. *Phys. Rev. Lett.*, 111:165002.

Kondratenko, A. and Saldin, E. (1980). GENERATING OF COHERENT RADIATION BY A RELATIVISTIC ELECTRON BEAM IN AN ONDULATOR. *Part.Accel.*, 10:207–216.

Kostyukov, I., Kiselev, S., and Pukhov, A. (2003). X-ray generation in an ion channel. *Physics of Plasmas (1994-present)*, 10(12):4818–4828.

Kostyukov, I., Nerush, E., Pukhov, A., and Seredov, V. (2010). A multidimensional theory for electron trapping by a plasma wake generated in the bubble regime. *New Jour. Phys.*, 12:045009.

Kotaki, H., Masuda, S., Kando, M., Koga, J. K., and Nakajima, K. (2004). Head-on injection of a high quality electron beam by the interaction of two laser pulses. *Physics of Plasmas (1994-present)*, 11(6):3296–3302.

Kruer, W. (2003). *The Physics of Laser Plasma Interactions*. Frontiers in physics. Westview Press.

Labat, M., Bellaveglia, M., Bougeard, M., Carré, B., Ciocci, F., Chiadroni, E., Cianchi, A., Couprie, M. E., Cultrera, L., Del Franco, M., Di Pirro, G., Drago, A., Ferrario, M., Filippetto, D., Frassetto, F., Gallo, A., Garzella, D., Gatti, G., Giannessi, L., Lambert, G., Mostacci, A.,

Petralia, A., Petrillo, V., Poletto, L., Quattromini, M., Rau, J. V., Ronsivalle, C., Sabia, E., Serluca, M., Spassovsky, I., Surrenti, V., Vaccarezza, C., and Vicario, C. (2011). High-gain harmonic-generation free-electron laser seeded by harmonics generated in gas. *Phys. Rev. Lett.*, 107:224801.

Lambert, G., Hara, T., Garzella, D., Tanikawa, T., Labat, M., Carre, B., Kitamura, H., Shintake, T., Bougeard, M., Inoue, S., et al. (2008). Injection of harmonics generated in gas in a free-electron laser providing intense and coherent extreme-ultraviolet light. *Nature physics*, 4(4):296–300.

Leemans, W. P., Catravas, P., Esarey, E., Geddes, C. G. R., Toth, C., Trines, R., Schroeder, C. B., Shadwick, B. A., van Tilborg, J., and Faure, J. (2002). Electron-yield enhancement in a laser-wakefield accelerator driven by asymmetric laser pulses. *Phys. Rev. Lett.*, 89:174802.

Leemans, W. P., Nagler, B., Gonsalves, A. J., Toth, C., Nakamura, K., Geddes, C. G. R., Esarey, E., Schroeder, C. B., and Hooker, S. M. (2006). Gev electron beams from a centimetre-scale accelerator. *Nat. Phys.*, 2:696.

Lefebvre, E., Cochet, N., Fritzler, S., Malka, V., Aléonard, M.-M., Chemin, J.-F., Darbon, S., Disdier, L., Faure, J., Fedotoff, A., Landoas, O., Malka, G., Méot, V., Morel, P., Gloahec, M. R. L., Rouyer, A., Rubbelynck, C., Tikhonchuk, V., Wrobel, R., Audebert, P., and Rousseaux, C. (2003). Electron and photon production from relativistic laser-plasma interactions. *Nuclear Fusion*, 43(7):629.

Lehe, R., Lifschitz, A., Thaury, C., Malka, V., and Davoine, X. (2013). Numerical growth of emittance in simulations of laser-wakefield acceleration. *Phys. Rev. ST Accel. Beams*, 16:021301.

Lehe, R., Thaury, C., Lifschitz, A., Rax, J.-M., and Malka, V. (2014). Transverse dynamics of an intense electron bunch traveling through a pre-ionized plasma. *Physics of Plasmas (1994-present)*, 21(4):043104.

Lifschitz, A. F., Davoine, X., Lefebvre, E., Faure, J., Rechatin, C., and Malka, V. (2009). Particle-in-cell modelling of laser-plasma interaction using fourier decomposition. *J. Comput. Phys.*, 228(5):1803–1814.

Liu, C. and Tripathi, V. (1994). *Interaction of Electromagnetic Waves with Electron Beams and Plasmas*. World Scientific.

Loulergue, A. (2013). Longitudinal and transverse beam manipulation for compact laser plasma accelerator based free-electron lasers. HBEB2013 Conference.

Lu, W., Huang, C., Zhou, M., Mori, W. B., and Katsouleas, T. (2006a). Nonlinear theory for relativistic plasma wakefields in the blowout regime. *Phys. Rev. Lett.*, 96:165002.

Lu, W., Huang, C., Zhou, M., Tzoufras, M., Tsung, F. S., Mori, W. B., and Katsouleas, T. (2006b). A nonlinear theory for multidimensional relativistic plasma wave wakefields. *Physics of Plasmas (1994-present)*, 13(5):056709.

Lu, W., Tzoufras, M., Joshi, C., Tsung, F. S., Mori, W. B., Vieira, J., Fonseca, R. A., and Silva, L. O. (2007). Generating multi-gev electron bunches using single stage laser wakefield acceleration in a 3d nonlinear regime. *Phys. Rev. ST Accel. Beams*, 10:061301.

Madey, J. M. J. (1971). Stimulated emission of bremsstrahlung in a periodic magnetic field. *Journal of Applied Physics*, 42(5):1906–1913.

Maier, A. R., Meseck, A., Reiche, S., Schroeder, C. B., Seggebrock, T., and Grüner, F. (2012). Demonstration scheme for a laser-plasma-driven free-electron laser. *Phys. Rev. X*, 2:031019.

Malka, V., Fritzler, S., Lefebvre, E., Aleonard, M.-M., Burgy, F., Chambaret, J.-P., Chemin, J.-F., Krushelnick, K., Malka, G., Mangles, S. P. D., Najmudin, Z., Pittman, M., Rousseau, J.-P., Scheurer, J.-N., Walton, B., and Dangor, A. E. (2002). Electron acceleration by a wake field forced by an intense ultrashort laser pulse. *Science*, 298(5598):1596–1600.

Mangles, S. P. D., Murphy, C. D., Najmudin, Z., Thomas, A. G. R., Collier, J. L., Dangor, A. E., Divall, E. J., Foster, P. S., Gallacher, J. G., Hooker, C. J., Jaroszynski, D. A., Langley, A. J., Mori, W. B., Norreys, P. A., Tsung, F. S., Viskup, R., Walton, B. R., and Krushelnick, K. (2004). Monoenergetic beams of relativistic electrons from intense laser-plasma interactions. *Nature*, 431(7008):535–538.

Marcus, G., Hemsing, E., and Rosenzweig, J. (2011). Gain length fitting formula for free-electron lasers with strong space-charge effects. *Phys. Rev. ST Accel. Beams*, 14:080702.

Martins, S. F., Fonseca, R. A., Lu, W., Mori, W. B., and Silva, L. O. (2010). Exploring laser-wakefield-accelerator regimes for near-term lasers using particle-in-cell simulation in lorentz-boosted frames. *Nat Phys*, 6(4):311–316.

McGuffey, C., Thomas, A. G. R., Schumaker, W., Matsuoka, T., Chvykov, V., Dollar, F. J., Kalintchenko, G., Yanovsky, V., Maksimchuk, A., Krushelnick, K., Bychenkov, V. Y., Glazyrin, I. V., and Karpeev, A. V. (2010). Ionization induced trapping in a laser wakefield accelerator. *Phys. Rev. Lett.*, 104:025004.

McNeil, B. W. J. and Thompson, N. R. (2010). X-ray free-electron lasers. *Nat Photon*, 4(12):814–821.

Mehrling, T., Grebenyuk, J., Tsung, F. S., Floettmann, K., and Osterhoff, J. (2012). Transverse emittance growth in staged laser-wakefield acceleration. *Phys. Rev. ST Accel. Beams*, 15:111303.

Michel, P., Schroeder, C. B., Shadwick, B. A., Esarey, E., and Leemans, W. P. (2006). Radiative damping and electron beam dynamics in plasma-based accelerators. *Phys. Rev. E*, 74:026501.

Migliorati, M., Bacci, A., Benedetti, C., Chiadroni, E., Ferrario, M., Mostacci, A., Palumbo, L., Rossi, A. R., Serafini, L., and Antici, P. (2013). Intrinsic normalized emittance growth in laser-driven electron accelerators. *Phys. Rev. ST Accel. Beams*, 16:011302.

Modena, A., Najmudin, Z., Dangor, A. E., Clayton, C. E., Marsh, K. A., Joshi, C., Malka, V., Darrow, C. B., Danson, C., Neely, D., and Walsh, F. N. (1995). Electron acceleration from the breaking of relativistic plasma waves. *Nature*, 377(6550):606–608.

Mora, P. and Antonsen, T. M. (1997). Kinetic modeling of intense, short laser pulses propagating in tenuous plasmas. *Physics of Plasmas*, 4(1):217–229.

Nakajima, K. (2008). Compact x-ray sources: Towards a table-top free-electron laser. *Nat. Phys.*, 4:92 – 93.

Nakajima, K., Fisher, D., Kawakubo, T., Nakanishi, H., Ogata, A., Kato, Y., Kitagawa, Y., Kodama, R., Mima, K., Shiraga, H., Suzuki, K., Yamakawa, K., Zhang, T., Sakawa, Y., Shoji, T., Nishida, Y., Yugami, N., Downer, M., and Tajima, T. (1995). Observation of ultrahigh gradient electron acceleration by a self-modulated intense short laser pulse. *Phys. Rev. Lett.*, 74:4428–4431.

Nakanishi, H., Yoshida, Y., Ueda, T., Kozawa, T., Shibata, H., Nakajima, K., Kurihara, T., Yugami, N., Nishida, Y., Kobayashi, T., Enomoto, A., Oogoe, T., Kobayashi, H., Newberger, B. S., Tagawa, S., Miya, K., and Ogata, A. (1991). Direct observation of plasma-lens effect. *Phys. Rev. Lett.*, 66:1870–1873.

Németh, K., Shen, B., Li, Y., Shang, H., Crowell, R., Harkay, K. C., and Cary, J. R. (2008). Laser-driven coherent betatron oscillation in a laser-wakefield cavity. *Phys. Rev. Lett.*, 100:095002.

Ng, J. S. T., Chen, P., Baldis, H., Bolton, P., Cline, D., Craddock, W., Crawford, C., Decker, F. J., Field, C., Fukui, Y., Kumar, V., Iverson, R., King, F., Kirby, R. E., Nakajima, K., Noble, R., Ogata, A., Raimondi, P., Walz, D., and Weidemann, A. W. (2001). Observation of plasma focusing of a 28.5 gev positron beam. *Phys. Rev. Lett.*, 87:244801.

Pae, K. H., Choi, I. W., and Lee, J. (2010). Self-mode-transition from laser wakefield accelerator to plasma wakefield accelerator of laser-driven plasma-based electron acceleration. *Physics of Plasmas (1994-present)*, 17(12):123104.

Pak, A., Marsh, K. A., Martins, S. F., Lu, W., Mori, W. B., and Joshi, C. (2010). Injection and trapping of tunnel-ionized electrons into laser-produced wakes. *Phys. Rev. Lett.*, 104:025003.

Paradkar, B. S., Cros, B., Mora, P., and Maynard, G. (2013). Numerical modeling of multi-gev laser wakefield electron acceleration inside a dielectric capillary tube. *Physics of Plasmas (1994-present)*, 20(8):083120.

Petrillo, V., Serafini, L., and Tomassini, P. (2008). Ultrahigh brightness electron beams by plasma-based injectors for driving all-optical free-electron lasers. *Phys. Rev. ST Accel. Beams*, 11:070703.

Phuoc, K. T., Burgy, F., Rousseau, J.-P., Malka, V., Rousse, A., Shah, R., Umstadter, D., Pukhov, A., and Kiselev, S. (2005). Laser based synchrotron radiation. *Physics of Plasmas (1994-present)*, 12(2):023101.

Pollock, B. B., Clayton, C. E., Ralph, J. E., Albert, F., Davidson, A., Divol, L., Filip, C., Glenzer, S. H., Herpoldt, K., Lu, W., Marsh, K. A., Meinecke, J., Mori, W. B., Pak, A., Rensink, T. C., Ross, J. S., Shaw, J., Tynan, G. R., Joshi, C., and Froula, D. H. (2011). Demonstration of a narrow energy spread, ~ 0.5 gev electron beam from a two-stage laser wakefield accelerator. *Phys. Rev. Lett.*, 107:045001.

Pukhov, A. (1999). Three-dimensional electromagnetic relativistic particle-in-cell code vlpl (virtual laser plasma lab). *Journal of Plasma Physics*, 61(03):425–433.

Pukhov, A. and Meyer-ter Vehn, J. (2002). Laser wake field acceleration: the highly non-linear broken-wave regime. *Applied Physics B*, 74(4-5):355–361.

Rax, J. M. (1992). Compton harmonic resonances, stochastic instabilities, quasilinear diffusion, and collisionless damping with ultra-high-intensity laser waves. *Physics of Fluids B: Plasma Physics (1989-1993)*, 4(12):3962–3972.

Rechatin, C., Davoine, X., Lifschitz, A., Ismail, A. B., Lim, J., Lefebvre, E., Faure, J., and Malka, V. (2009a). Observation of beam loading in a laser-plasma accelerator. *Phys. Rev. Lett.*, 103:194804.

Rechatin, C., Faure, J., Ben-Ismail, A., Lim, J., Fitour, R., Specka, A., Videau, H., Tafzi, A., Burgy, F., and Malka, V. (2009b). Controlling the phase-space volume of injected electrons in a laser-plasma accelerator. *Phys. Rev. Lett.*, 102:164801.

Rechatin, C., Faure, J., Lifschitz, A., Malka, V., and Lefebvre, E. (2007). Plasma wake inhibition at the collision of two laser pulses in an underdense plasma. *Physics of Plasmas (1994-present)*, 14(6):060702.

Reiche, S. (1999). GENESIS 1.3: a fully 3D time-dependent FEL simulation code. *Nuclear Instruments and Methods in Physics Research Section A: Accelerators, Spectrometers, Detectors and Associated Equipment*, 429(1-3):243–248.

Reiser, M. (2008). *Theory and Design of Charged Particle Beams*. Wiley Series in Beam Physics and Accelerator Technology. Wiley.

Rosenzweig, J. B., Breizman, B., Katsouleas, T., and Su, J. J. (1991). Acceleration and focusing of electrons in two-dimensional nonlinear plasma wake fields. *Phys. Rev. A*, 44:R6189–R6192.

Rousse, A., Phuoc, K. T., Shah, R., Pukhov, A., Lefebvre, E., Malka, V., Kiselev, S., Burgy, F., Rousseau, J.-P., Umstadter, D., and Hulin, D. (2004). Production of a kev x-ray beam from synchrotron radiation in relativistic laser-plasma interaction. *Phys. Rev. Lett.*, 93:135005.

Saldin, E. L. (1999). *The Physics of Free Electron Lasers*. Springer Berlin Heidelberg.

Schlenvoigt, H.-P., Haupt, K., Debus, A., Budde, F., Jackel, O., Pfotenhauer, S., Schwoerer, H., Rohwer, E., Gallacher, J. G., Brunetti, E., Shanks, R. P., Wiggins, S. M., and Jaroszynski, D. A. (2008). A compact synchrotron radiation source driven by a laser-plasma wakefield accelerator. *Nat Phys*, 4:130–133.

Schmid, K., Buck, A., Sears, C. M. S., Mikhailova, J. M., Tautz, R., Herrmann, D., Geissler, M., Krausz, F., and Veisz, L. (2010). Density-transition based electron injector for laser driven wakefield accelerators. *Phys. Rev. ST Accel. Beams*, 13:091301.

Schroeder, C. B., Esarey, E., Geddes, C. G. R., Benedetti, C., and Leemans, W. P. (2010). Physics considerations for laser-plasma linear colliders. *Phys. Rev. ST Accel. Beams*, 13:101301.

Schroeder, C. B., Lee, P. B., Wurtele, J. S., Esarey, E., and Leemans, W. P. (1999). Generation of ultrashort electron bunches by colliding laser pulses. *Phys. Rev. E*, 59:6037–6047.

Sheng, Z.-M., Mima, K., Sentoku, Y., Jovanović, M. S., Taguchi, T., Zhang, J., and Meyer-ter Vehn, J. (2002). Stochastic heating and acceleration of electrons in colliding laser fields in plasma. *Phys. Rev. Lett.*, 88:055004.

Spitkovsky, A. (2008). Particle Acceleration in Relativistic Collisionless Shocks: Fermi Process at Last? *The Astrophysical Journal Letters*, 682:L5–L8.

Sprangle, P., Esarey, E., Ting, A., and Joyce, G. (1988). Laser wakefield acceleration and relativistic optical guiding. *Applied Physics Letters*, 53(22):2146–2148.

Sprangle, P., Tang, C.-M., and Esarey, E. (1987). Relativistic self-focusing of short-pulse radiation beams in plasmas. *Plasma Science, IEEE Transactions on*, 15(2):145–153.

Sprangle, P., Zigler, A., and Esarey, E. (1991). Elimination of laser prepulse by relativistic guiding in a plasma. *Applied Physics Letters*, 58(4):346–348.

Steinhauer, L. C. and Ahlstrom, H. G. (1971). Propagation of coherent radiation in a cylindrical plasma column. *Physics of Fluids (1958-1988)*, 14(6):1109–1114.

Strickland, D. and Mourou, G. (1985). Compression of amplified chirped optical pulses. *Optics Communications*, 55(6):447 – 449.

Su, J. J., Katsouleas, T., Dawson, J. M., and Fedele, R. (1990). Plasma lenses for focusing particle beams. *Phys. Rev. A*, 41:3321–3331.

Ta Phuoc, K., Corde, S., Thaury, C., Malka, V., Tafzi, A., Goddet, J. P., Shah, R. C., Sebban, S., and Rousse, A. (2012). All-optical compton gamma-ray source. *Nat Photon*, 6(5):308–311.

Tajima, T. and Dawson, J. M. (1979). Laser electron accelerator. *Phys. Rev. Lett.*, 43:267–270.

Tanaka, T. and Shintake, T. (2005). SCSS X-FEL conceptual design report. *RIKEN Harima Institute, Hyogo, Japan.*

Thaury, C., Guillaume, E., Corde, S., Lehe, R., Le Bouteiller, M., Ta Phuoc, K., Davoine, X., Rax, J. M., Rousse, A., and Malka, V. (2013). Angular-momentum evolution in laser-plasma accelerators. *Phys. Rev. Lett.*, 111:135002.

Thomas, A. G. R. (2010). Algorithm for calculating spectral intensity due to charged particles in arbitrary motion. *Phys. Rev. ST Accel. Beams*, 13:020702.

Thompson, M. C., Badakov, H., Rosenzweig, J. B., Travish, G., Barov, N., Piot, P., Fliller, R., Kazakevich, G. M., Santucci, J., Li, J., and Tikhoplav, R. (2010). Observations of low-aberration plasma lens focusing of relativistic electron beams at the underdense threshold. *Physics of Plasmas (1994-present)*, 17(7):073105.

Togashi, T., Takahashi, E. J., Midorikawa, K., Aoyama, M., Yamakawa, K., Sato, T., Iwasaki, A., Owada, S., Okino, T., Yamanouchi, K., Kannari, F., Yagishita, A., Nakano, H., Couprie, M. E., Fukami, K., Hatsui, T., Hara, T., Kameshima, T., Kitamura, H., Kumagai, N., Matsubara, S., Nagasono, M., Ohashi, H., Ohshima, T., Otake, Y., Shintake, T., Tamasaku, K., Tanaka, H., Tanaka, T., Togawa, K., Tomizawa, H., Watanabe, T., Yabashi, M., and Ishikawa, T. (2011). Extreme ultraviolet free electron laser seeded with high-order harmonic of ti:sapphire laser. *Opt. Express*, 19(1):317–324.

Tomassini, P., Galimberti, M., Giulietti, A., Giulietti, D., Gizzi, L. A., Labate, L., and Pegoraro, F. (2003). Production of high-quality electron beams in numerical experiments of laser wakefield acceleration with longitudinal wave breaking. *Phys. Rev. ST Accel. Beams*, 6:121301.

Tzoufras, M., Lu, W., Tsung, F. S., Huang, C., Mori, W. B., Katsouleas, T., Vieira, J., Fonseca, R. A., and Silva, L. O. (2008). Beam loading in the nonlinear regime of plasma-based acceleration. *Phys. Rev. Lett.*, 101:145002.

Tzoufras, M., Lu, W., Tsung, F. S., Huang, C., Mori, W. B., Katsouleas, T., Vieira, J., Fonseca, R. A., and Silva, L. O. (2009). Beam loading by electrons in nonlinear plasma wakes. *Physics of Plasmas (1994-present)*, 16(5):056705.

Umstadter, D., Chen, S.-Y., Maksimchuk, A., Mourou, G., and Wagner, R. (1996a). Nonlinear optics in relativistic plasmas and laser wake field acceleration of electrons. *Science*, 273(5274):472–475.

Umstadter, D., Kim, J. K., and Dodd, E. (1996b). Laser injection of ultrashort electron pulses into wakefield plasma waves. *Phys. Rev. Lett.*, 76:2073–2076.

Vay, J.-L. (2007). Noninvariance of space- and time-scale ranges under a lorentz transformation and the implications for the study of relativistic interactions. *Phys. Rev. Lett.*, 98:130405.

Vay, J.-L. (2008). Simulation of beams or plasmas crossing at relativistic velocity. *Physics of Plasmas (1994-present)*, 15(5):056701.

Vay, J.-L., Geddes, C., Cormier-Michel, E., and Grote, D. (2011). Numerical methods for instability mitigation in the modeling of laser wakefield accelerators in a lorentz-boosted frame. *Journal of Computational Physics*, 230(15):5908 – 5929.

Vieira, J., Martins, J. L., Pathak, V. B., Fonseca, R. A., Mori, W. B., and Silva, L. O. (2012). Magnetically assisted self-injection and radiation generation for plasma-based acceleration. *Plasma Physics and Controlled Fusion*, 54(12):124044.

Vieira, J., Martins, S. F., Pathak, V. B., Fonseca, R. A., Mori, W. B., and Silva, L. O. (2011). Magnetic control of particle injection in plasma based accelerators. *Phys. Rev. Lett.*, 106:225001.

Wang, X., Zgadzaj, R., Fazel, N., Li, Z., Yi, S. A., Zhang, X., Henderson, W., Chang, Y.-Y., Korzekwa, R., Tsai, H.-E., Pai, C.-H., Quevedo, H., Dyer, G., Gaul, E., Martinez, M., Bernstein, A. C., Borger, T., Spinks, M., Donovan, M., Khudik, V., Shvets, G., Ditmire, T., and Downer, M. C. (2013). Quasi-monoenergetic laser-plasma acceleration of electrons to 2 gev. *Nat Commun*, 4. 1988.

Wangler, T., Crandall, K., Mills, R., and Reiser, M. (1985). Relation Between Field Energy and rms Emittance in Intense Particle Beams. *IEEE Trans.Nucl.Sci.*, 32:2196.

Whittum, D. H., Sessler, A. M., and Dawson, J. M. (1990). Ion-channel laser. *Phys. Rev. Lett.*, 64:2511–2514.

Williams, R., Clayton, C., Joshi, C., and Katsouleas, T. (1993). Studies of classical radiation emission from plasma wave undulators. *Plasma Science, IEEE Transactions on*, 21(1):156–166.

Xie, M. (2000). Exact and variational solutions of 3d eigenmodes in high gain fels. *Nuclear Instruments and Methods in Physics Research Section A: Accelerators, Spectrometers, Detectors and Associated Equipment*, 445:59 – 66.

Xu, X., Yu, P., Martins, S. F., Tsung, F. S., Decyk, V. K., Vieira, J., Fonseca, R. A., Lu, W., Silva, L. O., and Mori, W. B. (2013). Numerical instability due to relativistic plasma drift in em-pic simulations. *Computer Physics Communications*, 184(11):2503 – 2514.

Yee, K. (1966). Numerical solution of initial boundary value problems involving maxwell's equations in isotropic media. *Antennas and Propagation, IEEE Transactions on*, 14(3):302 –307.

Yi, S. A., Khudik, V., Kalmykov, S. Y., and Shvets, G. (2011). Hamiltonian analysis of electron self-injection and acceleration into an evolving plasma bubble. *Plasma Physics and Controlled Fusion*, 53(1):014012.

Yu, L.-H., Babzien, M., Ben-Zvi, I., DiMauro, L. F., Doyuran, A., Graves, W., Johnson, E., Krinsky, S., Malone, R., Pogorelsky, I., Skaritka, J., Rakowsky, G., Solomon, L., Wang, X. J., Woodle, M., Yakimenko, V., Biedron, S. G., Galayda, J. N., Gluskin, E., Jagger, J., Sajaev, V., and Vasserman, I. (2000). High-gain harmonic-generation free-electron laser. *Science*, 289(5481):932–934.

Résumé

Lorsque l'on focalise une impulsion laser courte et intense dans un gaz sous-dense, celle-ci peut accélérer une fraction des électrons du gaz, et ainsi générer un faisceau d'électrons ayant une énergie de quelques centaines de MeV. Ce phénomène, connu sous le nom d'accélération laser-plasma, pourrait avoir de nombreuses applications, notamment pour la réalisation de sources de rayons X ultra-intenses appelées lasers à électrons libres (LEL). Cependant, ces applications nécessitent que le faisceau d'électrons ait une excellente qualité (faible divergence, faible émittance et faible dispersion en énergie).

Au cours de cette thèse, différentes solutions ont été développées afin d'améliorer la qualité des faisceaux d'électrons issus de l'accélération laser-plasma. Ce travail est effectué à travers des modèles analytiques ainsi que des simulations Particle-In-Cell (PIC). Nous commençons cependant par montrer que les simulations PIC ont tendance à surestimer l'émittance du faisceau, en raison de l'effet Cherenkov numérique. Afin d'estimer correctement l'émittance ici, nous proposons un algorithme PIC modifié qui n'est pas sujet à l'effet Cherenkov numérique.

A l'aide de cet algorithme, un nouveau mécanisme permettant de générer le faisceau est observé puis étudié : il s'agit de l'*injection optique transverse*. Les faisceaux produits par ce mécanisme sont caractérisés par une forte charge, une faible divergence et une faible émittance. Par ailleurs, nous proposons un dispositif – la *lentille laser-plasma* – qui permet de fortement réduire la divergence finale des faisceaux. Ces résultats sont placés dans leur contexte, à travers une discussion des propriétés nécessaires pour un laser à électrons libres compact. Nous montrons en particulier que les accélérateurs laser-plasma pourraient être avantageusement combinés avec des onduleurs laser-plasma innovants, afin de produire des sources de rayons X intenses.

Abstract

When an intense and short laser pulse propagates through an underdense gas, it can accelerate a fraction of the electrons of the gas, and thereby generate an electron bunch with an energy of a few hundreds of MeV. This phenomenon, which is referred to as laser-wakefield acceleration, has many potential applications, including the design of ultra-bright X-ray sources known as free electron lasers (FEL). However, these applications require the electron bunch to have an excellent quality (low divergence, emittance and energy spread).

In this thesis, different solutions to improve the quality of the electron bunch are developed, both analytically and through the use of Particle-In-Cell (PIC) simulations. It is first shown however that PIC simulations tend to erroneously overestimate the emittance of the bunch, due to the numerical Cherenkov effect. Thus, in order to correctly estimate the emittance, a modified PIC algorithm is proposed, which is not subject to this unphysical Cherenkov effect.

Using this algorithm, we observed and studied a new mechanism to generate the electron bunch: *optical transverse injection*. This mechanism can produce bunches with a high charge, a low emittance and a low energy spread. In addition, we also proposed an experimental setup – the *laser-plasma lens* – which can strongly reduce the final divergence of the bunch. Finally, these results are put into context by discussing the properties required for the design of a compact FEL. It is shown in particular that laser-wakefield accelerator could be advantageously combined with innovative laser-plasma undulators, in order to produce bright X-rays sources.